Development of Electrical Quality Assurance Procedures and Methods for the Silicon Tracking System of the CBM Experiment

Dissertation
der Mathematisch-Naturwissenschaftlichen Fakultät
der Eberhard Karls Universität Tübingen
zur Erlangung des Grades eines
Doktors der Naturwissenschaften
(Dr. rer. nat.)

vorgelegt von
Iaroslav Panasenko
aus Oleksandrivka, Ukraine

Tübingen
2022

Gedruckt mit Genehmigung der Mathematisch-Naturwissenschaftlichen Fakultät der Eberhard Karls Universität Tübingen.

Tag der mündlichen Qualifikation:	17.03.2023
Dekan:	Prof. Dr. Thilo Stehle
1. Berichterstatter:	Prof. Dr. Hans Rudolf Schmidt
2. Berichterstatter:	Prof. Dr. Tobias Lachenmaier

to my mother

Abstract

Position-sensitive silicon detectors have been used in particle physics experiments for more than 40 years. Technological advances have made it possible to build large-area silicon trackers with millions of channels. Double-sided silicon microstrip detectors have been selected as the sensor technology for the Silicon Tracking System (STS) of the Compressed Baryonic Matter (CBM) experiment at the Facility for Antiproton and Ion Research (FAIR). The goal of the CBM experiment is to investigate the properties of strongly interacting matter at high baryon density in relativistic heavy ion collisions. The challenge is to perform measurements at interaction rates of up to 10 MHz. This will give access to extremely rare observables such as multi-strange hyperons or hadrons with charm quarks. Up to 700 particles per collision are expected within detector acceptance. Their tracks and thus their momentum are measured in the STS with high resolution. The STS consists of 876 microstrip sensors with a total area of about $4\,\mathrm{m}^2$. Each sensor has 1024 strips per side, resulting in a total of about 1.8×10^6 channels.

To ensure high-precision measurement, the STS must use high-quality microstrip sensors. The fraction of defective strips should not exceed 1.5 % per sensor. The sensors must also meet CBM specifications for the electrical parameters. The work presented in this thesis focuses on the quality assurance of microstrip sensors. For this purpose, a highly automated probe station was designed and built at the University of Tübingen. The methods for determining the electrical characteristics of microstrip sensors were developed. This made it possible to investigate the prototype sensors for STS in detail.

The results and challenges are discussed in detail. Suggestions are provided that can help improve sensor design. As a result of the conducted quality assurance, the acceptance criteria for CBM microstrip sensors at the series production stage were defined. The developed quality control methods made it possible to reliably identify defective strips. This allows for the selection of high-quality sensors for the construction of the STS and ensures high data quality during the operation of the CBM experiment.

Zusammenfassung

Positionsempfindliche Siliziumdetektoren werden seit mehr als 40 Jahren in Experimenten der Teilchenphysik eingesetzt. Technologische Fortschritte haben es möglich gemacht, großflächige Silizium-Tracker mit Millionen von Kanälen zu bauen. Als Sensortechnologie für das Silicon Tracking System (STS) des Compressed Baryonic Matter (CBM) Experiments an der Facility for Antiproton and Ion Research (FAIR) wurden doppelseitige Silizium-Mikrostreifen-Detektoren ausgewählt. Das Ziel des CBM-Experiments ist es, die Eigenschaften von stark wechselwirkender Materie bei hoher Baryonendichte in relativistischen Schwerionenkollisionen zu untersuchen. Dabei ist die Herausforderung die Messungen mit Wechselwirkungsraten von bis zu 10 MHz durchzuführen. Dies wird den Zugang zu extrem seltenen Observablen wie multi-seltsamen Hyperonen oder Hadronen mit Charm-Quarks ermöglichen. Innerhalb der Detektorakzeptanz werden bis zu 700 Teilchen pro Kollision erwartet. Ihre Spuren und somit ihr Impuls werden im STS mit hoher Auflösung vermessen. Der STS besteht aus 876 Mikrostreifensensoren mit einer Gesamtfläche von etwa 4 m^2. Jeder Sensor hat 1024 Streifen pro Seite, was insgesamt etwa 1.8×10^6 Kanäle ergibt.

Um eine hochpräzise Messung zu gewährleisten, muss der STS hochwertige Mikrostreifensensoren verwenden. Der Anteil fehlerhafter Streifen sollte 1.5 % pro Sensor nicht überschreiten. Die Sensoren müssen auch die CBM-Spezifikationen für die elektrischen Parameter erfüllen. Die in dieser Dissertation vorgestellten Arbeiten konzentrieren sich auf die Qualitätssicherung von Mikrostreifensensoren. Zu diesem Zweck wurde an der Universität Tübingen eine hochautomatisierte Sondenstation entworfen und gebaut. Die Methoden zur Bestimmung der elektrischen Eigenschaften von Mikrostreifensensoren wurden entwickelt. Dadurch war es möglich, die Prototyp-Sensoren für STS im Detail zu untersuchen.

Ergebnisse und Herausforderungen werden ausführlich besprochen. Es werden Vorschläge bereitgestellt, die zur Verbesserung des Sensordesigns beitragen können. Als Ergebnis der durchgeführten Qualitätssicherung wurden die Abnahmekriterien für CBM-Mikrostreifensensoren im Serienstadium definiert. Die entwickelten Methoden zur Qualitätskontrolle ermöglichten es, fehlerhafte Streifen zuverlässig zu identifizieren. Dies ermöglicht die Auswahl hochwertiger Sensoren für den Bau des STS und gewährleistet eine hohe Datenqualität während des Betriebs des CBM-Experiments.

Contents

1. Introduction **1**
1.1. Silicon Detectors 1
1.2. Nuclear Matter at Extreme Conditions 4
1.3. The Compressed Baryonic Matter Experiment 6
1.4. The Silicon Tracking System 8
1.5. Motivation for Characterization and Qualification of the Sensors . 11
1.6. Scope of the thesis 12

2. Silicon Microstrip Sensors for CBM-STS **13**
2.1. Design of the Sensors 14
2.2. Specifications for the Sensors 24
2.2.1. Silicon Wafer Properties 24
2.2.2. Sensor Geometrical Properties 24
2.2.3. Sensor Electrical Properties 25
2.2.4. Sensor Radiation Tolerance 25
2.2.5. Environmental Conditions 27
2.2.6. Number of Sensors 27

3. Custom Automated Probe Station **29**
3.1. Setup Overview 29
3.1.1. Motor Stages 29
3.1.2. Vacuum Chuck 30
3.1.3. Vacuum Line 31
3.1.4. Probes 31
3.1.5. Optical System 33
3.2. System Calibration 33
3.2.1. Optical Axis Alignment 33
3.2.2. Determination of Working Parameters 34
3.2.3. Light Intensity 34
3.2.4. Pixel Mapping 36
3.2.5. Sensor Alignment 37
3.2.6. Sensor Coordinate Transformation 37
3.2.7. Height Measurement 39
3.2.8. Height Adjustment 41
3.2.9. Performance Estimation 42
3.3. Measurement Equipment 44

3.3.1. Switching Scheme . . . 44
3.3.2. Capacitance Measurement . . . 45
3.3.3. Performance Estimation . . . 47
3.3.3.1. CMS Test Structures . . . 47
3.3.3.2. STS Micro Cables . . . 48
3.4. Software Solution . . . 49
3.4.1. Probe Station Control . . . 49
3.4.2. Measurement and Data Acquisition . . . 51
3.4.3. Data Analysis . . . 52
3.5. Throughput Estimation . . . 54

4. Electrical Characterization of Silicon Microstrip Sensors 55
4.1. Global Parameters . . . 55
4.1.1. Total Leakage Current . . . 55
4.1.2. Bulk and Surface Current . . . 60
4.1.3. Full Depletion Voltage . . . 70
4.2. Strip Parameters . . . 82
4.2.1. Strip Leakage Current . . . 82
4.2.2. Polysilicon Bias Resistance . . . 89
4.2.3. Punch-through Voltage . . . 97
4.2.4. Metal Strip Resistance . . . 103
4.2.5. Strip Coupling Capacitance . . . 108
4.2.6. Strip Backplane Capacitance . . . 127
4.2.7. Interstrip Capacitance . . . 132
4.2.8. Overlap Capacitance . . . 148
4.2.9. Total Strip Capacitance . . . 152
4.3. Strip Integrity . . . 157
4.3.1. Coupling Dielectric Layer . . . 158

5. SPICE Simulation of Microstrip Sensors 163
5.1. SPICE Model . . . 163
5.1.1. Microstrip Sensor . . . 164
5.1.2. LCR Meter . . . 166
5.1.3. Running the Simulation . . . 167
5.2. Strip Coupling Capacitance . . . 167
5.3. Bulk Capacitance . . . 172
5.4. Interstrip Capacitance . . . 173
5.5. Strip Leakage Current . . . 175

6. CBM-STS Quality Assurance Program 179
6.1. Acceptance Criteria . . . 179
6.2. Strip Defect Rate . . . 180
6.3. Defect Classes . . . 180
6.4. Quality Control Tests . . . 184

6.5. Infrastructure 184
6.6. Test Sockets for Sensors 185
6.7. Needles and Contact Pads 187
6.8. Strip Data Analysis 188
6.8.1. Signatures of Defects 189
6.8.2. Detection of Defective Strips 192
6.8.3. Recognition of Strip Defects 192
6.9. Quality of the CBM sensors 193
6.9.1. Prototype Testing Results 193
6.9.2. Production Testing Results 195

7. Summary **197**

A. List of the Investigated CBM Microstrip Sensors **199**

B. Measured Bulk Parameters of the CBM Prototype Sensors **201**

C. Switching Matrix Channel Configuration **203**

Bibliography **205**

List of Figures **219**

List of Tables **225**

Acknowledgments **227**

1. Introduction

1.1. Silicon Detectors

Our present understanding of the universe is described by the Standard Model of Particle Physics. Experimental confirmation of its predictions would not be possible without precision instrumentation — particle detectors. In particle physics experiments, electrons, protons and even heavy ions are accelerated to high energies and smash into each other or a fixed target, producing a variety of particles in the final state. Essentially, it is necessary to identify and measure the momentum and energy of stable charged particles. Tracking their trajectories in the magnetic field allows to determine momenta and charge. Reconstruction of unstable particles requires determination of their decay vertex. Therefore, the detector has to be located very close to the interaction point and provide high spatial resolution. The material budget of the detector has to be minimized to reduce multiple scattering, which limits the resolution for low momentum tracks. Central collisions of heavy ions lead to a large number of particles produced, which requires a high granularity of the detector to achieve good position resolution and to resolve tracks. Moreover, high collision rates are necessary to study rare processes, which means that the detector has to be fast. This also results in high radiation doses that the detector has to withstand during the lifetime of the experiment. Silicon sensors comply with the above requirements [1, 2]. In particular, silicon strip sensors have been used for many decades to build tracking detectors and do not lose their relevance even today.

The silicon tracking era began with the application of the planar process to the fabrication of *pn*-junction detectors in 1980 by J. Kemmer [3]. It made it possible to produce position-sensitive detectors with fine segmentation and low leakage current.The first successful application of such detectors was in the NA11 experiment [4, 5] at the CERN Super Proton Synchrotron (SPS) to measure the lifetime and mass of charmed mesons. Six single-sided DC-coupled sensors with 1200 strips, 20 µm pitch, active area of $24 \times 36\,\mathrm{mm}^2$ were arranged in 3 tracking planes. To each of the first two sensors 120 channels of readout electronics were connected, and 240 channels to each of the remaining sensors. Readout pitch of 60 µm(120 µm) provided a spatial resolution of 4.5 µm(7 µm). This allowed to identify the decays of D-mesons and reconstruct their flight paths. The ratio of the detector area to the electronics in the NA11 experiment was 1:300, and further application of silicon sensors was accompanied by the miniaturization of

the electronics.

Starting from 1989 several experiments were built and equipped with silicon detectors around the interaction points of colliders: ALEPH [6] and DELPHI [7, 8] at CERN Large Electron-Positron Collider (LEP), CDF [9, 10] and D0 [11] at Fermilab Tevatron collider. All detectors had several upgrade phases to improve performance.

ALEPH was the first experiment to use double-sided strip sensors in its vertex detector. The sensors were DC-coupled with 25 µm strip pitch. The sensitive area of the ALEPH vertex detector was $0.96\,\mathrm{m}^2$ with 95×10^3 channels[1]. The DELPHI vertex detector was upgraded from single-sided to double-sided strip sensors with integrated AC-coupling capacitors and polysilicon resistors. To maintain the same material budget, DELPHI developed the sensors with the 2nd metal layer on the n side making it possible to connect the electronics from both sides at the same edge of the sensor. The total sensitive area was $1.78\,\mathrm{m}^2$, covered with 736 strip sensors with 174×10^3 channels. In addition, its forward region was equipped with hybrid pixel detectors with about 1.2×10^6 pixels [12]. The information from these vertex detectors allowed to tag b quarks and determine the flight paths of short-lived particles with high precision.

CDF and D0 experiments operated at a hadron collider. Compared to electron machines, the inner layers of the detectors were exposed to severe radiation damage [2] and required radiation hard silicon sensors. Both single-sided and double-sided double-metal AC-coupled strip sensors were used. Part of the sensors were produced on 6-inch wafers for the first time. In the upgraded version, the $3\,\mathrm{m}^2$ D0 silicon tracker had 792×10^3 channels. The area of the CDF vertex detector was $6\,\mathrm{m}^2$ with 722×10^3 channels. With the help of silicon vertex detectors, the CDF and D0 collaborations discovered the top quark in 1995. Precision measurements of the top mass were performed with the upgraded detectors.

In 2008 the largest scale of integration was achieved in the ATLAS [14] and CMS [15] experiments at the CERN Large Hadron Collider (LHC). Vertexing is performed in the inner silicon pixel detectors, while tracking is handled by silicon strip detectors[3]. Both vertex detectors use hybrid pixel sensors produced on oxygenated n-type wafers with n^+ readout pixels. Their silicon trackers are equipped with single-sided n-type sensors with AC-coupled p^+ readout strips. The strip sensors were designed to operate up to a fluence of $2 \times 10^{14}\,\mathrm{n}_{eq}/\mathrm{cm}^2$. CMS decided to use wafers with $\langle 100 \rangle$ crystal orientation instead of a common $\langle 111 \rangle$. The choice was driven by the observation of a lower interstrip capacitance after irradiation.

[1] Here and further, the channel is a readout channel, i.e. a strip connected to readout electronics. To reduce the number of readout channels, typically every 2nd strip was connected.

[2] Details on radiation damage to silicon sensors are given in Ref. [13].

[3] Previously, tracking was mostly the task of gaseous detectors that allow covering a much larger volume. While there is a shift towards all-silicon trackers, the ALICE [16] experiment at the LHC uses the large Time-Projection Chamber(TPC) as its main tracking detector. It was optimized for momentum measurement and particle identification at high multiplicities of heavy-ion collisions.

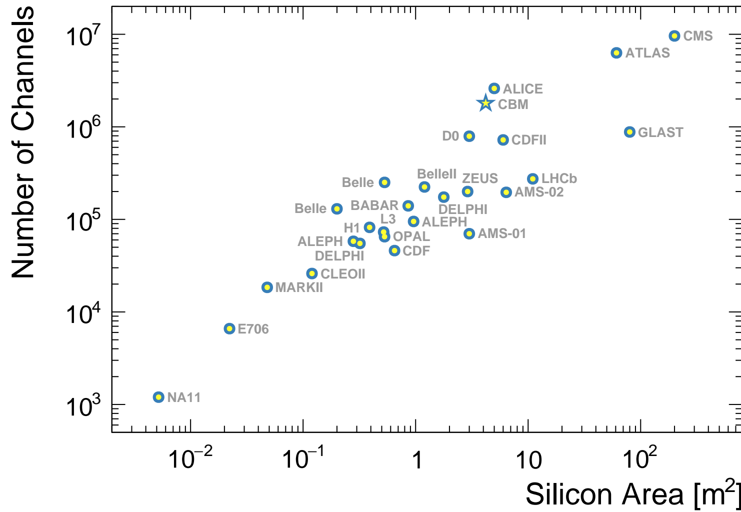

Figure 1.1.: The number of readout channels versus the silicon area for the strip detectors of the particle physics experiments. An increase in scale by 4 orders of magnitude took place over the past 40 years. Fixed-target, collider, and space-based experiments are shown. CBM as a future experiment is marked with a star.

The total area of the ATLAS silicon detector is about $60\,\mathrm{m}^2$ with 6.3×10^6 channels. The CMS silicon detector is even bigger — $200\,\mathrm{m}^2$ with 9.6×10^6 channels. With such large areas, special attention must be paid to integration, powering, cooling, and material support. The ATLAS and CMS silicon detectors allow for the reconstruction of complicated decays and the determination of interaction and secondary vertices with high precision. These led to the discovery of the Higgs boson in 2012.

Considering just these few examples, it is clear that silicon detectors have become a fundamental part of any particle physics experiment and are critical for many discoveries. Figure 1.1 shows the number of readout channels versus the silicon area for the strip detectors of the particle physics experiments. From the first application of the strip sensors, the instrumented area has grown from about $40\,\mathrm{cm}^2$ with a few hundred channels to $200\,\mathrm{m}^2$ with ~ 10 million channels. One of the key issues for strip sensors is the considerable degradation of charge collection efficiency after fluences of the order of $1 \times 10^{15}\,\mathrm{n}_{eq}/\mathrm{cm}^2$. The ATLAS [17] and CMS [18] collaborations decided to use *n-in-p*[4] silicon sensors for their strip trackers upgrade due to their higher radiation hardness compared to *p-in-n*[5]. The MAPS[6] manufactured using CMOS imaging technologies become the preferred option for vertex detectors. They can be made very thin providing a lower material budget than hybrid pixel sensors and a single-chip solution with-

[4] *n*-type implants in a *p*-type bulk.
[5] *p*-type implants in a *n*-type bulk.
[6] Monolithic Active Pixel Sensor.

out bump bonding. This allows for improved tracking precision and efficiency for low-momentum tracks, which is critical to achieving the physics goals. In 2014 MAPS have been installed in the STAR [19] vertex detector at the BNL Relativistic Heavy Ion Collider (RHIC). During the Long Shutdown-2 of the LHC, the entire silicon tracker of the ALICE [20] detector was replaced with a seven-layer MAPS-based tracker. They are also planned for the vertex detector of the CBM experiment at the FAIR facility.

Future and today's upgraded experiments will operate at extremely high interaction rates which are dictated by rare physics observables. The spacial resolution, radiation hardness, and timing precision of the sensors are required at the same time. New key technologies [21] are planar Low-Gain Avalanche Diodes (LGADs) and 3D sensors. The best performance in terms of timing precision for these sensors is about 20–30 ps. Sensors based on the LGAD technology have now been chosen for the timing layers to upgrade the ATLAS and CMS detectors for the HL-LHC[7]. The 3D sensors demonstrated noticeable efficiency even up to a fluence of $\sim 3 \times 10^{16}\,\mathrm{n}_{eq}/\mathrm{cm}^2$ [22] and will be used in the ATLAS [23] pixel detector at the HL-LHC.

The CBM [24] experiment dedicated to the study of dense baryonic matter enters the construction phase. It will have all-silicon vertex and tracking detectors designed to operate at the highest interaction rates of 0.1–10 MHz. The tracking detector will be built with double-sided double-metal strip sensors, which are the subject of this thesis.

1.2. Nuclear Matter at Extreme Conditions

Interesting phenomena begin to occur when the parameters describing the system reach high/critical values. Nuclear matter is expected to exist in different phases depending on temperature and density. Figure 1.2 shows the conjectured phase diagram of the strongly-interacting matter as a function of temperature T versus baryon chemical potential[8] μ_B. Quarks and gluons are bound into hadrons in the case of the hadron gas phase. The system of deconfined quarks and gluons is called a Quark-Gluon Plasma (QGP). A deconfinement transition becomes possible at sufficiently high temperature and/or baryon density. The investigation of the nuclear matter under extreme conditions is one of the main research topics of modern physics.

In the laboratory, QGP can be created by colliding heavy nuclei. The regions of the diagram that can be accessed depend on the collision energy. The very high beam energies at the RHIC and LHC facilities are suitable to produce a QGP at nearly vanishing baryon chemical potential. According to lattice QCD

[7] High Luminosity LHC

[8] The baryon chemical potential is a measure of the difference between matter and antimatter which is produced in the heavy-ion collisions.

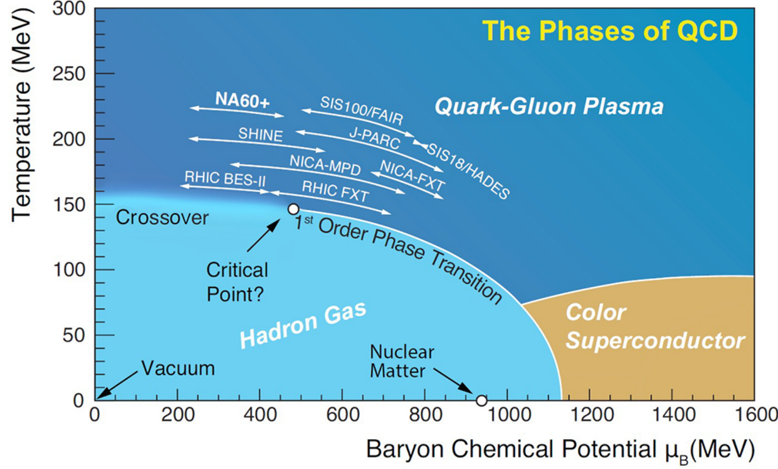

Figure 1.2.: Sketch of the phase diagram of strongly-interacting matter represented in the plane of temperature and baryochemical potential (Adapted from Ref. [25]).

calculations in Ref. [26], a smooth crossover transition to hadronic matter occurs at a pseudo-critical temperature of 156.5 ± 1.5 MeV and vanishing μ_B. This value is consistent with the chemical freeze-out temperature extracted from the particle yields measured by the ALICE collaboration for the most central Pb+Pb collisions [27]. At large values of μ_B, a first-order phase transition with a critical end point (CEP) is predicted. This region is essentially unknown and is of the highest experimental interest. Functional approaches to solving QCD indicate that the location of the CEP is disfavored for $\mu_B/T \leq 4$ [28]. Recent calculations in Ref. [29] for a $2+1$ - flavor QCD found a CEP at $T_{CEP} = 93$ MeV and $\mu_{B_{CEP}} = 672$ MeV. Figure 1.2 schematically shows the regions of the phase diagram accessible by ongoing and future heavy-ion facilities. The baryon chemical potential depends on the energy of the collision. For the quoted prediction of CEP, the required center-of-mass beam energy per nucleon is about 3.3 GeV. Therefore, its location will be accessible at SIS100/FAIR beam energies [30].

Another fundamental question to be addressed is the high-density equation of state (EoS) of nuclear matter. According to the different models' predictions in Ref. [31], in central Au+Au collisions at a beam energy of 5 AGeV, the nuclear fireball will be compressed to about 5 times the saturation density n_{sat}, and at 10 AGeV a density of $8n_{sat}$ is reached. Dense nuclear matter, similar to that produced in the heavy-ion collision, might exist during binary neutron star mergers, where temperature can reach up to 100 MeV [32]. Although the scale of the heavy-ion collision and the two colliding neutron stars are different, the dynamics of both events should follow the same high-density EoS. The equation of state can be mapped to a relationship between the macroscopic observables of neutron stars, such as their mass, radius, and tidal deformability. The tidal deformation of neutron stars spiraling into each other leads to a detectable imprint on the gravitational wave (GW) signal. Therefore, the constraints on the EoS of dense

matter can be deduced from the frequency analysis of the GWs. In 2017, the first GW signal from the merger of two neutron stars was reported by the LIGO-Virgo collaboration in an event labeled GW170817 [33]. The constraints on the EoS can also be established from the determination of the mass and radius of neutron stars in electromagnetic observations. The NICER telescope attempts to do this by recording the soft X-ray emission from hot spots on the surface of rotating neutron stars [34]. Modeling the X-ray waveform constrains the compactness (mass-to-radius ratio) of the neutron star and hence the EoS. To further constrain the EoS, information from nuclear theory, astrophysical observations of neutron stars, and results from HIC experiments have to be combined. Such an analysis was carried out in Ref. [35] and new constraints on the EoS of nuclear matter at densities up to about $2n_{sat}$ were obtained. The future CBM experiment will probe densities up to $8n_{sat}$ in HICs at SIS100/FAIR energies, which will further constrain the EoS of the high-density matter.

Nucleus-nucleus collisions at various energies allow to scan the phase diagram. The experimental observables which are sensitive to the properties of dense nuclear matter are the flow of identified particles, event-by-event fluctuations of conserved quantities, (multi-)strange hyperons and hyper-nuclei, di-leptons, and particles containing charm quarks [36]. For example, the collective flow of identified particles is driven by the pressure gradient in the reaction volume and is sensitive to the equation of state of nuclear matter. Most of the above observables are very rare, or have not been measured yet at high μ_B with high precision. High statistics can be acquired with high interaction rates. This leads to the necessity of the CBM experiment designed to operate at the highest interaction rates in the high-μ_B region. The rate capabilities of existing and planned HIC experiments are compared in Fig. 1.3 as a function of center-of-mass energy. The interaction rates shown are limited either by the detector capabilities or by luminosity. An overview of the facilities for high μ_B physics can be found in Ref. [37].

1.3. The Compressed Baryonic Matter Experiment

The Compressed Baryonic Matter (CBM) experiment at the Facility for Antiproton and Ion Research (FAIR) will investigate the properties of nuclear matter at extreme conditions created in relativistic heavy ion collisions. The SIS100[9] heavy ion synchrotron will deliver Au ion beams with energies between 2–12 AGeV, and protons up to 29 GeV. The energy range accessible by the CBM will allow exploration of the QCD phase diagram at baryon densities corresponding to $\mu_B \approx 500$–800 MeV. Theoretical investigations indicate that the CEP is located at a value that can be reached by the SIS100 synchrotron [29]. The discovery of

[9] SchwerIonenSynchrotron, GSI, Germany.

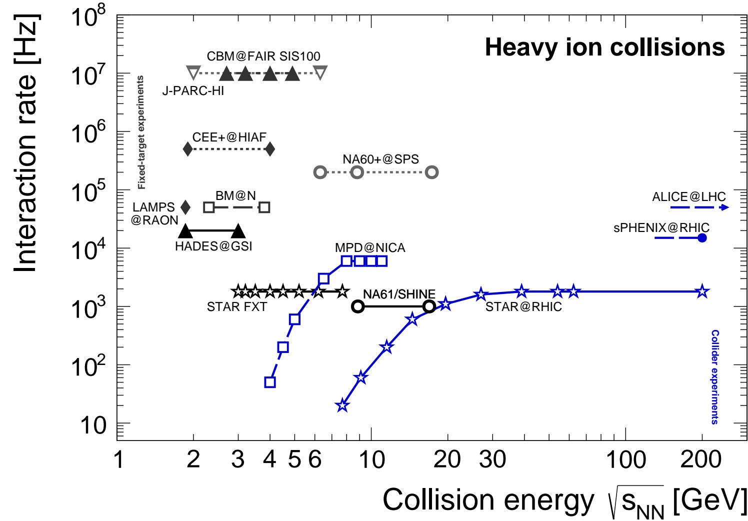

Figure 1.3.: Interaction rates achieved by existing and planned heavy ion experiments as a function of center-of-mass energy [37].

a first-order phase transition is expected.

The CBM experiment is designed to operate at reaction rates of 100 kHz up to 10 MHz. To utilize maximum rates, the data acquisition system is based on self-triggered front-end electronics. All detector signals are time-stamped and forwarded by a high-speed network to a high-performance computing center of GSI, the GreenIT cube, where the event reconstruction and selection are performed in software. The combination of high-intensity beams with a high-rate detector system provides a unique opportunity to perform measurements of rare particles as probes of dense baryonic matter with high precision. The overall physics program of CBM is outlined in Ref. [38] and addresses all topics relevant to the characterization of dense baryonic matter.

The layout of the CBM detector with its different subsystems is shown in Fig. 1.4. The CBM setup is a fixed-target experiment with the forward detector geometry. The central detector of the CBM experiment is the Silicon Tracking System (STS) [39], located in a magnetic field of a superconducting dipole magnet [40]. It will measure the tracks of charged particles emitted in beam-target collisions. The STS is described in the next section. The Micro-Vertex Detector (MVD), consisting of four layers of MAPS located in front of the STS, will provide a high-precision measurement of short-lived particles like charm mesons. The identification of hadrons will be performed by the Time-of-Flight (TOF) system [41], which consists of Multi-Gap Resistive Plate Chambers. Muons will be measured by the Muon Chamber (MUCH) system [42], consisting of hadron absorbers and GEM[10]/RPC[11] detector planes. The identification of electrons and

[10]Gas Electron Multiplier.
[11]Resistive Plate Chamber.

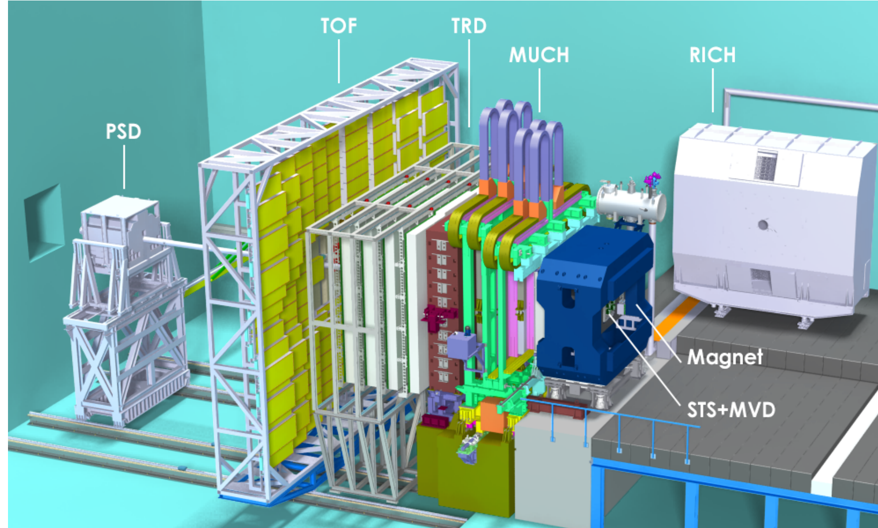

Figure 1.4.: The CBM experimental setup. The STS and MVD are placed inside the superconducting dipole magnet. The RICH is shown in a parking position. For electron measurements, the MUCH will be exchanged by the RICH.

positrons will be performed by the Ring Imaging Cherenkov (RICH) detector [43] and the Transition Radiation Detector (TRD) [44]. Determination of the centrality of the collision and the reaction plane angle will be performed by the Projectile Spectator Detector[12] (PSD) [45]. CBM can be operated in different configurations [24], with the STS being common to all setups.

According to the schedule, the CBM experiment with the day-1 setup will be ready to take the first collision data in 2028[13]. Detector installation is planned for 2024 ending with the commissioning phase that is anticipated for 2026. Detailed information on the hardware and software developments towards the realization of the CBM experiment is presented in Ref. [46]. In order to perform a full system test of the CBM pre-series and prototype detectors, data readout and acquisition chains, the mini-CBM (mCBM) setup [47] has been constructed and installed at SIS18.

1.4. The Silicon Tracking System

The Silicon Tracking System located in the gap of a 1 T m superconducting dipole magnet is the core detector of the CBM experiment. It will provide track reconstruction and momentum determination of the charged particles produced in

[12]PSD was supposed to be produced by Russia. Due to Russia's war of aggression against Ukraine, cooperation was terminated. At the moment, it is planned to replace the PSD with a forward wall with plastic scintillators.

[13]Due to Russia's war of aggression against Ukraine, all planning will have to be revised. Preliminary estimated start of operation — 2029.

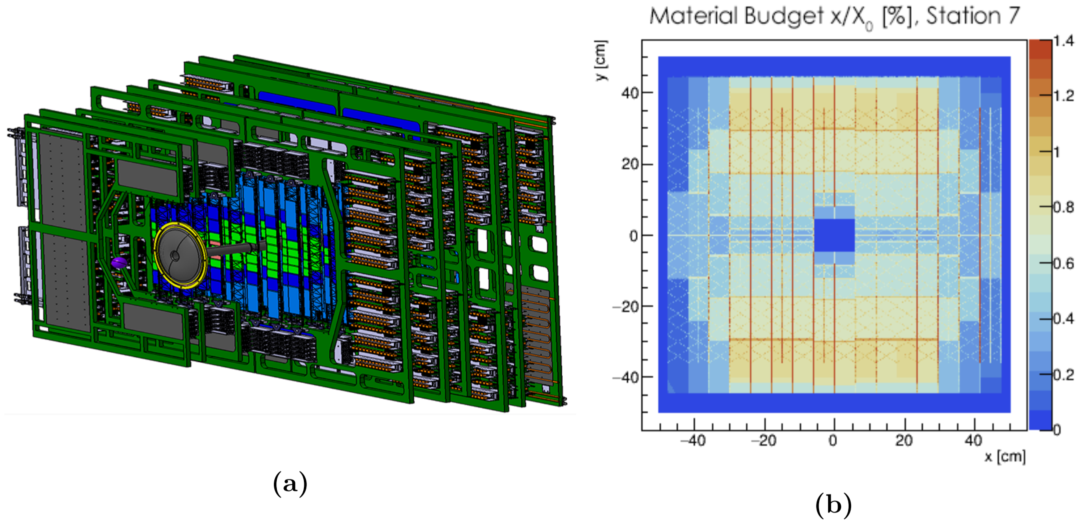

(a)

(b)

Figure 1.5.: The Silicon Tracking System of the CBM experiment: (a) The conceptual design of the STS. The silicon sensors are shown in blue and bright green colors, covering the space around the beam pipe. The readout electronics are located on C-shaped support structures shown in green. (b) Distribution of the material budget of the STS station 7. It increases to the periphery on top and bottom due to layers of micro-cables.

beam-target interactions. The STS consists of 8 tracking stations and has an aperture of $2.5° < \Theta < 25°$. The stations are located at distances between 30 and 100 cm downstream of the target. The momentum resolution of the STS required for physics observables is $\Delta p/p \approx 1.8\,\%$ (at $p \geq 1\,\mathrm{GeV}/c$, 1 T m field). It is dominated by multiple Coulomb scattering in the detector material. Therefore, the design of the STS is focused on minimization of the material budget. Front-end electronics, cooling and mechanical infrastructure are therefore located outside of the sensitive volume of the detector.

Figure 1.5a shows the conceptual design of the STS. The tracking stations are populated with 876 double-sided silicon microstrip sensors [48] with a total area of $4\,\mathrm{m}^2$. The sensors are 320 µm thick and contribute $0.34\,\%X_0$ to the total material budget of the station. They are mounted on low mass carbon-fiber (CF) support ladders [49]. Ultra-thin cables (up to 50 cm in length) connect strips of the sensor to the readout channels of the ASIC[14]. The micro-cables [50] are built from sandwiched polyimide-Aluminum layers several 10 µm thick with a total radiation length of 0.124 %. This increases the material budget in the outer sensitive regions of the STS to a maximum of $\approx 1\,\%X_0$ per station [51]. The material budget distribution of one of the STS stations is shown in Fig. 1.5b.

The functional building block of the STS is the detector module. It comprises a double-sided silicon sensor with 2048 strips, 32 micro-cables with 64

[14]Application Specific Integrated Circuit.

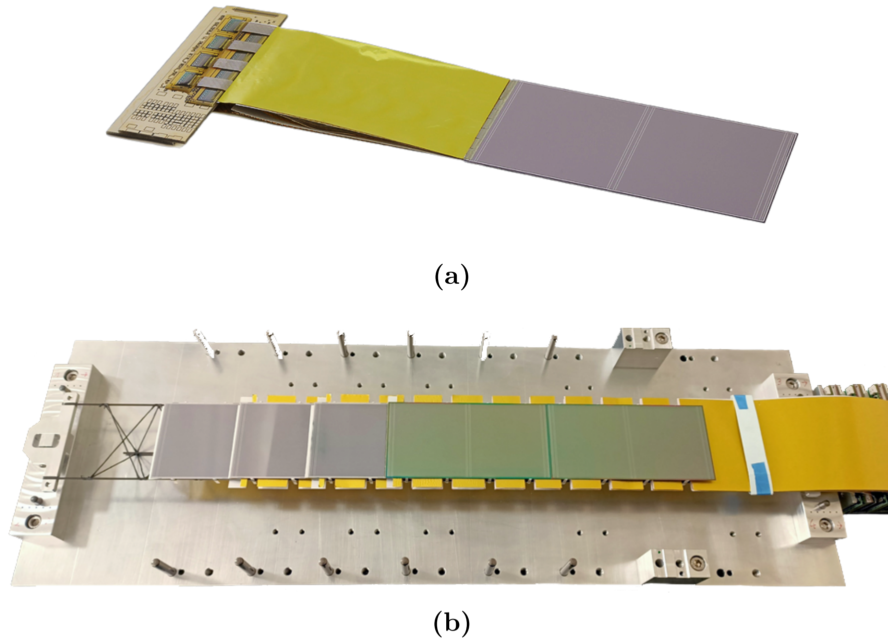

(a)

(b)

Figure 1.6.: STS detector component prototypes: (a) A module with a $62 \times 124\,\mathrm{mm}^2$ microstrip sensor is shown here. In the final assembly, the microstrip sensor is also covered with a metal shielding layer. (b) The assembled prototype of a half-ladder with 5 microstrip sensors is shown. The carbon-fiber support structure is visible on the left, and the front-end box is on the right.

lines each, and 2 front-end boards each carrying 8 ASICs with 128 channels each. The microstrip sensors have been manufactured by Hamamatsu Photonics KK, Japan. The micro-cables have been designed and manufactured at LTU in Kharkiv, Ukraine [52]. The readout ASIC STS-XYTER has been designed at AGH University of Science and Technology in Krakow, Poland [53, 54]. A photo of the prototype module is shown in Fig. 1.6a. Depending on the location within the STS station, modules of different form factors (sensor sizes and micro-cable lengths) will be produced. In total, 106 ladders will populate all tracking stations of the STS. A photo of the prototype half-ladder is shown in Fig. 1.6b.

The STS will perform measurements at interaction rates of up to 10 MHz. The multiplicity of charged particles reaches up to 700 within the detector acceptance. To keep the maximum strip occupancy at the level of a few percent and to match the particle density in different regions of the STS, sensors of 4 different sizes ($62 \times 22\,\mathrm{mm}^2$, $62 \times 42\,\mathrm{mm}^2$, $62 \times 62\,\mathrm{mm}^2$, $62 \times 124\,\mathrm{mm}^2$) will be used. To avoid pile-up of events, fast self-triggering front-end electronics will provide a time-stamp resolution of $< 5\,\mathrm{ns}$.

A total of $\approx 14\,000$ ASICs are necessary to readout signals from $\approx 1.8 \times 10^6$ strips. About 40 kW of power will be dissipated in a form of heat by the front-end readout electronics. A NOVEC mono-phase cooling system is under investigation

for heat removal. A thermal demonstrator is under construction at GSI [55]. According to the running scenario of CBM, the innermost regions of the STS will receive fluence of up to $1 \times 10^{14}\,\mathrm{n}_{eq}/\mathrm{cm}^2$ [39]. Irradiation results in several undesirable effects, such as an increase in leakage current (and, as a result, noise), a change in the effective doping concentration (and, as a result, the full depletion voltage), and a decrease in the charge collection efficiency. To minimize radiation induced effects and prevent reverse annealing, the sensors will be kept at $-10\,°\mathrm{C}$ and excess heat from the sensors will be removed by means of force gas flow [56]. The STS will be housed in a thermally insulating CF-foam enclosure with a section for the vacuum beam pipe in the center.

1.5. Motivation for Characterization and Qualification of the Sensors

The main task of the STS is to reconstruct tracks with high efficiency[15] and provide accurate momentum determination. Its performance is strongly influenced by the signal-to-noise ratio. Figure 1.7 shows the simulated STS performance for tracks with $p \geq 1\,\mathrm{GeV}/c$ as a function of the total system noise. Both charge collection efficiency and noise depend on the electrical parameters of the silicon microstrip sensors. In particular, the different capacitances between the structural elements of the sensor directly affect the magnitude of the signal and noise. The STS performance also depends on the number of broken/faulty strips. To exploit the full precision performance of the STS, the detector modules have to be constructed from high-quality microstrip sensors, preferably defect-free. This leads to two important tasks formulated for the thesis:

1. Detailed characterization of the prototype sensors to determine their electrical parameters. Many electrical parameters have not been systematically measured for the CBM sensors, and for others, there were no reliable measurement procedures. This information is essential for the optimization of the noise performance of the sensors. Therefore, this is an important step before starting series production of the CBM sensors.

2. Development of the quality control methods for the production phase to identify sensors that do not meet the CBM specifications. Compliance is required at the sensor and strip levels. The scale of the task is about 1200 sensors with 2×10^6 strips. Therefore, effective and reliable methods are necessary.

[15]The tracking efficiency is determined as the ratio between the reconstructed tracks and those which are considered reconstructable. A track is considered reconstructable if it has hits at least in four STS stations.

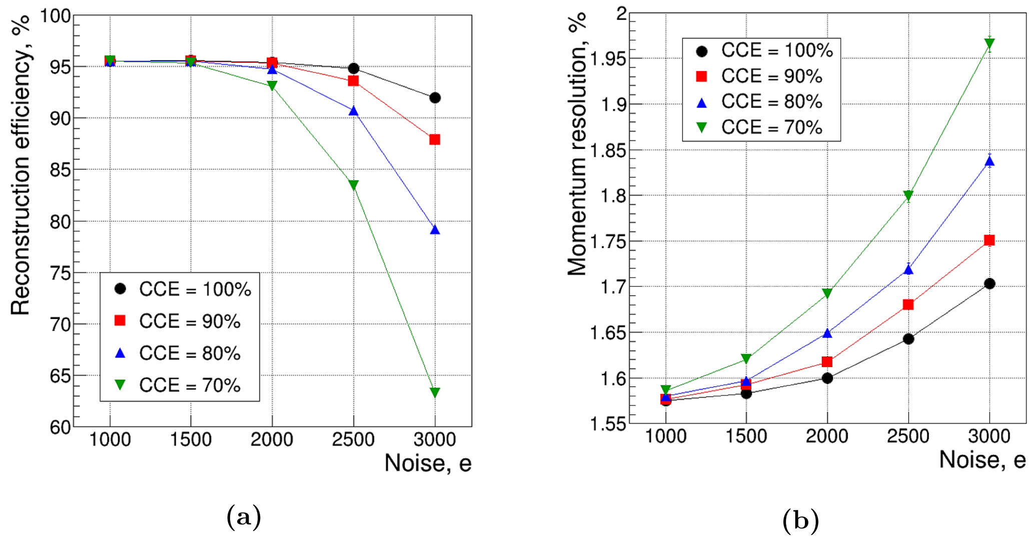

Figure 1.7.: Dependence of the track reconstruction efficiency and momentum resolution of the Silicon Tracking System on the overall system noise. Simulations are performed for different levels of the CCE [57].

1.6. Scope of the thesis

The thesis is focused on the silicon microstrip sensors that are main building blocks of the STS. First, a detailed overview of the CBM microstrip sensors is provided in Chapter 2. Specific design choices are discussed w.r.t. the STS performance requirements.

Characterization and qualification of the sensors require dedicated equipment. Chapter 3 describes the development of the custom automated probe station.

Chapter 4 is devoted to the characterization of microstrip sensors. Techniques and methods for accurate measurement of various electrical parameters of a sensor and strip are detailed. The results for CBM prototype sensors are discussed.

Since most electrical parameters cannot be measured directly, simulations can contribute to the understanding of the measured quantities and help to adjust the measurement procedures. The model of the CBM microstrip sensor was developed for the SPICE network simulator. The obtained results are discussed in Chapter 5.

Finally, armed with dedicated equipment, well-thought measurement procedures, and an understanding of measured quantities, the quality of the microstrip sensors can be assessed. Chapter 6 provides details of the STS QA program dedicated to the microstrip sensors.

2. Silicon Microstrip Sensors for CBM-STS

The Silicon Tracking System of the CBM experiment will be populated with 876 silicon microstrip sensors. The optimization of the STS design was driven by the requirement of high track reconstruction efficiency and a low material budget. The sensors went through a long development process since 2007 in order to achieve the required STS performance. The development and investigation of the first prototype sensors CBM01 – CBM05 are covered in Refs. [58, 59, 60, 61]. The final full-size prototypes, labeled as CBM06, were developed and manufactured. Figure 2.1 shows a microscopic photograph of the corner region of the CBM sensors manufactured by Hamamatsu and CiS. The layout of both sensors is the same, with some vendor specific technologies such as edge termination, *n*-side strip isolation, polysilicon processing, etc. To conclude the prototyping phase and prepare for the tendering process[1], a Production Readiness Review took place in April 2018 [64]. The following section describes the design of the CBM06 sensors.

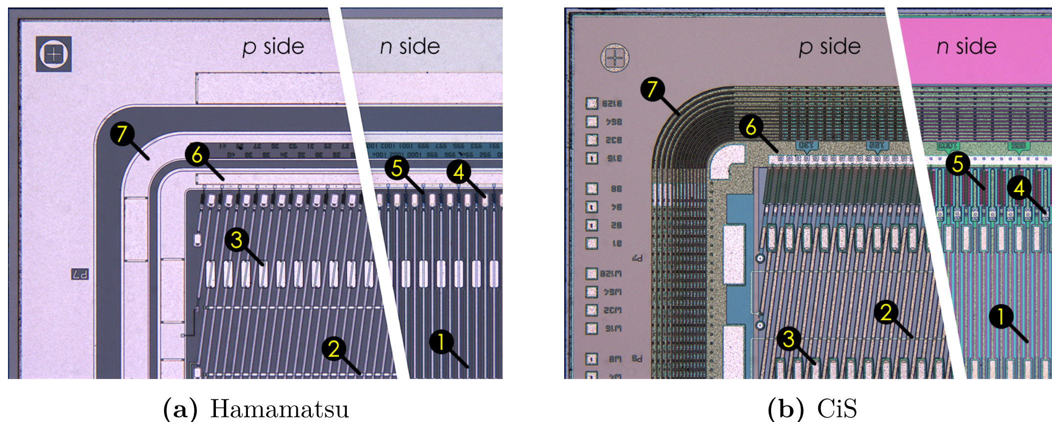

(a) Hamamatsu **(b)** CiS

Figure 2.1.: Layouts of the CBM silicon microstrip sensors manufactured by Hamamatsu (a) and CiS (b). Both *p* and *n* sides are shown split. Labels indicate: 1 – aluminum readout strips (1st metal layer), 2 – interconnecting strips (2nd metal layer), 3 – AC pads, 4 – DC pads, 5 – polysilicon bias resistors, 6 – bias ring, 7 – guard ring structure. A detailed description of all structures is given in Section 2.1.

[1]The tendering process concluded in March 2019. Production of the sensors was awarded to Hamamatsu Photonics and was launched in Summer 2019 [62, 63].

2.1. Design of the Sensors

Manufacturers

The prototype silicon microstrip sensors for the STS were produced by two vendors: CiS Research Institute of Microsensors GmbH (Erfurt, Germany) [65] and Hamamatsu Photonics K.K. (Hamamatsu, Japan) [66]. The layout with identical features within the design rules of the vendors has been established. These prototypes are the subject of research in this work. The series production of the sensors was awarded to Hamamatsu. It comprises about 1200 microstrip sensors and requires about a year for production [62].

Wafer Material

The CBM silicon sensors are produced using standard float-zone (FZ) n-type silicon. The crystal orientation of the wafers depends on the vendor: CiS uses $\langle 111 \rangle$ while Hamamatsu uses $\langle 100 \rangle$. The CMS Collaboration reported that sensors with $\langle 100 \rangle$ crystal orientation showed better noise performance and lower full depletion voltage after irradiation compared to sensors with $\langle 111 \rangle$ crystal orientation [67, 68]. As it is known from the literature [69], the $\langle 100 \rangle$ crystal lattice has fewer dangling bonds[2], so the fixed oxide charge density is lower than for the $\langle 111 \rangle$ crystal lattice. It results in the lower interstrip capacitance and noise.

Sensor Thickness

The thickness d_0 of the sensor is a critical geometrical parameter. The MIP[3] particle generates more charge in the thicker sensor, resulting in a higher signal-to-noise (S/N) ratio. At the same time, multiple scattering is proportional to the amount of material that the particle has to pass through: $\theta_m \sim \sqrt{x/X_0}$. It affects the momentum resolution and should be minimized for the STS. Another consequence of increasing the sensor thickness is an increase of the depletion voltage, which scales as the square of the sensor thickness $\sim d_0^2$.It was shown in Ref. [70] that increasing the sensor thickness from 300 µm to 500 µm causes the onset of thermal runaway at a lower fluence than expected for the STS operation. On the other hand, the bulk capacitance decreases with thickness as $\sim 1/d_0$, which reduces the load capacitance by about 8 % for the considered case. In addition, the size of the insensitive region of the sensor must be increased along with the thickness of the sensor to avoid early edge breakdown.

The 300 µm thick sensors were chosen for the STS to provide an acceptable balance of S/N ratio and material budget. The contribution to the material

[2]Open bonds of silicon at the Si−SiO_2 interface. Their number is approximately 10^{10} cm^{-2} for the $\langle 100 \rangle$ crystal orientation and an order of magnitude higher for the $\langle 111 \rangle$.

[3]Minimum ionizing particle.

budget of one sensor layer is 0.3 %X_0. STS performance studies in Ref. [71] did not find a significant advantage of using thicker sensors. Also, with 500 µm thick sensors, the momentum resolution deteriorates from 1.6 % to 1.9 % for $p \geq$ 1 GeV/c. The sensors produced by CiS and Hamamatsu have different thickness: 285 µm and 320 µm, respectively.

Bulk Resistivity

The initial bulk resistivity ρ_{bulk} of the CBM sensors is in the range of 2–8 kΩ cm. The resistivity is defined by the effective doping concentration N_{eff}, which is controlled during the manufacturing process. A lower resistivity corresponds to a higher initial doping concentration. This means that the sensor can receive a higher fluence before the type inversion. The CBM sensors will undergo type inversion at a fluence of about 2×10^{13} $\mathrm{n}_{eq}/\mathrm{cm}^2$ according to studies in Ref. [61].

Full Depletion Voltage

Double-sided silicon sensors have to operate in a full depletion regime. The full depletion voltage V_{FD} is directly related to the effective doping concentration of the bulk. The CBM sensors were required to have an operating voltage $V_{op} <$ 500 V after receiving the expected maximum fluence of 1×10^{14} $\mathrm{n}_{eq}/\mathrm{cm}^2$. For non-irradiated sensors of the type to be used in the CBM, V_{FD} is expected to be in the range of 40–150 V. Characterized CBM06 prototypes have the full depletion voltage in the range of 40–100 V before irradiation.

Leakage Current

The leakage current contributes to the noise of the readout electronics. Silicon wafers have to be of high quality, which is a prerequisite for a low leakage current. The CBM sensors from Hamamatsu typically have a leakage current of around 30 nA/cm^2, while 150 nA/cm^2 current is typical for sensors from CiS. The quoted values are for non-irradiated sensors at 20 °C and bias voltage of 100 V.

Sensor Segmentation

Double-sided technology is chosen to satisfy the requirement of a minimum material budget. It has the advantage of providing two-coordinate measurement with the same sensitive volume compared to single-sided technology. p^+ strips are implanted on the front side of the CBM sensor, and n^+ strips on the back side.

Strip Isolation

The p-side strips in the n bulk are self-isolated from each other, and the n-side strips are shorted through the electron accumulation layer. The CBM sensors use different isolation methods for n-side strips. The Hamamatsu sensors use 8 µm

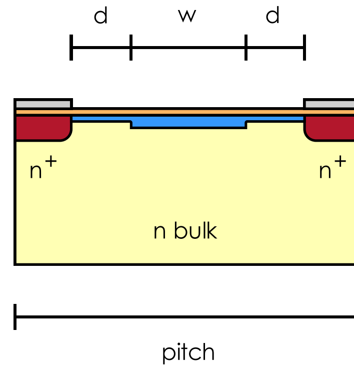

Figure 2.2.: Schematic view of the n side of the CBM microstrip sensor manufactured by CiS. The strip implant (shown in red) width is 20 µm; the gap d is 9 µm wide and doped with boron at a peak concentration of 1 % of the main p-spray area (shown in blue) that has width $w = 20$ µm [73].

wide common p-stop structures, interconnected at the ends of the strips[4]. The CiS sensors use a moderated p-spray technology that requires fine tuning as shown in Ref. [72]. The currently applied doping of $\sim 3.3 \times 10^{12}\,\mathrm{cm}^{-2}$ corresponds to a peak doping concentration of about $2.4 \times 10^{17}\,\mathrm{cm}^{-3}$. It ensures operation even after the oxide charge density reaches a saturation value of about $2 \times 10^{12}\,\mathrm{cm}^{-2}$. In addition, the moderated p-spray technology can give up to 10–15 % lower inter-strip capacitance before irradiation compared to the combination of p-spray and p-stop [72]. Figure 2.2 shows a schematic view of the n side of the CBM sensor from CiS, showing an interstrip gap with a moderated p-spray structure.

Stereo Angle

Front- and back-side strips need to form a stereo angle to enable two-dimensional space-point measurement. For CBM sensors, an optimum was found for 7.5° [39]. This value allows to minimize the number of combinatorial matches (so-called ghosts) and still maintain a good two-dimensional space-point measurement with small errors. To simplify the design, the strips on the n side are parallel to the vertical edge of the sensor, and the strips on the p side are rotated by 7.5°, as schematically shown in Fig. 2.3.

Strip Pitch

Simulation studies have shown that the required momentum resolution ($\Delta p/p \approx 1.8\,\%$ for $p \geq 1\,\mathrm{GeV}/c$) can be achieved with a single-hit resolution of about 25 µm [39]. A read-out strip pitch of 58 µm was chosen to provide the best performance for the STS. A larger pitch decreases resolution and increases system

[4]See Fig. 2.6b.

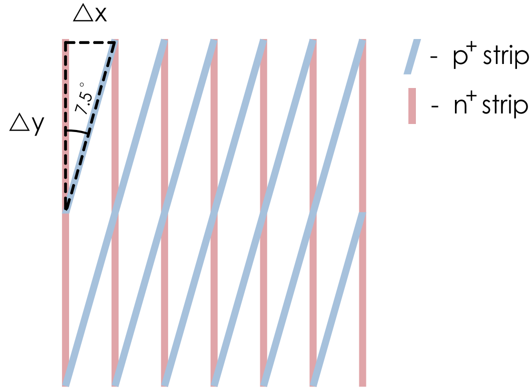

Figure 2.3.: Strip grid of the CBM microstrip sensor. The strip pitch is 58 µm and the stereo angle is 7.5°. The resolution in the horizontal and vertical directions is determined by Δx and Δy, respectively.

occupancy, but also reduces the number of readout channels. On the other hand, a smaller pitch results in higher interstrip capacitance [74] and noise.

The intersection of p- and n-side strips at a stereo angle of 7.5° defines a right triangle with short and long sides, as shown in Fig. 2.3:

$$\Delta x = pitch = 58\,\mu\text{m}; \quad \Delta y = \frac{pitch}{\tan 7.5°} = 440.6\,\mu\text{m}. \tag{2.1}$$

Therefore, the resolution in the vertical direction is worse than in the horizontal direction.

Strip Width

The strip is a sensor element that consists of a metal line, an implant, and a layer of dielectric between them. The metal strip has a width of 25 µm and 20 µm on the p and n sides of the CiS sensors, respectively. The Hamamatsu sensors use the same metal width of 22 µm on both sides of the CBM sensors. The metal strip is usually made wider than the implant, the so-called metal-overhang technology. It has been proven that it has a beneficial effect on the breakdown voltage [75]. The implant has a width of 20 µm on the CiS sensors. The Hamamatsu sensors have 10 µm wide strip implants.

An important parameter is the width-to-pitch[5] ratio w/p, which is used to parameterize the interstrip capacitance. Higher values increase the breakdown stability of the strips, while lower values decrease the interstrip capacitance. A value of 0.25 was used for all sensor geometries for the CMS Silicon Strip Tracker [76]. The width-to-pitch ratio is 0.34 and 0.17 for the CBM sensors manufactured by

[5]Throughout the text, where the width-to-pitch ratio is mentioned, the width of the implant is assumed.

CiS and Hamamatsu, respectively. Therefore, the interstrip and coupling capacitance are expected to be lower for Hamamatsu sensors.

Strip Length

In the innermost regions of the STS, particle rates will reach up to 10 MHz/cm^2 and fall off by 2 orders of magnitude in the outer regions [39]. Short strips provide high granularity of the detector and allow to minimize the occupancy at high interaction rates. The total strip capacitance scales linearly with the length of the strip. On the other hand, a sensor with longer strips can cover a larger area and reduce the number of redout channels. To meet these requirements, 2, 4, 6 and 12 cm long strips will be used for different regions of the STS.

Number of Strips

The sensitive area of the silicon sensor consists of all the strips surrounded by the bias ring. The number of readout strips on each side of the CBM sensor is 1024, which corresponds to 8 readout chips with 128 channels each. The p side has more actual strips than 1024 due to the stereo angle. Short strips in two opposite corners are connected by the 2$^{\mathrm{nd}}$ metal layer. Different connection schemes are considered as a possibility to reduce the number of readout channels [77].

Sensor Sizes

With the current choice of the pitch and number of strips, the width of the sensitive area is about 59.4 mm. The guard ring structure of the CiS sensors causes a non-sensitive band about 1 mm wide around the bias ring. Therefore, the overall width of the sensor is 62 mm. The Hamamatsu sensors use a different edge terminating structure. But the width of the sensors was adjusted to the width of the CiS sensors. The length of the sensors depends on the length of the strips. Therefore, sensors of 4 different sizes ($62 \times 22\,\mathrm{mm}^2$, $62 \times 42\,\mathrm{mm}^2$, $62 \times 62\,\mathrm{mm}^2$, $62 \times 124\,\mathrm{mm}^2$) will populate different regions of the STS. Figure 2.4 shows an artist photo of the CBM microstrip sensors of all sizes.

12 cm Big Sensors

Initially, it was planned to assemble two daisy-chained $62 \times 62\,\mathrm{mm}^2$ sensors to cover the outer regions of the STS. However, this increases the complexity of the module assembly process. It was decided to replace the two daisy-chained sensors with one big sensor with an area of $62 \times 124\,\mathrm{mm}^2$. Two additional pairs of bond rows are added in the center of the sensor to provide connectivity to the readout electronics. Fabrication of such sensors requires the use of 6 inch wafers, which are standard at Hamamatsu. CiS integrated it in the production process just recently (by 2016). Therefore, the quality of the first prototype sensors for CBM was low. Figure 2.4 shows a $62 \times 124\,\mathrm{mm}^2$ sensor next to smaller ones.

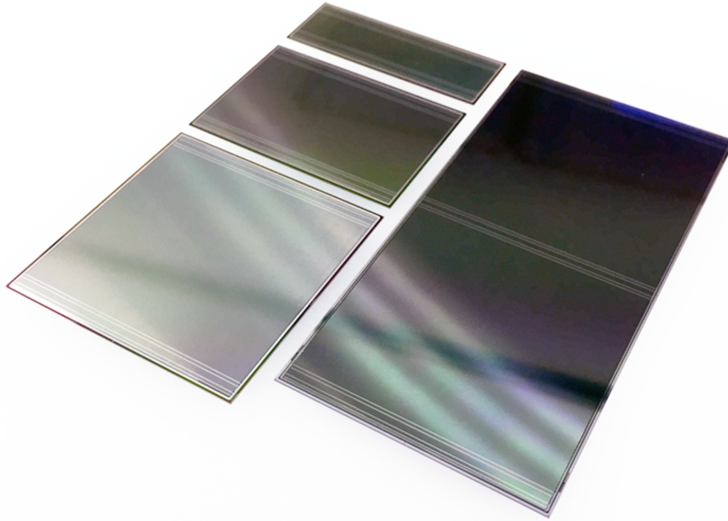

Figure 2.4.: A photo of the CBM microstrip sensors of 4 different sizes (photography courtesy of A. Lymanets).

Second Metal Layer

The *p* side of the CBM sensors has short strips in two opposite corners. They have to be interconnected to connect to the electronics at the same edge and thus simplify the design of the detector module. This can be implemented using two technologies: adding a second metal layer to the sensor design (Fig. 2.5b) or bonding a special microcable (Fig. 2.5a). The microcable increases the complexity of the assembly process and requires the production of different microcables for different sensor sizes. Additional contact pads have to be added to the sensor design. The disadvantage of the second metal layer is the increased complexity of the manufacturing process. It also introduces a network of additional parasitic capacitances. The LHCb collaboration reported a drop of the cluster finding efficiency for double-metal sensors after a certain fluence [78]. Studies by the CBM-STS working group found no significant difference in the performance of single- and double-metal sensors under irradiation [79]. However, Ref. [80] reported crosstalk issues for several sensor prototypes.

The final design of the CBM sensors uses a 2nd metal layer on the *p* side. The insulation between the 1st and 2nd metal layers is made of SiO_2. Its thickness is 1 µm on CiS sensors. Line widths are 10 µm and 20 µm for CiS and Hamamatsu sensors, respectively.

Integrated Coupling Capacitors

The CBM sensors have integrated coupling capacitors — the metal layer is isolated from the implant by a thin layer of dielectric. It blocks the strip leakage current from reaching the amplifier and simplifies the design of the readout electronics. A

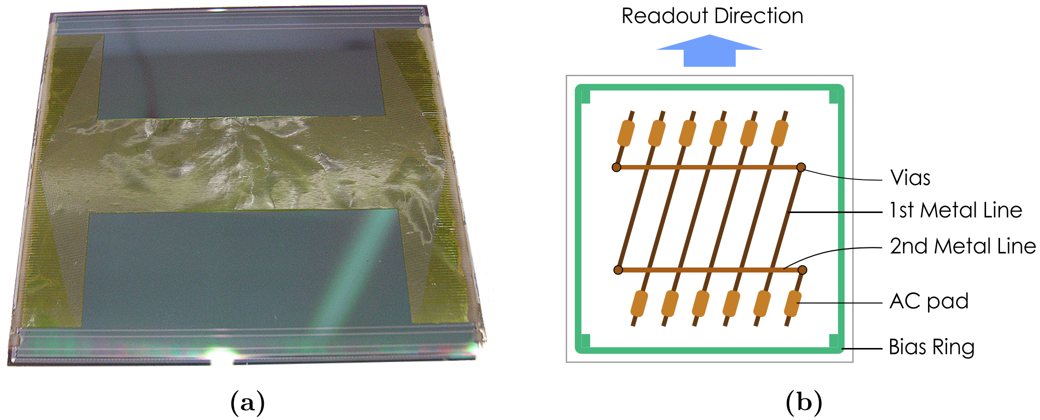

Figure 2.5.: Interconnecting technologies for short strips of the CBM prototype sensors: (a) single-metal sensor with attached H-shaped microcable and (b) schematic view of p side with double-metal technology.

large coupling capacitance is required to ensure that most of the charge is coupled to the corresponding metal strip. The CBM sensors manufactured by Hamamatsu have a coupling capacitance of 10 pF/cm, and sensors manufactured by CiS have 20 pF/cm. This is determined by the thickness of the insulation layer and the geometry of the strip. The CiS sensors use a 300–400 nm thick ON dielectric layer (SiO_2+Si_3N_4).

Biasing Resistors

The bias voltage is supplied to the common bias ring of the sensor and then to the individual strips. The polysilicon biasing method is used for CBM sensors. A high resistance value is preferred due to lower thermal noise [81]. The bias resistance must be much larger than the input impedance of the charge-sensitive amplifier, which is 0.1–2 kΩ for the STS-XYTER chip in the signal band from 100 kHz to 10 MHz [59]. On the other hand, it should not drop all the bias voltage due to the leakage current.

Meandering structures are deposited to achieve high resistance values:

$$R_{poly} = R_S \frac{l}{w} \tag{2.2}$$

where R_S is the sheet resistance that depends on the implantation dose, l is the length of the resistor, w is its width. Figure 2.6 shows the polysilicon resistors of the CBM sensors. The sensors manufactured by Hamamatsu have a polysilicon resistance of about 0.5 MΩ. It was later proposed to increase it to 1.5 MΩ to reduce thermal noise [48]. The sensors manufactured by CiS have polysilicon resistance in the range of 1–2 MΩ. Several batches with polysilicon resistance up to 3 MΩ were produced.

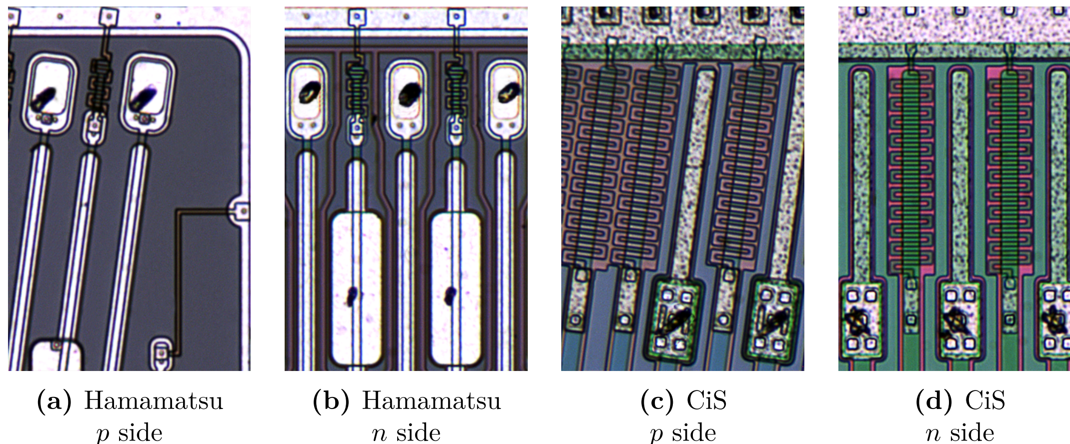

(a) Hamamatsu p side **(b)** Hamamatsu n side **(c)** CiS p side **(d)** CiS n side

Figure 2.6.: A close-up view of the polysilicon resistors of the CiS and Hamamatsu sensors. The zoom level is the same for all images.

Punch-Through Protection

When the beam is unstable, many charged particles pass through the sensor, accumulating a large amount of charge on the strip implant, before the coupling capacitor. To prevent it from feeding into the amplifier, a punch-through structure is used. It is formed by strip and bias ring implants and the gap between them — either n bulk or p-isolation structure. The resistance of the structure drops when the onset voltage is reached. Its value depends on the gap width. For CiS sensors, it is 8 µm and 14 µm for the p and n sides, respectively. For Hamamatsu sensors, it is approximately 30 µm for both sides.

Guard Rings

Silicon microstrip sensors require edge termination to increase the breakdown voltage and protect the sensitive area from the current generated outside of it. Typically, additional rings are produced around the bias ring. They develop a gradual voltage drop between the bias ring and the edge of the sensor. The number of the rings and their geometry are determined from simulation by the requirement of a certain breakdown voltage.

The CBM06 prototype sensors manufactured by CiS have 14 guard rings, while the sensors from Hamamatsu have only one guard ring with a wide n^+ ring next to the cut edge. Figure 2.7 shows a schematic drawing of the non-sensitive region of the CiS sensor. The distance from the last ring to the physical edge is about twice the width of the entire guard ring structure. Usually, the width of the non-sensitive area is about three times the thickness of the sensor [82].

The latest CBM06 prototype sensors also have a guard ring structure on the n side. It is the same as on the p side. However, none of the isolation methods were used for guard rings on the n side.

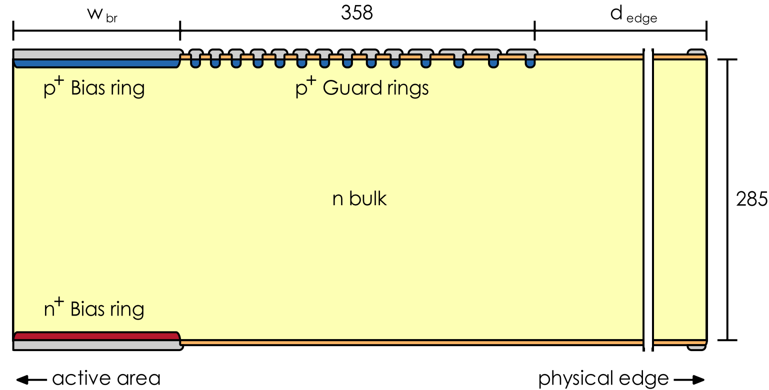

Figure 2.7.: Schematic drawing of the guard ring structure of the CBM sensor manufactured by CiS. It consists of 14 concentric rings. Distances are in µm. The thickness of implants and metals is increased for clarity. The active area is not shown. The distance between the metal rings is the same due to the overhang technology.

Cut Edge

By design, all CBM sensors have a 20 µm wide aluminum line along the edge of the sensor to indicate the nominal sensor area. Usually, the cut is made slightly apart this line yielding 20–80 µm extra width per edge. Hamamatsu uses stealth dicing (SD) technology. CiS used blade dicing (BD) with a diamond blade for all produced CBM prototype sensors. Its accuracy is about 10 µm. With SD technology, the cut can be as narrow as 1 µm without chips and surface contamination [83]. BD results in a "fuzzy" edge and has higher probability of chips.

Alignment Marks

Alignment marks (AM) are reference marks required for module assembly and quality assurance procedures. The CBM sensors have AM in all four corners as well as in the middle of each side. The positions of the marks relative to the center of the sensor are identical on both sides of the sensor. However, the distance to the physical edge is vendor dependent. Figure 2.8 shows AM of CiS and Hamamatsu sensors. In order to facilitate optical metrology of the sensors when mounted on the detector ladders, additional marks are placed on the inactive rim of the sensor in the final design [48].

Contact Pads

The CBM sensors have several types of contact pads for read-out, biasing and testing. Each strip has 4 AC pads. The nominal dimensions of one AC pad are $65 \times 185\,\mu m^2$. They are organized into 8 rows labeled P0 – P7/N0 – N7. Rows P0 – P1/N2 – N3 are reserved for read-out, while others can be used for strip testing.

Each strip has only one DC pad that provides direct contact to the implant. By

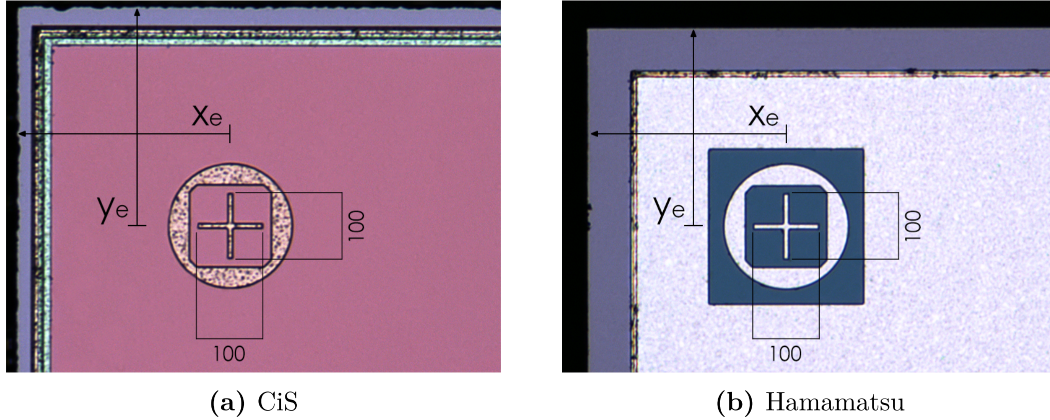

(a) CiS **(b)** Hamamatsu

Figure 2.8.: Alignment marks in the corners of the CiS and Hamamatsu sensors. x_e and y_e designate the distance to the physical edge of the sensor. All dimensions are in µm. The edge region of the Hamamatsu sensors has a wide n^+ ring with metal on top. The metal layer has a square window at the place of the alignment mark.

design, the DC pad and the bias resistor are located at opposite ends of the strip. The nominal dimensions of one DC pad are $55 \times 96\,\mu\text{m}^2$. Due to these dimensions, odd- and even-numbered strips have their DC pads located at opposite ends of the strip.

The bias ring has $150 \times 400\,\mu\text{m}^2$ large contact pads for bonding. There are 16 available bias pads.The final CBM06 prototype sensors have openings in the passivation layer above the bias ring in the middle of the sensor. This was done to provide bias through a dedicated test socket during electrical characterization. Due to their size, the guard rings only have small windows in the passivation layer for testing purposes only.

Numbering of Strips

The numbering of the strips on the n side of the sensor is straight forward from 0 to 1023. On the p side of early CBM sensor prototypes, the strip numbering was not consistent between vendors. The current numbering scheme is shown in Fig. 2.9. The CBM sensors manufactured by Hamamatsu have all strips numbered in decimal numbers. CiS sensors have every 8th strip marked.

Naming Conventions for Sensors

The microstrip sensors are supplied with unique identification numbers from vendors. It includes batch number, wafer number and piece number[6]. The sensors have dedicated scratch pads on the p side within the non-sensitive area. It allows the identification numbers to be encoded in binary form, providing 1 byte

[6] One wafer can contain, for example, three $62 \times 22\,\text{mm}^2$ sensors

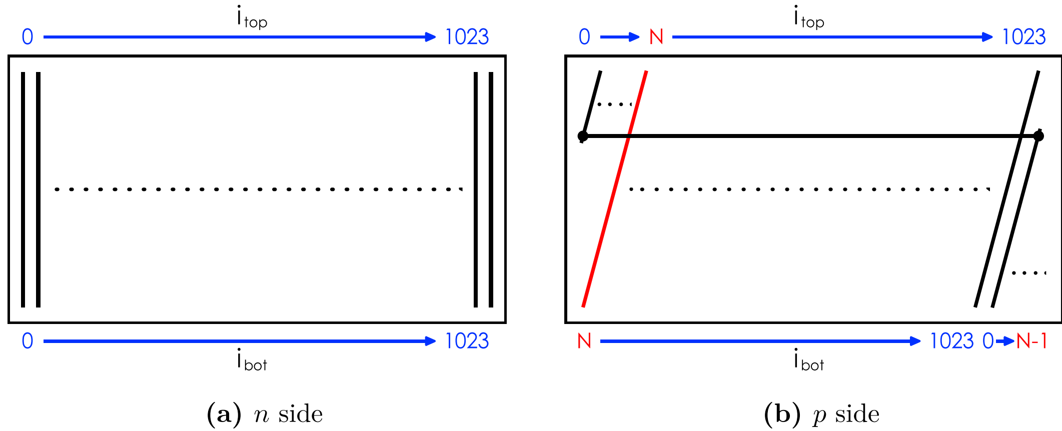

(a) n side

(b) p side

Figure 2.9.: Strip numbering scheme for CBM06 prototype sensors. The 0$^{\text{th}}$ strip ($i_{top} = 0$, first strip with an AC pad) is always in the top left corner of the sensor. N is the first long strip of the p side. It takes values 42, 88, 134 and 274 depending on the sensor size.

for each number. The identification numbers and corresponding names for all sensors investigated in this work are listed in Appendix A.

2.2. Specifications for the Sensors

The following subsections summarize the specifications for the CBM microstrip sensors. The current sensor design is labeled as CBM06 and is the result of a long development phase.

2.2.1. Silicon Wafer Properties

The properties of the silicon wafers used for production of the CBM microstrip sensors are summarized in Table 2.1. The wafer material is float-zone n-type silicon. Double-sided photo lithography technology at both vendors allows handling wafers up to 500 µm thick.

2.2.2. Sensor Geometrical Properties

The important geometrical properties of the CBM microstrip sensors are summarized in Table 2.2. Most of the geometrical properties can be verified by optical inspection. They directly affect the electrical properties of the sensor. For example, the thickness of the coupling dielectric t_c affects the coupling capacitance and its breakdown tolerance. Data on t_c are not available for CBM sensors manufactured by Hamamatsu.However, its variation within the sensor should be $< 5\,\%$, as verified by an ellipsometer [84]. This is consistent with the coupling capacitance

Table 2.1.: Properties of the silicon wafers for the CBM microstrip sensors.

Parameter	Symbol	CiS	Hamamatsu
Material		n-type FZ Si	n-type FZ Si
Resistivity	ρ_{bulk}	2–6 kΩ cm	4–8 kΩ cm
Thickness	d_w	285 ± 5 µm	320 ± 15 µm
Size		4 inch (6 inch under test)	6 inch
Crystal orientation		⟨111⟩	⟨100⟩
Segmentation		double-sided	double-sided
Implantation		p^+-n-n^+	p^+-n-n^+
Coupling dielectric		ON structure (SiO_2+Si_3N_4)	SiO_2, (Si_3N_4)
Metalization		single on n side, double on p side	single on n side, double on p side
Passivation		SiO_2, both sides	SiO_2, both sides

measurements performed in this work[7].

2.2.3. Sensor Electrical Properties

The most important electrical properties of the CBM microstrip sensors are summarized in Table 2.3. The total leakage current values are for the diced sensors that were reversed biased to 150 V at room temperature. The latest iteration of the CBM06 prototypes, manufactured by Hamamatsu, have 1.5 MΩ polysilicon bias resistors. All electrical properties can be verified by electrical inspection.

2.2.4. Sensor Radiation Tolerance

The electrical properties of the CBM microstrip sensors will change under irradiation. According to FLUKA calculations [39], after 1 month of operation with Au+Au collisions at 10 AGeV and 10^9 Au ions/s the silicon sensors will receive a fluence of approximately $5 \times 10^{12}\,n_{eq}/cm^2$. This results in an accumulated non-ionizing dose of $5 \times 10^{13}\,n_{eq}/cm^2$ after 10 months of operation. The silicon sensors undergo type inversion under such conditions. At this exposure, the leakage current is expected to be 9 µA/cm² [39]. Charge collection efficiency will decrease by about 10 % as reported in Ref. [85]. The radiation hardness of the CBM microstrip

[7] See section 4.2.5 for details.

Table 2.2.: Geometrical properties of the CBM microstrip sensors.

Parameter	Symbol	CiS	Hamamatsu
Width		62 mm	62 mm
Height		22, 42, 62 and 124 mm	22, 42, 62 and 124 mm
Strip length		20, 40, 60 and 122 mm	20, 40, 60 and 122 mm
Strip pitch	p	58 µm	58 µm
Number of strips	N_{strips}	1024 per side	1024 per side
Number of short strips		42, 88, 134 and 274	42, 88, 134 and 274
Stereo angle	θ	7.5°	7.5°
Width of strip implant, p/n side	w_{imp}	20 µm/20 µm	10 µm/10 µm
Junction depth	x_j	3 µm	–
Width of strip metal, p/n side	w_m	25 µm/20 µm	22 µm/22 µm
Thickness of strip metal	t_m	1 µm	1 µm
Width of 2nd metal layer line	w_{2m}	12 µm	20 µm
Thickness of 2nd metal layer line	t_{2m}	1 µm	1 µm
Thickness of coupling dielectric	t_c	300–400 nm	–
Thickness of oxide layer between strips	t_{ox}	300 nm	–
Thickness of insulation between 1st and 2nd metal	t_{2ox}	1.4 µm	–
Thickness of passivation layer	t_{pass}	0.5 µm	–

Table 2.3.: Electrical properties of the CBM microstrip sensors.

Parameter	Symbol	CiS	Hamamatsu
Full depletion voltage	V_{FD}	50–100 V	40–90 V
Breakdown voltage	V_{BD}	> 200 V	> 200 V
Total leakage current	I_{TOT}	150 nA/cm^2	30 nA/cm^2
Bulk capacitance	C_{bulk}	36 pF/cm^2	33 pF/cm^2
Coupling capacitance	C_c	20 pF/cm	10 pF/cm
Total strip capacitance	C_{tot}	1.3 pF/cm	1.1 pF/cm
Aluminum resistance	R_m	12 Ω/cm	12 Ω/cm
Polysilicon resistance	R_{poly}	1.5 MΩ	0.5 MΩ

sensors was confirmed up to a fluence of $2 \times 10^{14}\,n_{eq}/cm^2$ [61, 86]. According to CBMRoot calculations [39], the silicon sensors in the central regions of the STS stations will receive an ionizing dose of about 10 kGy per month of operation. This corresponds to an induced surface charge density of $(1–2) \times 10^{12}\,cm^{-2}$ after 10 months of operation. As a results, the interstrip capacitance will increase, and the interstrip resistance will decrease [72].

2.2.5. Environmental Conditions

During the CBM experiment, the sensors will be kept below −5 °C to limit the leakage current induced by radiation. This will be achieved by using forced gas cooling [56] to ensure that minimal additional material budget is introduced into the STS aperture. A dry nitrogen atmosphere will prevent condensation on the surface of the sensor. However, the quality assurance and assembly of modules, ladders and stations will be performed at room temperature and relative humidity of $\sim 30\,\%$.

2.2.6. Number of Sensors

The current layout of the STS includes sensors of 4 geometrical sizes, which will be assembled into different types of modules. Table 2.4 summarizes the total number of sensors (and strips) required for 8 STS stations plus 20 % extra to account for the finite STS assembly yield [48]. The numbers were additionally adjusted to match the two 6 inch layouts holding one pair of two sensor variants each ($62 \times 124\,mm^2$ and $62 \times 22\,mm^2$, $62 \times 62\,mm^2$ and $62 \times 42\,mm^2$). The number of strips defines a challenge for the electrical quality assurance program.

Table 2.4.: The number of sensors required for the construction of the STS. The number of spare sensors is about 20 % of the initial number.

Variant	Minimal number	Strips	Including spares	Strips
$62 \times 22\,\mathrm{mm}^2$	80	163 840	108	221 184
$62 \times 42\,\mathrm{mm}^2$	272	557 056	349	714 752
$62 \times 62\,\mathrm{mm}^2$	204	417 792	353	722 944
$62 \times 124\,\mathrm{mm}^2$	320	655 360	392	802 816
Total amount	876	1 794 048	1202	2 461 696

3. Custom Automated Probe Station

The quality assurance (QA) of the microstrip sensors is an important task before the assembly of the STS detector modules. Large-volume tests of the sensors require a dedicated test station. Automation is necessary for alignment, stepping through all strips, measurements, etc. The specifics of microstrip sensors require high accuracy for both positioning and measurement equipment. Commercial probe stations are generally not well suited for testing microstrip sensors. Dedicated software solutions are simply not available. Therefore, a custom probe station was designed and built at the University of Tübingen.It includes assembling individual custom-made parts and commercial instruments.The developed probe station is suitable for the measurement of global and strip parameters of the sensors. It is operation-ready and can be further optimized for the QA task, in hardware and software, if needed. This chapter gives an overview of the Tübingen probe station, describes calibration routines, hardware and software solutions.

3.1. Setup Overview

Figure 3.1 shows the probe station built in this work. It consists of optical, mechanical, and vacuum systems placed in a light-tight enclosure (black box), which also provides electromagnetic shielding. Its frame is made of Item [87] $40 \times 40\,\mathrm{mm}^2$ high-strength aluminum profile. The probe station resides on a massive granite table from THOME Precision [88]. The mechanical setup consists of a custom-designed vacuum chuck to hold the microstrip sensor, which can be positioned in XYZΘ with high-precision motors. It also accommodates an optical system that includes a microscope with a camera and a light source. Four probes on a custom-made support table are available for contacting individual strips. The setup is controlled by a PC running a LabVIEW 2019 software [89].

3.1.1. Motor Stages

The electrical inspection of strips requires a reliable contact between the needle and the strip's AC pad to be provided repetitively over a distance of 60 mm. Accuracy and repeatability of horizontal and vertical positioning of the microstrip sensor are critical parameters. They are fulfilled with the high-accuracy motors

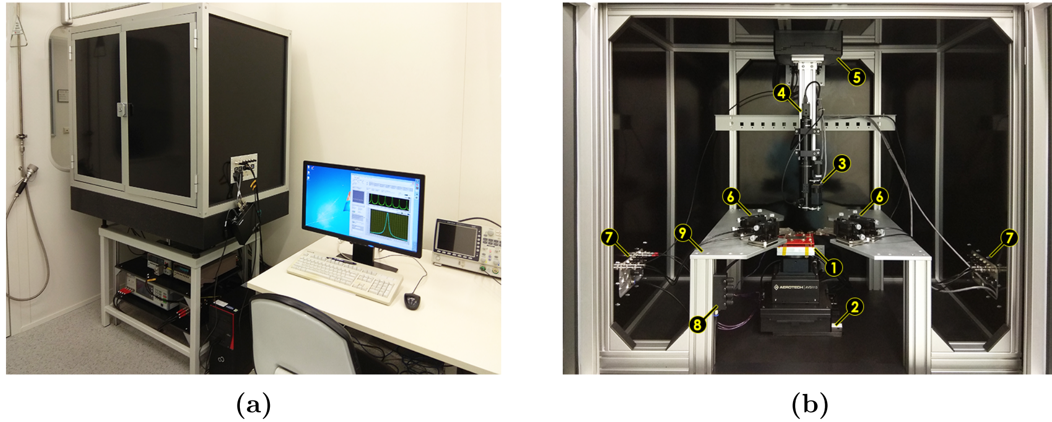

(a) (b)

Figure 3.1.: View of the custom-built probe station which is installed in a cleanroom at the University of Tübingen: (a) the complete setup with the probe station residing on the granite table, measurement instruments underneath it, and PC to the right; (b) inside of the black box. Labels indicate: 1 – vacuum chuck carrying the microstrip sensor, 2 – XYZΘ motor stages for positioning of the chuck, 3 – optical system with motorized zoom and focus stages, 4 – digital camera, 5 – XY motor stages for positioning of the optical system, 6 – probes with needles, 7 – feed-through panels for connections to the measurement equipment and control systems, 8 – vacuum manifold, 9 – stainless steel table.

from Aerotech GmbH [90]. The heart of the probe station is the XYZΘ motor assembly with a chuck. Its XY axes are direct-drive linear servo motors with a travel range of 100 mm × 100 mm and an accuracy of better than 0.4 µm. The screw-driven lift stage provides precise elevation of the microstrip sensor in the vertical plane. The rotary stage allows for precise angular alignment of the microstrip sensor. The XYZ axes of the assembly are calibrated at the Aerotech factory for optimal performance. The optical system of the probe station is equipped with a 2-axis motor stage for additional flexibility. This is necessary for measurements that require contacting strips at their opposite ends. The Aerotech Npaq MR motion controller provides positioning control and a feedback loop for all six axes. Important specifications of the motor axes are listed in Table 3.1.

3.1.2. Vacuum Chuck

A typical probe station chuck is designed for round wafers and is not suitable for rectangular objects such as microstrip sensors. A custom multi-zone vacuum chuck was designed to hold the different-size CBM sensors in place during the inspection. It has three vacuum areas. The active suction area can be adjusted according to the size of the sensor under inspection. Figure 3.2a shows a photograph of the chuck made of aluminum. Its dimensions are $12.2 \times 12.2\,\text{cm}^2$, and the vacuum zone is $5 \times 5\,\text{cm}^2$. On the side, it has push-to-connect vacuum fittings for 4 mm tubes. The chuck is mounted on the XYZΘ motor assembly.

Table 3.1.: Aerotech motor axes specifications [90].

Assembly	Chuck				Optics	
Axis	X	Y	Z	Θ	X	Y
Model	PLANAR DL		AVSI113	ADRS100	PLANAR DL	
Travel	100 mm	100 mm	13 mm	Continuous	100 mm	100 mm
Accuracy	±0.4 µm	±0.4 µm	±1 µm	±80″	±3 µm	±3 µm
Repeatability	±0.1 µm	±0.1 µm	±0.75 µm	±3″	±0.1 µm	±0.1 µm
Calibrated	Yes	Yes	Yes	No	No	No

After manufacturing, the chuck was polished to improve its surface quality. Figure 3.2b shows the height map of the $9 \times 9\,\mathrm{cm}^2$ central region of the chuck obtained by the focus variation method while moving the chuck under the microscope. A non-parallelism of about 35 µm is observed. Figure 3.2c shows the height map after subtraction of a plane that fits the data in Fig. 3.2b. The estimated flatness is within 9 µm. Such values were considered sufficient to avoid significant deformation of the microstrip sensor when placed on the vacuum chuck.

3.1.3. Vacuum Line

Figure 3.2d shows the scheme of the vacuum line of the probe station and its control circuit. A Becker VT4.4 [91] 150 mbar (abs.) vacuum pump supplies the vacuum to the chuck. The manual manifold provides independent vacuum control to three zones. An electrically controlled 3/2-way valve from Norgren [92] releases a vacuum so the microstrip sensor can be removed or adjusted. The control circuit includes Guenther 3570 5 V reed relay connected to the Aerotech Npaq MR controller. Protection diodes are installed near each switching device.

3.1.4. Probes

Four probes from Cascade Microtech [93] are available to contact individual strips. Positioning of the probes on the custom-made support table is manual. The probes have a magnetic base system that ensures a stable position during all measurements. Tungsten needles of SE-T type with 5 µm tip diameter from Signatone [94] are attached to B50-138687 probe arms. They are connected to external devices using triaxial/coaxial cables through custom-designed feed-through panels. The probe needles can be moved in XYZ using the PH110 micropositioner. For electrical testing, the microstrip sensor is moved in a way so that the strips are positioned sequentially underneath the stationary probe needles.

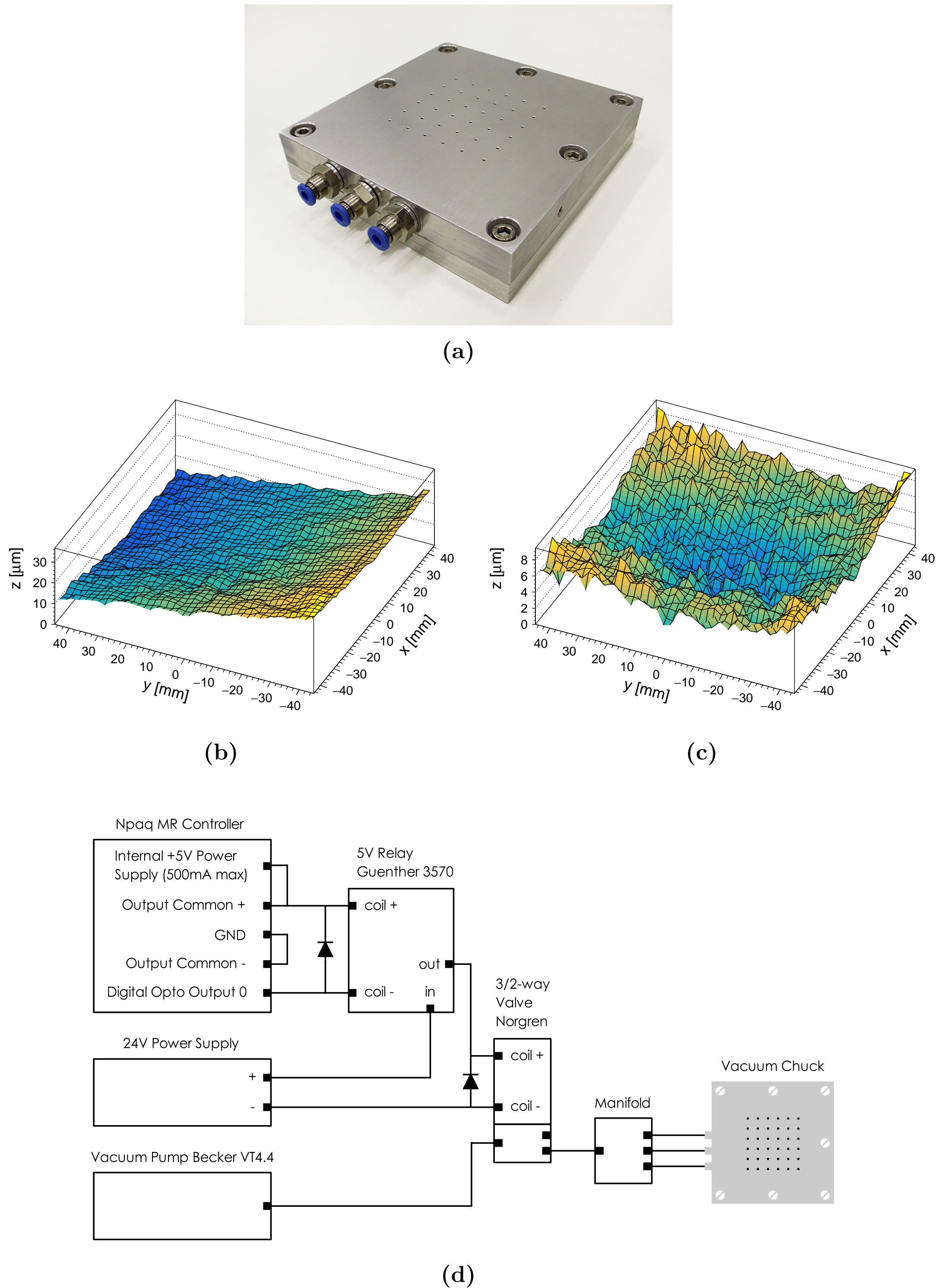

Figure 3.2.: Custom-made multi-zone vacuum chuck for the CBM microstrip sensors: (a) a photo of the vacuum chuck, (b) height map of the vacuum chuck surface showing its non-parallelism, (c) height map of the vacuum chuck surface showing its flatness, (d) scheme of the vacuum line of the probe station and its control circuit.

3.1.5. Optical System

The optical assembly of the probe station consists of a 12x Zoom-motorized tube from Navitar [95]. The employed configuration has a 12x zoom (0.58x – 7x magnification) and a 3 mm fine focus motorized axes. The working distance of the assembly is 86 mm and the depth of field range is 1.39–0.05 mm. The optical tube allows direct light illumination by a flexible 8 mm light guide connected to the Roma LED3 cold light source from Starlight [96]. The 1.9M pixel USB3.0 CCD camera from The Imaging Source [97] is attached to the optical tube via a C-mount coupler. It has a global shutter and can capture images at 15 fps. The optical system mounted on the XY motor stage is suspended above the vacuum chuck. It can be positioned anywhere over the surface of the microstrip sensor under inspection.

3.2. System Calibration

The AC pad size is $60 \times 180\,\mu m^2$. The two pad rows for even and odd strips have a horizontal pitch of 116 µm, twice the strip pitch. The contact pads for measurements are spread over a distance of 60 mm. It is important to ensure the accurate positioning of the microstrip sensor under the probe needles over the entire distance. Figure 3.3 shows a two-dimensional representation of the relevant coordinate frames of the probe station: motors, camera, microstrip sensor. In general, all three frames are misaligned relative to each other. The probe station is equipped with the calibrated XYZ motor stages. Stepping through all contact pads has to be performed in the sensor plane. Therefore, dedicated calibration and characterization procedures were developed for the probe station. They are performed in an automated way by means of LabVIEW subprograms.

3.2.1. Optical Axis Alignment

To ensure that a given object field always appears in the center of the image, the camera has to be aligned with the optical center of the zoom optics. The C-mount ring with three centering screws allows lateral displacement of the camera in any direction. The alignment mark of the microstrip sensor served as a reference object. The position of the camera was adjusted based on AM's displacement when zooming in and out. After tightening the screws, the displacement of the AM was recorded at different zoom values. Figure 3.4a shows the obtained deviations in X and Y directions. Figure 3.4b shows the absolute distance measured in micrometers. When the deviations are zero, the system is called parcentric. The obtained deviations are used for maintaining proper position by adjusting the XY-stage when changing magnification.

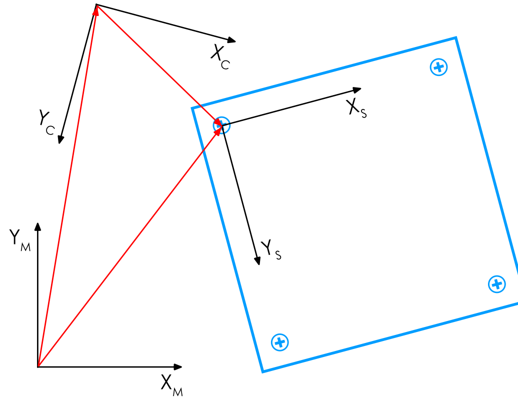

Figure 3.3.: Schematic representation of three coordinates frames of the probe station: motors, camera, microstrip sensor. The blue rectangle represents the coordinate frame of the microstrip sensor with the $X_S Y_S$ coordinate system set to the upper left alignment mark. $X_M Y_M$ and $X_C Y_C$ are the coordinate systems of the motors and the camera, respectively.

3.2.2. Determination of Working Parameters

To automate the position calibration procedures, it is necessary to establish the dependence of the working parameters on the zoom motor stage. The magnification power of the system was estimated by measuring the pixel size of the alignment mark and comparing it to its real size. Edge detection and caliper tools from the NI Vision package were used for this purpose. Figure 3.4c shows the obtained dependence of the magnification on the zoom value. The same data allow establishing the micrometer-to-pixel conversion for an arbitrary zoom value. Figure 3.4d shows the obtained dependence. The field of view was calculated from the single-pixel size multiplied by the number of pixels the camera has in the horizontal direction. The number of recording pixels of the camera used is 1600×1200. Using the previously obtained magnification dependence, the field of view is plotted for different zoom values in Fig. 3.4e. All the data are fitted with an exponential function.

To facilitate the calibration procedures, the zoom value was fixed. All further procedures are performed at a zoom value of 1000. It provides 2x magnification with a field of view of about 3.7 mm. The corresponding micrometer-to-pixel conversion factor is 2.33.

3.2.3. Light Intensity

When zooming in or out, the field of view changes, as does the amount of light reflected back to the camera sensor. The intensity of the light source has to be adjusted to ensure optimal lighting conditions. Calibration procedures are performed at a fixed zoom value. Therefore, only a rough adjustment of the in-

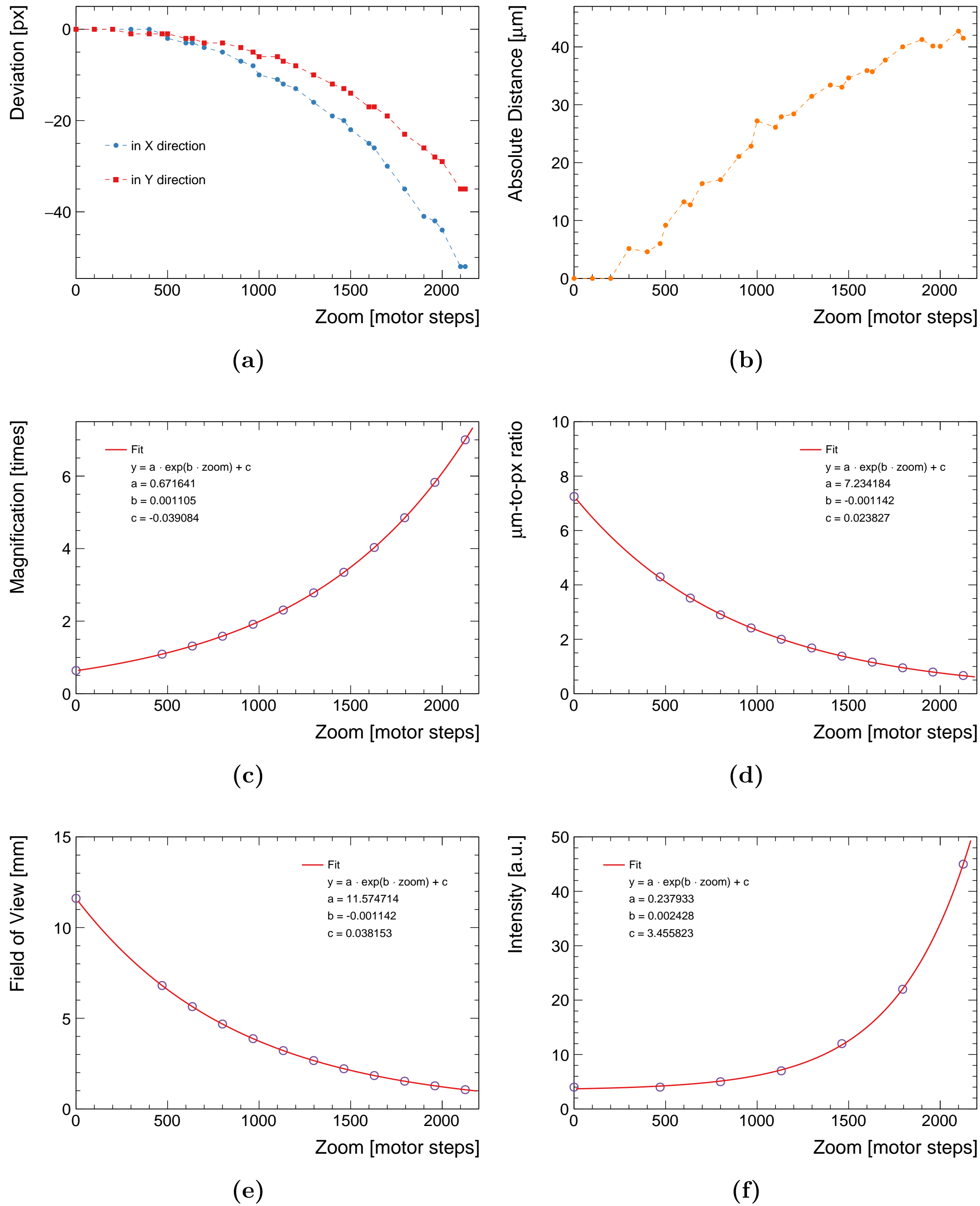

Figure 3.4.: Characterization of the optical system of the probe station: (a) deviation of the image center from the optical center, measured in pixels, (b) absolute distance from the image center to the optical center, measured in micrometers, (c) dependence of the magnification power on the zoom value, (d) dependence of the µm-to-px conversion ratio on the zoom value, (e) dependence of the projected field of view on the zoom value, (f) dependence of the light source intensity on the zoom value.

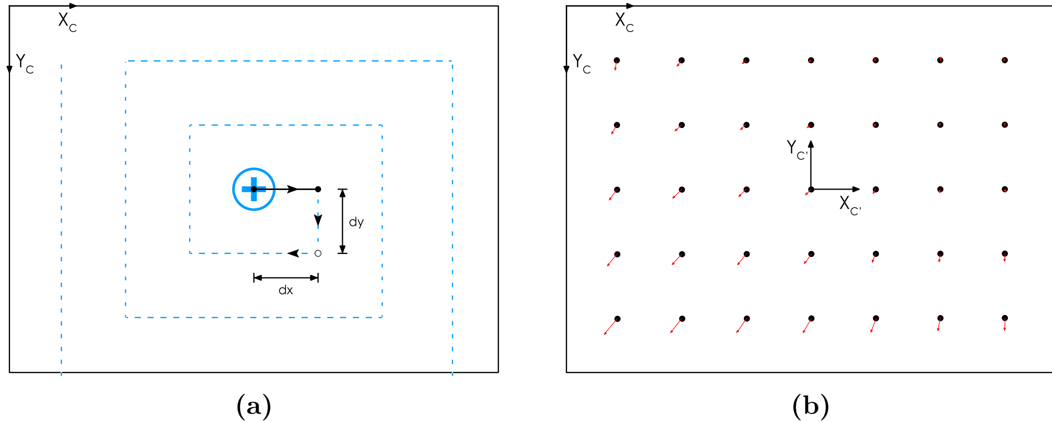

Figure 3.5.: Calibration grid for the optical system of the probe station. (a) The alignment mark (depicted as a blue cross in a circle) of the microstrip sensor is used to create a manual calibration grid of dots with arbitrary spacing in the X and Y directions. The dashed line represents the motion pattern. (b) The resulting calibration grid with superimposed point distortion errors (red arrows). The errors are scaled by a factor of 30 for presentation purposes. The black rectangle represents the coordinate space of the camera.

tensity over the full zoom range was performed. Figure 3.4f shows the obtained dependence. The data points are fitted with an exponential function. It allows automatic intensity control and ensures the same lighting conditions for calibration procedures.

3.2.4. Pixel Mapping

The established micrometer-to-pixel conversion is not sufficient for accurate positioning of the microstrip sensor in the coordinate space of the motors. An optical setup is characterized by radial, tangential, and perspective distortions. Spatial calibration is required to account for distortion errors and to compute the camera-to-motor coordinate transformation.

The manual calibration template was defined using the calibrated XY motor stages. In this approach, the alignment mark of the CBM microstrip sensor is taken as a reference object. Its location in the camera coordinate space is detected using the Pattern Matching tool of the NI Vision package. The dot grid array is created by moving the chuck with the sensor under the camera and recording its location at each step. Figure 3.5a shows the described approach. Because NI Vision computes the mappings around each dot, only the area in the image covered by the grid dots is accurately calibrated. It is recommended to keep the steps in the X and Y directions equal ($dx = dy$) and cover as much image area as possible with the dot array. In this work, a step size of 100 µm was used, resulting in a grid of 31×27 dots.

Once the calibration grid is defined, learning for perspective and non-linear

distortions is performed using the NI Vision calibration tools. The algorithm computes the corrected position of the dots and provides a pixel-to-micrometer mapping around each dot in the calibration grid. Figure 3.5b shows an example of the calibration results for a test grid with a step of 500 µm. Position distortion errors are represented as red arrows pointing in the direction of the corrected position. The arrows are scaled by a factor of 30 for presentation purposes. The NI Vision software calculates the distortion percentage as the error divided by the distance from the optical axis for each pixel. The average result for the shown example is 0.64 %. A calibration grid with a step of 100 µm improved the quality of the calibration, indicating 0.12 % distortion. The estimated mean positional error that can be expected when converting from pixel to micrometer units is 0.83 µm. The error value has a confidence interval of 95 %.

To make measurements in the motor coordinate space, it is necessary to define a coordinate system. After calibration, the origin of the $X_{C'}Y_{C'}$ camera coordinate system is in the center of the image. Then the transformation between the camera and motor coordinate spaces is a simple translation:

$$\vec{p}_M = \vec{p}_C + \vec{t} \tag{3.1}$$

where $\vec{p}_M$ is a point in the motor coordinate space, $\vec{p}_C$ is a point in the camera coordinate space, and $\vec{t}$ is the translation vector between the origins of coordinate spaces.

3.2.5. Sensor Alignment

After placing the microstrip sensor on the vacuum chuck, it has to be aligned with the coordinate axis of the motor stages. The two alignment marks are used as reference points. Figure 3.6a shows a schematic representation of the automatic alignment procedure implemented for the probe station. The starting position can be arbitrary. First, the upper left AM is located and its position in the motor coordinates is recorded. The Pattern Matching tool also extracts its rotation angle. It is used to facilitate the search for the upper right AM. Knowing the coordinates of both alignment marks, the angle between the corresponding line and the X_M axis is extracted. The rotary motor stage then performs a precise angular alignment.

3.2.6. Sensor Coordinate Transformation

The angular alignment of the microstrip sensor is limited by the accuracy of the rotary stage. The sensor plane is not parallel to the XY plane of the motors. This introduces stretching in the X and Y directions. Therefore, a spatial calibration is performed to compute the sensor-to-motor coordinate transformation.

Four alignment marks, one from each corner of the microstrip sensor, are used as reference points. Figure 3.6b shows a schematic representation of the coordinate calibration procedure implemented for the probe station. The coordinate

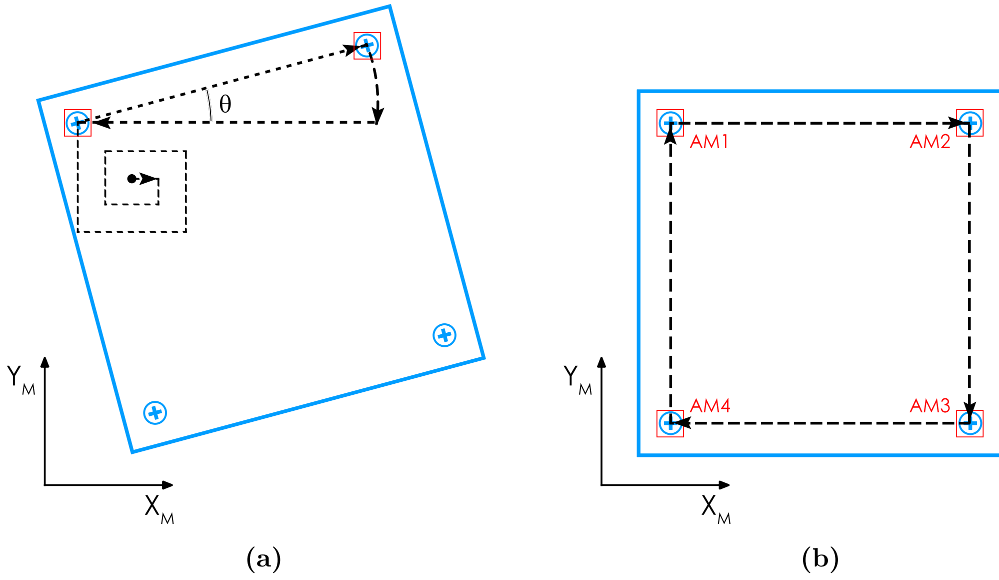

Figure 3.6.: Principles of sensor alignment and coordinate calibration. The blue rectangle represents the microstrip sensor. The dashed line indicates the movement pattern. (a) The alignment of the sensor with the X axis of the motors is performed by determining the position of the two alignment marks. (b) The coordinate calibration starts at the upper left corner of the sensor with subsequent detection of four alignment marks.

calibration immediately follows the alignment procedure. It starts in the upper left corner where the 1$^{\text{st}}$ alignment mark is detected. Three remaining marks are detected by scanning clockwise around the perimeter of the sensor. Their positions in the motor coordinate space are recorded.

The transformation from the sensor to motor coordinates can be expressed in standard matrix form:

$$\vec{p}_M = \mathbf{SR}\vec{p}_S + \vec{t} \tag{3.2}$$

where $\vec{p}_M$ is a point in the motor coordinate space, $\vec{p}_S$ is a point in the sensor coordinate space, $\vec{t}$ is the translation vector between the origins of coordinate spaces, $\mathbf{R}$ is the rotation matrix, and $\mathbf{S}$ is the stretching matrix. Knowing the topology of the sensor from the CAD files, the solution is obtained by fitting the Eq. 3.2 to the calibration data points using the Minuit package [98]. The fitting procedure is performed by calling the ROOT-based macro from the LabVIEW subprogram.

Having best-fit parameter values, the coordinates from sensor coordinate space can be converted to motor coordinate space. Thus, stepping through all strips of the microstrip sensor can be performed in a calibrated way. For convenience, the origin of the sensor coordinate system is located at the position of the upper left alignment mark. This allows the AC pads for contacting to have the same coordinates regardless of the sensor size.

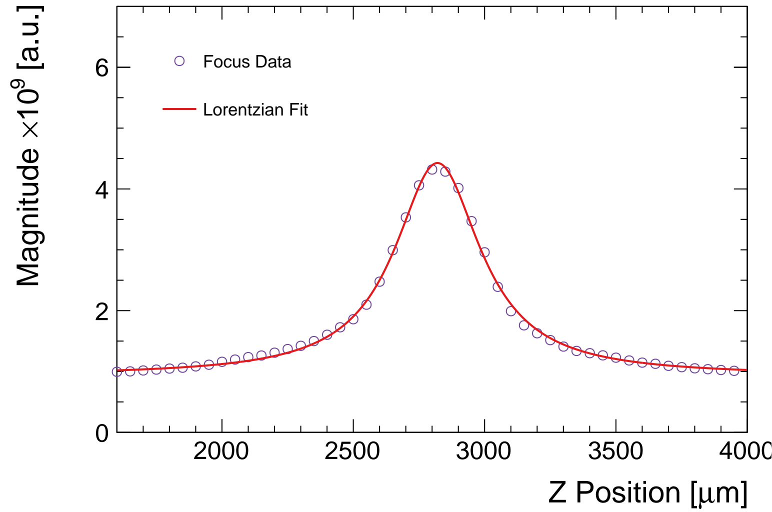

Figure 3.7.: Example of the acquired focus curve with a fitted Lorentzian function. Images are recorded in 50 µm steps using the calibrated Z stage of the probe station. The zoom value is set to 1000 (in motor steps).

3.2.7. Height Measurement

A contactless approach to the measurement of the height was implemented in the probe station. It is based on the analysis of the image's sharpness. Details and sharp edges in the image are associated with high spatial frequencies.While low frequencies are associated with slowly varying patterns. The sharpness of the image increases when approaching the "in-focus" position. To quantify it, the image is transformed to the frequency domain using the Fast Fourier Transformation (FFT) algorithm in LabVIEW [99]. The FFT creates a complex image of the same size. The sum of the magnitudes of all complex pixels is used as a measure of the image sharpness. By adjusting the distance from the object to the optical system, the total magnitude is calculated at several positions and the focus curve is acquired. Figure 3.7 shows an example of the focus curve. The maximum of the curve is the point of highest sharpness and therefore corresponds to the "in-focus" position. To extract it, the focus curve is fitted with a Lorentz function with four parameters:

$$f(z) = m_0 + A \cdot \frac{1}{\gamma\left[1 + \left(\frac{z-z_0}{\gamma}\right)^2\right]}, \tag{3.3}$$

where m_0 is the offset, z_0 is the location parameter that specifies the location of the peak, γ is the scale parameter that specifies the half width at half maximum, A is the height of the peak. The extracted peak position is at 2821 µm. The fitting procedure is performed with the nonlinear Levenberg-Marquardt method in LabVIEW. The offline analysis is performed in ROOT with the Minuit package.

The automated search for the most focused position, the so-called auto-focusing,

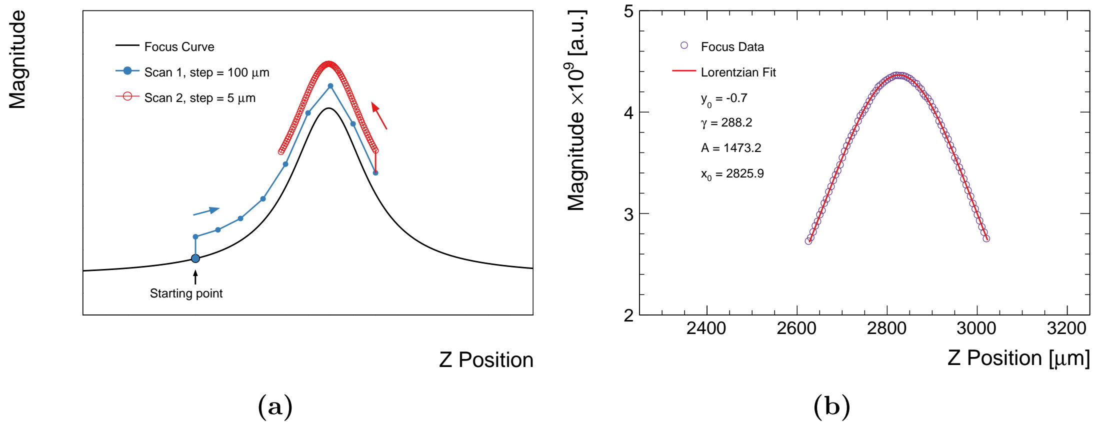

(a) (b)

Figure 3.8.: Measurement of the object height by auto-focusing method. (a) First, a scan with a rough step is performed to determine the approximate location of the peak. Next, a scan with a precise step is performed around the peak. (b) The acquired focus curve is fitted with the Lorentzian function and peak position is extracted.

was implemented using the calibrated Z stage of the probe station. Figure 3.8a shows the principle of the implemented method. First, a rough Z scan with a step of 100 µm is performed to determine the approximate location of the peak. The step size for the rough scan is chosen from the requirement to have several points in the peak at a fixed zoom value. As the peak is passed, a precise Z scan with a step of 5 µm is performed in the opposite direction. The turning and end-points are set to 60 % of the maximum magnitude. This approach results in more data points around the peak, which improves the fit. Figure 3.8b shows an example of the acquired focus curve and the corresponding fit. The precision of the auto-focusing method was estimated by carrying out a series of repetitive measurements. The same "in-focus" position was measured 50 times. The estimated precision is ±0.8 µm. The motorized focus stage of the optical system was not used for accurate height measurements in this work.

In this method, auto-focusing does not provide an absolute height measurement. Only the associated Z coordinate is extracted for the most focused image. Performing auto-focusing over a grid of regions of the object under test allows measurement of its height map. Figure 3.9a shows the obtained height map of the CBM $62 \times 62\,\mathrm{mm}^2$ prototype sensor. It shows the characteristic warp that is a result of the mechanical stress induced on a silicon wafer during different manufacturing steps [69]. When mounted in the test socket for electrical inspection, the height map of the sensor changes significantly. Figure 3.9b shows the height map of the sensor held in place by the socket clamps.

A highly optimized auto-focusing method was implemented in the optical inspection setup at the University of Tübingen [100, 101]. It was successfully applied in the optical quality control to measure the warp of the CBM microstrip sensors during the series production [102].

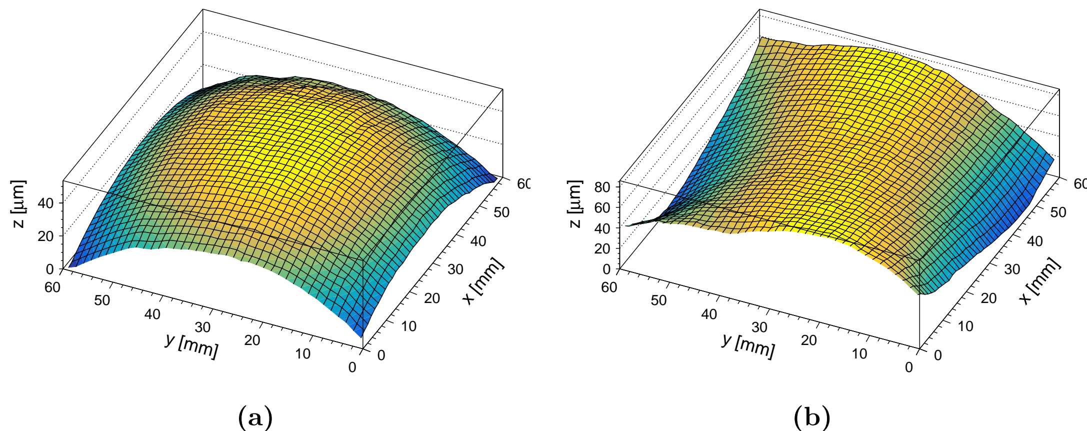

Figure 3.9.: Height map of the p side of the CBM $62 \times 62\,\mathrm{mm}^2$ prototype sensor obtained with auto-focusing method: (a) the sensor rests freely on the vacuum chuck, and (b) the sensor is held in place by the clamps in the support frame. The grid step is 2 mm in the X and Y directions.

3.2.8. Height Adjustment

It is important to provide a reliable contact between the probe needles and the test pads of the strips for the electrical inspection. Figure 3.9 shows that the surface of the microstrip sensor is never flat. This has implications for large area inspection of strips. Without additional actions, in some positions, contact may be lost or the sensor may be damaged by the needles. To avoid such a situation, it is necessary to adjust the vertical position when stepping through the strips.

The height adjustment procedure was implemented for the probe station. The auto-focus method is used to measure the height profile along rows of AC pads[1]. The obtained Z coordinates are referenced to the Z coordinate of the first AC pad. The data are fitted with a 5$^{\text{th}}$ order polynomial to compute the positioning profile for height adjustment. The sensor can then be positioned vertically in a way that the probe needles have reliable contact with the test pads.

The Z profile scan is performed after the coordinate calibration procedure described in Section 3.2.6. Figure 3.10 shows an example of the obtained positioning profile. It was measured along the first row of AC pads with the horizontal step of 2 mm. Without height adjustment, loss of contact would occur after the first few strips when moving along the x-axis. Towards the end, the needle would cause a deep scratch on the AC pads. The implemented height adjustment procedure ensures a uniform and consistent contact quality for all strips of the sensor under inspection, with a precision better than $\pm 1.5\,\mu\mathrm{m}$.

[1] AC contact pads are used for the electrical inspection of strips

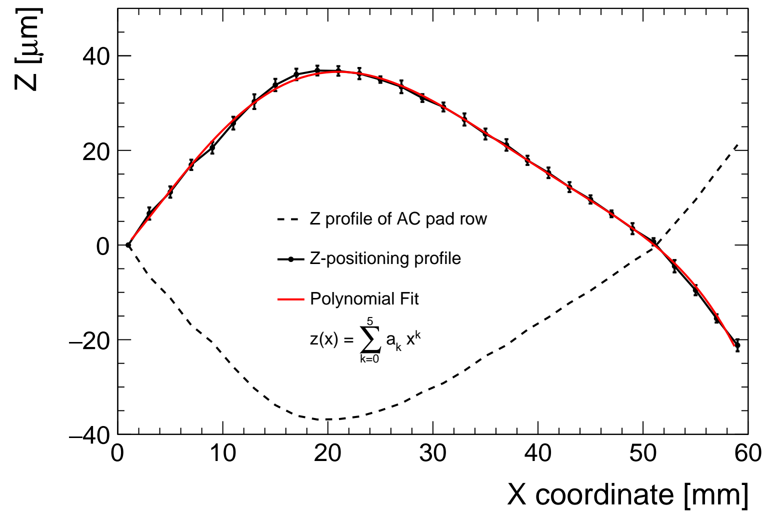

Figure 3.10.: Z profile of the AC pad row and the corresponding positioning profile used for height adjustment during the electrical inspection of strips. The data are fitted with a 5th order polynomial. The Z profile was measured ten times for the same row of the AC pads and the error bars indicate one standard deviation.

3.2.9. Performance Estimation

The final performance of the probe station after all calibration procedures was characterized in terms of positioning accuracy and repeatability. An important question is how accurately the microstrip sensor can be positioned under the probe needle when stepping through strips. It was estimated by conducting a series of repetitive measurements.

In the standard stepping procedure, the CBM microstrip sensor is moved in fixed increments of 116 µm along the x-axis in the sensor coordinate space. At each step, the position of the target AC pad is detected by the NI Vision Pattern Matching tool as shown in Fig. 3.11a and Fig. 3.11b. It is compared to its true position in the sensor coordinate space and the positioning error is calculated. The sensor is moved through its full length and each step is repeated 50 times. The collected data, the average error and the standard deviation for each AC pad, are plotted in Fig. 3.11c and Fig. 3.11d for the X and Y errors, respectively. The overall accuracy is calculated as a difference between the highest and lowest error. The repeatability is calculated from the positioning data of all 510 AC pads measured 50 times in both forward and reverse stepping directions. The specified repeatability values represent one standard deviation.

The obtained results indicate that at the end of the stepping procedure the probe needle will remain within a few microns of where it was initially positioned. Using position error profiles, a correction table can be generated. This allows the positioning accuracy to be further improved, limited only by the repeatability performance of the system.

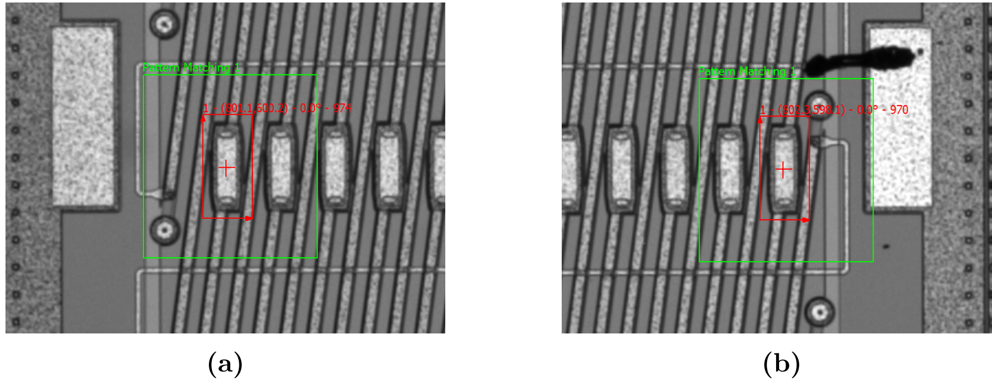

(a) (b)

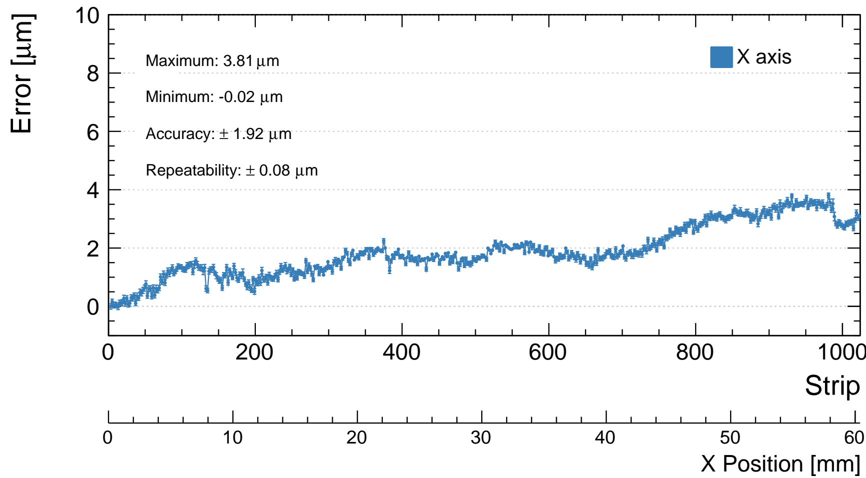

(c)

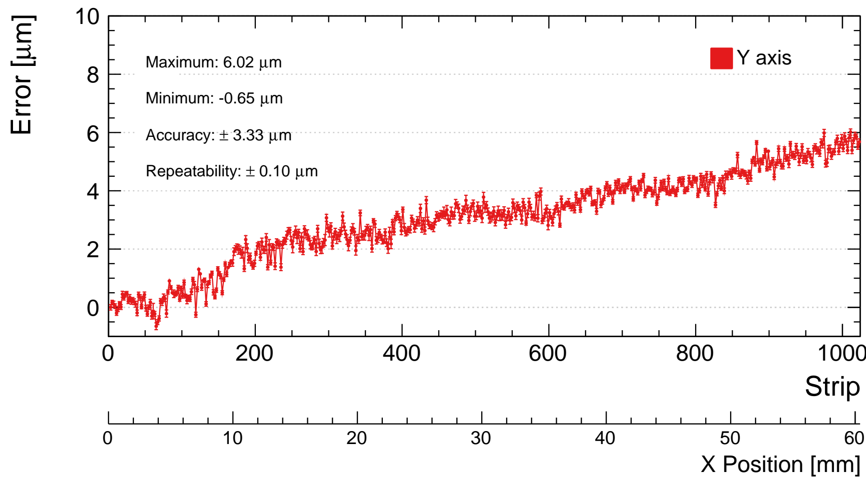

(d)

Figure 3.11.: Performance estimation of the probe station in terms of accuracy and repeatability of the positioning of the sensor under the probe needle. (a)-(b) The position of the AC pads is detected by the Pattern Matching tool. It is compared to the true position in the sensor coordinate space and positioning errors are calculated for every AC pad. (c)-(d) Positioning accuracy plots. The data points represent the average inaccuracy at the position of the AC pad, the error bars represent one standard deviation.

3.3. Measurement Equipment

The probe station is equipped with the following measurement instruments:

- Keithley 2410 Source-Meter unit [103] (SMU) for supplying bias voltage up to ±1100 V;
- Keithley 6487 picoammeter/voltage source [104] for precision current measurement and small test voltage application, with measurement range from 2 nA to 20 mA and high resolution voltage source up to ±505 V;
- QuadTech 7600 Precision LCR meter [105] for impedance measurement, with wide frequency range from 100 Hz to 2 MHz, 0.05 % measurement accuracy, and programmable ac test signal.

Standard coaxial cables and BNC connectors are used to establish the connections between devices and probe needles. All measurement instruments are connected to a PC via GPIB or RS-232 interface and controlled by LabVIEW-based software.

3.3.1. Switching Scheme

Large-scale testing requires automation of the measurement process. Manual reconfiguration of the setup at each step is time-consuming. Because silicon sensors are fragile objects, it is advisable to touch them as little as possible with needles. This leads to a necessity to acquire several parameters at each step. The Tübingen probe station is equipped with a switching device to fulfill these requirements.

A switching matrix Keithley 708B [106] with switch card 7072-HV [107] is used in this work. It has 8 inputs and 12 outputs. The first two rows are optimized for low leakage measurements with < 1 pA offset current. Four general-purpose rows have a low offset current of < 20 pA making them suitable to measure sensor leakage current. In addition, the 7072-HV switch card features two rows optimized for capacitance measurement. These rows have 5 MHz bandwidth and a low stray capacitance of 0.6 pF. The maximum signal level between any two pins or chassis is 200 V.

Figure 3.12 shows the scheme of connection of devices to the switching matrix of the probe station. Additional elements, such as capacitors and resistors, are omitted here for clarity, and details are given in Chapter 4. The measurement instruments are connected to inputs “C-H”. Low-current inputs were not used in this work. The front side of the microstrip sensor is connected to output “2”. Its backside is connected to output “1” and the HI terminal of Keithley 2410. Four available probe needles are connected to outputs “3-6”. Any combination of needles can be connected to any instrument by closing the switch at the appropriate cross-point. Using a switching matrix allows performing all integrity tests in a

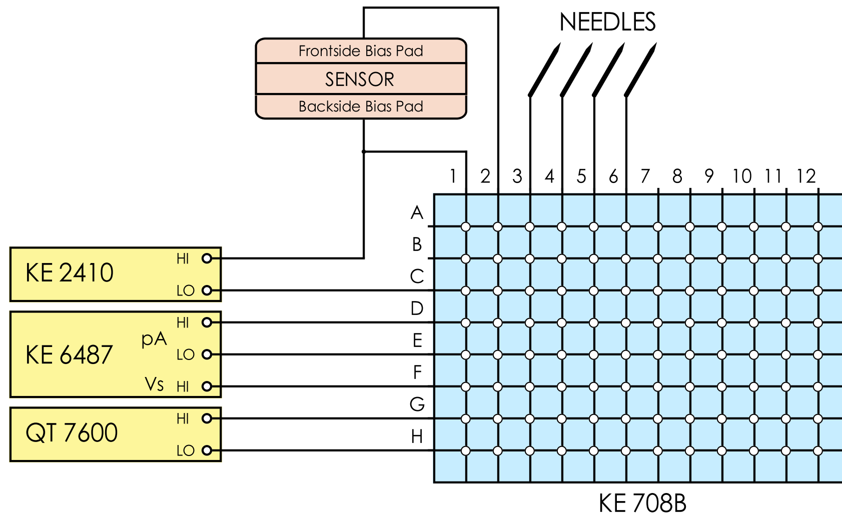

Figure 3.12.: The scheme of connection of devices to the switching matrix of the probe station. The measurement instruments are connected to inputs C-H. The microstrip sensor is connected to outputs 1-2. Probe needles are connected to outputs 3-6.

sequence so that each strip is contacted only once. Fast reconfiguration of the setup by switching leads to significant reduction in the inspection time per sensor and eliminates possible testing errors.

3.3.2. Capacitance Measurement

One of the important parameters of the silicon microstrip sensor is the capacitance between its structural elements. For example, the noise of the readout channel depends on the interstrip capacitance. Its typical values are in the range of 1–10 pF for the CBM prototype sensors. The measured capacitance is subject to systematic errors due to various residuals in the measuring setup. Figure 3.13a shows a schematic representation of the probe station measurements. The accuracy of the LCR meter is specified at the calibration plane[2]. It deteriorates by the parasitic impedance of the cables, isolation box, switching matrix, test socket, needles, etc., which are connected between the sensor and the calibration plane. The procedure to perform compensation with the actual measurement setup is the key to obtaining accurate capacitance values.

The most common errors in capacitance measurement are offset and gain errors. Offset errors are compensated by performing “OPEN/SHORT” zeroing of the LCR meter. The residual impedance is measured when the probe needles are shorted. The stray admittance is measured when the circuit is opened between probe needles. The actual capacitance value is then calculated by the LCR me-

[2]The calibration plane is a reference plane at the terminals of the measuring instrument where the measurement accuracy is specified.

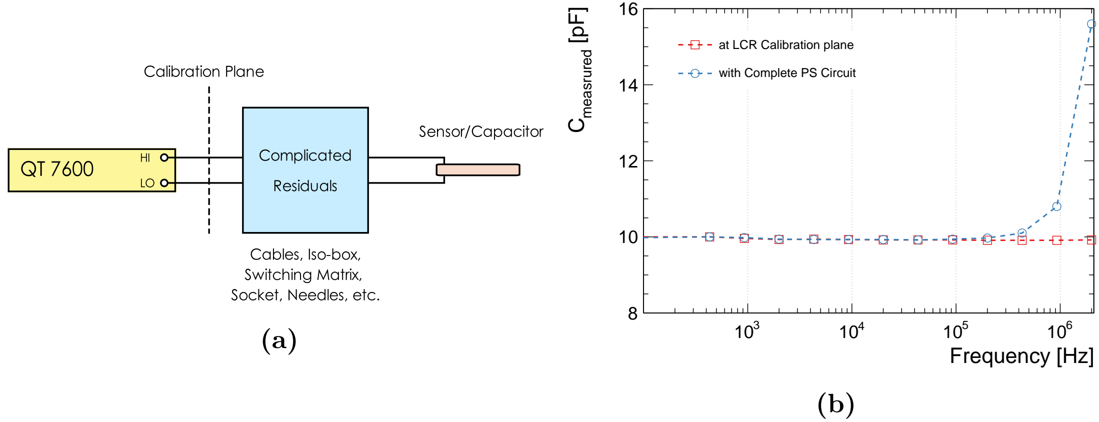

Figure 3.13.: Capacitance measurement with the probe station: (a) schematic representation of the measurement circuit and its residuals due to the test fixtures between the device under test and the calibration plane of the LCR meter, (b) comparison of the capacitance measurement at the calibration plane and at the end of the complete circuit of the probe station (only "OPEN/SHORT" compensation is applied).

ter by applying the measured corrections. Figure 3.13b shows an example of the capacitance measurement of a 10 pF ceramic capacitor. After "OPEN/SHORT" compensation, both curves coincide in a broad frequency range. At high frequencies[3], the gain error becomes significant, which is manifested in an increase in the measured capacitance.Usually, "LOAD" compensation is suggested in addition to the "OPEN/SHORT" one. However, to be effective, an appropriate load close in value to the test impedance must be found. This is not practical for accurate capacitance measurements on microstrip sensors of different geometries and types. Therefore, an alternative procedure was developed in this work to correct the gain error.

Since the gain error is a function of the capacitance of the device under test, a set of seven ceramic capacitors with nominal values ranging from 2 pF to 10 pF was used for the compensation procedure. Their values were chosen to cover the typical range of strip capacitances measured at high frequency. First, the reference capacitors are measured at the calibration plane to determine their capacitance. Uniform values were obtained in the whole frequency range. The LCR meter is then connected to the switching matrix and probe needles, and a careful "OPEN/SHORT" compensation is performed as discussed earlier. The reference capacitors attached to the probe needles are measured again. Figure 3.14a shows the obtained CF curves, where the plateau values correspond to the actual capacitance values of the reference capacitors. A polynomial fit is used to extract the capacitance at any frequency. By fixing one frequency, the dependence between measured and actual values is obtained. Figure 3.14b shows the plotted dependencies for several reference frequencies. The x-axis represents what the probe

[3]In this work, frequencies above 100 kHz are referred to as high frequencies.

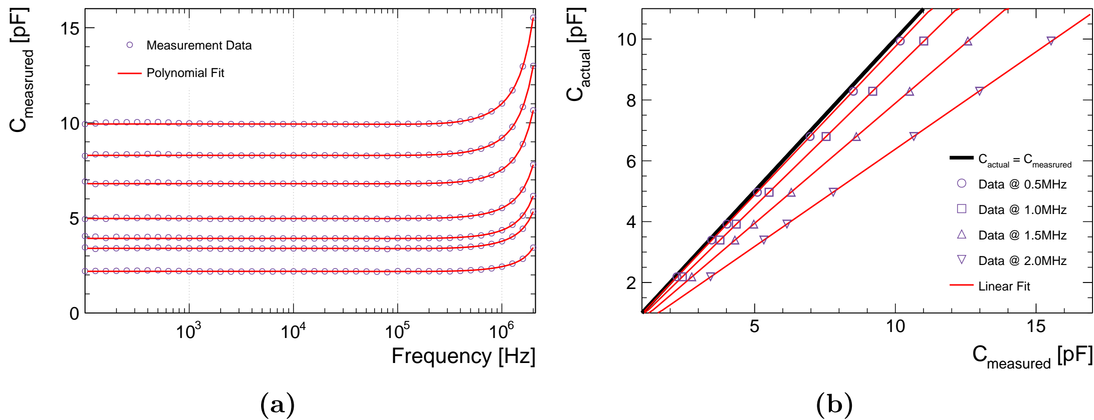

Figure 3.14.: Gain error compensation method that is implemented in the probe station. (a) CF curves of seven ceramic capacitors. The measurement is performed in a 4-probe configuration, with the complete circuit, and after "OPEN/SHORT" zeroing. The data are fitted with a polynomial. (b) Relationship between the measured and actual capacitance. The data are fitted with a linear function for each frequency.

station measures, including errors. The y-axis represents the actual value of capacitance. The data are fitted with a linear function for each frequency. Then the actual capacitance can be obtained from a simple relationship:

$$C_{actual} = a + b \cdot C_{measured}, \tag{3.4}$$

where a and b are fit coefficients. Below 100 kHz no correction is needed. The gain error causes the measured capacitance to be increased by about 11 % at 1 MHz and by 57 % at 2 MHz. Since the interstrip capacitance is measured at frequencies $\geq$ 1 MHz, the established correction procedure is of high importance for quality assurance of the microstrip sensors.

The results in Fig. 3.14a were obtained in a 4-probe configuration[4], with the complete measurement circuit of the probe station. For the best measurement accuracy, the described procedure was repeated for all configurations used, and the fit results are stored. The "GAIN" correction procedure was implemented in the software for automatic correction of the measured capacitance.

3.3.3. Performance Estimation

A number of tests were conducted to ensure the expected performance of the probe station's measuring equipment.

3.3.3.1. CMS Test Structures

The performance of the probe station in terms of capacitance measurement was cross-checked using test structures from the CMS standard "half-moon". It was

[4] See Chapter 4 for details.

(a)

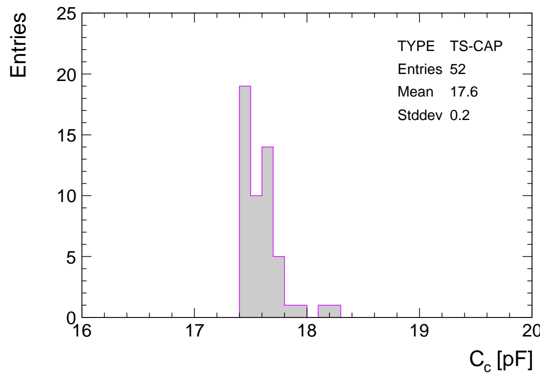

(b)

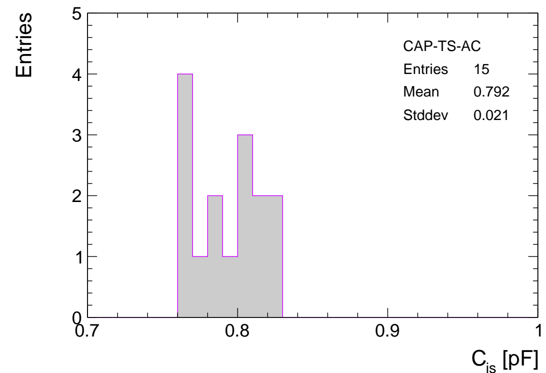

(c)

Figure 3.15.: Results of the electrical performance cross-check using CMS test-structures. (a) A photo of the CMS standard "half-moon" containing nine test structures. (b) Distribution of the measured coupling capacitance. (c) Distribution of the measured interstrip capacitance.

designed by the CMS collaboration to monitor the stability of the fabrication process. A set of nine structures is placed along the periphery of the wafer. A detailed description of all structures can be found in Ref. [76]. One of the two "half-moons" tested by the Tübingen probe station is shown in Fig. 3.15a. The distribution of the measured coupling and interstrip capacitance is shown in Fig. 3.15b and Fig. 3.15c, respectively. The obtained results correspond to those reported in Ref. [108] for equivalent structures. Cross-checking provided confidence in the ability of the custom-built probe station to accurately measure strip capacitances.

3.3.3.2. STS Micro Cables

Ultra-light micro-cables are a key component for the CBM Silicon Tracking System. A micro-cable stack that consists of four signal and two shielding layers will be used for the module assembly. Figure 3.16a shows a photo of the tested micro-cable. In addition to the total strip capacitance, micro-cables also contribute to the load capacitance seen by the FEE. Therefore, it is important to know the total parasitic capacitance C_{tot} of the individual trace. The micro-cable

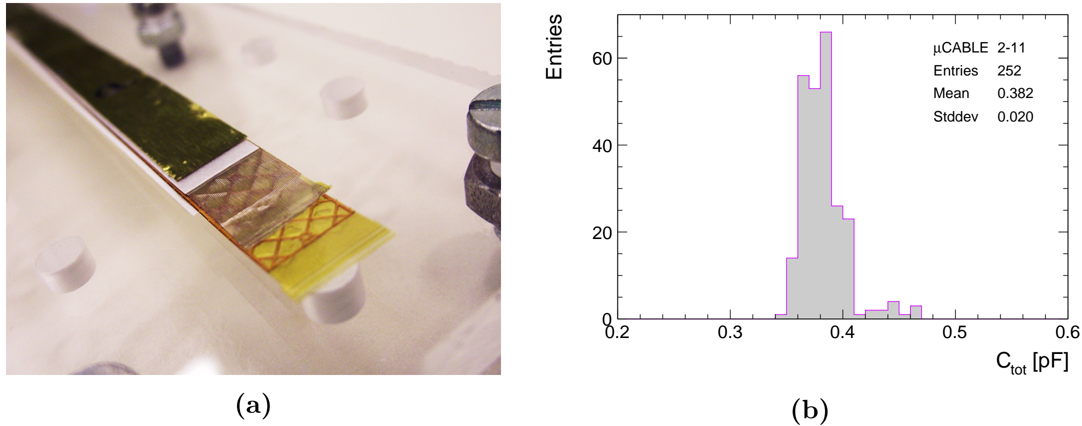

(a)

(b)

Figure 3.16.: Results of the capacitance measurements of the STS micro-cables. (a) A photo of the tested STS micro-cable. It is composed of four signal and two shielding layers. (b) Distribution of the measured total trace capacitance.

stack can be considered as an array of small capacitors without resistors. The measurements were carried out at the Tübingen probe station using the developed procedures. Figure 3.16b shows the distribution of the measured C_{tot} of all traces of the micro-cable. The obtained results were then compared with the simulations in Ref. [109] and found to be in agreement. This indicates that the probe station configuration and measurement procedures are well optimized.

3.4. Software Solution

The setup is controlled with a PC running NI LabVIEW 2019[5] software. Custom LabVIEW-based programs were developed to provide flexible control of all instruments and to automate calibration and measurement routines. The goal was to implement features that are really needed to perform a fast and reliable inspection of microstrip sensors. Special attention was paid to the graphical interface of the developed software to make it intuitive and user-friendly.

3.4.1. Probe Station Control

Figure 3.17 shows the front panel of the "MAIN.vi" program. It provides complete control of the probe station. Its window consists of a sidebar with controls and an image area to display images captured by the camera. The crosshair is drawn in the center for reference. The scale bar in the lower corner indicates the current scale information. It is automatically updated for different zoom values of the optical system.

[5] LabVIEW by National Instruments is a graphical programming environment used to develop measurement, test, and control systems [89].

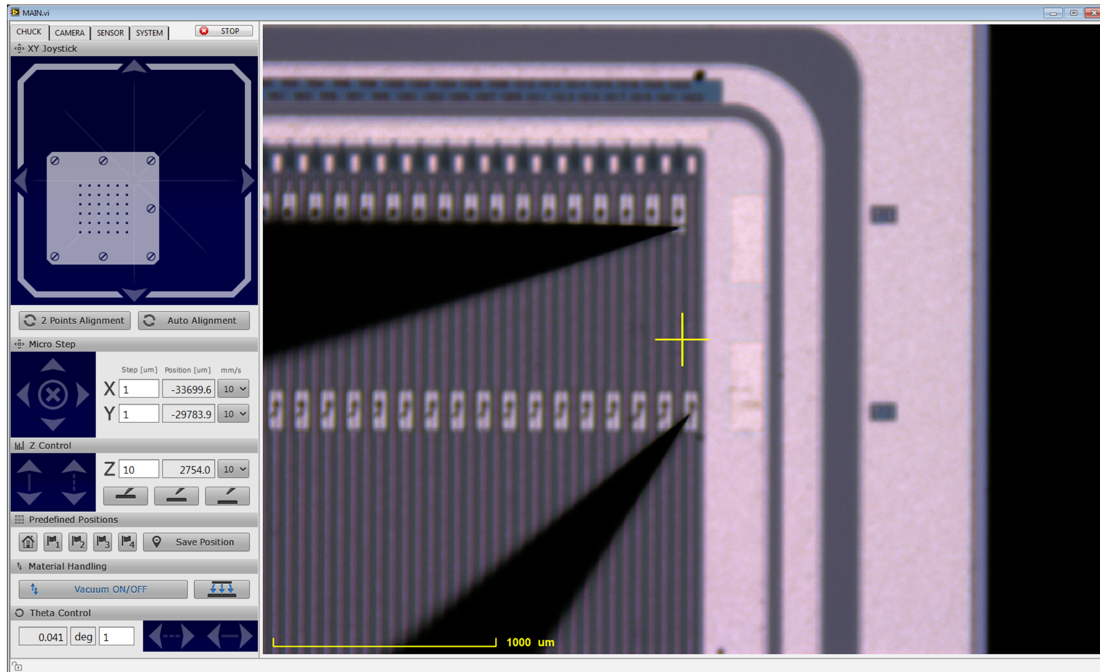

Figure 3.17.: The graphical user interface of the probe station control program.

The sidebar contains four tabs with thematically grouped controls: chuck, camera, sensor, and system. The "Chuck" tab provides means to position the XYZΘ stages, which carry the vacuum chuck. In addition to the standard controls that allow continuous and step-like movement, a handy joystick was implemented that allows the XY stages to be positioned by simply dragging the chuck figure. Controls for manual/auto-alignment are located below the joystick. Z controls can have predefined positions corresponding to "contact" and "no contact". The "Chuck" tab also contains controls for switching on/off the vacuum.

Figure 3.18 shows the other three tabs of the sidebar of the "MAIN.vi" program. The "Camera" tab provides means to position the XY stages, which carry the optical system of the probe station. A similar joystick allows fast and easy repositioning of the camera. The zoom and focus of the system can be adjusted here or set to predefined values. The "AF" control allows the system to autofocus. The "Camera" tab also contains controls for switching on/off the light. In addition, the "Chuck" and "Camera" tabs have controls to save the current position that can be used, for example, to easily navigate between the alignment marks.

The "Sensor" tab contains a set of controls specific to the spatial calibration and positioning of the microstrip sensor[6]. After placing the sensor on the vacuum chuck, it is necessary to select the type of sensor and its size. The "Coordinate

[6]It should be noted that the functionality can be easily adapted to work with any type of sensor/chip by updating the configuration file.

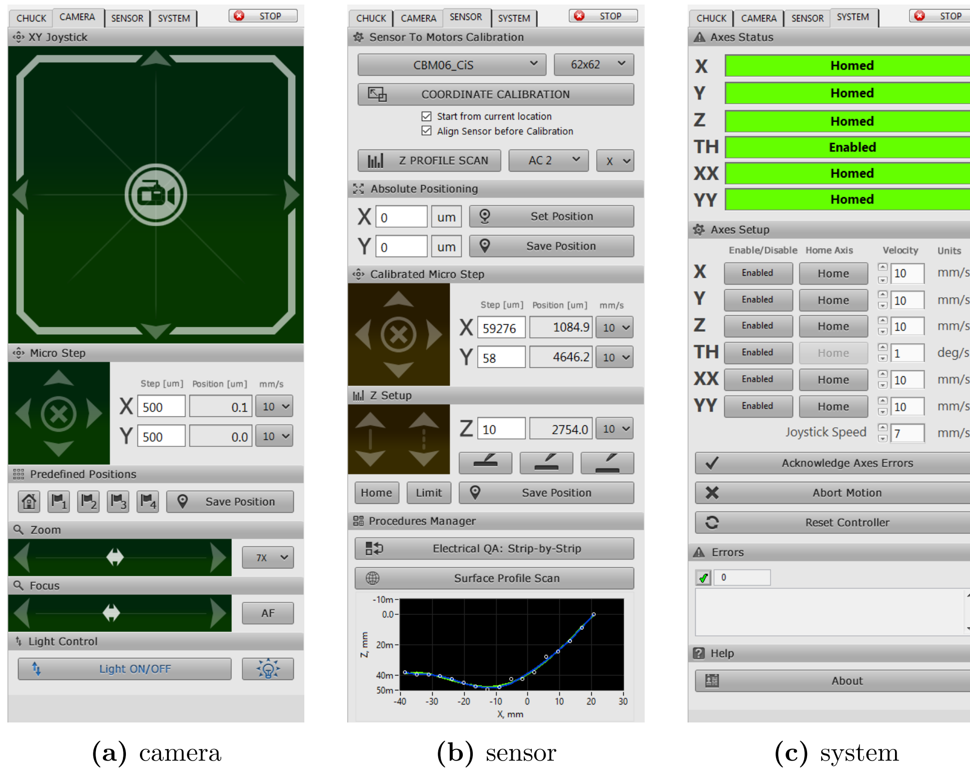

(a) camera **(b)** sensor **(c)** system

Figure 3.18.: Camera, sensor, and system tabs of the probe station control program.

Calibration" and "Z Profile Scan" controls can then be used to run the corresponding procedure. After calibration, the controls for calibrated positioning in the sensor coordinate space can be used. The "Sensor" tab also provides means to define "contact" and "no contact" Z positions. From this tab, the inspection program can be launched by pressing "Electrical QA: Strip-by-Strip".

The "System" tab allows to monitor the status of the motors and the controller. Error messages appear here and are duplicated in short form in the status bar at the bottom of the window.

3.4.2. Measurement and Data Acquisition

Several programs were written for individual characterization procedures to perform various voltage and frequency scans of the sensor and individual strips. A dedicated program was developed to automate repetitive measurement steps on all strips. Figure 3.19 shows the front panel of the "Strip-by-Strip-QA.vi" inspection program. It is launched from within the "MAIN.vi" program after the coordinate calibration is complete[7]. Its window consists of several tabs and always starts with the "Configuration" one. Here, four panels can be found: Sensor, Devices, QA Tests, and Data.

[7]Also, it can run standalone without calibration information.

The “Sensor” panel combines all necessary information about the sensor under inspection and allows to specify starting strip, number of steps, and step size. The “Side” field affects the polarity of the bias voltage. Additional options like movement axis, stepping direction, and sensor orientation can be specified here.

The “Devices” panel provides the means to adjust the selected device. For example, field “Keithley 708B” allows to change the switching matrix channel configuration if a non-standard test is required. By default, standardized settings are loaded from the configuration file.

The “QA Tests” panel contains a list of quality assurance tests grouped by category. By selecting one, the test-specific settings can be adjusted. A simplified electrical diagram is displayed below the list for the selected test. Procedures for all required electrical tests were developed and integrated. Additional tests can be easily added to the list if a non-standard strip-by-strip test is required. The “QA Tests” panel also allows to configure the bias voltage. Figure 3.19a shows the selected “Pinhole Test” and “Strip Open-Short Test”, which are a standard set of QA tests for the production phase of the CBM microstrip sensors.

The “Data” panel allows to specify where and how to save the strip inspection results.

The front panel of the “Strip-by-Strip-QA.vi” program becomes active only when the “Configured” control is pressed. The inspection can be launched by pressing “Start”. Figure 3.19b shows a screenshot of the running inspection. In the middle of the window is a strip chart that provides a graphical representation of the test status for each strip. The information can be accessed by mouse-clicking on the strip of interest. Simplified color coding indicates whether the strip meets the global acceptance criteria or not.

The “Graphs” and “Data Table” tabs provide a corresponding representation of the measurement data. The “System” tab collects and lists error information.

When the inspection is finished, a pop-up window with the inspection summary appears. Figure 3.20 shows two examples with different inspection results. The strip test results and information about the inspected sensor are stored in a text file for further analysis.

3.4.3. Data Analysis

The measurement results are saved in text format. Processing of the measurement data has been done within the ROOT[8] analysis framework using macros. Advanced analysis of the strip test data is described in Chapter 6.

[8]ROOT is an object-oriented framework for large scale data processing [110].

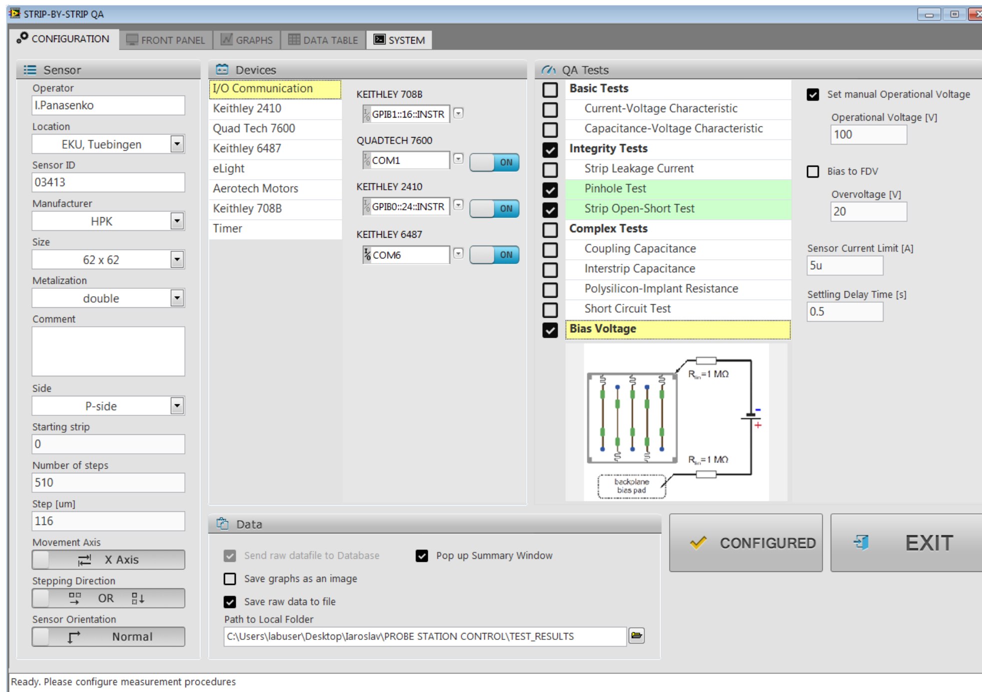

(a)

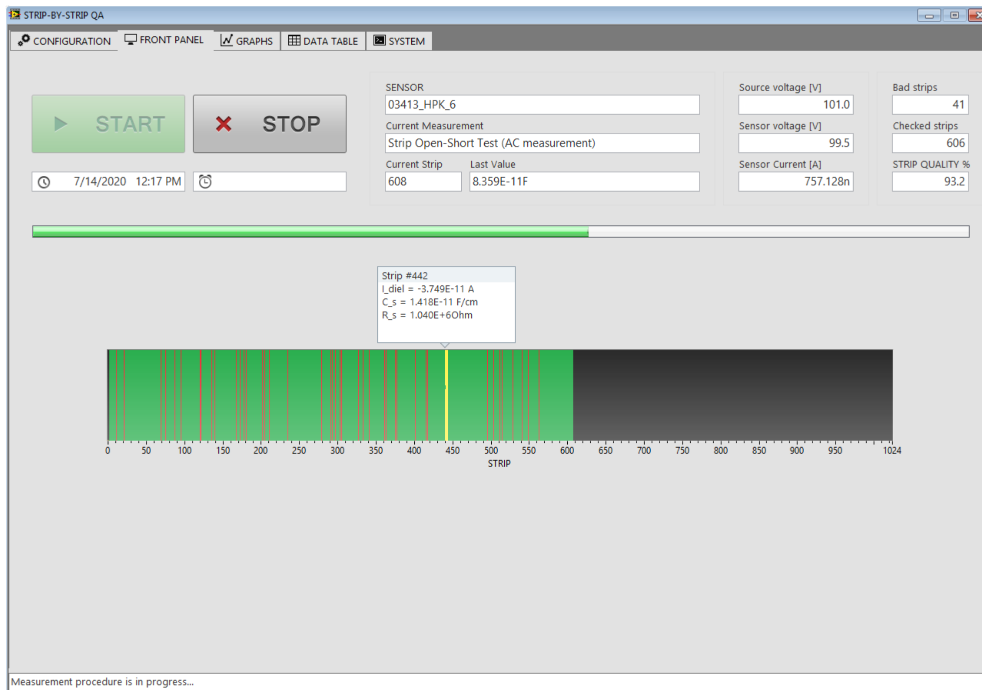

(b)

Figure 3.19.: The graphical user interface of the electrical inspection program: (a) configuration panel, (b) front panel of the running inspection.

Figure 3.20.: Summary window of the strip electrical inspection.

3.5. Throughput Estimation

The probe station was designed to perform quality assurance and control tests of the CBM microstrip sensors. Optimization of the stepping and measurement procedures was done for the strip integrity tests. When the sensor is placed on the vacuum chuck, automatic coordinate calibration procedures are performed. The time required is about 10 min. For the electrical inspection, the vacuum chuck moves to test every single strip. The stepping procedure alone takes 6 min for 1024 strips. The standard set of strip integrity tests[9] takes about 103 min, including biasing of the sensor. Therefore, the total time required to inspect one side of the CBM microstrip sensor is 2 h. Additional time is necessary for assembly, positioning of the probe needles, and a quick visual check of the sensor. This results in about 5 h for a complete inspection of one CBM sensor. The estimated throughput of the Tübingen probe station satisfies the foreseen quality control task for the series production of the CBM microstrip sensors [64].

[9] See Section 6.4.

4. Electrical Characterization of Silicon Microstrip Sensors

There are existing common techniques for the characterization of silicon microstrip sensors. It is often challenging to compare corresponding measurements which were performed on different sensors and at different measurement conditions, as well as to extend them to the new sensors. Therefore, it is reasonable to dive into characterization techniques and investigate how measurements have to be performed. The main objective is to address the issue of proper measurement conditions which is of particular importance for the case of measurements on individual strips. It is also important to give proper interpretation of the results of electrical measurements with respect to sensor properties.

This chapter describes techniques and methods for characterization of the microstrip sensors which were implemented and applied in the framework of the CBM-STS project. They were used for in-depth investigation and characterization of prototypes of the CBM sensors. The developed methods can be applied for the characterization of any silicon microstrip sensors. Results that were obtained with non-irradiated CBM06 sensors are highlighted and discussed.

4.1. Global Parameters

The global sensor parameters are total leakage current, breakdown voltage, full depletion voltage, bulk capacitance, effective doping concentration and bulk resistivity. Refer to Appendix B for a summary of the measured global parameters for all investigated sensors.

4.1.1. Total Leakage Current

The total leakage current at operating voltage is an essential global parameter of a silicon sensor. It contributes to the noise of the readout electronics and to power consumption. Measurement of the current-voltage (IV) characteristic is a common way to extract this parameter. Also, it allows for the extraction of the breakdown voltage V_{BD} of the sensor. It represents the maximum voltage up to which the operation of the sensor is stable. Beyond it, a breakdown occurs, which is characterized by a vast increase in the leakage current with the reverse bias voltage. It depends on electrode geometry, number and size of guard rings,

oxide quality and junction fabrication, presence of defects, etc. A sensor has to be designed in such a way that operating voltage[1] stays below breakdown voltage during the whole lifetime of the experiment. Thus, a silicon sensor should have a low leakage current at the operating voltage and a high breakdown voltage as a prerequisite for its functionality.

The total leakage current I_{TOT} consists of two components — bulk current I_{bulk} and surface current I_{surf}:

$$I_{TOT} = I_{bulk} + I_{surf}. \tag{4.1}$$

The bulk leakage current is mainly caused by the generation of electron-hole pairs in the Si volume. It is collected by the bias ring (BR) of the sensor. The surface current is the extra current that comes from the non-sensitive areas of the sensor. It is collected by the guard ring (GR) that surrounds the sensitive area. Bad oxide quality, surface contamination and scratches, edge chips and depletion region extending to the sensor edge, etc., are common sources of high surface current.

Measurement method

The measurement of IV characteristic requires connection to bias rings on p and n sides of the double-sided sensor. It is recommended to use a dedicated socket with pogo-pins to avoid possible stress and bonding damage to the sensor. Such a socket for the CBM sensors is described in Section 6.6. The bias ring of one side of the sensor is connected to the LO terminal of the voltage source, which is grounded. The opposite side is connected to the HI terminal. The ammeter is inserted between the LO terminal and the bias ring. The guard ring(s) remains floating. The connection scheme is shown in Fig. 4.1. In such a scheme, the total leakage current is measured. A current-limiting resistor has to be used to protect the sensor from an irreversible breakdown in case of an uncontrolled increase of current. It should be noted that the actual bias voltage across the sensor is now different from V_{source} and can be calculated using the equation:

$$V_{bias} = V_{source} - I_{TOT} R_{lim}. \tag{4.2}$$

The current is measured and recorded in steps of 5 V with a 5-second delay between voltage increments up to maximum source voltage or breakdown, whichever occurs first. A ramp rate of 1 V/s is recommended to achieve reproducibility of the IV curves of the CBM sensors. After the IV curve is recorded, the bias voltage has to be reduced in steps of 2 V/s.

[1]The operating voltage is defined as full depletion voltage plus some over-voltage, typically 20 % for non-irradiated sensors. Additional factors that affect operating voltage for sensors with segmented n side are discussed in Sections 4.2.5 and 4.2.7.

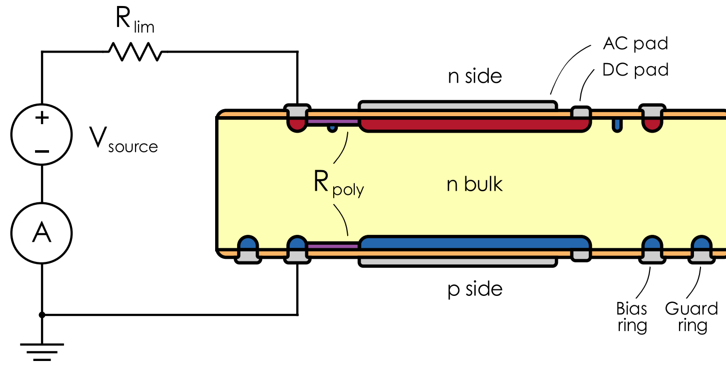

Figure 4.1.: Connection scheme for the total leakage current measurement of the microstrip sensor. p side is grounded while n side is at positive HI potential. Guard ring is left floating. Current-limiting resistor $R_{lim} = 1\,\mathrm{M\Omega}$ is introduced into scheme to protect the sensor from the breakdown.

Experimental setup

IV measurements are performed in a clean room environment with a constant temperature[2] of $T = 22.5 \pm 0.5\,°\mathrm{C}$ and a relative humidity $\approx 45\,\%$. During the measurement, the silicon sensor has to be placed in a light-tight box. A Keithley 2410 Source-Measure unit is used to supply bias voltages up to 1000 V and to measure sensor leakage current with high accuracy. Measurement resolution of 1 nA (corresponds to 100 µA measurement range of Keithley 2410 [103]) is sufficient to measure total leakage current of the typical CBM prototype sensor. The systematic uncertainty on the current from the device measurement accuracy specifications is $0.025\,\% + 6\,\mathrm{nA}$ at above specified measurement range. In case of connecting devices via switching matrix a voltage protection limit[3] has to be set to avoid damage to the devices.

Temperature dependence

The bulk leakage current strongly depends on temperature [111]. It should be normalized to one standard temperature (20 °C) for proper comparison of sensors:

$$\frac{I_2(T)}{I_1(T)} = \left(\frac{T_2}{T_1}\right)^2 \cdot exp\left[-\frac{E_g}{2k_B}\left(\frac{T_1 - T_2}{T_1 T_2}\right)\right] \tag{4.3}$$

where $E_g = 1.12\,\mathrm{eV}$[4] is the band gap width of Si, $k_B = 8.62 \times 10^{-5}\,\mathrm{eV/K}$ is the Boltzmann constant. Sensors inside the STS box will be kept at or below

[2] Hamamatsu measures the leakage current at 25 °C. CiS provides data normalized to 20 °C. Any comparison in this work is made for leakage current normalized to 20 °C.
[3] It is 200 V for general-purpose channels of Keithley 708B used in the present work [106].
[4] At room temperature and under normal atmospheric pressure.

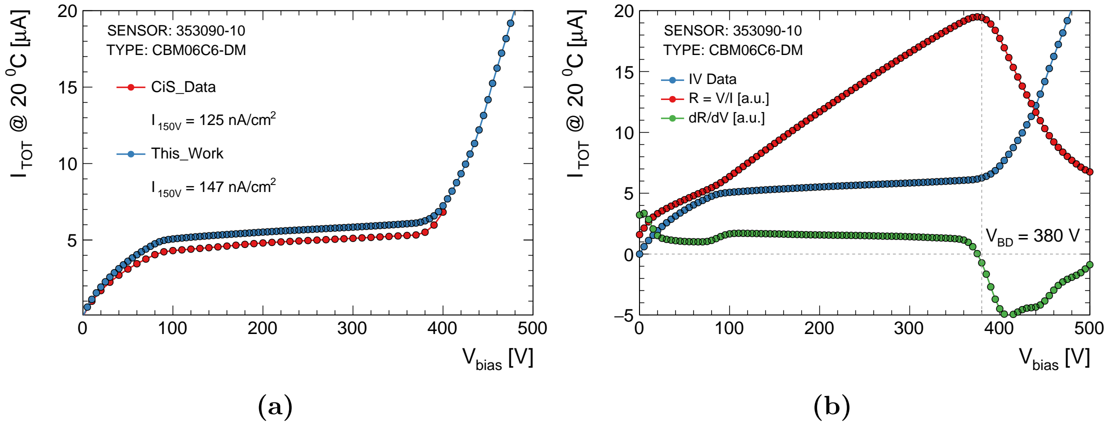

(a) **(b)**

Figure 4.2.: (a) Current-voltage characteristic of the microstrip sensor manufactured by CiS. The current is normalized to 20 °C. The bias voltage is corrected for the voltage drop across 1 MΩ resistor. (b) Determination of the breakdown voltage using the first derivative of the resistance with respect to the bias voltage: $V_{BD} = 380\,\mathrm{V}$.

−5 °C [39]. It yields a tenfold reduction of the leakage current compared to measurements at room temperature. Surface currents depend less on temperature [112]. Non-irradiated sensors without defects usually have low bulk current and a few orders of magnitude lower surface current. Assuming effective guard rings, the measured total leakage current is mostly bulk generated. Therefore, normalization can be applied to the total leakage current.

Results for CBM prototype sensors

Figure 4.2a shows the typical IV characteristic of the CBM $6 \times 6\,\mathrm{cm}^2$ double-sided microstrip sensor manufactured by CiS. Before full depletion the total leakage current is proportional to $\sqrt{V_{bias}}$.Full depletion of the sensor is reached at $\approx 90\,\mathrm{V}$, the leakage current saturates to $\approx 150\,\mathrm{nA/cm^2}$ and further exhibits a typical plateau. The linearity of the plateau is ensured by low surface currents. The breakdown voltage is determined by the following method: calculation of the first derivative of the inverse slope (resistance) of the IV curve with respect to the bias voltage. Under breakdown conditions, the resistance drops, and the derivative changes its sign from positive to negative (see Fig. 4.2b). The corresponding bias voltage is defined as the breakdown voltage of the sensor. The bias voltage source accuracy is 0.02 %+100 mV according to Keithley 2410 specifications [103]. The error on the breakdown voltage due to the bias voltage step size is ±5 V. IV measurements agree within 15 % with the measurements performed by the manufacturer.

Figure 4.3 shows measured IV curves of the investigated CBM06 prototype sensors produced by CiS and Hamamatsu. The leakage current is normalized to the surface area to compare sensors of 4 different sizes. The measurement

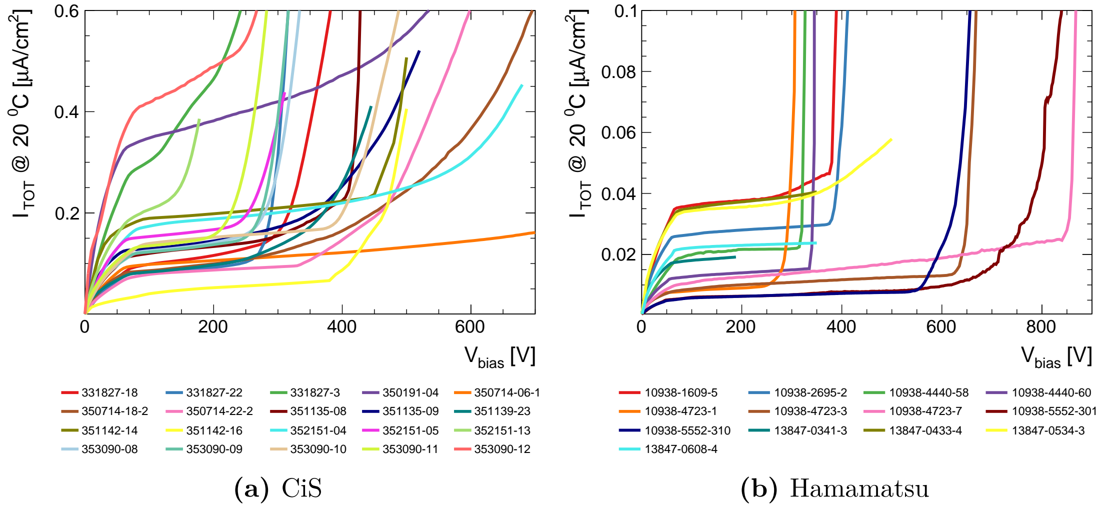

(a) CiS **(b)** Hamamatsu

Figure 4.3.: Current-voltage characteristics of the investigated CBM06 prototype sensors. They belong to different batches and were produced by two vendors. The leakage current is normalized to 20 °C and to the surface area. Note the difference in vertical and horizontal scale for each plot.

results show that the leakage current after full depletion is below 200 nA/cm^2 and 40 nA/cm^2 for CiS and Hamamatsu sensors, respectively. It satisfies the initial design requirements of $I_{TOT} < 1\,\mu\text{A/cm}^2$ and $V_{BD} > 200\,\text{V}$. A few CiS sensors have above average leakage current and early breakdown. According to recent studies [61], the CBM sensors after receiving fluence $1 \times 10^{14}\,\text{n}_{\text{eq}}/\text{cm}^2$ will have full depletion voltage of 105 V and 140 V (CiS and Hamamatsu, respectively). These values double at twice the lifetime fluence. Taking into account necessary over-voltage of up to 50 %, the sensors have to operate without breakdown up to a bias voltage of 300–400 V in the STS. Some of the tested sensors do not meet this requirement. The next section will discuss the origin of the high leakage current and early breakdown of the investigated sensors.

For quality control purposes, a parameter called slope was used to judge early sensor breakdown. It is defined as a ratio of leakage current at two bias voltages: depletion voltage (max. 100 V) and operating voltage of non-irradiated sensor (max. 150 V). A slope close to 1 ensures that there is no early breakdown. Figure 4.4 shows test data in comparison with vendor data. For most tested sensors, slope is less than 1.15 and agrees with the vendor's data within 10 %. Several sensors have higher slope values, indicating a problem. A few more slope parameters at higher bias voltages were defined in Ref. [113] to facilitate grading of the CBM sensors at the production stage.

Repeatability of IV measurements was checked for all investigated sensors. Measurements were performed up to 50 times for each sensor with different time intervals between consecutive measurements. All tested sensors showed no dependence on previous biasing history. However, it was observed that after a full

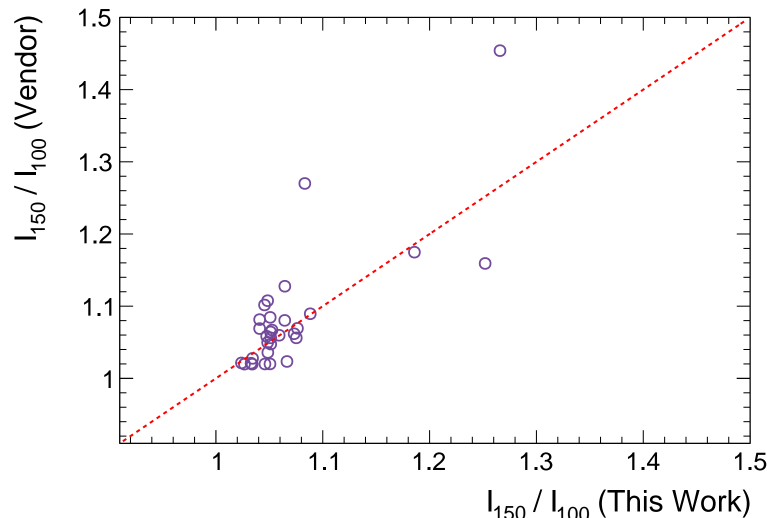

Figure 4.4.: The slope of the IV curves of the investigated sensors. Results are shown against vendor data. 5 defective sensors are identified (one data point is outside of the graph range). The dashed line shows a one-to-one match.

set of characterization procedures[5], the measured leakage current was in some cases 5–10 % higher. The ATLAS Collaboration also reported a 10–20 % increase in leakage current after a similar set of acceptance tests [114], and the LHCb Collaboration reported an average of 6 % for VELO strip sensors [115].

4.1.2. Bulk and Surface Current

The previous section discussed the measurement of total leakage current. It is important to reduce surface and edge effects on sensor performance, which is usually achieved with a properly designed guard ring structure. The design and operation of such structures with different number of rings for p^+-n sensors can be found in Refs. [116, 117, 118, 119, 120]. The edge of the sensor is a highly damaged region (especially when blade dicing is used). As the depletion region approaches it, the leakage current increases sharply, exhibiting breakdown-like behavior. This effect is different in nature from bulk avalanche breakdown. In fact, this is a so-called "soft" breakdown. Another distinct effect is the development of a high field at the edge of the ring implant due to oxide charges. This can cause an avalanche breakdown at a voltage lower than the bias voltage required for sensor operation. The guard ring structure reduces this effect by developing a uniform potential drop along the surface of the sensor.

If the bias and guard rings are separated, the currents from sensitive and non-sensitive regions can be measured independently, as well as the potentials of the individual guard rings. Therefore, it is possible to conclude about the origin of

[5]Global and strip tests.

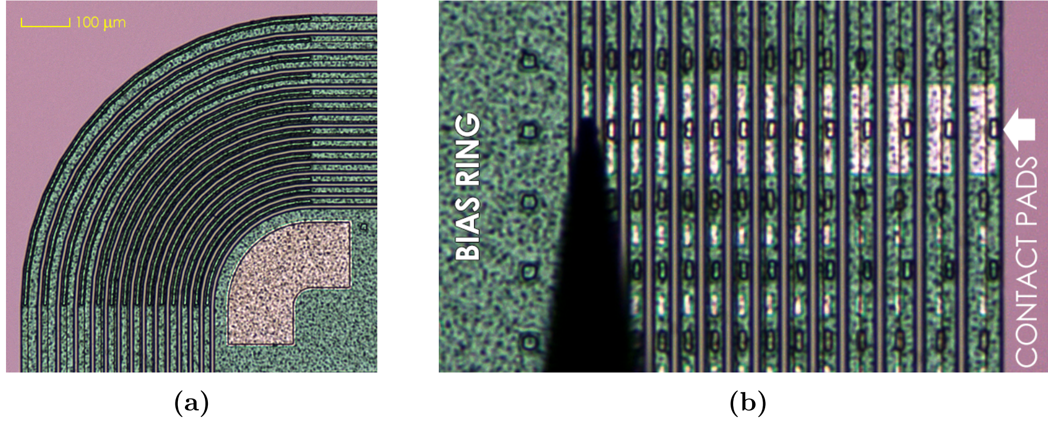

(a) (b)

Figure 4.5.: Guard ring structure of the CBM06 sensor manufactured by CiS: microscopic view of (a) its corner area and (b) area with contact pads. The probe needle contacts the 1st guard ring GR01 to measure the contribution from the non-sensitive region of the sensor to the total leakage current.

the breakdown.

The CBM sensors employ two different vendor-dependent guard ring designs[6]. Figure 4.5a shows a microscopic view of a corner region of the CiS guard ring structure, and Fig. 4.5b shows the area with contact pads — a window in the passivation layer that is 5.5 µm wide for the innermost ring (GR01) and 0.5 µm wider for each successive ring. The distance between adjacent contact pads is 14 µm. The diameter of the needle tip is only 5 µm. Therefore, high positioning accuracy and optical magnification of the probe station[7] are necessary for a successful measurement.

Measurement method

Two types of measurements are necessary for characterization of the guard ring performance: the measurement of the current collected independently by bias and guard rings — IV curves, and the measurement of the potentials of individual guard rings — VV curves.

Since the guard rings are on the p side, its bias ring is set to the ground potential and connected to the *LO* terminal of the voltage source. The n side is connected to the *HI* terminal. Two ammeters are needed: one to measure the current collected by the guard ring, the other to measure the current collected by the bias ring. Ammeters are connected to the grounded side of the sensor. A detailed connection scheme is shown in Fig. 4.6. The bias voltage is ramped up in steps of 5 V with a 5-second delay between voltage increments and current is recorded. In such a measurement scheme, the innermost guard ring is effectively grounded through the ammeter. It means that the sensor operates with a reduced

[6]See Section 2.1 for details.
[7]See Chapter 3 for a description of such a probe station.

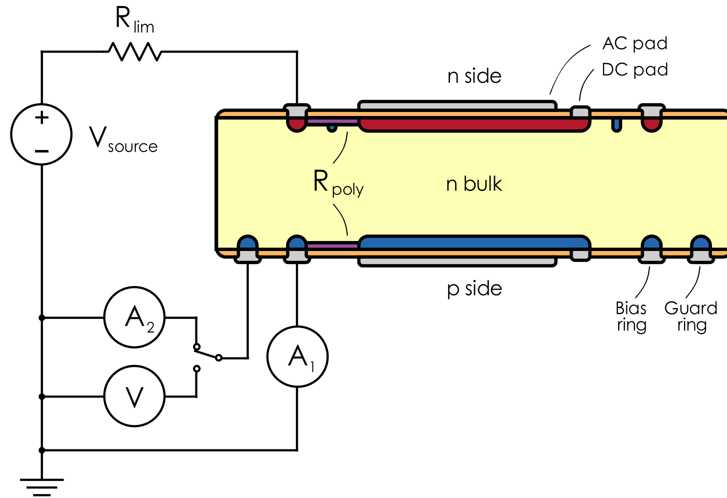

Figure 4.6.: Connection scheme for simultaneous measurement of bias and guard ring currents of the microstrip sensor. Two ammeters are used for this purpose. Circuit can be switched to the configuration with a voltmeter to measure potentials of individual rings. The p side is grounded and the n side is at positive HI potential.

number of rings and a higher voltage can be dropped across the edge of the sensor for the same bias voltage. In the case of Hamamatsu sensors, all the voltage drops between the n^+ edge implant and one guard ring.

To measure the VV curves, the circuit is switched to a configuration with a voltmeter. The procedure is the same as for IV measurements and has to be repeated for all 14 rings of the CiS sensors and one ring of the Hamamatsu sensors. Three single-metal CiS sensors are early CBM06 prototypes and their guard rings do not have openings in the passivation layer. Four of the Hamamatsu sensors are without guard rings. These sensors were not investigated here.

Experimental setup

The measurements are performed in a clean room as described in Section 4.1.1. A Keithley 6487 voltage source is used to supply a bias voltage of up to 500 V. A Keithley 6487 ammeter is connected to the bias ring of the sensor and measures bulk current. It is configured for a measurement range of 20 µA with a default resolution of 100 pA. Keithley 2410 is used as an ammeter/voltmeter for the corresponding type of measurement. The 10 µA range with a default resolution of 100 pA is used to measure the surface current. The systematic uncertainty on the current from the device measurement accuracy specifications is $0.027\,\% + 700\,\text{pA}$. A manual current limit has to be applied to the measured bulk current to stop the measurement in case of bulk breakdown. The input impedance of the Keithley 2410 voltmeter is greater than 10^{10} Ω. It allows to measure the potentials of individual guard rings with minimal impact on the potential distribution. The

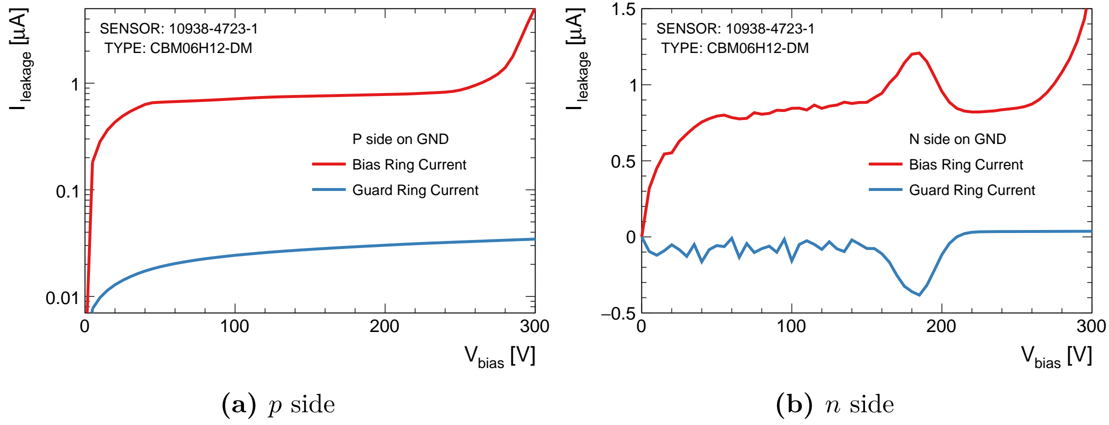

(a) p side

(b) n side

Figure 4.7.: Bias and guard ring currents of the CBM06H12 sensor as a function of the bias voltage. The breakdown occurs at 245 V in the sensor bulk. Measurements on the n side show meaningful current only after the guard ring becomes isolated from the bias ring.

systematic uncertainty from the device measurement accuracy specifications is 0.015 % + 50 mV. The instruments are connected directly to the sensor and the switching matrix is not used in this type of measurement due to its voltage tolerance.

The sensor under test is put on the vacuum chuck inside the enclosure of the custom probe station. The light must be off during the measurement. Due to the non-periodic structure of the rings, it is necessary to step over the contact pads manually between successive measurements. The correct location of the probe needle is shown in Fig. 4.5b.

Results for CBM prototype sensors

The investigated Hamamatsu sensors demonstrated very low values of the current collected by the guard ring. For measurements on the p side, the n side was positively biased. Figure 4.7a shows the bias and guard ring currents of the CBM06H12 sensor as a function of bias voltage. The current collected by the guard ring is about 30 nA after full depletion. Its contribution to I_{TOT} is less than 5 %. The breakdown of this particular sensor starts at 245 V. Obviously, this is due to an increase in the current from the sensitive area of the sensor. Figure 4.7b shows the measured IV curves from the n-side bias and guard rings. Here, the p side was negatively biased and the n side was grounded. The measured current below 220 V is affected by the lack of isolation between the rings. The p-stop structure was not added for this iteration of the sensors, and the electron accumulation layer is present even after the sensor is fully depleted. The ammeter creates an extra circuit with $V = V_{burden}$ that affects the measured current. Above 220 V this effect disappears, and the currents have the same level as those

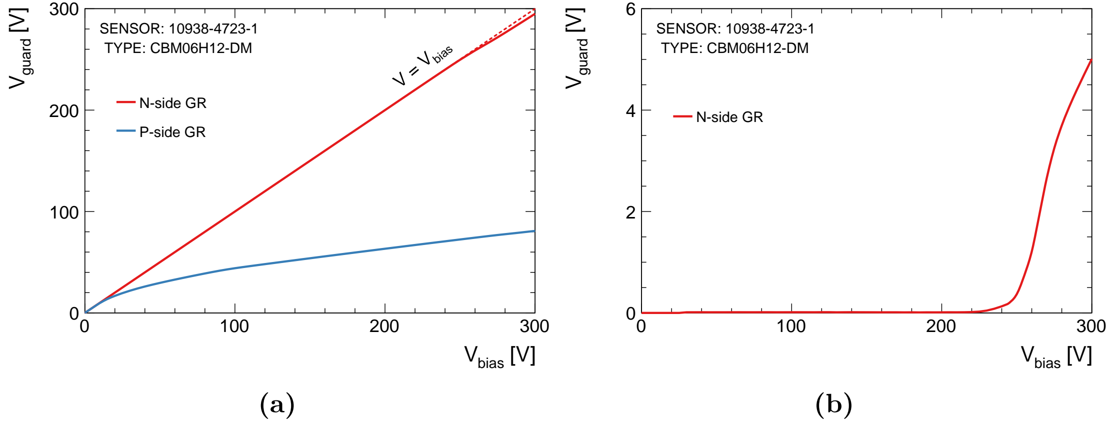

Figure 4.8.: Potentials of p- and n-side guard rings as a function of the bias voltage of the CBM06H12 sensor: (a) the potentials of the individual rings with respect to the grounded bias ring on the p side and (b) the potential difference between the guard ring on the n side and the bias ring. Below 220 V, the rings on the n side are shorted through the electron accumulation layer.

measured on the p side. The voltage of 220 V corresponds to the moment when the potential difference between the guard and bias rings develops, as shown in Fig. 4.8. It can be attributed to the depletion of the electron accumulation layer between the rings.

Two $62 \times 22\,\text{mm}^2$ and two $62 \times 62\,\text{mm}^2$ Hamamatsu sensors showed the same trends of IV and VV curves as the CBM06H12 sensor and no breakdown within the measured voltage range.

The investigated CiS sensors can be grouped into four distinct categories with respect to measured bias and guard ring currents. Figure 4.9 shows typical IV curves representing these categories. The total leakage current curves are taken from Section 4.1.1 and represent a standalone measurement. Bulk and surface current components are well distinguished and satisfy Eq. 4.1.

These categories are:

(I) shown in Fig. 4.9a. The sensors show no signs of breakdown up to $V_{bias} =$ 500 V. The bias ring current exhibits a plateau after full depletion. The guard ring current contributes less than 10 % to the total leakage current. 2 out of 14 investigated sensors fell into this category.

(II) shown in Fig. 4.9b. There is an avalanche breakdown through the bulk of the sensor. The guard ring current increases slowly. Its contribution to the total leakage current is well below 10 %. 3 out of 14 investigated sensors fell into this category.

(III) shown in Fig. 4.9c. The guard ring current increases with the lateral extension of the depletion region. The presence of the crystal damage along the cut edge, which can extend deep towards the sensitive area, leads to a

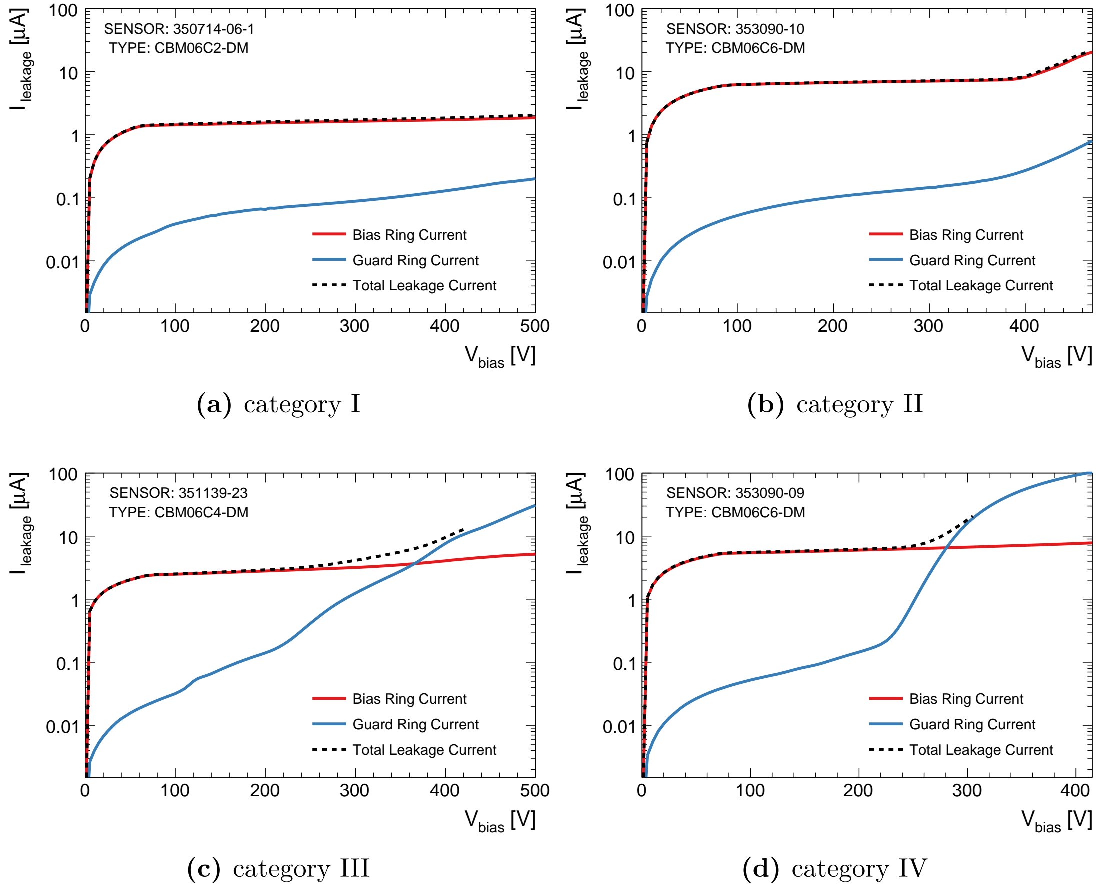

(a) category I

(b) category II

(c) category III

(d) category IV

Figure 4.9.: Typical bias and guard ring currents as a function of the bias voltage of CBM06 prototype sensors manufactured by CiS. The total leakage current was measured in a standalone measurement and satisfies Eq. 4.1. (a) No signs of breakdown up to $V_{bias} = 500\,\text{V}$, surface current remains low throughout the whole voltage range. (b) Avalanche breakdown through the bulk of the sensor. (c) The phenomenon of "soft" breakdown, when the surface current increases with the lateral extension of the depletion region. (d) Avalanche breakdown occurs at one of the ring implants, while the bulk current remains unchanged.

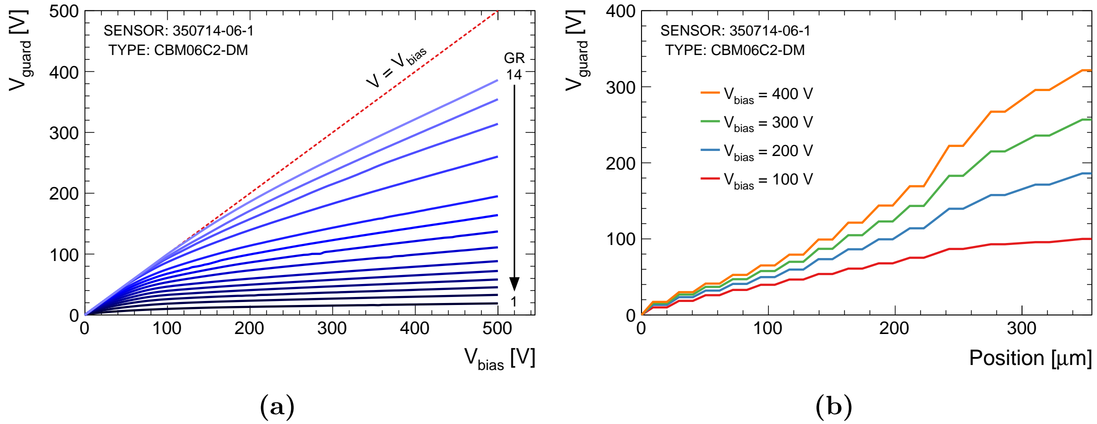

(a) (b)

Figure 4.10.: Potentials of the 14 floating guard rings of the CiS sensor: (a) as a function of the bias voltage and (b) as a function of the GR position relative to the bias ring at V_{bias} = 100, 200, 300 and 400 V. The horizontal sections of the V_{guard} versus position plots correspond to the potentials of the individual implants, and the lines in-between are drawn to guide the eye.

significant increase in the leakage current. At some point it overtakes the bias ring current and its contribution to the total leakage current becomes dominant. The total leakage current exhibits a slow breakdown-like behavior. It is often referred to as a "soft" breakdown.3 out of 14 investigated sensors fell into this category.

(IV) shown in Fig. 4.9d. There is an avalanche breakdown at one of the ring implants. The guard ring current increases by several orders of magnitude over 100 V. The bias ring current remains on the plateau. 5 out of 14 investigated sensors fell into this category.

The effectiveness of the guard ring structure can be characterized by means of the potential distribution. Figure 4.10 shows typical GR potentials of the CiS sensor as a function of the bias voltage and as a function of the GR position relative to the bias ring at V_{bias} = 100, 200, 300 and 400 V. When a bias voltage is applied, the depletion region also expands laterally toward the edge of the sensor. Once it reaches a certain GR, its potential starts to deviate from the applied bias voltage, as can be seen in the V_{guard} vs. V_{bias} plot. At $V_{bias} \approx V_{FD}$, the depletion region is confined within only twelve rings for all investigated sensors. The GR12 is 281 µm away from the outer edge of the bias ring, corresponding to the thickness of the CiS sensor. A common feature of all investigated CiS sensors is that the potential drop between GR10 and GR11 is larger than for other pairs of rings due to the increased gap between them. All 14 guard rings acquire their potential already at 100 V. The depletion region expands beyond GR14 with a further increase in the bias voltage. The breakdown is then limited by the size of this non-sensitive region. The sensors of the categories I and III have an identical

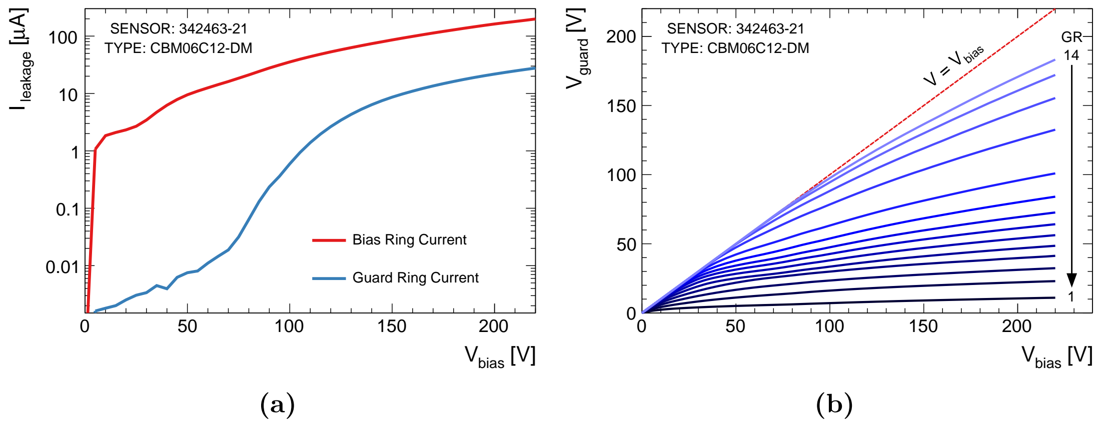

(a) (b)

Figure 4.11.: (a) Leakage current and (b) guard ring potentials as a function of the bias voltage of the CBM06C12 prototype sensor. The sensor exhibits breakdown in both the sensitive and non-sensitive regions as suggested by the IV curves. The potential of GR14 starts to deviate from the applied bias voltage just before the guard ring current increases.

potential distribution. Therefore, it can be concluded that the leakage current of the category III sensors is due to the crystal damage caused by the dicing procedure or improper handling. Application of the stealth dicing can improve the leakage current. The surface of the sensor periphery should be terminated with a wide n^+ implant, as suggested in Ref. [121]. This design is implemented for the CBM sensors manufactured by Hamamatsu and results in a very low surface current.

A different situation was observed for the category IV sensors. The potential of the GR14 turned out to be higher compared to the sensors of other categories. This may be an indication of a higher oxide charge density. As a result, the depletion region does not expand much beyond GR14, as shown in Ref. [122] for similar structures. However, a larger voltage drop between adjacent rings results in higher fields and an increased probability of an avalanche breakdown.

One CBM06C12 sensor belongs to a separate category V with respect to measured currents. Figure 4.11a shows the corresponding bias and guard ring current. The bias ring current increases rapidly starting at 25 V and then again at about 50 V. This is a micro-discharge breakdown localized in individual strips[8]. It is related to a high local electric field [112]. Starting at 75 V, the guard ring current increases by a few orders of magnitude over less than 100 V. Figure 4.11b shows the potential distribution over the guard rings of the CBM06C12 sensor. It can be seen that the potential of GR14 starts to deviate from V_{bias} exactly at 75 V. This means that the depletion region has already reached the outermost ring. A sharp increase in current occurs due to the fact that the depletion region touches the edge regions with deep crystal damage, as can be concluded from Fig. 4.12.

[8]See Section 4.2.1 for the strip leakage current data of the CBM06C12 sensor.

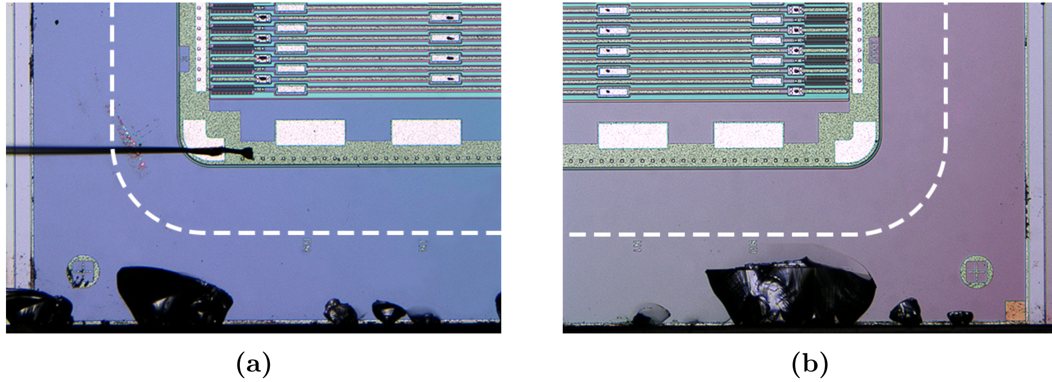

(a) (b)

Figure 4.12.: Edge region of the CBM06C12 sensor 342463-21 with deep large-scale chips. The n side is shown. The white dashed line is the projection of the p-side GR boundary.

Such a sensor should not be assembled into the detector module.

2 of the 14 sensors were found to have several adjacent guard rings at the same potential. Figure 4.13 shows the potential distribution for one of the CBM06C6 sensors. Its GR01 – GR04 behave like a one ring. The GR05 acquires its potential at a much lower bias voltage than a normal sensor. About 80 µm of the Si bulk has the same potential. Voltage drops between further pairs of rings are larger. This can lead to a decrease in the breakdown voltage.

After electrical testing, these sensors were visually inspected. Two types of guard ring defects were found: due to the manufacturing process (see Fig. 4.14a) and due to improper handling (see Fig. 4.14b). The first type of defect implies a permanent electrical short between GR01 – GR04. Another may cause an interruption of a guard ring or short circuit. A breakdown will occur if the implant under the metal ring is affected by a scratch.

The presence of such defects has led to the investigation of the operation of the sensor with a reduced number of guard rings. It can be simulated by connecting guard rings one by one to the p-side bias ring. The depletion region then begins to grow from the corresponding ring. The IV characteristics of the investigated CBM06C2 sensor with different number of active guard rings on the p side are shown in Fig. 4.15. It can be seen that the breakdown occurs earlier when the number of active guard rings is reduced. The situation when GR14 is grounded corresponds to an operation without protection against low-voltage breakdown. It occurs at $V_{bias} = 20\,\mathrm{V}$ and agrees within 10 % with measurements performed on other prototype sensors.

n-side guard ring structure

Half of the investigated sensors also have a guard ring structure on the n side. The p-side structure was mirrored onto the n side. However, p-stop/p-spray isolation is missing for both CiS and Hamamatsu sensors. Therefore, the entire

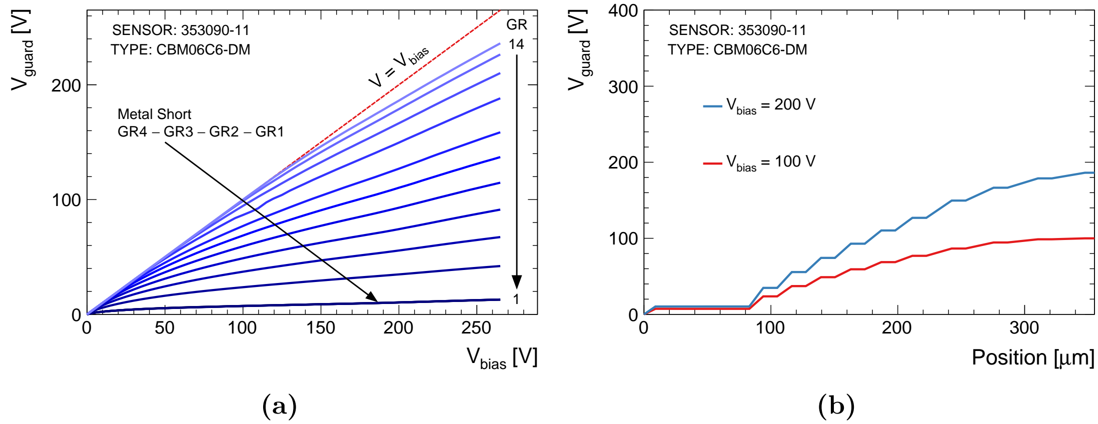

(a) **(b)**

Figure 4.13.: Potentials of the 14 floating guard rings of the CBM06C6 sensor with short circuit between the four innermost rings: (a) as a function of the bias voltage and (b) as a function of the GR position relative to the bias ring.

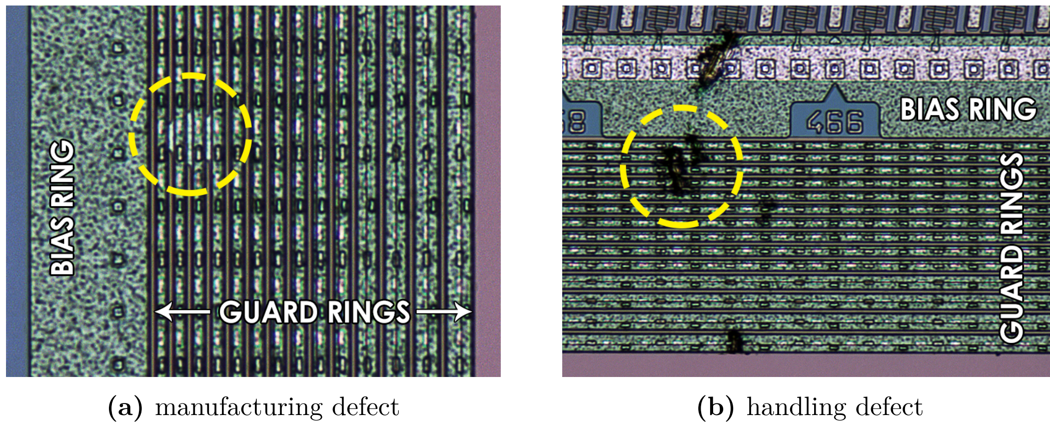

(a) manufacturing defect **(b)** handling defect

Figure 4.14.: Manufacturing and handling defects of the guard ring structure detected on the CBM06C6 sensor 353090-11. (a) The metal spreads over GR01 – GR04, causing a short circuit between these rings. This is a failure of the manufacturing process. (b) Five rings are scratched, potentially shorting or breaking the ring structure.

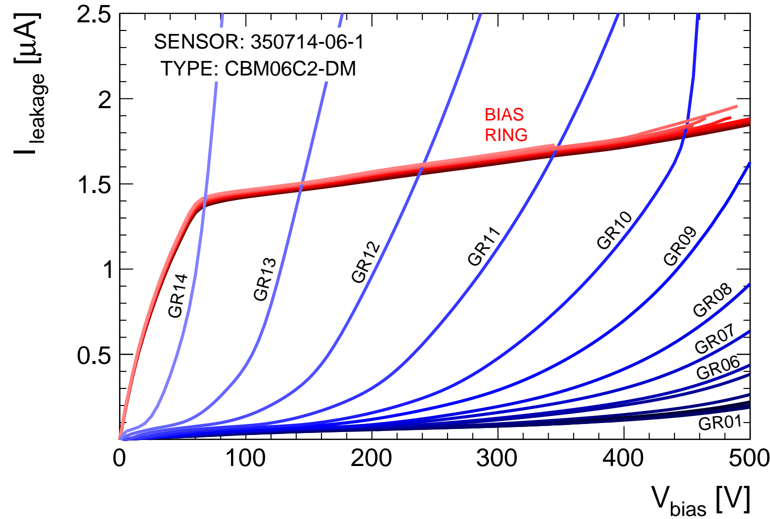

Figure 4.15.: IV characteristics of the CBM06C2 sensor with different numbers of active guard rings on the p side. The red curves show the bias ring current, and the blue curves show the current of the corresponding guard ring. The situation when GR14 is grounded corresponds to an operation without the guard rings.

guard ring structure is at the potential of the n-side bias ring. A suggestion to implement isolating structures was provided for the detector working group. Studies of double-sided guard ring structures were performed in Ref. [119]. The authors show that the structures on both sides share the task of dropping the high bias voltage, thus preventing high fields at the implant edges on both sides. The guard rings on the n side drop most of the potential after the type inversion caused by the irradiation. Therefore, n-side guard rings play an important role for the operation of the double-sided sensors.

4.1.3. Full Depletion Voltage

Silicon microstrip sensors have to operate fully depleted to collect charges from the entire volume of the sensor. It is also a prerequisite for the operation of the double-sided sensor. It is achieved by biasing the sensor to or above the full depletion voltage V_{FD}. In the case of a planar diode, the depletion region acts like a parallel-plate capacitor [69]. Before full depletion, its capacitance is inversely proportional to the square root of the bias voltage. After full depletion, its capacitance is constant and limited by the thickness of the diode:

$$C_{bulk_0} = \begin{cases} \sqrt{\dfrac{\varepsilon_0 \varepsilon_{Si}}{2\mu_e \rho V_{bias}}} A, & V_{bias} < V_{FD_0} \\ \dfrac{\varepsilon_0 \varepsilon_{Si} A}{d}, & V_{bias} \geq V_{FD_0} \end{cases} \tag{4.4}$$

and full depletion voltage:

$$V_{FD_0} = \frac{d^2}{2\varepsilon_0 \varepsilon_{Si} \mu_e \rho} \tag{4.5}$$

where C_{bulk_0} is the capacitance of the diode, V_{FD_0} is the full depletion voltage of the diode, A is the area of the diode plates, d is the width of the fully depleted bulk, ρ is bulk resistivity, μ_e is electron mobility, $\varepsilon_0 = 8.85 \times 10^{-12}\,\mathrm{F/m}$ is free space permittivity, $\varepsilon_{Si} = 11.68$ is dielectric constant of Si.

For a given bulk thickness, the full depletion voltage depends only on the resistivity of the bulk material. Such a dependence, for example, results in a range of V_{FD} of up to 200 V for CMS microstrip sensors [112, 108].

Knowing ρ, the effective doping concentration of the bulk can be obtained using the following equation:

$$N_{eff} = \frac{1}{q \mu_e \rho}. \tag{4.6}$$

Equations 4.4, 4.5, 4.6 apply only to the planar diodes and cannot be applied to the microstrip sensors. A correction is required that takes into account the segmented sides of the microstrip sensor.

Geometrical correction

The full depletion voltage and bulk capacitance of a microstrip sensor differ from those of a diode. It is because of the segmented nature of the microstrip sensor sides. The impact of the finite implant width w and pitch p on the sensor electrical parameters was studied in Refs. [123, 74]. The relationship between corresponding diode and microstrip sensor electrical parameters is obtained by a semi-analytical solution of the Poisson equation. The authors show that the full depletion voltage V_{FD} of the microstrip sensor increases and the bulk capacitance C_{bulk} decreases relative to a diode of the same material and thickness. The relationship between the microstrip sensor and the diode parameters is expressed as:

$$V_{FD} = V_{FD_0} \left[1 + 2\frac{p}{d} f(\tfrac{w}{p}) \right], \tag{4.7}$$

$$C_{bulk} = \varepsilon_0 \varepsilon_{Si} \frac{p}{d + p f(\frac{w}{p})} = C_{bulk_0} \frac{1}{1 + \frac{p}{d} f(\frac{w}{p})} \tag{4.8}$$

where $f(\frac{w}{p})$ is a function of width to pitch ratio:

$$f(\tfrac{w}{p}) = -0.00111 \left(\tfrac{w}{p}\right)^{-2} + 0.0586 \left(\tfrac{w}{p}\right)^{-1} + 0.240 - 0.651 \left(\tfrac{w}{p}\right)^{1} + 0.355 \left(\tfrac{w}{p}\right)^{2}. \tag{4.9}$$

When $\frac{w}{p} \to 1$, $f(\frac{w}{p}) \to 0$ and diode case is obtained. The linear dependence of the depletion voltage and bulk capacitance has been experimentally confirmed for 320 µm thick *p-in-n* CMS microstrip sensors of different geometries as reported in Refs. [75, 68] and in Ref. [124] for *n-in-p* sensors of different thicknesses.

This approach was applied to evaluate the depletion parameters of the CBM prototype sensors. $f(\frac{w}{p})$ function values are 0.218 and 0.441 for CiS and Hamamatsu sensors, respectively. Therefore, the correction for Hamamatsu sensors is larger than for CiS one.

After applying this correction, the corresponding diode equations can be used to estimate additional parameters (thickness, resistivity, etc.) of the microstrip sensor.

Measurement method

The full depletion voltage of the sensor can be determined in the CV measurement, where the capacitance of the depletion layer is measured as a function of the bias voltage V_{bias}. The connection scheme is shown in Fig. 4.16. The impedance of the circuit is measured by the LCR meter. A three-terminal (or guarded) connection technique is used. The HI[9] terminal of the LCR meter is connected to the n-side bias ring and the LO[10] terminal to the p-side bias ring of the sensor[11]. The role of the guard terminal is to remove any stray path, capacitive or conductive. All connections are made using coaxial cables. The outer shield of the cables is connected to the guard terminal of the LCR meter. Then the considerable stray capacitance between the inner lead and the outer shield[12] is not measured.

The bias voltage is supplied by the voltage source V_{source} connected in the same way as described in the previous sections. In such a scheme, the voltage source (and its impedance) appears in parallel with the sensor and will distort the measurement of its impedance. Also, it is not recommended that any DC potential be present at the LCR meter terminals to avoid damage to the device. Decoupling capacitors and resistors are introduced in the circuit as shown in Fig. 4.16 to overcome this problem. A similar approach was already used in Refs. [58, 59] for studies of previous prototypes.

The capacitors C_1 and C_2 block the DC current so that it flows only in the voltage source circuit. The AC signal passes through the sensor bulk and returns to the LCR meter because of resistors R_1 and R_2. Several requirements have to be met for an undistorted measurement of the bulk capacitance as a function of bias voltage. When not depleted, the bulk capacitance of the CBM sensor can be as high as 50 nF. The capacitance of C_1 and C_2 must be much larger than the bulk capacitance in order not to distort the measurement:

$$C_1, C_2 \gg C_{bulk}. \tag{4.10}$$

[9] Combined PH and IH terminals.

[10] Combined PL and IL terminals.

[11] In general, the connection to the sensor can be flipped in the case of fully floating terminals of the LCR meter. If the bias voltage source is connected via the LCR meter, then the $HI(LO)$ terminal will also carry the $HI(LO)$ DC potential superimposed with the AC test signal. Then, one should keep in mind the polarity of the DC voltage.

[12] The capacitance of RG58/RG174 coax cables commonly used in the laboratory is about 100 pF/m [125].

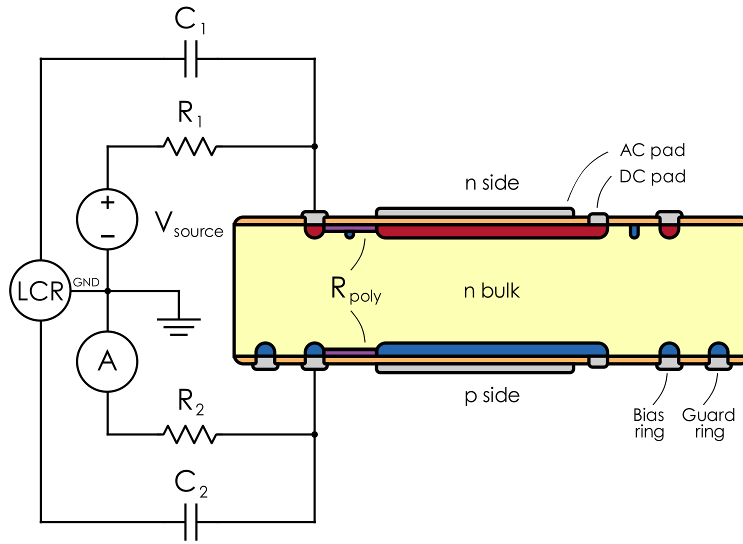

Figure 4.16.: Connection scheme for measurement of the CV characteristic of the microstrip sensor. The LCR meter is connected in parallel with the voltage source V_{source} to the n- and p-side bias rings. To decouple the LCR meter from the DC current of the sensor, two capacitors $C_1 = C_2 = 1\,\mu F$ are introduced into the circuit. AC current does not flow into V_{source} because of the two resistors $R_1 = R_2 = 1\,M\Omega$ which also limit the leakage current in case of the breakdown. The guard terminal of the LCR meter and the LO terminal of the V_{source} are directly grounded.

The resistance of R_1 and R_2 must be much higher than the impedance of C_1 and C_2, respectively, at the measurement frequencies:

$$R_1 \gg \frac{1}{wC_1}, R_2 \gg \frac{1}{wC_2} \tag{4.11}$$

where frequency $w = 2\pi f$. On the other hand, R_1 and R_2 should not be too large, so the voltage drop across them is a few volts. Therefore, C_1 and C_2 were selected to be $1\,\mu F$ each, and R_1 and R_2 were selected to be $1\,M\Omega$ each. Since a small fraction of the AC current always flows into V_{source}, its LO terminal is connected to the guard terminal of the LCR meter, which is directly grounded.

Bias voltage is ramped up in steps of 2 V[13] with a 2-second delay between voltage increments up to a maximum of 200 V[14]. It should be taken into account that the actual bias voltage across the sensor differs from V_{source} due to the voltage drop across resistors R_1 and R_2. This is more important for CiS sensors, which can have a leakage current of about $10\,\mu A$ after full depletion. Therefore, the sensor bias voltage is corrected for the voltage drop by subtracting the IR product:

$$V_{bias} = V_{source} - I_{TOT}(R_1 + R_2). \tag{4.12}$$

[13] Initially, all CV measurements were performed with a voltage step of 5 V. After careful investigation, it was reduced to 2 V as a compromise between speed and quality.

[14] The upper limit is related to the voltage tolerance of the switching matrix.

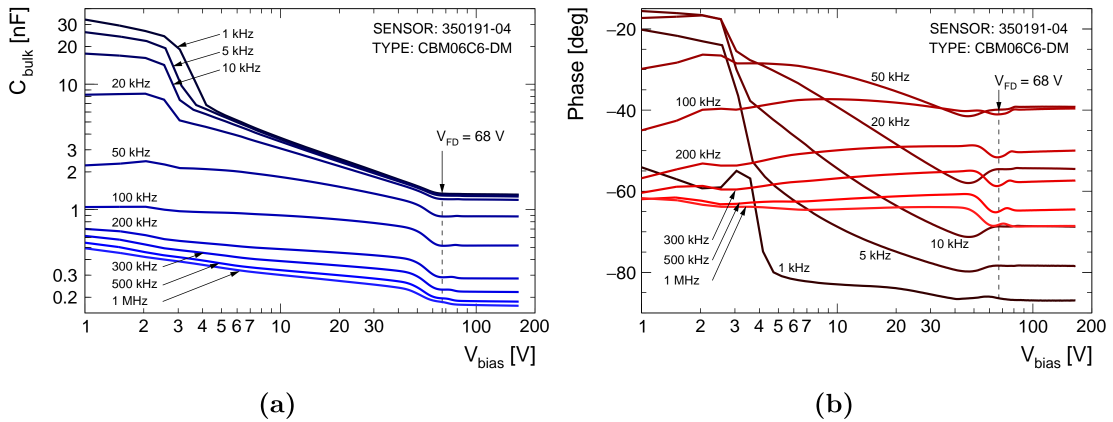

Figure 4.17.: (a) Bulk capacitance and (b) phase angle as a function of bias voltage measured at different frequencies of the test signal. The influence of voltage-dependent series and parallel resistances is manifested in the complex dependence of capacitance and phase angle on the bias voltage.

At each step, the capacitance and phase angle are recorded as a function of bias voltage. The LCR meter supplies a sinusoidal voltage signal with frequency $f = 2\,\mathrm{kHz}$ and RMS amplitude $v_{ac} = 0.5\,\mathrm{V}$ and measures the induced current and phase angle with respect to the applied voltage signal. It then calculates the capacitance according to the selected model — series or parallel.

Capacitance model

In the case of a simple diode, a parallel model is appropriate, as suggested in Ref. [126]. However, this conclusion cannot be applied to microstrip sensors. The choice of model depends on the test frequency, bias conditions and the measurement circuit itself.

A microstrip sensor can be thought of as a huge bulk capacitance connected in series with the strip implant and polysilicon resistance. Figure 4.17 shows the bulk capacitance and phase angle as a function of bias voltage measured at different frequencies for the CBM06C6 sensor. The bulk capacitance drops from about 30 nF to about 1 nF after full depletion. Therefore, its impedance increases from $5\,\mathrm{k\Omega}$ to $159\,\mathrm{k\Omega}$ at 1 kHz. For simplicity, all polysilicon resistors of one side can be considered as one with a resistance of $5\,\mathrm{M\Omega}/1024 \approx 5\,\mathrm{k\Omega}$ in series with $0.5\,\mathrm{k\Omega}$ combined implant resistance. When the depletion region reaches the n side, the series resistance doubles because the n-side strips become isolated. It leads to a bump on the phase curve around the point of full depletion. Since the capacitance does not change after the full depletion, the phase angle approaches $-87°$ but never $-90°$ like in a purely capacitive circuit. Figure 4.18 shows the bulk capacitance as a function of test frequency (CF curve) measured at different bias voltages and for CBM prototype sensors of different size. The full bulk

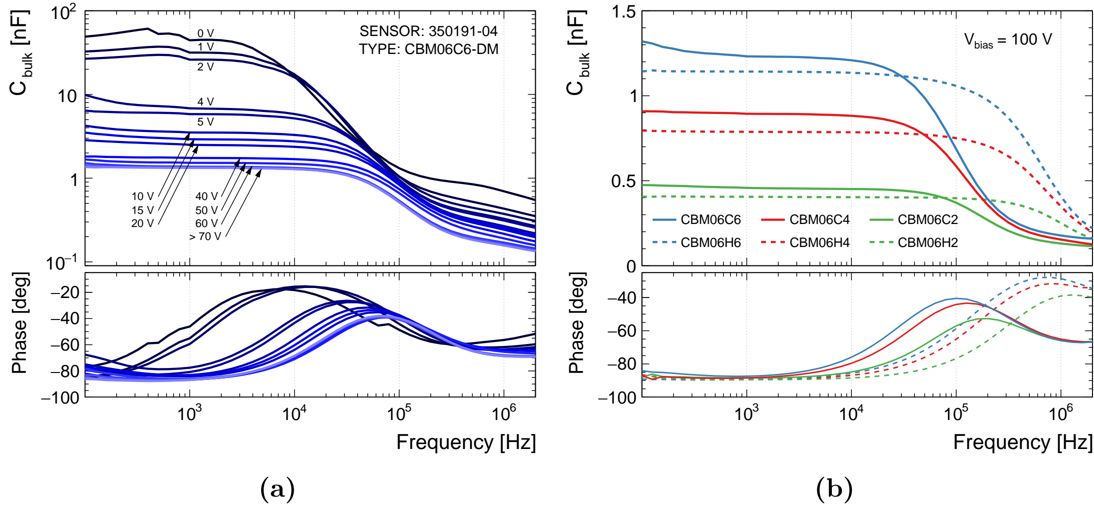

Figure 4.18.: (a) Bulk capacitance as a function of test frequency measured at different bias voltages. Both capacitance and series resistance depend on the bias voltage and this is reflected in the CF curve. (b) Bulk capacitance as a function of test frequency measured for CBM sensors of different size at $V_{bias} = 100\,\mathrm{V}$. Sensors produced by the same manufacturer have similar polysilicon resistance values and therefore have an inflection point around the same frequency.

capacitance can only be measured at frequencies below about 10 kHz. Due to the distributed nature of capacitance and resistance along the length of the strip, the test signal is filtered through low-pass filters, and less capacitance is measured at high frequencies. It gives a characteristic bend in the shape of the CF curve. The resistance of the undepleted bulk decreases when approaching full depletion. Therefore, the position of the inflection shifts toward higher frequencies with the applied bias voltage. At full depletion, a small shift in the opposite direction occurs due to the n-side resistance.

Therefore, the series resistance cannot be ignored, especially at low biases. The C_s−R_s series capacitance model gives an appropriate description of the bulk capacitance in the case of the CBM sensors, while the parallel model approximation will underestimate its value:

$$C_s = C_p(1 + D^2) \tag{4.13}$$

where D is the dissipation factor of a capacitor which is inversely proportional to the tangent of the phase angle. CV curves at frequencies above 10 kHz do not represent the entire bulk of the CBM sensors and thus the inflection point of the curve may not correspond to the depletion point due to sensor thickness variation or inhomogeneity of resistivity. Since parallel resistance is also present, it is reasonable to perform measurements at a frequency at which the dissipation factor is small or the phase angle is close to −90°. Frequencies of 1–5 kHz satisfy this requirement and were used for measurements on the CBM prototype sensors.

Voltage step

The bulk is completely depleted when the measured capacitance and phase angle form a plateau. The full depletion voltage corresponds to the inflection point of the CV curve. To extract it, the falling and flat regions are fitted with the corresponding functions. The intersection of the two curves is defined as V_{FD}. Typically, CV data are represented in the $1/C^2(V)$ form and two straight line fits are used. However, due to the segmented sides, the CV curve has features at low bias and around the inflection point that are not pronounced in the $1/C^2(V)$ form. Another consequence is that the power term of the dependence $C(V)$ is not exactly 0.5. For CBM prototype sensors, it was found to be:

$$
\begin{aligned}
CiS:&\ 0.53 \pm 0.01 \\
Hamamatsu:&\ 0.56 \pm 0.02
\end{aligned}
$$

where the error represents one standard deviation. In this work, the CV data are presented in log−log scale applying fits with:

$$
\begin{aligned}
V_{bias} < V_{FD}:&\ C = kV^n \\
V_{bias} > V_{FD}:&\ C = const
\end{aligned}
$$

It requires careful selection of the fitting ranges and bias voltage step for the measurement, otherwise it may result in incorrectly extracted CV parameters or even failed fits.

Figure 4.19a shows the CV curve of the CBM06C6 sensor, which was measured with a bias voltage step of 0.1 V. Depletion starts at individual strips on the p side and leads to a characteristic feature of the CV curve below 4 V unlike a simple diode. Then it merges and forms a planar boundary with a non-depleted region. It occurs at a bias voltage of ≈ 4 V and is accompanied by a drop in capacitance. Using a simple parallel-plate capacitor model, the depletion depth at this voltage can be estimated to be $x \approx 58$ µm, which corresponds to the strip pitch of the CBM sensors. Non-linearity of the CV curve persists up to about 10 V and can be attributed to depletion of the interstrip gaps and sideways expansion of the space charge region. About 10 V before the inflection point, the CV curve deviates from the power law as it approaches the n side. The most linear region in log−log is used for fitting and corresponds to the voltage range from 15 V to $V_{FD} - 15$ V. Figure 4.19b shows the CV curve of the same sensor, which was measured with $V_{step} = 10$ V. Strip features cannot be recognized anymore.

The importance of performing a CV measurement with a small V_{step} can be seen in Fig. 4.19c, which was measured with $V_{step} = 1$ V. The linear shape of the CV curve at low bias indicates that the depletion region has a planar boundary already at the beginning. This is equivalent to a simple diode case. It can only be explained by the absence of strip isolation on the p side of the microstrip sensor. This fact was later confirmed by the resistance and capacitance measurements

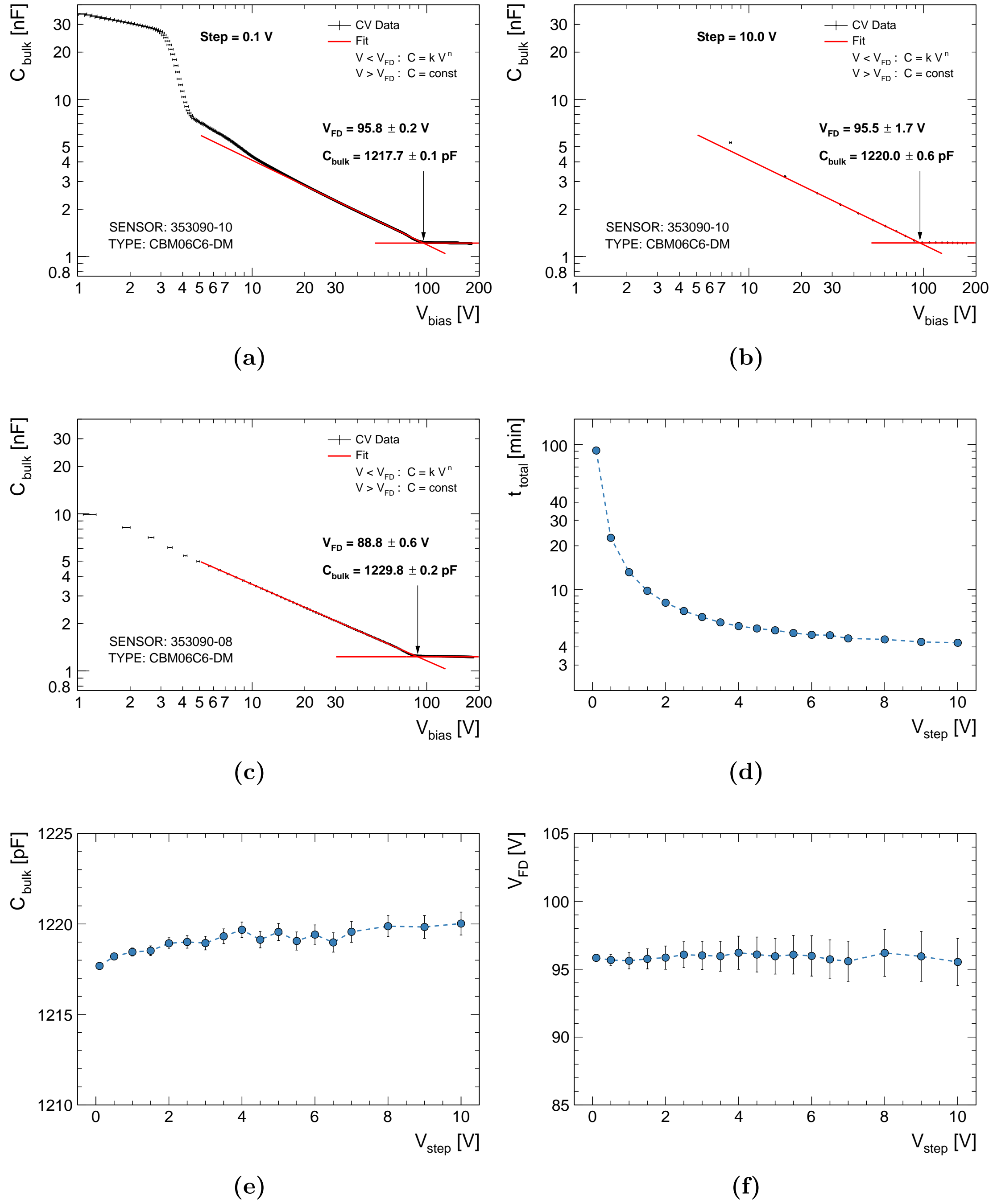

Figure 4.19.: CV characteristic and its properties. (a) CV curve measured with $V_{step} = 0.1\,\mathrm{V}$. (b) CV curve measured with $V_{step} = 10\,\mathrm{V}$. (c) CV curve of the sensor with non-insulated strips of the p side. (d) Dependence of the total measurement time on the bias voltage step. (e) Dependence of the bulk capacitance on the bias voltage step. (f) Dependence of the full depletion voltage on the bias voltage step.

for this sensor[15]. This observation can be useful for QC at the production stage. Sensors can be judged on strip isolation immediately after CV measurement.

The CBM sensors can have full depletion voltage as low as 40 V. Considering the choice of fit ranges, 10 V remains for the falling region of the CV curve. At least 2 data points are required for a fit which sets limit $V_{step} < 5\,\mathrm{V}$.

It is desirable to perform measurements as fast as possible because the same setup is used for strip measurements. Figure 4.19d shows the total measurement time as a function of bias voltage step. It shows that the best achievable measurement time is around 4 min. Measurement with $V_{step} = 2\,\mathrm{V}$ takes 8 min, and with $V_{step} = 1\,\mathrm{V}$ already requires 5 extra minutes. Smaller steps are impractical for QC purposes.

Figure 4.19e and Fig. 4.19f show the extracted bulk capacitance and full depletion voltage as a function of bias voltage step. Both parameters can be reliably determined. A larger voltage step translates into a reduced accuracy. Taking all factors into account, CV measurements on CBM sensors were performed with $V_{step} = 2\,\mathrm{V}$.

Experimental setup

Like all measurements in this work, the CV measurements are performed in a clean room with constant temperature and no light. A Keithley 2410 source-measure unit is used to supply a bias voltage of up to 200 V and to measure the sensor leakage current. The capacitance is measured by the QuadTech 7600+ LCR meter [105]. The resolution is 7 digits at any specified range.The systematic uncertainty on the AC test signal frequency and amplitude is 0.01 % + 0.10 Hz and 5 % + 1 mV, respectively, according to the device accuracy specification.

Unlike previously described measurements, a switching matrix is used to facilitate CV measurement and avoid re-cabling for strip tests. The microstrip sensor under test and measurement devices are connected to a Keithley 708B [106] switching matrix as described in Section 3.3.1. The matrix channel configuration is given in Appendix C.

A set of compensation procedures has to be performed to accurately analyze the measured CV data:

- The Keithley 2410's *LO* terminal, the *GND* terminal of the switching matrix, and the shield of the coaxial cable have to be connected to the guard terminal of the LCR meter. The situation with and without connection is compared in Fig. 4.20. The false capacitance can be measured at low frequencies where CV measurements are usually performed. The effect depends on the measurement frequency, isolation resistors and the sensor under test.
- The basic accuracy of the QuadTech 7600+ LCR meter at medium speed is ±0.25 %. The actual accuracy depends on the configuration of the LCR

[15] See Section 4.2.7.

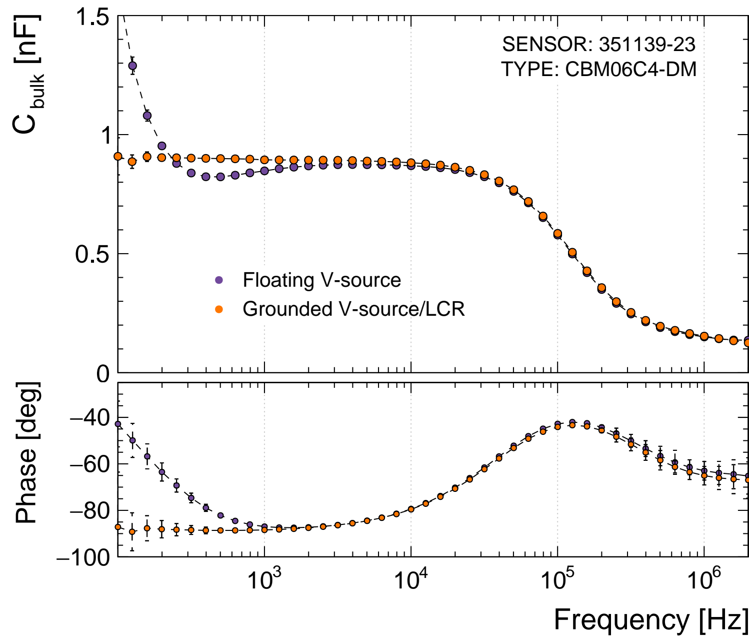

Figure 4.20.: Frequency dependence of the bulk capacitance for the case with a floating and grounded voltage source. Measurements are carried out at a bias voltage of 120 V.

meter for the specific measurement type, on the measured impedance and phase angle, and is calculated at each measurement step using the equation from the device's measurement accuracy specification [105]. Therefore, for the capacitance 1 nF measured at 2 kHz in the $C_s - R_s$ mode, the actual accuracy of the device is ±0.12 %.

- An "OPEN/SHORT" zeroing of the LCR meter must be performed to ensure such accuracy[16]. The corresponding matrix channels has to be closed. The test socket is connected at the end of the measurement circuit. The procedure is performed without a microstrip sensor. For "SHORT" zeroing the bias pads of the test socket has to be electrically shorted.

- The additional parasitic impedance is due to the contact capacitance and resistance. It can not be eliminated by the zeroing procedure. In this work, the investigated sensors were wire-bonded to the biasing pad, so the effect is negligible. However, sockets with pogo-pins may have such a contribution.

- The distributed inductance along the cables and switches and the corresponding phase shift causes gain error[17]. This effect is negligible for low-frequency bulk CV measurements.

[16]The procedure takes about 5 min for medium accuracy of the QuadTech 7600+ LCR meter. During production phase this time can be reduced to below 1 min by performing "Quick OPEN/SHORT" zeroing at a given frequency.

[17]See Section 3.3.2.

Results for CBM prototype sensors

CV characterization was performed for 32 CBM06 prototype sensors manufactured by CiS and Hamamatsu. The full depletion voltage and bulk capacitance of the sensor were determined as described above. The investigated sensors are depleted between 45 V and 100 V, which meets the CBM specifications.

Figure 4.21a shows a comparison of the full depletion voltages that were determined in this work with the data provided by the vendors. A good agreement between the data sets can be observed. It should be noted that CiS performs CV measurements on pad diodes from the same wafer as the main sensor. For the purpose of comparison, the provided diode depletion voltages were converted to sensor V_{FD} according to Eq. 4.7. Despite the good agreement, Hamamatsu performs CV measurements at higher frequencies (≥ 10 kHz) than recommended in this work.

The full depletion voltage is used to determine the operating voltage of the sensor. Strip parameters have to reach effective stable values, as a prerequisite. The optimum operating voltage for non-irradiated CBM sensors is $2 \cdot V_{FD}$, while the lowest recommended voltage is $1.5 \cdot V_{FD}$. The actual bias voltage between the p-side and n-side strips differs from the applied bias voltage due to the voltage drop across the polysilicon resistors. For non-irradiated sensors with $R_{poly} = 5\,\mathrm{M\Omega}$ and $I_{TOT} = 10\,\mu\mathrm{A}$ it is only 100 mV and can be neglected.

After taking into account the geometrical correction, the bulk resistivity was estimated for all sensors. Figure 4.21b shows a comparison of the estimated ρ_{bulk} with the data provided by CiS. The data agree within 20 % and meet the CBM specifications. It should be noted that the extracted ρ_{bulk} values represent the average resistivity of the entire sensor. Reference [127] describes a method for non-destructive mapping of resistivity in silicon detectors. The authors show that the variation in resistivity across detector surface can reach 10–15 %.

To estimate the thickness of the sensor, it is important to accurately determine the bulk capacitance of the sensor. Several corrections were taken into account. The depletion region extends towards the edges of the sensor, increasing the measured capacitance. The edge capacitance C_{edge} introduces a systematic error in the CV measurement. It can be estimated by performing a CV measurement with an additional connection to the guard ring. GR01 was connected to the guard terminal of the LCR meter, but remains isolated from the bias ring through $1\,\mathrm{M\Omega}$ resistor. It was found that the measured capacitance is always lower when GR01 is grounded. It is equivalent to the reduction of the capacitor plate area. However, such a configuration does not eliminate the edge capacitance, but only reduces it by a factor of ≈ 3, as concluded from the investigations on pad diodes with guard rings in Ref. [128]. Finally, the estimated average value of C_{edge} for CBM06 sensors is 0.51 ± 0.04 pF/cm, resulting in 12 pF extra capacitance for CBM $62 \times 62\,\mathrm{mm}^2$ sensor. Quoted uncertainty is one standard deviation from measurements on three CiS sensors. After full depletion, C_{edge} changes a little with bias voltage and can

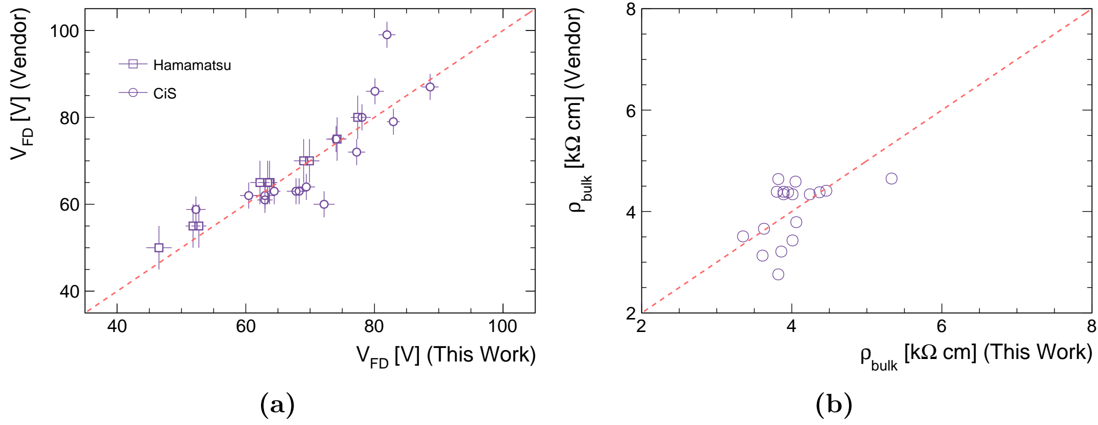

(a)

(b)

Figure 4.21.: Comparison of the full depletion voltages and bulk resistivity that were determined in this work with the data provided by the vendors for the investigated CBM06 sensors. Horizontal error bars indicate propagated uncertainties from fits. Vertical error bars (corresponding to vendor data) indicate systematic uncertainty due to bias voltage step only.

simply be subtracted. After application of the geometrical correction to C_{bulk}, the depletion width w_{FD} of the sensor can be estimated.

The sensor thickness is determined as the depletion width plus the additional thickness due to "dead" material. It consists of implantation/oxide/metal/passivation layers on both sides. Its overall thickness t_{dead} is 10 µm and 11.6 µm for Hamamatsu and CiS sensors, respectively, according to the sensor design specification [129]. The uncertainty of 10 % is assigned to t_{dead} based on the spread of the measured strip parameters for the investigated sensors.

The thickness of the investigated prototype sensors was determined in Ref. [100] by performing a direct optical measurement at a high magnification level and using focus variation method, with precision of ±3.5 µm or better. The sensors were placed vertically on the chuck under the microscope for direct measurement. Figure 4.22 shows a comparison of the total thickness of the sensor d_{sensor} determined by electrical and optical methods. The data agree very well for 80 % of the investigated sensors and are within the specified tolerance range for the wafer thickness specified by the vendors. One batch of the CBM06 sensors was manufactured by CiS using 300 µm thick wafers and it is consistent with the presented results. Disagreement by about 5 % between "optical" and "electrical" data is observed for five sensors. It should be noted that "electrical" thickness represents average thickness over the entire sensor, while "optical" corresponds to the edge thickness[18].

[18] As noted in Ref. [100], the edges perpendicular to the sensor readout plane were inspected because they are used for alignment procedures during ladder assembly.

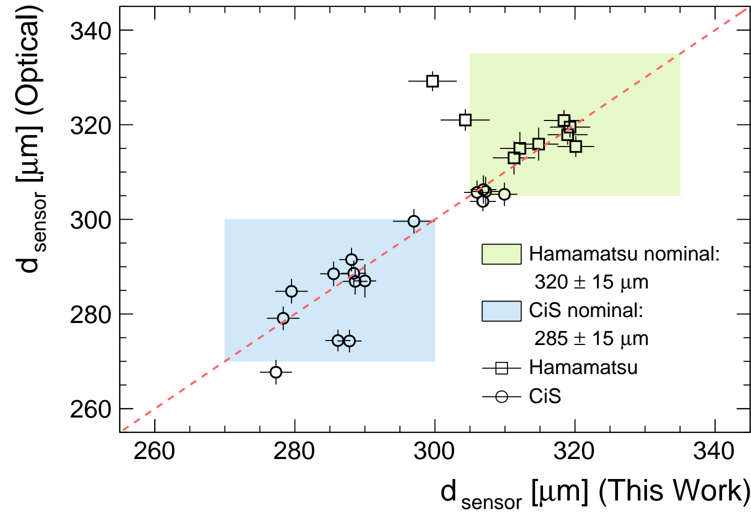

Figure 4.22.: Comparison of total sensor thickness determined by electrical (this work) and optical methods. Colored areas indicate tolerance in the wafer thickness as specified by the vendors. Horizontal error bars indicate propagated uncertainty in thickness due to uncertainty in C_{bulk} determination. Vertical error bars indicate measurement precision of optical method. "Optical" thickness data is courtesy of Evgeny Lavrik [100].

4.2. Strip Parameters

The electrical parameters of individual strips are described in this section. It includes measurement of small currents $O(100\,\text{pA})$, small capacitances $O(\text{pF})$ and large resistances $O(\text{M}\Omega)$. Because the microstrip sensor is a single entity and an individual strip is not electrically isolated from others, each type of measurement requires a careful design. Specifics of the sensor layout have to be taken into account. All measurements in this section were performed in a clean room with a constant temperature of $22.5 \pm 0.5\,°\text{C}$ at the University of Tübingen.

4.2.1. Strip Leakage Current

The bulk leakage current determined in the global IV measurement[19] is uniformly distributed over the sensor bulk. Every strip collects a small portion of it. The average leakage current per strip can be estimated from the bulk current:

$$I_{strip} = \frac{I_{bulk}}{N^i_{strips}} \tag{4.14}$$

where I_{bulk} is the bulk current, N^i_{strips} is the number of strips on the side $i = (n, p)$. In the case of low surface currents, I_{TOT} can be used instead of I_{bulk} for

[19] See Section 4.1.1.

estimation.

The leakage current can be measured for each strip if there is a direct contact to the strip implant. Uniform values across all strips indicate bulk homogeneity and absence of defects. A high leakage current of a single strip or group of strips indicates a problem. Usually, in this case, the global IV curve is also affected.

The measurement of the strip leakage current helps to identify such defect classes as implant breaks and shorts. Strips with high leakage current are commonly called "leaky" strips. They increase the noise in the readout channels. In combination with the pinhole[20] such strips can be dangerous for the operation of the readout chip.

Measurement method

Conventional measurement techniques foresee connecting a picoammeter between the DC pad of the strip implant and the bias ring. In this case, the strip leakage current will flow through the picoammeter, bypassing the polysilicon resistor. The connection scheme is shown in Fig. 4.23. This measurement has to be performed on a fully depleted sensor. The bias ring of the measured side is kept at ground potential, and the opposite side is biased to the operating voltage with the appropriate sign. The CBM prototype sensors were measured at $V_{bias} = 100\,\mathrm{V}$, which is equivalent to $1.5 \cdot V_{FD}$.

The CBM06 sensors have a feature that makes the measurement of the strip leakage current not straightforward. Each strip has one DC pad that is at the opposite end of the strip relative to that strip's polysilicon resistor. For simplicity, the strip implant can be represented by a single resistor R_{imp} and the strip leakage current by a current source. Connecting a picoammeter to the DC pad creates a loop where R_{poly} and R_{imp} appear in parallel. This means that the measured current I_{meas} is only a portion of the strip leakage current I_{strip}. The equivalent circuit for the p-side strips is shown in Fig. 4.24. The interstrip resistance R_{is} is considered high enough, so it does not affect the current. According to Kirchhoff's circuit laws:

$$\begin{cases} I_{strip} = I_{imp} + I_{poly} \\ I_{imp}R_{imp} - I_{poly}R_{poly} = 0 \end{cases} \tag{4.15}$$

where I_{poly} is the current through the polysilicon resistor, I_{imp} is the current through the strip implant, R_{imp} is the resistance of the strip implant, R_{poly} is the polysilicon bias resistance. I_{imp} is the current measured by a picoammeter. Then:

$$I_{strip} = I_{meas}\left(1 + \frac{R_{imp}}{R_{poly}}\right). \tag{4.16}$$

It means that less than half of the strip leakage current will be measured on $62 \times 124\,\mathrm{mm}^2$ sensors, where R_{imp} is expected to be greater than R_{poly}. The real

[20] Defect of the coupling dielectric layer. See Section 4.3.1.

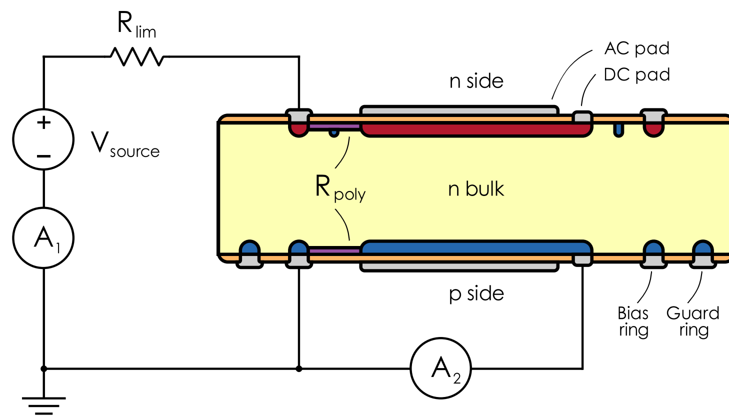

Figure 4.23.: Connection scheme for measurement of the leakage current of an individual strip. A picoammeter A_2 is connected between the bias ring and the DC pad of the strip. The side being measured is kept at ground potential. $\pm 100\,\mathrm{V}$ is applied to the opposite side.

dependence is more complex and takes into account the distributed nature of R_{imp} and I_{strip} along the strip. It was simulated using SPICE and is discussed in Section 5.5.

In some cases, for example, when there is an early breakdown or the total leakage current is constantly increasing, it may be useful to check the IV characteristics of individual strips. The basic procedure is the same as for the global IV measurement, but at each voltage step the strip current is recorded along with the total current.

Experimental setup

The bias voltage is supplied by a Keithley 2410 voltage source. The strip leakage current is measured by a Keithley 6487 [104] high precision picoammeter. Its *HI* terminal is connected to the DC pad of the strip using a needle probe. The shields of the cable are connected to its *LO* terminal, which is at ground potential. The device measurement range of 200 nA with a default resolution of 1 pA was used for most sensors. Hamamatsu $62 \times 22\,\mathrm{mm}^2$ sensors have the bulk leakage current of about 100 nA at normal conditions. The lowest device measurement range of 2 nA with a default resolution of 10 fA was used for these sensors. The systematic uncertainty on the current is $0.15\,\% + 10\,\mathrm{pA}$ at 200 nA range and $0.3\,\% + 400\,\mathrm{fA}$ at 2 nA, according to the device measurement accuracy specification [104]. Like any modern picoammeter, the Keithley 6487 has a voltage burden[21] that is specified to be $< 200\,\mu\mathrm{V}$. For a typical CBM06 sensor, it can cause an offset current of about

[21] Voltage burden is the voltage drop caused by current flowing through a current measuring device. It is a function of the current that flows in the circuit and the range selection on the meter.

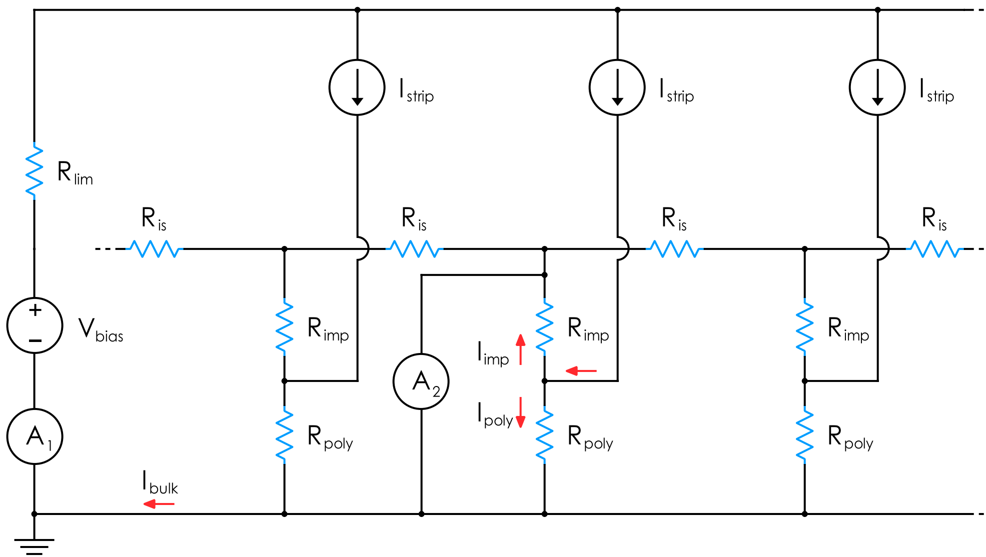

Figure 4.24.: Equivalent circuit of the p side of the CBM microstrip sensor with a picoammeter connected between the DC pad and the bias ring to measure the strip leakage current. Three strips are shown. Current sources represent the bulk leakage current. The red arrows show the direction of current flow. Picoammeter A_2 measures only a portion of the strip leakage current. The other part flows through the polysilicon resistor and is not measured.

10 pA. This effect can be reduced by performing offset correction procedures, such as "zero check" and "zero correct" for Keithley 6487 [104].

All strip measurements are performed using a Keithley 708B [106] switching matrix. The connection of devices is described in Section 3.3.1. The matrix channel configuration is given in Appendix C.

A dedicated probe station with high positioning accuracy is required to measure all 1024 strips of the microstrip sensor. Before probing each strip, several preparatory procedures are performed: alignment, coordinate calibration, and measurement of the height profile[22] of the DC pads. The even/odd strips of the CBM06 sensors have DC pads at opposite ends of the strip. When scanning strip by strip, both rows of DC pads cannot be probed at the same time, as their height profiles are significantly different and the strips may be damaged by needles. Therefore, only half of the strips can be measured in one pass.

Results for CBM prototype sensors

Figure 4.25 shows the measured current of each strip of the 17 CBM06 sensors selected for this work. A total of 8 Hamamatsu and 14 CiS sensors of all sizes

[22] See Section 3.2.8

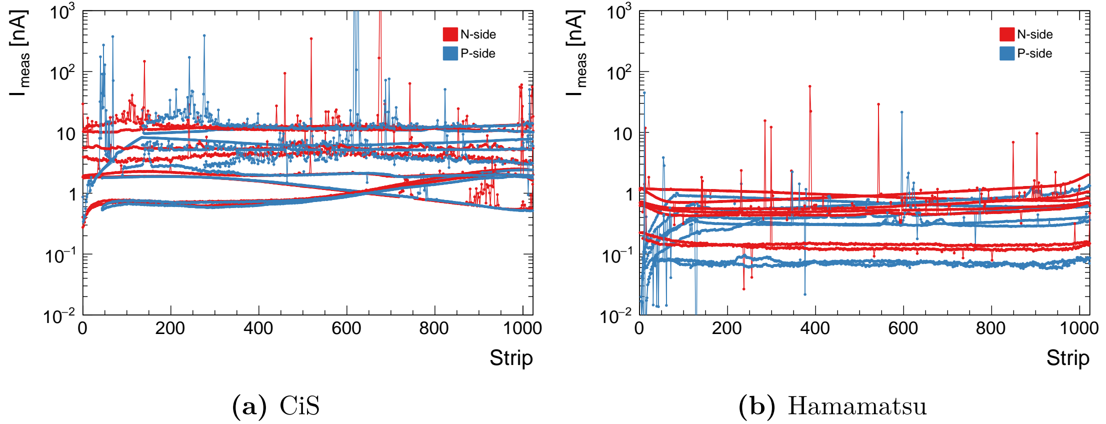

(a) CiS

(b) Hamamatsu

Figure 4.25.: Measured leakage current of each strip of the 17 investigated CBM06 sensors: both CiS and Hamamatsu are shown. The measurements were performed at $V_{bias} = \pm 100$ V. I_{meas} represents only a portion of the actual strip leakage current.

were investigated, resulting in about 45 000 tested strips[23]. The measured leakage current is below 11 nA and 2 nA at $V_{bias} = 100$ V for CiS and Hamamatsu sensors, respectively. Two CiS sensors have a significant number of strips with high leakage current. The absence of surface defects suggests that bulk or implantation defects exist for these sensors. Broken implants appeared to be more common for Hamamatsu sensors, which in most cases are identified by lower than average current. The measured current of three CBM06C2 sensors from the same batch has a significant difference between the first and last strips. This may indicate a significant variation in sensor thickness.

It was previously shown that I_{meas} represents only a portion of the strip leakage current and depends on the ratio R_{imp}/R_{poly}. Figure 4.26a shows a comparison of the average measured current on the n side and on the p side of the CBM sensors. The implant resistance on the n side is about three times smaller than on the p side for a typical CBM06 sensor manufactured by Hamamatsu. Therefore, the measured current is higher on the n side because less current flows through the polysilicon resistor. On the contrary, the measured currents on both sides of the CiS sensors are similar. Using Eq. 4.16, the measured current from both sides of CiS $62 \times 22\,\text{mm}^2$ sensors should differ from the strip leakage current by about 5 %. This value is larger for larger sensors and sensors with a smaller R_{poly} value. Figure 4.26b shows a comparison of the summed-up measured strip current on the n side with the total leakage current of the sensor. The discrepancy is larger for Hamamatsu sensors, since their polysilicon resistors are about three times smaller than of CiS sensors[24].

[23] It should be noted that these sensors do not represent the actual quality of the CBM06 sensors, as they were intentionally selected to investigate the strip characteristics.

[24] According to the datasheets provided by the vendors, R_{poly} is about 0.5 MΩ and 1.5 MΩ for Hamamatsu and CiS sensors, respectively.

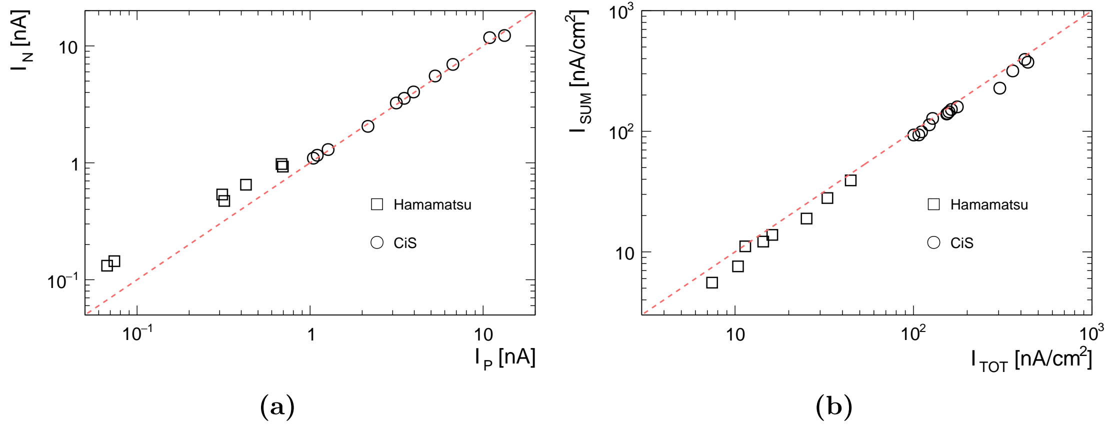

Figure 4.26.: Comparison between the measured strip current on the p and n sides and the total leakage current: (a) Hamamatsu sensors have a higher measured current for the n-side strips due to the lower implant resistance with respect to the p side; (b) the summed-up measured strip current is lower than the total leakage current. Dashed lines are drawn to guide the eye.

Observed problems

The strip leakage current measurements are sensitive to bulk and implant defects. Typically, they are localized in individual strip implants and appear during the manufacturing process. Several large clusters of defects were found on the CBM sensors under study.

Figure 4.27a shows the deviation of the measured leakage current for a group of strips of the CBM06H12 sensor. Its corresponding n-side strip area is shown in Fig. 4.27b. The two implants are shorted through a channel that interrupts the p-stop implant. The next five implants are broken, so the measured current is lower. Considering the dependence of I_{meas} on the R_{imp}/R_{poly} ratio, the actual strip leakage current of the CBM06H12 sensor is ≈ 0.75 nA. Therefore, the measured current of 0.35 nA and 0.42 nA is collected only from 45 % and 55 % of the implant, respectively, with the rest of the current flowing to the bias ring through a polysilicon resistor. Due to the layout of the CBM06 sensors, geometrically it is the same area of the sensor affected by the breaks.

Another consequence of this strip layout is a possible misinterpretation of the measured strip current. A higher current can be measured for a broken strip, depending on the ratio R_{imp}/R_{poly}. If the implant break is near the polysilicon resistor, then the measured current is the actual strip leakage current and twice[25] the average measured current of the other strips. If the implant is broken approximately in the middle, the measured current will be the same as the average measured current of the other strips, and the defect cannot be detected. To avoid such situation, it is preferable to have DC pads near the polysilicon resistors.

[25] Here, $R_{imp}/R_{poly} \approx 1$ is assumed.

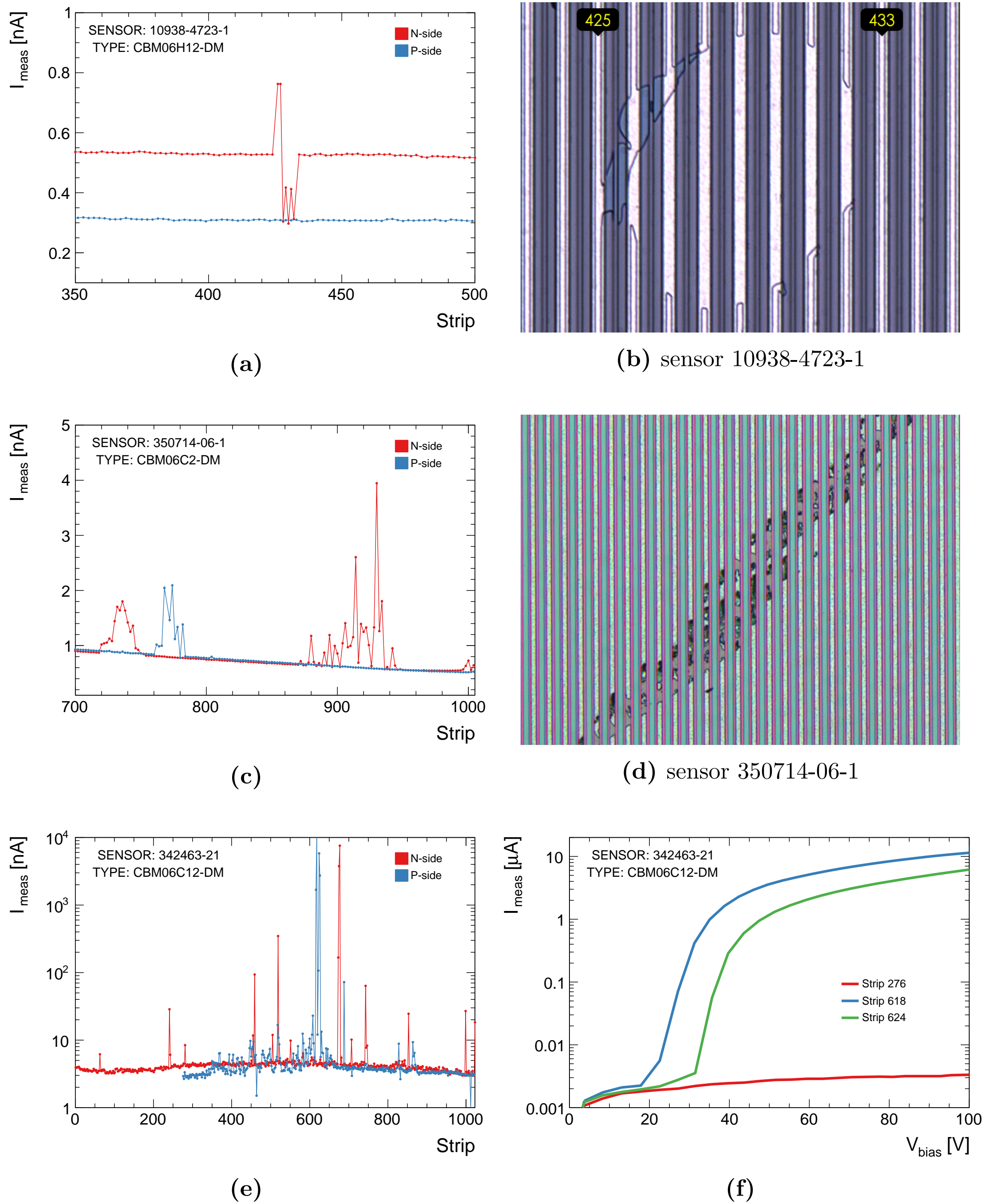

Figure 4.27.: Correlation between irregular strip leakage current and visually identified defects. (a)-(b) Measured strip current and defect cluster on the n side of CBM06H12 sensor. (c)-(d) Measured strip current and defect cluster of CBM06C2 sensor. (e)-(f) Measured strip current of CBM06C12 sensor and IV curves for a few strips. See text for details.

Figure 4.27c shows the measured strip current for the CBM06C2 sensor. The high current of strips 880 – 950 is the result of the defect cluster shown in Fig. 4.27d. Visual inspection did not confirm the defects of strips 720 – 780 on both sides of the sensor. Since they are in geometrical correspondence, the bulk or implantation inhomogeneity should be the cause of the high current.

Figure 4.27e shows the measured strip current for the CBM06C12 sensor. It was shown in Section 4.1.2 that the surface leakage current of this sensor only partially contributes to breakdown. About 200 strips are considered "leaky", while about 20 strips have a current several orders of magnitude above average. The IV curves for two such strips are shown in Fig. 4.27f. The leakage current of regular strips saturates to 3.5 nA at 100 V. The breakdown of the defective strips occurs before full depletion, which increases the total leakage current.

4.2.2. Polysilicon Bias Resistance

The CBM06 prototype sensors use a polysilicon biasing method on both sides. Each strip has one polysilicon resistor that connects its implant to the common bias ring. Previous iterations of the CBM sensors, as well as baby sensors, use a punch-through biasing method. However, it is not as radiation hard as the polysilicon biasing method. Uniform values of polysilicon resistors are required for the entire sensor to put strips on the same potential. In Ref. [130] it is shown that even a large spread of the R_{poly} values only marginally affects the field distribution inside the detector as long as the resistance remains in the MΩ range and the leakage current is small. However, a large spread would indicate a possible problem in the manufacturing process.

To minimize the contribution of thermal noise to the overall system noise, high polysilicon resistance values are preferable. It is 1.50 ± 0.25 MΩ for CiS sensors and 0.50 ± 0.05 MΩ for Hamamatsu sensors according to the datasheets provided by the vendors. Noise performance studies of the STS readout system have set a requirement to increase R_{poly} to about 5 MΩ [81]. Recent prototypes of the CBM06 sensors were produced with R_{poly} in the range 2–5 MΩ.

Measurement method

Resistance can be measured by sourcing a known current and measuring the resulting voltage drop or by sourcing a known voltage and measuring the resulting current. The DC voltage method is used in this work. The connection scheme for resistance measurement of a single strip on the CBM prototype sensor is shown in Fig. 4.28. The sensor has to be biased to the operating voltage if measurements are performed on the n side, while for measurements on the p side a small bias of 5 V is sufficient[26]. The measurements on the CBM sensors were performed at

[26] As was shown in Section 4.1.3, the depletion regions of the individual strips on the p side of the CBM sensors should merge around this voltage.

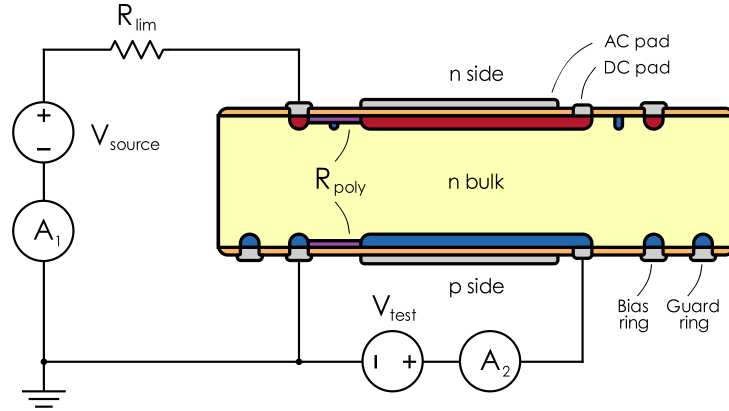

Figure 4.28.: Connection scheme for the DC resistance measurement of one strip on the CBM06 sensor. The side being measured is kept at ground potential. A bias voltage of 100 V is applied to the opposite side (with the appropriate sign). The test voltage V_{test} varies between 0 V and 1 V, and the resulting current is measured by a picoammeter A_2.

$V_{bias} = 100\,\text{V}$. The side being measured is kept at ground potential. The *HI* terminal of the test voltage source V_{test} is connected to the DC pad that is in direct contact with the implant, and its *LO* terminal is at ground potential. The resulting current is measured by a picoammeter A_2.

A few things have to be considered to make proper measurements. As discussed in the previous section, each strip has only one DC pad, which is at the opposite end of the strip relative to that strip's polysilicon resistor. It means that direct measurement of polysilicon resistance on the CBM prototype sensor is not possible. The measurement circuit includes a series combination of strip implant resistance R_{imp} and polysilicon resistance R_{poly}:

$$R_{DC} = R_{poly} + R_{imp}. \tag{4.17}$$

The equivalent circuit for the p-side strips is shown in Fig. 4.29. For simplicity, the strip implant is represented by a single resistor. The strip leakage current is represented by a single current source that provides a constant offset to the measured current. Since the isolation between the strips is not perfect, the measurement circuit includes the interstrip resistance R_{is}, which is connected in parallel with R_{poly} and R_{imp}. According to Kirchhoff's circuit laws:

$$\begin{cases} I_{meas} = I_1 + 2I_{is} \\ I_1 + I_{strip} = I_2 \\ I_1 R_{imp} + I_2 R_{poly} = V_{test} \\ I_{is} R_{is} + I_{is} R_{imp} + (I_{is} + I_{strip}) R_{poly} = V_{test} \end{cases} \tag{4.18}$$

where I_{meas} is the current measured by the picoammeter A_2, I_1 is the current through the implant, I_2 is the current through the polysilicon resistor, I_{is} is the

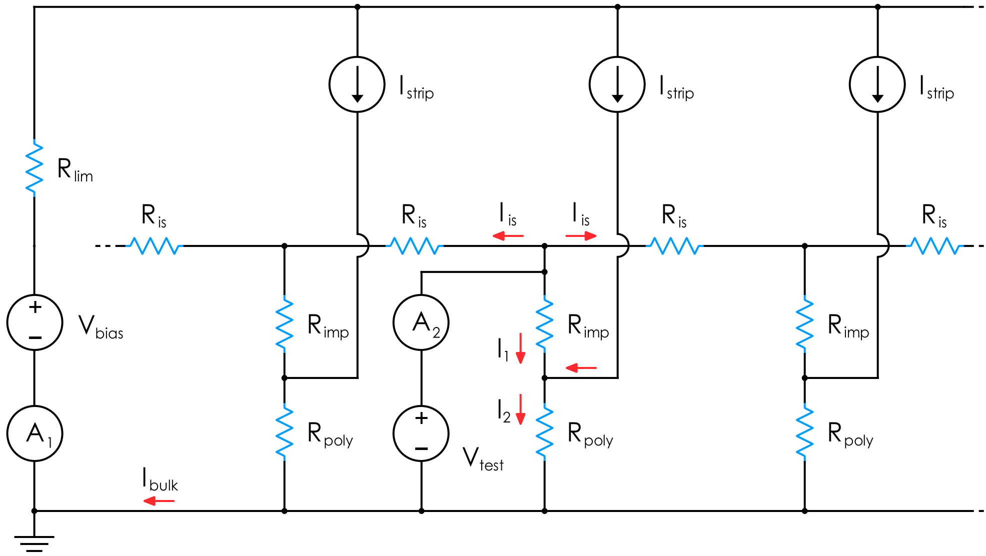

Figure 4.29.: Equivalent circuit of the p side of the CBM microstrip sensor with a picoammeter and a voltage source connected between the DC pad and the bias ring to measure the DC resistance. Three strips are shown. Current sources represent the bulk leakage current. The red arrows show the direction of current flow. The interstrip resistance R_{is} provides an additional current path.

current through the interstrip gap, and I_{strip} is the strip leakage current. Solving this system with respect to the measured current I_{meas} gives:

$$I_{meas} = (V_{test} - I_{strip}R_{poly})\left(\frac{1}{R_{DC}} + \frac{2}{R_{is} + R_{DC}}\right). \tag{4.19}$$

The interstrip resistance is an important parameter of microstrip sensors. It has to be high enough to avoid resistive division of the charge between the strips and, as a result, a decrease in the spatial resolution of the sensor. A typical value of R_{is} for non-irradiated sensor is of the order of GΩ[27]. Since $R_{is} \gg R_{DC}$, the corresponding term in Eq. 4.19 can be neglected. Then:

$$R_{DC} = \frac{V_{test} - I_{strip}R_{poly}}{I_{meas}}. \tag{4.20}$$

The error in R_{DC} due to this assumption should not exceed 1 % for a typical non-irradiated CBM06 sensor. To get rid of I_{strip}, IV curve is recorded and the resistance is determined from its slope:

$$R_{DC} = \frac{dV_{test}}{dI_{meas}}. \tag{4.21}$$

[27]Interstrip resistance decreases with irradiation and serves as the end-of-life criteria of microstrip sensors.

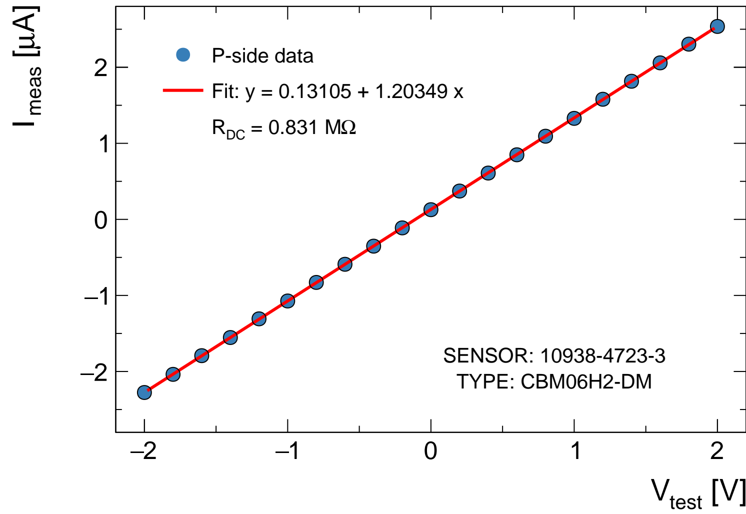

Figure 4.30.: DC resistance measurement: IV curve for one strip of the p side of the CBM06H2 sensor. The straight line fit to the data is used and the resistance is extracted from the slope. Its value is the sum of the implant resistance and polysilicon resistance.

The test voltage ramp from 0 V to 1 V is performed in steps of 0.1 V for each strip with the DC pad. V_{test} higher than 5 V is not recommended for CBM06 sensors to exclude punch-through resistance[28]. Figure 4.30 shows the IV curve measured for one strip of the p side of the CBM06H2 sensor. Measurements were performed for a wider range of voltages to verify linearity. The DC resistance is extracted from the slope of the line that fits the data. The polysilicon resistance can now be determined using Eq. 4.16.

For the bias voltage dependence, the DC resistance measurement is performed when the bias voltage is increased in steps of 5 V.

Experimental setup

A Keithley 2410 voltage source is used to bias the CBM sensors to ±100 V. The test voltage V_{test} is supplied by a Keithley 6487 voltage source. The ±10 V source range was used to measure the DC resistance. The accuracy of the device at specified voltage range is 0.1 % + 1 mV according to the device accuracy specification [104]. The induced current was measured by a Keithley 6487 picoammeter. The DC resistance range for the CBM sensors under study is 0.4–5 MΩ. For a maximum $V_{test} = 1$ V, the expected current is in the range of 0.2–2.5 µA. Therefore, the measurement range 20 µA with a default resolution of 100 pA was used for the measurements. The systematic uncertainty on the current is 0.1 % + 1 nA, according to the device measurement accuracy specification [104]. To achieve

[28] See Section 4.2.3 for details.

optimal resistance measurement accuracy, it is recommended to perform a zero correction of the picoammeter. The built-in feature of Keithley 6487 to measure resistances was not used in this work, and manual IV measurements were always performed instead.

One needle is required to contact the DC pad of the strip. All strip measurements are performed using a Keithley 708B [106] switching matrix. The connection of devices is described in Section 3.3.1. The matrix channel configuration is given in Appendix C. Strip-by-strip measurements require a probe station with high positioning accuracy. Similar to the strip leakage current measurement, only half of the strips can be measured in one pass.

Results for CBM prototype sensors

A total of 7 Hamamatsu and 16 CiS sensors of all sizes were investigated, resulting in about 28 000 strips[29]. In addition, 5 strips on each side were measured on each of 2 Hamamatsu and 3 CiS sensors dedicated to the mSTS project [47]. Figure 4.31 shows the measured DC strip resistance of the investigated CBM06 sensors from both vendors. It ranges from 1.5 MΩ to 3 MΩ for CiS sensors. While strip-to-strip variation is less than 1 %, the DC resistance variation across the sensor is as high as 20 % for some CiS sensors. It cannot be distinguished from these measurements alone, rather it is due to the non-uniformity of the polysilicon resistance or the strip implantation. The measured DC resistance shows high uniformity across all strips on both sides of the Hamamatsu sensors. Values range from 0.5 MΩ to 1.3 MΩ, and 2 MΩ curve corresponds to the p side of $62 \times 124\,\mathrm{mm}^2$ sensor. The vertical spikes in both graphs are due to implant breaks, resulting in high series resistance. Data points with low resistance typically indicate a short between strip implants. The defective strips correspond to those identified during strip leakage current measurements.

The primary purpose of the DC resistance measurement is to obtain an estimate of the polysilicon bias resistance for the CBM06 sensors. This is done using Eq. 4.16 and the strip leakage currents from the previous section. This approach relies heavily on accurate strip and bulk leakage current measurements. The latter is used to estimate the average strip leakage current, and hence the contribution from the “leaky” strips has to be subtracted beforehand. Otherwise, wrong R_{poly} values will be obtained. For several sensors, the strip leakage current was not measured and R_{poly} was estimated by subtracting the implant resistance.

On the p side, the length of the corner strips[30] increases with the strip number until the 1st full-length strip is reached. The implant resistance increases in proportion to the length of the strip. Figure 4.32a and Fig. 4.32b show an example of

[29] The total number of strips is about 47 000. However, resistance measurement is a time-consuming procedure due to necessity to measure IV curve for each strip. It takes about 20 s per strip, resulting in about 5 h of measurements for one side of the sensor. Therefore, only every 2nd strip was measured, and each strip was measured on only a few sensors.

[30] On the p side, short strips appear due to the stereo angle of this side.

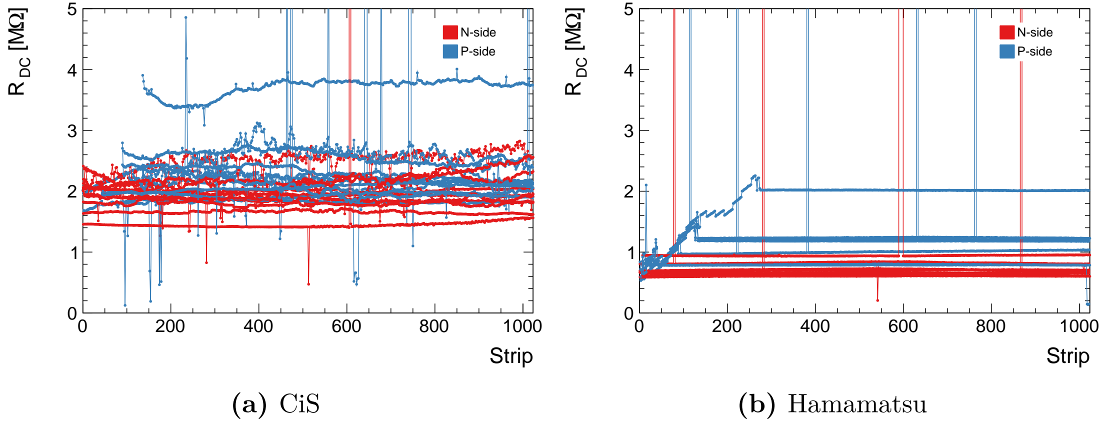

(a) CiS **(b)** Hamamatsu

Figure 4.31.: Measured DC strip resistance of 23 CBM06 prototype sensors under investigation: both CiS and Hamamatsu are shown. Measurements were performed on both sides of the sensors at $V_{bias} = \pm 100\,\mathrm{V}$. As explained in the text, $R_{DC} = R_{poly} + R_{imp}$.

CiS and Hamamatsu $62 \times 62\,\mathrm{mm}^2$ sensors. Fitting a straight line to the measured DC resistance of the short strips gives R_{poly} and R_{imp} values. A perfect linear relationship is evident for the Hamamatsu sensor, indicating a high uniformity of implantation for all strips. For the CiS sensor, only the most linear region was used for fitting.

Figure 4.32c and Fig. 4.32d show the dependence of the DC resistance on the strip length for the sensors of 4 form-factors that will be used in the STS. The CiS sensors do not show a clear dependence, since the strip parameters were subject to adjustment at the prototyping stage. The Hamamatsu sensors show a linear relationship and a straight line fit gives a polysilicon resistance of $0.52\,\mathrm{M\Omega}$ on both sides. The estimation for R_{imp} is $117\,\mathrm{k\Omega/cm}$ and $30\,\mathrm{k\Omega/cm}$ for the p and n sides, respectively. This is consistent with the SPICE simulation results for the Hamamatsu sensors[31].

Figure 4.33 summarizes the polysilicon bias resistance for all investigated sensors. Average values for 512 strips of each side are plotted. The results are compared with the values reported by the vendors in the final inspection sheet. The estimated values of R_{poly} for the Hamamatsu sensors are between $0.4\,\mathrm{M\Omega}$ and $0.8\,\mathrm{M\Omega}$ on both sides. This is consistent with the vendor's data and with the $0.52\,\mathrm{M\Omega}$ estimate obtained from the strip length fit. The polysilicon resistance of the CiS sensors ranges from $1\,\mathrm{M\Omega}$ to $3.2\,\mathrm{M\Omega}$ and is uniform within batches. The values specified by CiS are somewhat lower than those estimated in this work. A very low R_{poly} was obtained for the CBM06C12 sensor. It may be due to the high leakage current of this sensor, which affects the calculation of R_{poly}. To meet the CBM specifications, the polysilicon resistance is required to be at least $1.5\,\mathrm{M\Omega}$ for the final CBM sensors, which were not available at the time of this work.

[31] See Chapter 5.

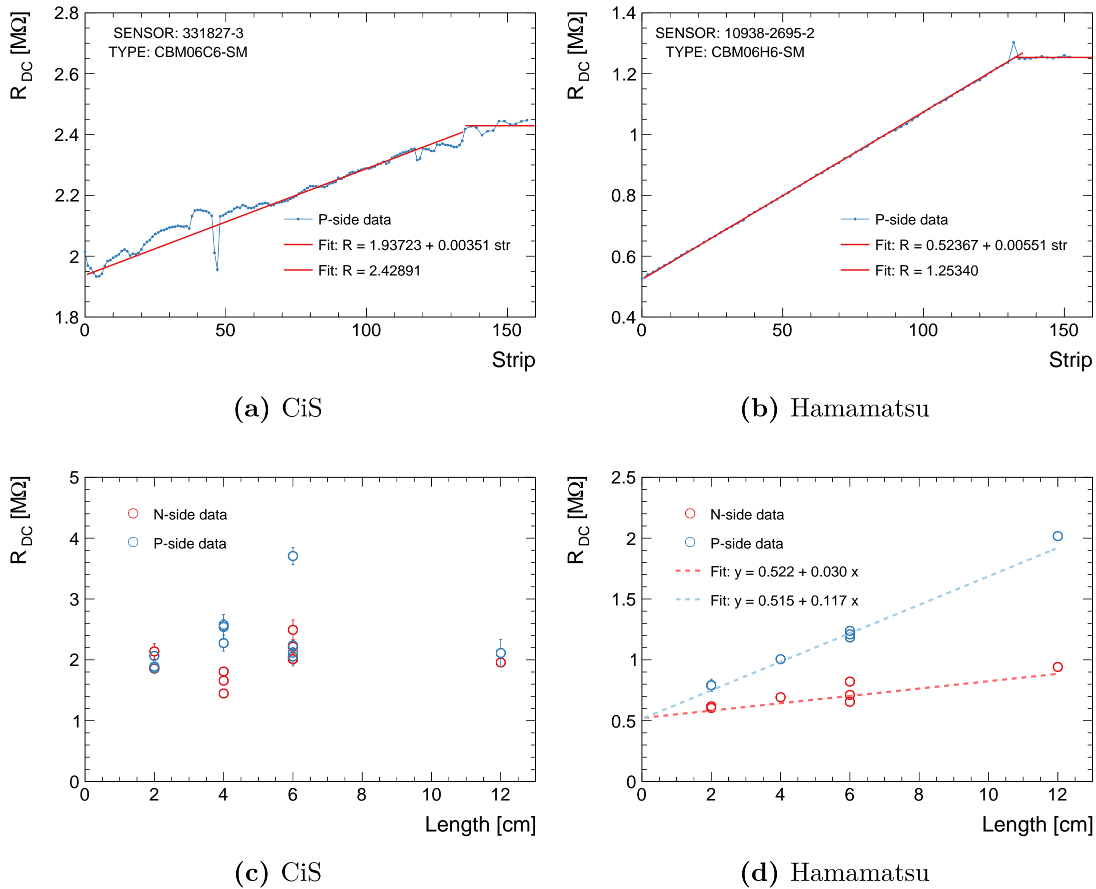

(a) CiS

(b) Hamamatsu

(c) CiS

(d) Hamamatsu

Figure 4.32.: Dependence of the measured DC resistance on the physical length of the strip for the investigated sensors. (a)-(b) The length of the corner strips on the p side increases with the strip number and, therefore, their DC resistance. A straight line fit of the data is shown for two $62 \times 62\,\mathrm{mm}^2$ sensors. (c)-(d) The dependence of the DC resistance on the strip length is shown for the sensors of 4 form-factors that will be used in the STS. The Hamamatsu sensors show an excellent linear dependence on the strip length, while this is not the case for the CiS sensors. The reason is that the strip parameters were adjusted at the prototyping stage.

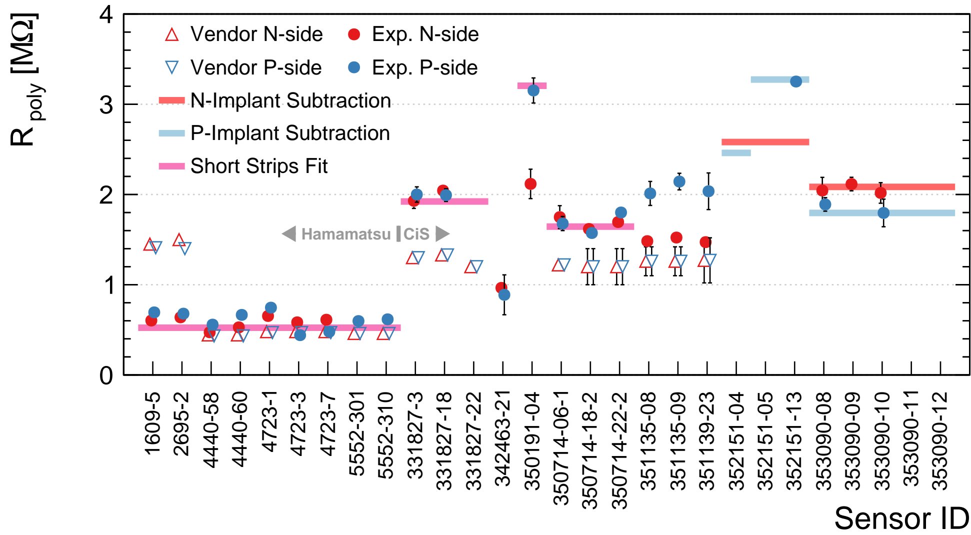

Figure 4.33.: Polysilicon bias resistance of the investigated CBM06 prototype sensors determined in the DC resistance measurements. Each data point is an average for 512 strips of the sensor, and the error bars indicate one standard deviation.

The dependence of the DC resistance of the strip on the bias voltage was checked for several sensors. Figure 4.34 shows an example for the Hamamatsu $62 \times 124\,\mathrm{mm}^2$ sensor. On the p side, the strips are self-isolated, and the total resistance is measured even at low biases. The strips on the n side are isolated only after the sensor is fully depleted. For $V_{bias} < V_{FD}$, the interstrip resistance is low on the n side. Therefore, a parallel network of resistors is measured, which leads to low values.

Observed problems

CBM05 and the first CBM06 sensor prototypes were manufactured in both single- and double-metal variants to study the effect of the 2nd metal coupling on the charge collection efficiency [39]. A special microcable[32] was used to connect the short strips on the p side of the single-metal sensors. Additional contact pads along the left and right edges of the sensor were integrated in the 1st metal layer. The design mask of the 1st metal layer was kept the same for both sensor variants and remained unchanged for the CBM06 prototypes investigated in this work. Polysilicon resistors of odd-numbered strips are also located along the same edges as these pads. It turned out that there is a certain impact on the electrical parameters of the short strips of the Hamamatsu sensors due to these additional pads. Figure 4.35 shows the measured DC resistance of the short strips of the CBM06H6 sensor. While even-numbered strips show a linear increase in R_{DC} with implant length, an unexpected pattern is observed for odd-numbered strips.

[32]See Fig. 2.5.

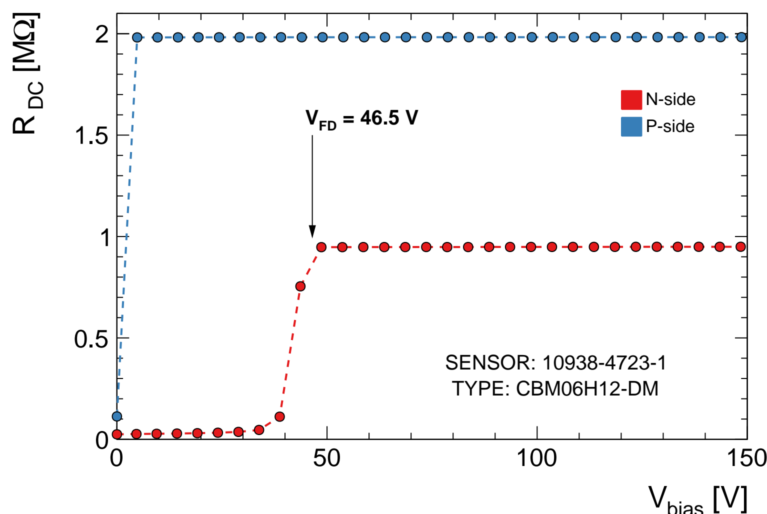

Figure 4.34.: Dependence of the DC resistance of the strip on the bias voltage for the CBM06H12 sensor. On the *p* side, the strips are self-isolated. On the *n* side, the strips are isolated only after full depletion of the sensor.

For some of these strips, the 1st metal line goes over a polysilicon resistor. This results in an increase of the measured DC resistance of the strip by a constant value of about 110 kΩ. The number of crossings varied from 0 to 3, and their pattern corresponds to the measured DC resistance, as shown in Fig. 4.35. The reason probably lies in the manufacturing process. If there is no passivation layer on top of the resistor, it will be in direct contact with every metal line above it. This leads to unexpected couplings that affect strip performance. Therefore, it was suggested to remove these additional contact pads from the design mask in the final iteration of the CBM06 sensors [64]. This effect was not observed on the CiS sensors because all polysilicon resistors of the short strips reside on the upper edge of the sensor.

4.2.3. Punch-through Voltage

Microstrip sensors can be biased without polysilicon resistors using a punch-through mechanism. It is based on the fact that current starts to flow between the strip implant and the bias ring if there is a difference of a few volts between them [69]. This biasing method is simple to implement, but it is less radiation hard than the polysilicon method. It is used, for example, to bias the double-sided microstrip sensors in the ALICE Inner Tracking System [131], where the expected fluence is about $3 \times 10^{11}\,\mathrm{n}_{eq}/\mathrm{cm}^2$ over ten years of operation.

The punch-through structures are usually implemented to protect the coupling capacitors from accidental high voltages on them. The voltage drop across the polysilicon resistor is small during normal sensor operation. It can exceed

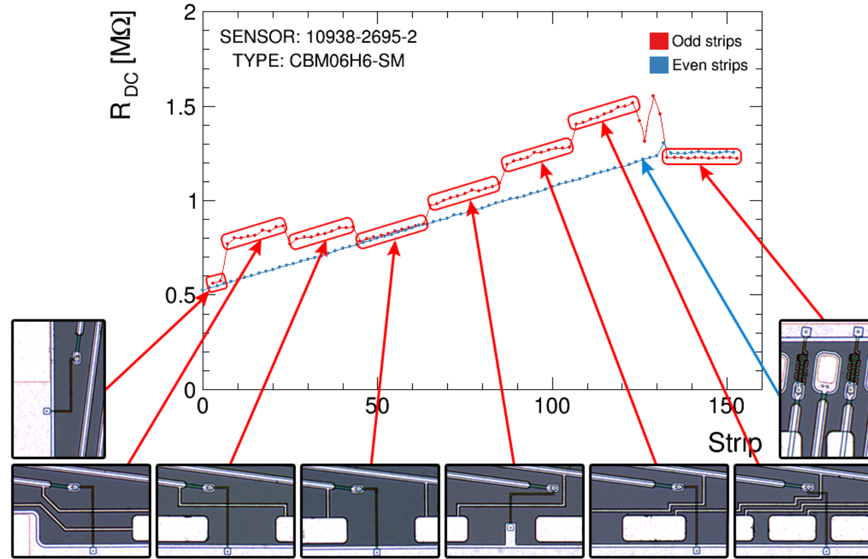

Figure 4.35.: The observed non-uniformity of the measured DC resistance of the short strips on the p side of the Hamamatsu sensors. Each crossing of a polysilicon resistor by a metal line increases the measured DC resistance by a constant value of about 110 kΩ. The maximum number of crossings is 3. The effect is absent for even strips that have polysilicon resistors on the upper edge of the sensor.

the breakdown voltage of the coupling capacitor if a large current flows through the bulk. This can happen, for example, in a beam loss accident. The punch-through structure provides a low impedance path and limits the voltage drop across the polysilicon resistor, thus acting as a protective structure. In a fixed-target experiment such as CBM, it is not likely to happen because the beam is well collimated after extraction from the accelerator ring. Nevertheless, the performance of the punch-through protection (PTP) structures of the CBM06 sensors was evaluated. PTP structures of various geometries have been comprehensively investigated by the ATLAS collaboration for the Inner Tracker upgrade as reported in Refs. [132, 133, 134, 135, 136].

The PTP structure has a *pnp* or *npn* configuration formed by a strip implant, a bias ring, and a gap between them — either n-type bulk or p-isolation structure. The onset voltage depends on the gap size, the doping concentration, and the metal overhang [134]. Figure 4.36 shows the drawings of the PTP structures of the CBM06 microstrip sensor manufactured by CiS. The distance between the strip implant and the bias ring is 8 µm and 14 µm for the p and n sides, respectively. For Hamamatsu sensors, it is about 30 µm for both sides[33].

[33]Technical drawings of Hamamatsu sensors did not include implants. Therefore, the gap width was obtained using optical measurements.

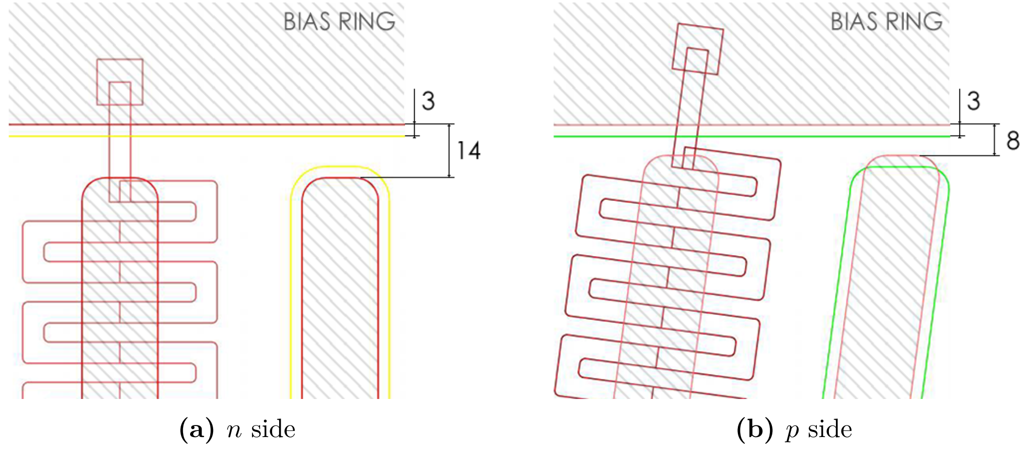

(a) n side **(b)** p side

Figure 4.36.: Drawings of the punch-through structures of the CBM06 microstrip sensor manufactured by CiS. The boundaries of the metal layer are shown in green and yellow. The metal overhang of the bias ring is the same on both sides and reduces the punch-through voltage. Dimensions are in µm.

Measurement method

The PTP structure is characterized by the onset voltage V_{PT} at which its resistance drops and the current is drained to the bias ring. The punch-through resistance together with R_{poly} and R_{imp} constitutes the effective strip resistance. The connection scheme is the same as for the strip DC resistance measurements, and is shown in Fig. 4.28. Measurements on the CBM sensors were performed at $V_{bias} = \pm 100\,\mathrm{V}$. The bias ring on the measured side is kept at ground potential. A test voltage V_{test} is applied between the DC pad of the strip and the bias ring, and the induced current is measured. It consists of the bulk leakage current, the punch-through current and the current flowing through the polysilicon resistor. The measurements are performed up to $V_{test} = 50\,\mathrm{V}$ with a step of 1 V and a 1-second delay or until a current of 1 mA is reached. Since the n-side strips collect electrons, a negative test voltage is applied to the DC pad with respect to the bias ring. On the p side, a positive test voltage is applied.

The effective resistance between the DC pad and the bias ring is determined from the IV curve as:

$$R_{eff} = \frac{dV_{test}}{dI_{test}}. \tag{4.22}$$

Onset voltage

Each strip of the CBM06 sensor has two PTP structures. Its operation is similar to a TVS[34] diode. Figure 4.37 shows the equivalent circuit of one strip with a PTP structure at each end of the strip implant R_{imp}. PT_1 is in parallel with the

[34]Transient Voltage Suppression diode.

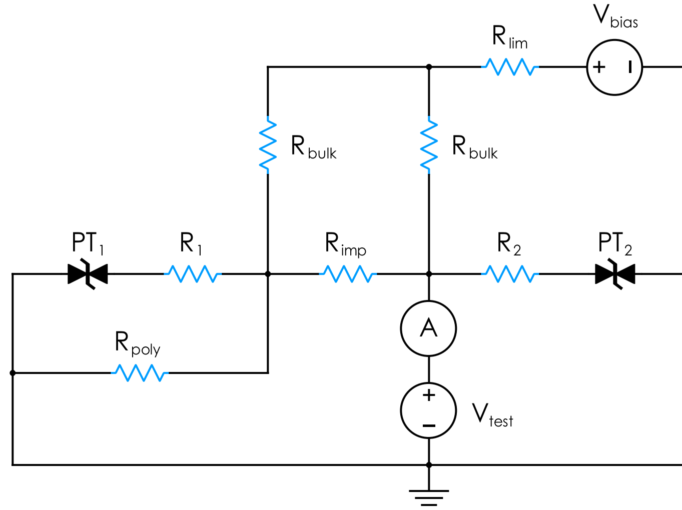

Figure 4.37.: Equivalent circuit of one strip with its PTP structures on the p side of the CBM prototype sensor. Two PTP structures — PT_1 and PT_2 — are schematically represented as TVS diodes. The test voltage source V_{test} is connected between the DC pad and the bias ring. Resistors R_1 and R_2 are of the order of several kΩ.

polysilicon resistor R_{poly}, while PT_2 is next to the DC pad. A small resistance $R_1 \approx 5\,\text{k}\Omega$ is in series with PT_1 due to the connection point of R_{poly}. The DC pad is located at a distance of 300 µm from the strip implant end. This results in a small series resistance $R_2 \approx 5\,\text{k}\Omega$[35] between PT_2 and the measurement point. The effective resistance of such a circuit:

$$\frac{1}{R_{eff}} = \frac{1}{R_2 + R_{PT2}} + \frac{1}{R_{imp} + \left(\frac{1}{R_{poly}} + \frac{1}{R_1 + R_{PT1}}\right)^{-1}} \tag{4.23}$$

where R_{PT1} and R_{PT2} are the resistances of PT_1 and PT_2, respectively. For simplicity, bulk and interstrip resistances are neglected.

When the PTP structure is inactive, it is equivalent to an open circuit. The effective resistance is then determined by the strip DC resistance discussed in the previous section. When the test voltage is applied to the DC pad, punch-through occurs first at PT_2. Its resistance becomes low, while PT_1 still has high resistance. The punch-through voltage is defined as the voltage $V_{PT} = V_{test}$ at which:

$$R_2 + R_{PT2} = R_{imp} + R_{poly} \tag{4.24}$$

or the effective resistance is equal to half the strip DC resistance:

$$R_{eff} = \frac{R_{imp} + R_{poly}}{2}. \tag{4.25}$$

[35]Some of the CBM06 sensors have metal extending from the DC pad to the strip implant end. Therefore, R_2 can be neglected.

PT_2 will maintain V_{PT} across itself and any excess voltage $V_{test} - V_{PT}$ will drop across R_2. Both PTP structures are geometrically identical and should have the same punch-through voltage. Punch-through at PT_1 occurs when:

$$R_1 + R_{PT1} = R_{poly}. \tag{4.26}$$

Corresponding effective resistance:

$$R_{eff} = \left(\frac{1}{R_2 + R_{PT2}} + \frac{1}{R_{imp} + \frac{1}{2} R_{poly}} \right)^{-1}. \tag{4.27}$$

The current through the polysilicon resistor saturates and no longer increases. PT_1 will maintain V_{PT} across itself, allowing more current to flow. The corresponding test voltage V_{test} applied to the DC pad is higher than V_{PT}:

$$V_{test} = \frac{V_{PT}}{R_{poly}} R_{imp} + V_{PT} = V_{PT} \left(1 + \frac{R_{imp}}{R_{poly}} \right). \tag{4.28}$$

Excess voltage drops across the strip implant resistance R_{imp} and should not exceed the breakdown voltage of the coupling capacitor. After V_{test} is set to 0 V, both PTP structures return to the initial high resistance state.

Experimental setup

The switching matrix of the Tübingen probe station is equipped with the Keithley 7072-HV card. It is designed for a peak power of 10 V A with a resistive load [107]. To avoid possible damage to the device, measurements of PTP structures on CBM sensors were performed without a switching matrix. Besides that, the setup arrangement is the same as for the strip DC resistance measurement. The test voltage V_{test} is supplied by the Keithley 6487 voltage source. The maximum compliance current limit is 2.5 mA at 505 V source range. The accuracy of the device at the specified voltage range is 0.15 % + 40 mV, according to the device accuracy specification [104]. The induced current is measured by a Keithley 6487 picoammeter. Measurements are performed on 200 µA range until higher currents are induced. The device is then programmed to up-range to 2 mA range. The systematic uncertainty on the current is 0.1 % + 100 nA at 2 mA range, according to the device measurement accuracy specification [104].

Results for CBM prototype sensors

The punch-through structure has to protect the coupling capacitor from large transient voltages across it. Coupling capacitors of the CBM06 sensors have a breakdown voltage[36] above 150 V and 100 V for CiS and Hamamatsu sensors,

[36]The breakdown voltage is determined from the IV curve measured at a slow voltage ramp. Instant application of high voltage can permanently destroy the coupling capacitor.

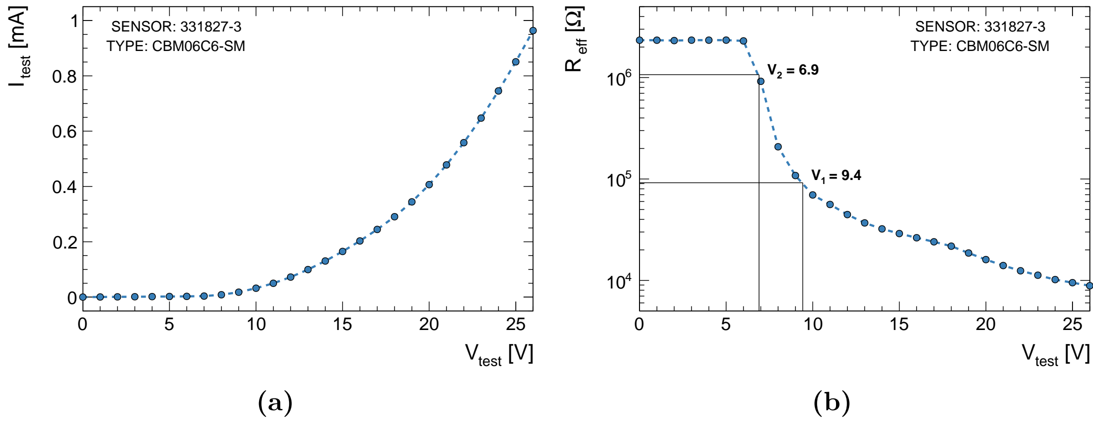

Figure 4.38.: IV characteristic and effective resistance of one strip on the p side of the CBM06C6 sensor. Punch-through at PT_2 occurs at 6.9 V and is accompanied by an exponential increase in the current. Punch-through at PT_1 occurs when the DC pad potential reaches 9.4 V. It means that 2.5 V drops across the strip implant when PT_1 is activated.

respectively. It is desirable that the PTP structure has a low V_{PT} and provides a low resistance path for transient current.

The measured current I_{test} as a function of the test voltage is shown in Fig. 4.38a and the effective resistance R_{eff} is shown in Fig. 4.38b for the p-side strips of the CBM06C6 sensor. Punch-through at PT_2 occurs at $V_{PT} = 6.9$ V and is accompanied by an exponential increase in the current through it. The voltage drop across the strip implant results in a delay for PT_1 structure in this measurement configuration. Punch-through at PT_1 occurs when the DC pad potential reaches 9.4 V according to Eq. 4.28. The resistance of PT_2 drops below 100 kΩ taking a current of $\approx$ 21 µA out of 25 µA. A test current of 1 mA would result in a voltage drop between DC pad and bias ring of only 26 V.

The measurement results for all the investigated sensors are shown in Fig. 4.39. For CiS sensors, the punch-through voltage is 6.5 ± 0.4 V and -5.1 ± 0.2 V on the p and n sides, respectively. The uncertainties represent one standard deviation of the data.Only one Hamamatsu sensor was measured, and the corresponding V_{PT} is 12.2 V and -7.3 V on the p and n sides, respectively. Lower value on the n side is explained by the width of the p-stop structure, which is only 8 µm. Thus, its V_{PT} is close to V_{PT} of the CiS sensors.

The voltage across the coupling capacitor is limited to V_{PT} only if the implant resistance is negligible. The disadvantage of the DC measurement method is that the test voltage can only be applied to the DC pad, and almost all the current is diverted through PT_2. This method allows determination of V_{PT} but does not allow measurement of the actual voltage across the implant which can exceed the breakdown voltage of the coupling capacitor [133] and make PTP structures ineffective, particularly on sensors with relatively long strips.

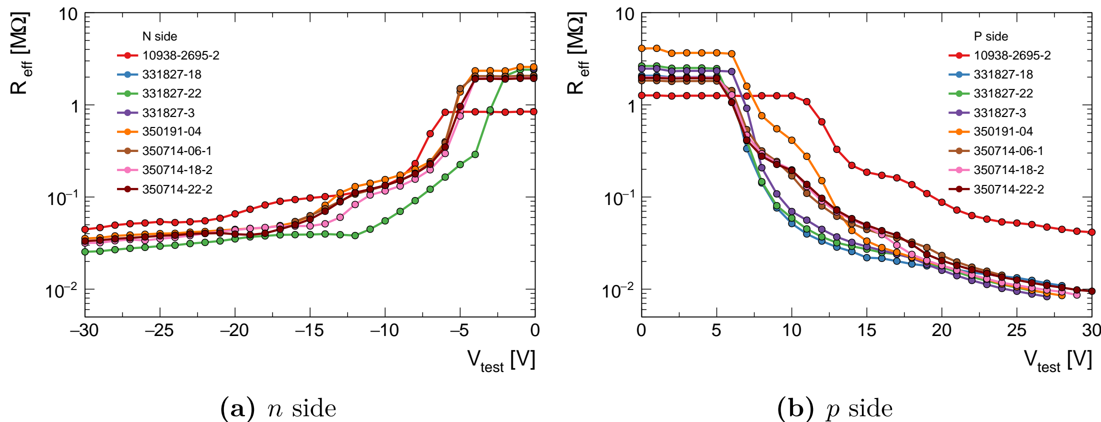

(a) n side

(b) p side

Figure 4.39.: Effective resistance R_{eff} as a function of the test voltage for all investigated CBM06 sensors. Measurements were performed at $V_{bias} = \pm 100\,\mathrm{V}$. Only one Hamamatsu sensor is presented. It has higher V_{PT} on both sides than CiS sensors.

4.2.4. Metal Strip Resistance

The upper electrode of the coupling capacitor of the microstrip sensor is formed by a metal strip. It is produced by deposition of aluminum on top of a patterned dielectric layer. The AC pads of the metal strips allow for connection to the readout electronics. The series resistance R_m of the metal strip is a source of thermal noise. The corresponding equivalent noise charge is:

$$ENC^2_{R_s} \sim 1/\tau_p \cdot k_B T R_m \tag{4.29}$$

where τ_p is the peaking time, k_B is the Boltzmann constant, T is the operating temperature [81]. A low series resistance is required to minimize noise. It is particularly important for the CBM sensors due to the short peaking time of STS-XYTER[37]. Noise performance studies of the STS set the requirement that R_m does not exceed $10.5\,\Omega/\mathrm{cm}$ [81].

The resistance R_m depends on the geometrical parameters of the strip:

$$R_m = \rho_{\mathrm{Al}} \frac{L}{w_m t_m} \tag{4.30}$$

where $\rho_{\mathrm{Al}} = 2.82 \times 10^{-6}\,\Omega\,\mathrm{cm}$ is the aluminum resistivity, w_m, t_m, L are width, thickness and length of the metal strip, respectively. Width and length are fixed by the design of the CBM sensors. The thickness of the metal layers can be changed to adjust the resistance if necessary.

Measurements were performed on the CBM06 prototype sensors to determine the resistance of the metal strips and its compliance with the CBM specification.

[37]Each channel of the STS-XYTER readout chip includes slow and fast shapers with peaking times of 90 ns and 40 ns, respectively [137].

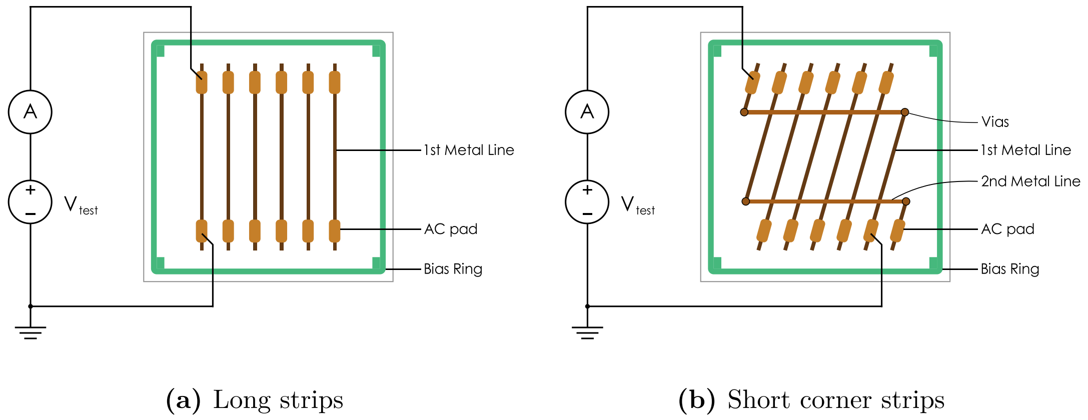

(a) Long strips

(b) Short corner strips

Figure 4.40.: Connection schemes for the metal strip resistance measurement on the CBM microstrip sensors: (a) the case of long strips on the p and n sides; (b) the case of short strips on the p side connected by the 2nd metal lines.

Measurement method

The resistance of the metal strip is measured between two AC pads located at opposite ends of the strip. Measurements have to be performed for long strips and short corner strips of the CBM sensors. The short strips on the p side have only one AC pad. Therefore, the measurement is performed between the AC pads of two short strips that are connected by the 2nd metal line. The total resistance of the 1st and 2nd metal strips is:

$$R_{ss} = R_m + R_{2m} \tag{4.31}$$

where R_{ss} is the measured total resistance, R_m is the resistance of the 1st metal strip and corresponds to the resistance of the long strip, R_{2m} is the resistance of the 2nd metal line. The connection schemes are shown in Fig. 4.40 for both types of strips. A microstrip sensor requires no biasing for this type of measurement.

Two-wire and four-wire methods can be used to measure resistance. The four-wire method[38] is preferred when measuring low resistances, especially $< 10\,\Omega$. The expected resistance of the metal strip of the CBM sensors is in the range of 20–300 Ω depending on the length of the strip. In this work, the two-wire method was used due to the established fast switching configuration. IV curves are measured to get rid of various offsets. One voltage source and one ammeter are required. The test voltage is applied in steps of 10 mV from 0 V to 100 mV and the induced current is measured. An example of the IV curve for one strip of the CBM06H4 sensor is shown in Fig. 4.41. A straight line is fitted to the data points and the resistance is extracted from the slope. Oxide films or incomplete removal of the dielectric layer over the AC pads can result in non-ohmic contacts. Usually, it manifests itself in a non-linear IV curve.

[38]Kelvin sensing.

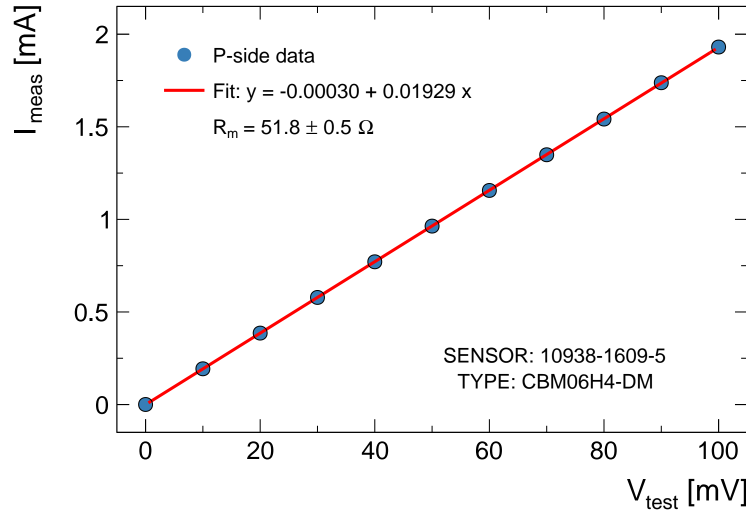

Figure 4.41.: Strip metal resistance measurement: IV curve for one strip of the CBM06H4 sensor. Resistance is extracted from the slope of a straight line fitted to the data points. The result includes the resistance of the test leads.

When measuring low resistance with the two-wire method, it is important to consider the series resistance of the test leads [138]. The induced current causes a small voltage drop across the resistance of the wires, probes, channels of the switching matrix. The equivalent circuit of the measurement setup is shown in Fig. 4.42. The voltage drop across the metal strip is less than the applied test voltage:

$$R_m I_{meas} + 2R_{lead} I_{meas} = V_{test} \tag{4.32}$$

where I_{meas} is the measured current, V_{test} is the test voltage at the terminals of the voltage source, R_{lead} is the total resistance of the test leads. The resistance of the metal strip is:

$$R_m = \frac{V_m}{I_{meas}} \tag{4.33}$$

where V_m is the voltage drop across the metal strip. The leakage current through the shielding of the BNC cable is negligible here. The metal strips are isolated from each other by a layer of dielectric. The offset error associated with the lead resistance was estimated by shorting the probe needles together and measuring the resulting resistance. The obtained value for the setup used is $2R_{lead} = 1.8\,\Omega$ and is subtracted from all measurements.

An LCR meter and a conventional DMM[39] were used to quickly cross-check the measured resistance. The LCR meter is configured in $R_s{-}Ph$ mode with AC voltage signal of 100 mV. An "OPEN/SHORT" zeroing of the LCR meter has to be performed before taking measurements. The DMM was mostly used to quickly check the contact reliability.

[39] Digital Multimeter.

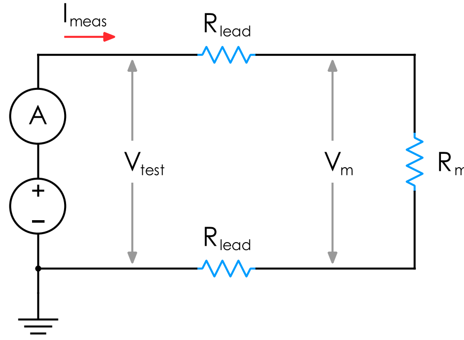

Figure 4.42.: Equivalent circuit for the metal strip resistance measurement. The resistance R_{lead} is in series with the resistance of the metal strip. The voltage drop V_m across R_m is less than test voltage V_{test} at the terminals of the voltage source.

Experimental setup

The test voltage V_{test} is supplied by a Keithley 6487 voltage source. The lowest selectable range is ±10.1 V with accuracy of 0.1 %+1 mV, according to the device's accuracy specification [104]. The induced current is measured by a Keithley 6487 picoammeter. For a maximum $V_{test} = 100\,\text{mV}$ and a minimum resistance of 20 Ω, the expected maximum current is 5 mA. Therefore, 20 mA device measurement range with a default resolution of 100 nA was used for the measurements. The systematic uncertainty on the current is 0.1 % + 1 µA, according to the device measurement accuracy specification [104]. For measuring higher resistance and resistance of the 2$^{\text{nd}}$ metal lines, 2 mA current measurement range can be used which has a higher accuracy. To achieve optimal accuracy, it is recommended to zero the ammeter.

The measurements are performed using a Keithley 708B [106] switching matrix. The connection of devices is described in Section 3.3.1. Two needle probes are required to contact the AC pads of the strip. The matrix channel configuration is given in Appendix C. The matrix card path resistance is $< 1\,\Omega$ per conductor[40] according to the 7072-HV matrix card specification [107]. This resistance is taken into account in the total resistance of the leads. However, it has only been measured for the specified channel list and a new measurement is required if other matrix channels are to be used.

To position the needles at opposite ends of the strip, the travel range of the motor stages of the custom-built probe station[41] is sufficient for all CBM06 sensors except the $62 \times 124\,\text{mm}^2$ size. The maximum area of coverage is $100 \times 100\,\text{mm}^2$ by both optical and chuck motor stages. Therefore, an additional microscope was used to place the needles on the distant AC pads of the $62 \times 124\,\text{mm}^2$ sensors.

[40] At end of life of the contact, after about 1×10^7 closures, the specified resistance is $< 3.5\,\Omega$.
[41] See Chapter 3.

Results for CBM prototype sensors

Measurements were performed in manual mode for at least ten strips on each side of the sensor. Stepping through all strips in automated manner is not recommended. It is due to the different height profiles of the rows of AC pads at opposite ends of the strips. Therefore, the sensor may be damaged by the needle. It can be overcome if each probe needle moves in the Z direction. Individual height adjustment can then be implemented for each needle.

The resistance was measured for long strips as well as short corner strips connected by the 2$^{\mathrm{nd}}$ metal lines. Figure 4.43 shows the results for the 21 investigated CBM06 sensors. Uniform values of R_m were obtained for Hamamatsu sensors and for CiS sensors within separate batches. The average resistance values of the 1$^{\mathrm{st}}$ metal layer strips for n and p sides are:

$$\begin{aligned} CiS: &\ (n)18.8 \pm 1.1\,\Omega/\mathrm{cm},\ (p)17.8 \pm 2.1\,\Omega/\mathrm{cm} \\ Hamamatsu: &\ (n)13.5 \pm 0.4\,\Omega/\mathrm{cm},\ (p)13.2 \pm 0.3\,\Omega/\mathrm{cm} \end{aligned}$$

where uncertainties indicate one standard deviation. The strip-to-strip resistance variation was always below 1 %. The measured resistance R_{2m} of the 2$^{\mathrm{nd}}$ metal lines is higher than of the 1$^{\mathrm{st}}$ metal layer strips:

$$\begin{aligned} CiS: &\ 31.1 \pm 2.4\,\Omega/\mathrm{cm} \\ Hamamatsu: &\ 15.5 \pm 0.6\,\Omega/\mathrm{cm} \end{aligned}$$

The larger value for CiS sensors is explained by the smaller width of the metal. It should be noted that the length of the 2$^{\mathrm{nd}}$ metal lines is approximately 6 cm for all sensors. Therefore, the total resistance of the interconnected strips is dominated by the resistance R_{2m}.

The measured resistance does not meet the CBM specification for series resistance, which should be $\lesssim 10.5\,\Omega/\mathrm{cm}$ [81]. The only way to reduce it is to increase the thickness of the metal layer, which can be estimated according to Eq. 4.30. The metal layers on the CiS sensors are 0.76 µm and 0.65 µm thick on the n and p sides, respectively. It is 0.97 µm on both sides of the Hamamatsu sensors. To meet the specification for series resistance, the thickness of the 1$^{\mathrm{st}}$ metal layer has to be increased to 1.1 µm and 1.3 µm for the p and n sides of the CiS sensors, respectively. Because of the narrower metal strips, it has to be increased to 1.2 µm for Hamamatsu sensors. The thickness of the 2$^{\mathrm{nd}}$ metal layer is 0.77 µm and 0.92 µm for CiS and Hamamatsu sensors, respectively. While the same thickness increase as for 1$^{\mathrm{st}}$ metal layer is necessary for Hamamatsu sensors, the width of the 2$^{\mathrm{nd}}$ metal lines has to be increased for CiS sensors as well as thickness. For the final prototype sensors, it was required to increase the thickness of the metal layers to 1.5 µm in order to achieve a resistance of $\approx 9\,\Omega/\mathrm{cm}$ and minimize the corresponding noise contribution [48].

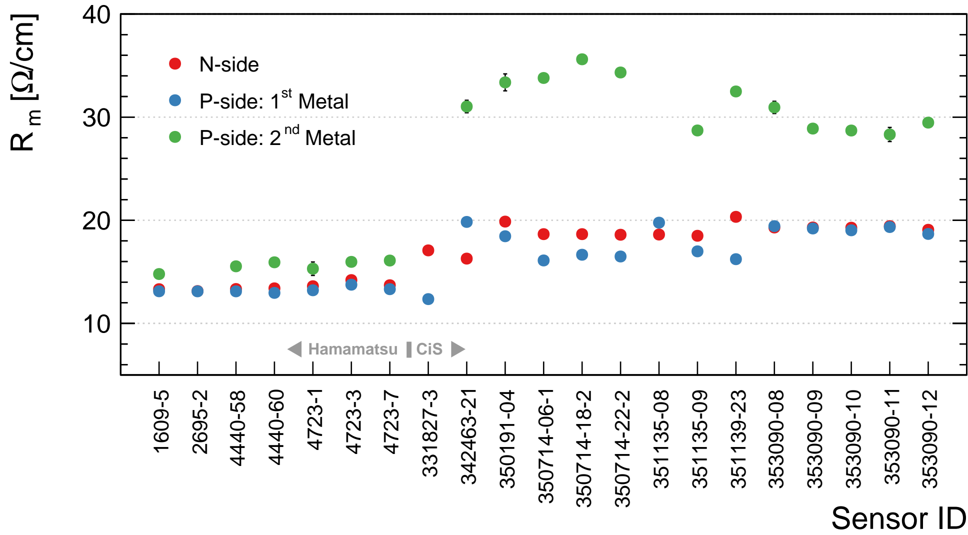

Figure 4.43.: Metal strip resistance of the investigated CBM06 prototype sensors. The metal layers of the CiS sensors are thinner than of the Hamamatsu sensors, resulting in a higher resistance. All 2nd metal lines are approximately 6 cm long for all sensors. They are twice as wide on Hamamatsu sensors compared to CiS sensors.

4.2.5. Strip Coupling Capacitance

The charge released by the ionizing particle is collected by the strip implant and capacitively coupled to the metal strip. The coupling capacitors are integrated into the design of the microstrip sensor. The capacitor is formed by an implant and a metal strip with a dielectric layer between them. Silicon oxide SiO_2 is used as a standard material. Today, a double-layer structure with a second layer of silicon nitride Si_3N_4 is a common choice. It allows to achieve high capacitance values, and increase the breakdown voltage and yield, as was shown, for example, in Ref. [139]. The total dielectric thickness is about 200 nm, which gives high capacitance values of about 1.3 pF/cm per µm width [112].The Si_3N_4 layer is usually removed from the interstrip gap, as there have been observations of an increase in the surface generation current, which negatively affects the interstrip resistance [140].

A single strip within a silicon sensor is not an isolated structure, but forms a capacitive network to other strips, as well as to the sensor backplane. Therefore, the collected charge is divided between these capacitances. In a simple approximation, the amount of charge induced on the metal strip can be estimated as:

$$Q_{metal} = Q_{collected} \frac{C_c}{C_c + C_{tot}} \tag{4.34}$$

where C_c is the coupling capacitance and C_{tot} is the total strip capacitance[42]. In

[42]See Section 4.2.9 for details.

order to ensure that a sufficient fraction of the charge is coupled to the readout circuit, C_c must be much larger than C_{tot}. Detailed studies of the total collected and integrated charge were conducted in Ref. [57] for CBM sensors.

High values of the coupling capacitance imply the production of very thin dielectric layers. It reduces voltage tolerance and increases the probability of local defects like "pinholes". Operation in a high multiplicity environment requires high integrity of the coupling capacitors. In addition, uniform capacitance values across all strips will ensure uniform charge collection.

This section focuses on the measurement of the coupling capacitance to determine the actual capacitance between the metal strip and the implant. Systematic measurements of the coupling capacitance for all strips of the CBM sensors have not been performed before. In addition, this measurement is sensitive to defects such as pinholes, shorts, and breaks[43]. The electrical reliability and yield of the coupling capacitors are discussed in Section 4.3.1.

Measurement method

The coupling capacitance is measured between the implant and the metal strip. Two measurement configurations are extensively used in this work. In the first case, two needles contact the DC and AC pads of the strip. This configuration will be referred to as AC-DC one. In the second case, one of the needles contacts the bias ring instead of the DC pad. This configuration will be referred to as AC-BR one.

The connection schemes are shown in Fig. 4.44. The impedance of the circuit is measured with an LCR meter. A three-terminal connection technique is used. The *HI* terminal of the LCR meter is in contact with the DC pad or bias ring of the sensor according to the selected configuration, while its *LO* terminal is connected to the AC pad of the strip. The terminals of the LCR meter are isolated from the strip DC current by capacitors $C_{iso} = 1\,\mu F$. Even though, this is not necessary for its *LO* terminal, a decoupling capacitor was used to simplify the overall circuit design. The measuring side of the sensor is kept at ground (low) potential. In the AC-BR configuration, $R_{iso} = 1\,M\Omega$ is introduced between the bias ring and the *LO* terminal of the bias voltage source. The additional voltage drop across R_{iso} has to be taken into account when biasing the sensor. The role of the guard terminal of the LCR meter is to remove any stray path that may affect the measurement. All connections are made using a coaxial cable. The *LO* terminal of the bias voltage source and the cable shields are connected to the guard terminal (GND).

Neighboring strips remained floating during all measurements. Their contribution to the measured capacitance was found to be negligible. A 0.1 % difference is reported in Ref. [59] when comparing results without and with grounding of up to

[43] A description of the types of defects is given in Section 6.3.

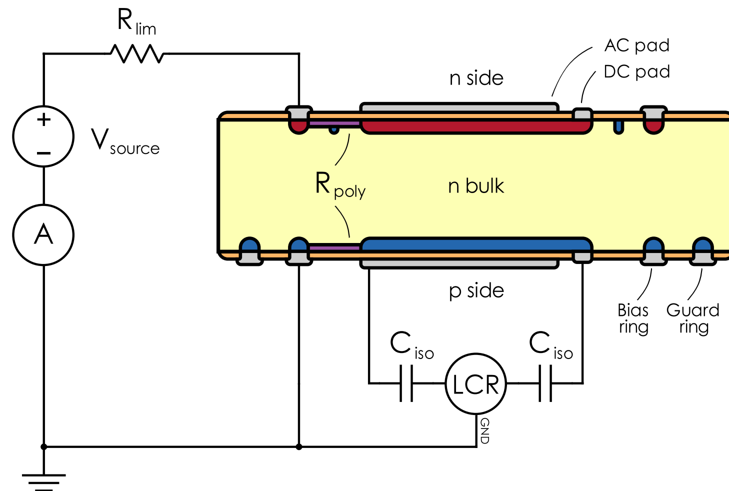

(a) AC-DC

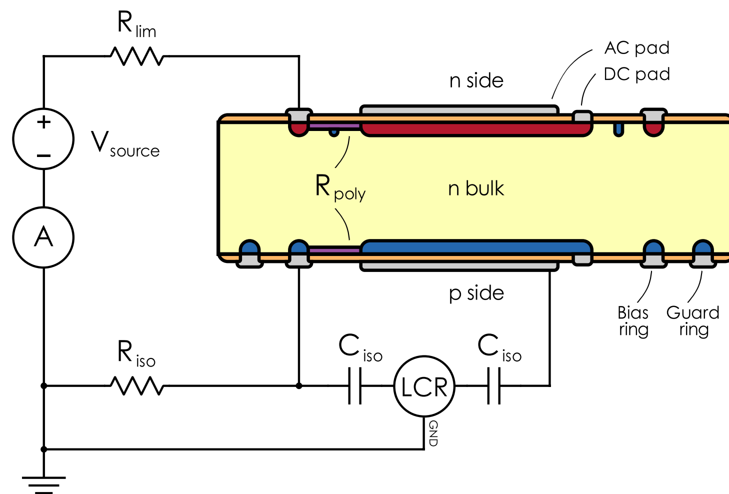

(b) AC-BR

Figure 4.44.: Connection schemes for measurement of the coupling capacitance of one strip. Two configurations are used in this work: AC-DC and AC-BR. The *HI* terminal of the LCR meter applies a sinusoidal voltage signal at the DC pad or bias ring, depending on the selected configuration. The *LO* terminal of the LCR meter is connected to the AC pad of the strip to measure the induced current. The *LO* terminal of the bias voltage source and the cable shields are connected to the guard terminal of the LCR meter. In the AC-BR configuration, resistor $R_{iso} = 1\,\mathrm{M\Omega}$ isolates the bias voltage source from the AC current. Decoupling capacitors C_{iso} block the strip DC current.

four neighbors on each side of the measured strip[44]. If the bias ring is not guarded and all ground paths are eliminated, then neighboring strips will contribute to the measured capacitance. Given that strip coupling capacitance is much larger than other strip capacitances, this contribution will be mostly determined by the coupling between neighboring metal strips:

$$C_m = C_c + 2\left(\frac{1}{C_c} + \frac{1}{C_{is}^{DC}} + \frac{1}{C_{is}^{AC}}\right)^{-1} \approx C_c + 2C_{is}^{AC} \tag{4.35}$$

where C_{is}^{DC} is the capacitance between the implants of the strip and C_{is}^{AC} is the capacitance between the metal strips[45].

Three types of measurements are performed:

- Capacitance-Voltage characterization — measurement of the coupling capacitance as a function of bias voltage at a fixed frequency of the test signal. The bias voltage is increased in steps of 5 V up to 200 V, and the capacitance and phase angle are recorded after a delay of about 5 s.
- Capacitance-Frequency characterization — measurement of the frequency dependence of the coupling capacitance at a fixed bias voltage. A logarithmic frequency sweep of 44 points from 100 Hz to 2 MHz is used. Capacitance and phase angle are recorded at each step.
- Strip-by-strip measurement of the coupling capacitance at fixed frequency and bias voltage, for all 1024 strips on each side of the sensor. In the AC-DC configuration, a frequency of 1 kHz was used for all sensors. In the AC-BR, lower frequency was used depending on the sensor being measured.

Capacitance model

The equivalent circuit of the capacitor consists of an ideal capacitance C, a parallel resistance R_p, a series resistance R_s, and an inductance L. Since the LCR meter assumes a two-component model, measurements in series or parallel mode may give different results. The measured capacitance is closer to the actual value if the appropriate model is used. The impedance magnitudes of the relevant components have to be considered to select one.

Typical coupling capacitance values are $O(100\,\text{pF})$. This is usually considered a high impedance, and the $C_p - R_p$ model is suggested to measure the capacitance [141]. However, the strip cannot be considered an ideal capacitor with low R_s. The resistance R_p of the dielectric layer represents its leakage and is in the GΩ range. The reactance of a 100 pF capacitor at a typical measurement frequency of 1 kHz is 1.59 MΩ. The implant, one of the electrodes of the coupling capacitor,

[44] It should be noted that the results reported in Ref. [59] are for CBM sensor of earlier versions, which have some differences in layout compared to sensors of the CBM06 type.

[45] See Section 4.2.7.

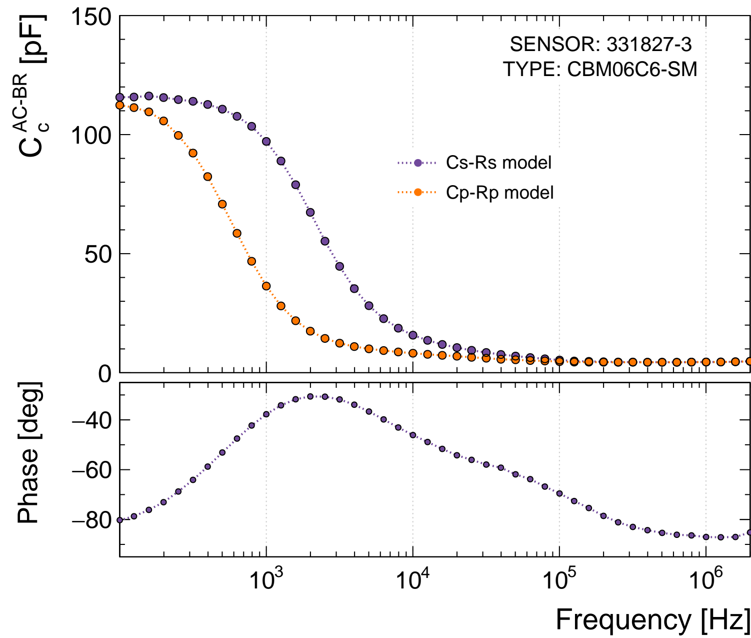

Figure 4.45.: Frequency dependence of the coupling capacitance measured in the AC-BR configuration on the CBM06C6 sensor. Capacitance representations with series and parallel models are compared. The phase angle does not depend on the choice of model. The measurements were performed at a bias voltage of 70 V.

constitutes a series resistance R_s from tens of kΩ to several MΩ. It is comparable with the reactance X_c of the coupling capacitor at the measurement frequencies. Therefore, in the AC-DC configuration, the C_s–R_s model is more suitable. In the AC-BR configuration, a MΩ polysilicon resistor in series with the strip implant increases R_s and the $C_s - R_s$ model is used again. A parallel model will give an underestimated capacitance value according to Eq. 4.13. This is especially important in the case of the AC-BR configuration, where due to the high R_s the phase angle is significantly different from $-90°$, while in the AC-DC configuration due to the low R_{imp} the phase angle is close to $-90°$ over a wide frequency range, and both models can be used safely. Some sensors may have increased contact resistance during probing, and the capacitance measured in parallel mode will be even lower. Figure 4.45 shows a comparison of the coupling capacitance measured in series and parallel modes using the AC-BR configuration. At 1 kHz the phase angle is $-37°$, and the parallel capacitance is only about 37 % of the series one.

The observed frequency dependence in Fig. 4.45 cannot be explained by a simple two-component model of a series or parallel connection of a capacitor and a resistor. To understand it, the strip should be considered as an object with spatially distributed capacitance and resistance. Dividing it into small sections and representing these sections as lumped elements leads to the circuit model shown in Fig. 4.46. It consists of cascaded RC stages of $r_{imp} = R_{imp}/N$ in series

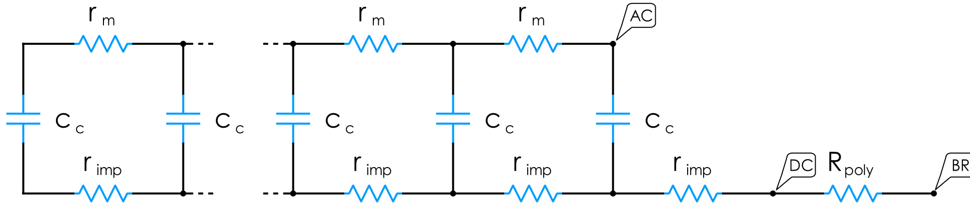

Figure 4.46.: Equivalent circuit of one strip, where physically distributed capacitance and resistance are represented as a series combination of *RC* stages. The *AC* and *DC* labels indicate the connection points to the AC and DC pads. The *BR* label indicates a bias ring.

with $c_c = C_c/N$, where N is the number of sections. Each stage attenuates the input signal according to the voltage divider relationship:

$$V_{out} = V_{in}\frac{Z_c}{Z_r + Z_c} = V_{in}\frac{1}{1 + j\omega r_{imp}c_c}. \tag{4.36}$$

This circuit is, in fact, a low-pass filter. At low frequency, the reactance X_c is high, and the whole strip is probed. At high frequency, X_c is like a short circuit for the signal, and the measured capacitance is reduced. The low-pass filter is characterized by a corner frequency $2\pi f_c RC = 1$. It can be concluded, that the coupling capacitance has to be measured at frequencies lower than f_c, which roughly corresponds to the inflection point of the CF curve:

$$f < \frac{1}{2\pi R_s C_c} \tag{4.37}$$

where R_s is defined by the implant resistance R_{imp} in the AC-DC configuration and by the polysilicon resistance R_{poly} in the AC-BR configuration.

The examined frequency dependencies for CBM06 sensors of all sizes from both vendors are shown in Fig. 4.47. As expected, the corner frequency is lower when measured in the AC-BR configuration. At high frequencies in the AC-DC configuration, the CF curves converge, which is expected due to same values of R_{imp} and C_c per cm. There is a significant offset at low frequencies between the CF curves measured in the AC-DC and AC-BR configurations. In particular, this is noticeable for Hamamatsu sensors in addition to the overall smaller capacitance values compared to CiS. This cannot be explained by different corner frequencies or a certain measurement mode. Therefore, the electrical circuit of the strip has to be considered in more details to understand what is actually being measured.

Measured capacitance

The principle of operation of the LCR meter is based on the measurement of the current I_m flowing through the device, the voltage V_m across it and the phase

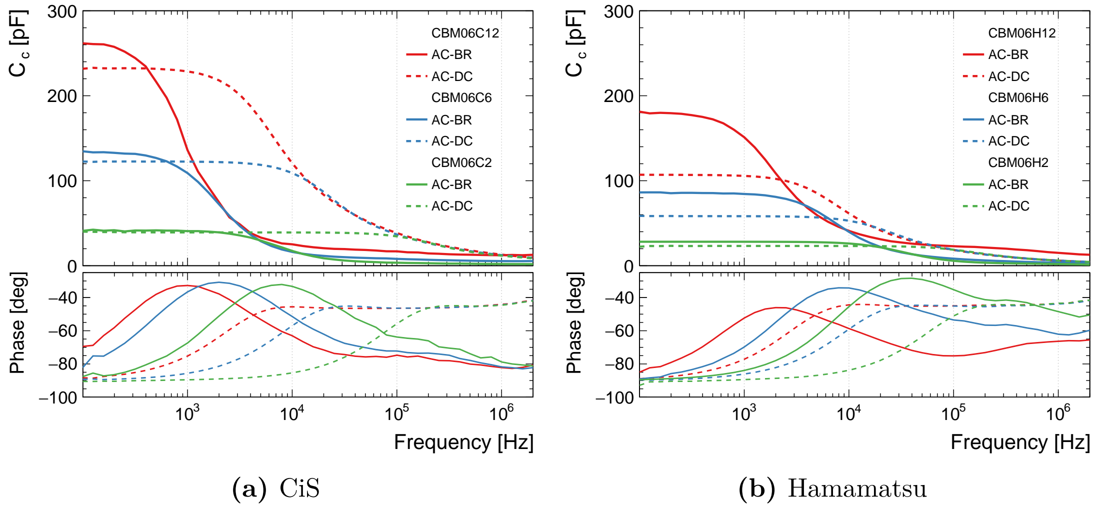

(a) CiS

(b) Hamamatsu

Figure 4.47.: Frequency dependence of the coupling capacitance measured on the p side of CBM06 sensors of different sizes using the $C_s - R_s$ model. Two configurations are compared: AC-DC and AC-BR. Hamamatsu sensors have a lower coupling capacitance due to design. The measurements were performed at $V_{bias} = 100\,\text{V}$.

angle between the measured current and voltage. The impedance of the device is defined by Ohm's law as the ratio of the voltage across it to the current through it. The values displayed by the LCR meter are the calculated values according to the selected two-component equivalent circuit — series or parallel. A single isolated strip is well described by the series $C_s - R_s$ model when measuring the coupling capacitance. Its equivalent circuit is shown in Fig. 4.48a, where R_m and R_{imp} are the resistance of the metal strip and the implant, and C_c is the actual coupling capacitance. Impedance of such a circuit is:

$$Z_0 = R_s + jX_s = (R_{imp} + R_m) + \frac{1}{j\omega C_s}. \tag{4.38}$$

The resistance R_m is further neglected due to its low value compared to R_{imp}. The measured capacitance of such a two-component circuit corresponds to the actual capacitance $C_s = C_c$.

Now let's consider a single strip that is connected to the bias ring of the sensor. The equivalent circuit includes a polysilicon resistor R_{poly}, as shown in Fig. 4.48b. It corresponds to the CBM06 sensor, where the DC pad and R_{poly} are at opposite ends of the implant. The measurement is performed in the AC-DC configuration. The AC and BR nodes are effectively at the same potential. The implant and polysilicon resistors form a voltage divider:

$$\frac{V_{out}}{V_{in}} = \frac{V_c}{V_m} = \frac{R_{poly}}{R_{imp} + R_{poly}} \tag{4.39}$$

where V_m is the measured voltage across the circuit, and V_c is the voltage drop across the coupling capacitor. The measured current I_m is only the current flow-

ing through C_c. This leads to a discrepancy in the measured series capacitance, as the LCR meter cannot properly account for the voltage dividing effect of the polysilicon resistor when using the series two-component model in Fig. 4.48a. The impedance of such a circuit is modified, and its associated parameters can be derived considering the three-component equivalent circuit in Fig. 4.48b. According to Ohm's law, the measured impedance is:

$$Z_m = \frac{V_m}{I_m} = \frac{V_c}{I_m} \frac{R_{imp} + R_{poly}}{R_{poly}} = \frac{V_c}{I_c} \left(1 + \frac{R_{imp}}{R_{poly}}\right). \tag{4.40}$$

The impedance of the capacitor is defined as:

$$Z_c = \frac{V_c}{I_c} = jX_c. \tag{4.41}$$

Substituting Z_c into Z_m:

$$Z_m = jX_c \left(1 + \frac{R_{imp}}{R_{poly}}\right) = \frac{1}{j\omega C_c} \left(1 + \frac{R_{imp}}{R_{poly}}\right) \equiv \frac{1}{j\omega C_m}. \tag{4.42}$$

Thus, the measured capacitance is related to the actual capacitance as:

$$C_m = \frac{C_c}{1 + \dfrac{R_{imp}}{R_{poly}}} \tag{4.43}$$

or, rearranging for the actual capacitance:

$$C_c = C_m \left(1 + \frac{R_{imp}}{R_{poly}}\right). \tag{4.44}$$

This relationship is the same as the relationship in Eq. 4.16 for the strip leakage current. Therefore, the measured coupling capacitance of a strip is always reduced compared to the series capacitance of a two-component circuit. A larger R_{imp} leads to smaller values of the measured capacitance. The voltage divider effect will be completely eliminated if there is no R_{imp} at all. Resistance measurements on the CBM sensors[46] suggest that the measured capacitance in the AC-DC configuration should be significantly lower for Hamamatsu sensors, especially on the p side. For CiS sensors, the discrepancy should be smaller and have a similar magnitude on both sides.

If all ground connections and stray paths are eliminated, R_{poly} can be considered floating and the voltage dividing effect is removed. Then the measured capacitance will be equal to the actual capacitance. However, in a real setup it turned out to be unattainable. If the current through R_{poly} goes in the ammeter,

[46] See Section 4.2.2.

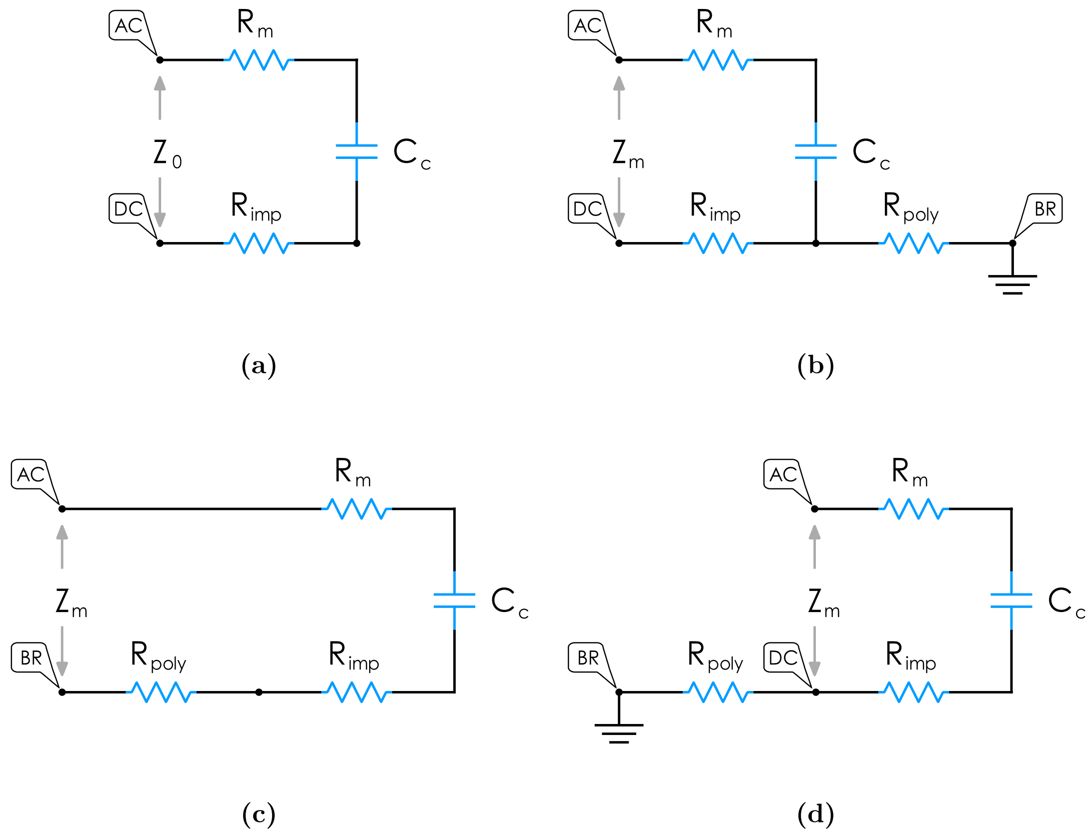

Figure 4.48.: Equivalent circuit models of a strip for estimation of the measured coupling capacitance. *AC*, *DC*, and *BR* labels correspond to the AC and DC pads and the bias ring. The measured impedance is denoted as Z_m. The following models are considered: (a) A simple two-component model which is assumed by the LCR meter; (b) Equivalent circuit of the strip in the AC-DC measurement configuration, which takes into account the features of the layout of the CBM sensors — the DC pad and the polysilicon resistor at the opposite ends of the strip; (c) Equivalent circuit of the strip in the AC-BR measurement configuration, which can be approximated by a simple two-component model; (d) Equivalent circuit of the strip in the AC-DC measurement configuration for the case where the DC pad is located near the polysilicon resistor.

then the equivalent circuit includes a parallel connection of C_c and R_{poly} with impedance:

$$Z_m = R_{imp} + \left(\frac{1}{R_{poly}} + \frac{1}{jX_c}\right)^{-1}. \tag{4.45}$$

The measured capacitance becomes frequency dependent and is defined as:

$$C_m = C_c + \frac{1}{\omega^2 R_{poly}^2 C_c}. \tag{4.46}$$

Additional capacitance in series with R_{poly} will slightly modify this dependence. In a real measurement setup, this capacitance is represented by any parasitic capacitance. Figure 4.49a shows the frequency dependencies of the coupling capacitance measured for one strip of the CBM06H4 sensor in the AC-DC configuration. Different grounding schemes were used for the bias ring and voltage source circuit. Two cases can be distinguished: the bias ring is directly grounded and not[47]. In the first case, the measured capacitance is in correspondence with Eq. 4.43 regardless of the connection method of the voltage source shown in Fig. 4.49c and Fig. 4.49e. If the ground is disconnected from the bias ring, the measured capacitance increases towards lower frequencies. It depends on the total parasitic capacitance, which is shown in gray in Fig. 4.49b, Fig. 4.49d and Fig. 4.49f. Most of it comes from the capacitance of the coaxial cables, which provides a low impedance path to the grounded shields. The frequency dependence in Fig. 4.49a corresponds to the total parasitic capacitance to the ground of about 800 pF. If the cable shields are not be guarded and the voltage source is isolated, then the current flows into the ammeter and the boundary case of Eq. 4.46 for high parasitic capacitances is reached. However, a voltage source is required to bias the sensor. Typically, it introduces about 1 nF capacitance to ground [103] if not grounded directly. Unfortunately, the situation with a perfectly isolated strip cannot be achieved in a real-world setup. Therefore, the bias ring is grounded in order to remove uncontrolled stray paths and allow the actual capacitance to be estimated in the AC-DC configuration according to Eq. 4.44.

When the coupling capacitance is measured in the AC-BR configuration, the bias ring is not grounded. Any stray impedance appears in parallel and is easily removed by connecting it to the guard terminal. The equivalent circuit can be well described by a two-component model, as shown in Fig. 4.48c. The series resistance is increased by R_{poly} and the series capacitance corresponds to the actual capacitance. Now, the offset in Fig. 4.47 is clearly explained by the relationship between the measured and actual capacitance. Therefore, the AC-BR configuration is a good approximation for measuring a single isolated strip.

Typically, the DC pad is located near the polysilicon resistor to facilitate electrical inspection. This applies, for example, to the CMS single-sided microstrip sensors [76]. Measurement of the coupling capacitance in the AC-DC configuration is well described by the equivalent circuit in Fig. 4.48d, which corresponds

[47] Referenced to the guard terminal of the LCR meter.

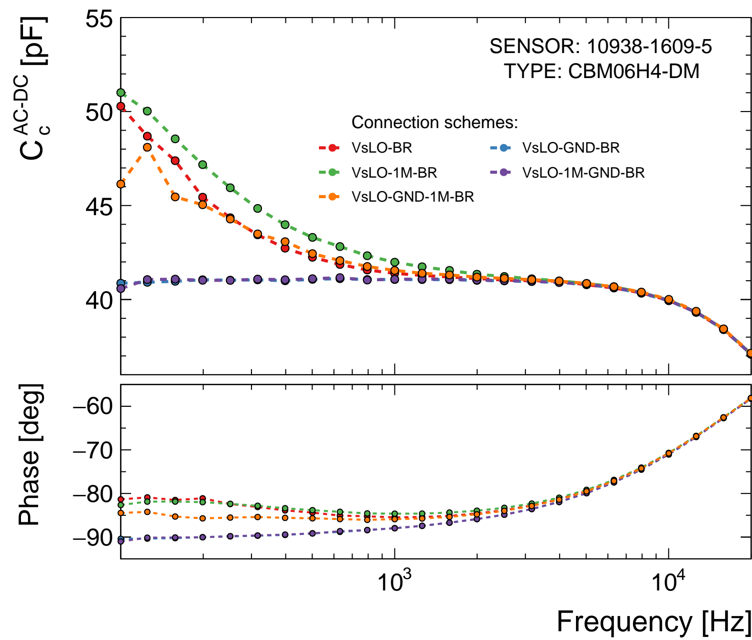

(a)

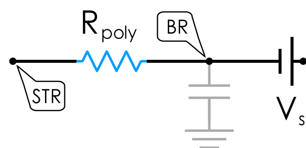

(b) VsLO-BR

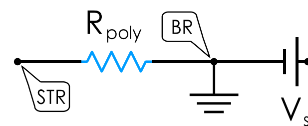

(c) VsLO-GND-BR

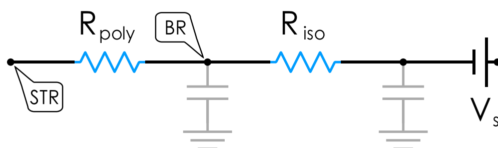

(d) VsLO-1M-BR

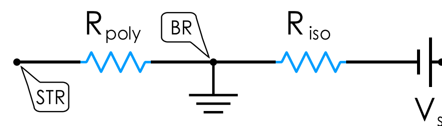

(e) VsLO-1M-GND-BR

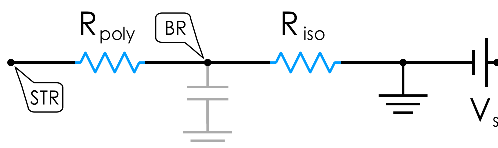

(f) VsLO-GND-1M-BR

Figure 4.49.: Frequency dependence of the coupling capacitance and the effect of grounding on its measurement. Measurements were performed on the CBM06H4 sensor in the AC-DC configuration. Labels indicate: VsLO – *LO* terminal of the voltage source, BR – bias ring, GND – ground (guard) terminal, 1M – 1 MΩ isolation resistor, STR – strip implant. The grayed-out capacitor and GND represent a stray path to the cable shield.

to a two-component series model. Therefore, the measured capacitance will correspond to the actual capacitance for sensors with this design.

The distributed capacitance and resistance along the strip further modify the capacitance measured in the AC-DC configuration. In this case, the voltage dividing effect cannot be properly described by the three-component equivalent circuit in Fig. 4.48b. A simple universal relationship between measured and actual capacitance was obtained performing SPICE simulations[48] for a wide range of C_c, R_{imp}, and R_{poly}:

$$\frac{C_m}{C_c} = \frac{a}{1 + \frac{R_{imp}}{R_{poly}}} + b \tag{4.47}$$

where $a = 0.5052$ and $b = 0.4938$ are the fit parameters. The relationship is valid for frequencies lower than the corner frequency in the AC-DC configuration:

$$100\,\mathrm{Hz} \leq f_c < \frac{1}{2\pi R_{imp} C_m} \tag{4.48}$$

where the lower limit comes from the lowest measurement frequency used. Due to low accuracy, measurements below 100 Hz were not performed. The obtained relationship was verified by performing measurements on the CMS baby-sensor from the "standard half-moon" structure[49]. Its strips have DC pads at both ends, which makes it possible to compare the measured capacitance of two different circuits. The frequency dependence of the coupling capacitance for two AC-DC configurations is shown in Fig. 4.50. Due to the low implant resistance and the short length of the strip, the observed difference is only 1.3 pF when the frequency is below corner frequency. The accuracy of the custom probe station is sufficient to distinguish such a small difference, which is perfectly described by the relationship in Eq. 4.47. At high frequencies, both CF curves converge because the voltage dividing effect becomes irrelevant.

Bias voltage dependence

The capacitance of the coupling dielectric layer does not depend on the biasing conditions of the microstrip sensor. However, the measured capacitance may depend on the electrical circuit of a particular configuration. Figure 4.51 shows the bias voltage dependence of the coupling capacitance for two $62 \times 62\,\mathrm{mm}^2$ sensors from CiS and Hamamatsu. Measurements were performed in the AC-DC configuration. The p-side capacitance does not show any dependence on the bias voltage over the entire voltage range. On the n side before full depletion, the implants are shorted through the bulk and the R_{imp}/R_{poly} ratio in Eq. 4.44 becomes large. Therefore, the measured capacitance shows low values and a phase angle of $-90°$. The 1 µF capacitor prevents short-circuiting of the HI and guard

[48] See Section 5.2 for details on the simulation model and the resulting capacitance dependence.
[49] See Section 3.3.3.1 for a description of the CMS "standard half-moon" structure.

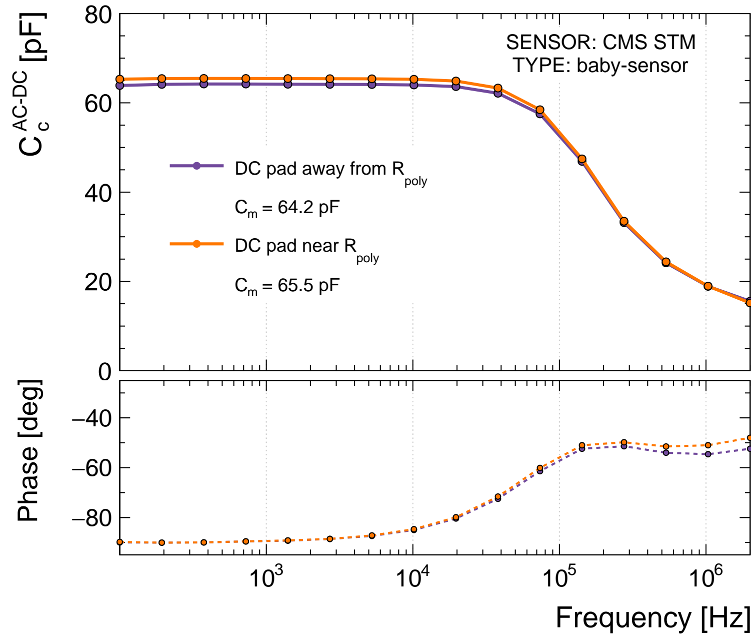

Figure 4.50.: Frequency dependence of the coupling capacitance measured in the AC-DC configuration on the CMS baby-sensor from the "standard half-moon" structure. Measurements were performed on the same strip contacting the DC pad near and away from the polysilicon resistor. The sensor was biased to 70 V. The quoted capacitance values correspond to the plateau region.

terminals of the LCR meter. At the depletion point, the implants are isolated and the expected capacitance is measured. This does not apply to the AC-BR configuration where the bias ring is not guarded.

The difference in the shape of the bias voltage dependence on the n side can be attributed to the effect of the different isolation structures used by the two vendors. CiS uses the p-spray method[50] with sufficient doping to compensate for the positive oxide charge. As a result, the interstrip gap is depleted at V_{FD}. An additional voltage is required to deplete the gap between the p-stop and the n implant of the Hamamatsu sensor. The electron accumulation layer increases the effective width of the implant, affecting the measured capacitance. In order to extract stable coupling capacitance values, strip-by-strip measurements on the n side have to be performed on fully-depleted CiS sensors and at bias voltages > 110 V on Hamamatsu sensors.

Experimental setup

A Keithley 2410 source-measure unit is used to bias the sensor under test up to 200 V and measure the leakage current of the sensor. The capacitance is

[50] Moderated p-spray method.

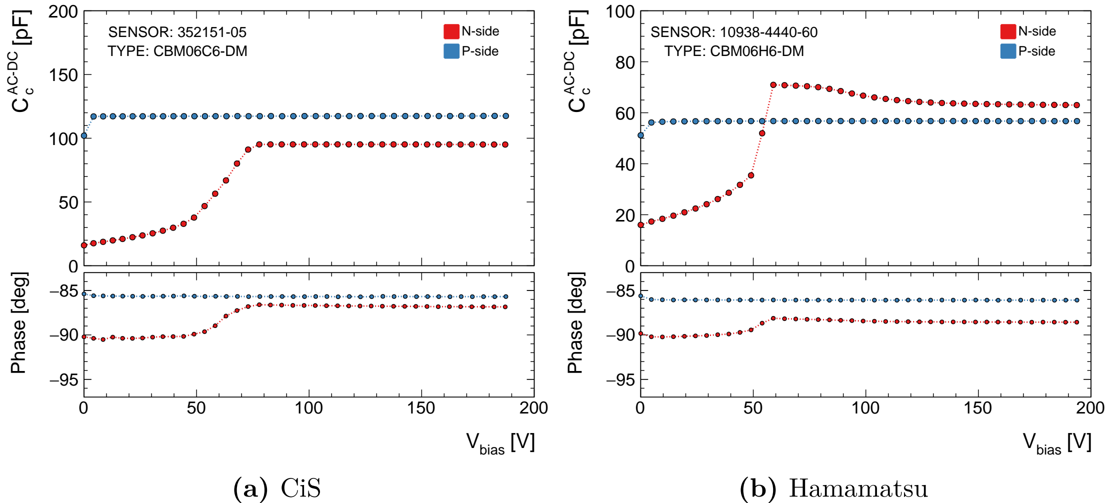

(a) CiS **(b)** Hamamatsu

Figure 4.51.: Bias voltage dependence of the coupling capacitance measured in the AC-DC configuration on both sides of the CBM06 sensors. Results are shown for two $62 \times 62\,\text{mm}^2$ sensors from both vendors. The frequency of the test signal is 1 kHz. Note the difference in vertical scale for each plot.

measured by a QuadTech 7600+ LCR meter with “slow speed” settings for CV and CF measurements, while “medium speed” is used for the strip-by-strip scan. The measurement resolution is 7 digits at any specified range. The measurement range is set to “auto”. The systematic uncertainty on the AC test signal frequency and amplitude is $0.01\,\% + 0.10\,\text{Hz}$ and $5\,\% + 1\,\text{mV}$, respectively, according to the device accuracy specification [105]. The measurements are performed using a Keithley 708B [106] switching matrix. The connection of devices is described in Section 3.3.1. The matrix channel configuration is given in Appendix C.

Similar to the other strip measurements in this work, a dedicated probe station with high positioning accuracy is used to probe and step through all strips of the sensor under test. The strips are contacted with tungsten needles with a tip diameter of 5 µm. Two needles are required to measure coupling capacitance in the AC-DC configuration. Only every second strip can be measured in one pass due to alternating location of DC pads. Measurements in the AC-BR configuration require only one needle, two needles on adjacent strips were used during strip scan to probe all strips in one pass. The corresponding channels of the matrix are closed sequentially. Figure 4.52 shows the positioning of the needles for both measurement configurations.

The compensation procedures described in Section 3.3.2 have to be performed for accurate measurement of the coupling capacitance. This includes general “OPEN/SHORT” zeroing routines. The accuracy of the measurement is very sensitive to the geometry of the connection. Therefore, spacing between the needles should remain the same for both zeroing and actual measurement. Zeroing has to be performed separately for AC-DC and AC-BR configurations. Re-zeroing

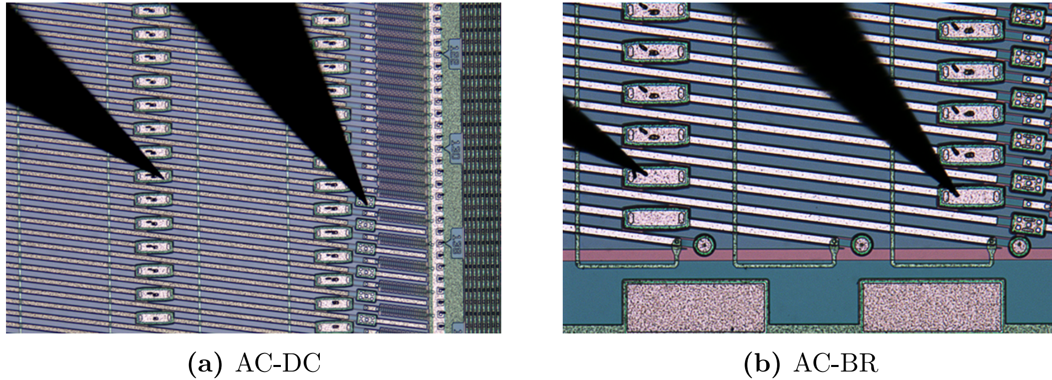

(a) AC-DC **(b)** AC-BR

Figure 4.52.: Needles placement for the coupling capacitance measurement in AC-DC and AC-BR configurations. The AC-BR configuration requires only one needle, while an additional needle is used to probe all strips in one pass. Only every second strip can be measured in the AC-DC configuration in one pass.

is required when switching between configurations. Therefore, both configurations cannot be used in the same strip scan. "GAIN" correction applies only to the high frequency region of the CF curves and is not required for regular strip scan.

Results for CBM prototype sensors

The CBM specification requires all sensors to have a coupling capacitance greater than 10 pF/cm [48]. Calculated values are around 25 pF/cm for CiS sensors using the parallel-plate capacitor approximation and the thickness of the dielectric layer specified in Ref. [64]. Hamamatsu does not disclose the thickness. The Hamamatsu sensors are expected to have lower values due to narrower implants for the same dielectric layer thickness[51].

The capacitance was measured for a total of 9 Hamamatsu and 23 CiS sensors of all sizes, resulting in 65 536 probed strips. Figure 4.53 shows the measured capacitance of the investigated CBM06 sensors from both vendors. The measurements were performed using both configurations and AC-DC gives lower values as expected. Overall, the capacitance profile is very uniform for all sensors. Significantly scattered values were obtained for the CiS $62 \times 124\,\mathrm{mm}^2$ sensor in the AC-BR configuration. It can be attributed to too high a test frequency and poor contact due to insufficient removal of the passivation layer at the AC pads. Vertical spikes indicate defective strips, particularly broken and with pinholes, and are discussed in detail in Chapter 6.

The p side has short strips in the two opposite corners of the sensor. Two short strips are connected by a 2$^{\text{nd}}$ metal line. In the AC-BR configuration they exhibit higher capacitance due to the additional contribution of the 2$^{\text{nd}}$ metal layer[52]. A bell-shaped capacitance profile for short strips was observed for some

[51] The width of the implant on Hamamatsu sensors is 10 µm, and it is 20 µm on CiS sensors.
[52] See Section 4.2.8 for details.

CiS sensors. It turned out that the strip-by-strip measurements for these sensors were performed above the corner frequency. As a result, depending on the length of the short strip, a reduced capacitance was measured. If the frequency is low enough, then a uniform profile for short strips is obtained.

The obtained coupling capacitance values for all sensors are summarized in Fig. 4.54. Each data point represents the average of 1024 strips for each side of the sensor. The error bars indicate one standard deviation. The measurement uncertainties are discussed in more detail in the next subsection. Although the raw AC-DC capacitances have much lower values, the values calculated using Eq. 4.47 are consistent with the AC-BR values for most sensors. Deviations may be associated with not optimal measurement conditions, in particular the choice of frequency. The sensors from batch 352151 have high R_{poly} values, resulting in a difference of only 3 % between measured and calculated AC-DC values. Even better agreement is obtained for the $62 \times 22\,\mathrm{mm}^2$ sensors from batch 350714, where the short implants lead to a small R_{imp}/R_{poly} ratio. While the 353090-10 sensor shows agreement in capacitance values, sensors from the same batch have significantly lower calculated AC-DC capacitance on the p side. It is due to the observed low interstrip resistance of these sensors, which is not taken into account in Eq. 4.47.

The average coupling capacitance values for the n and p sides of the CBM06 prototype sensors obtained in the AC-BR measurement:

$$\begin{aligned} CiS:&\ (n)17.9 \pm 2.1\,\mathrm{pF/cm},\ (p)21.7 \pm 1.8\,\mathrm{pF/cm} \\ Hamamatsu:&\ (n)14.1 \pm 0.1\,\mathrm{pF/cm},\ (p)14.5 \pm 0.2\,\mathrm{pF/cm} \end{aligned}$$

and calculated from the results of the AC-DC measurements:

$$\begin{aligned} CiS:&\ (n)18.7 \pm 2.1\,\mathrm{pF/cm},\ (p)21.4 \pm 2.1\,\mathrm{pF/cm} \\ Hamamatsu:&\ (n)13.1 \pm 0.6\,\mathrm{pF/cm},\ (p)13.9 \pm 0.2\,\mathrm{pF/cm} \end{aligned}$$

where the uncertainties represent one standard deviation. The resulting capacitance values satisfy the CBM specifications for microstrip sensors. They are also in fair agreement with the parallel-plate capacitor model. The total strip capacitance[53] is estimated to be around 1.1 pF/cm and 1.5 pF/cm for the Hamamatsu and CiS sensors, respectively. The measured values of C_c are high enough relative to C_{tot} to ensure that most of the signal charge goes to the readout electronics.

Uncertainties

Uncertainties in the measurement of coupling capacitance arise from many sources, including random errors, systematic errors related to the measurement setup (LCR-meter accuracy, cabling) and sensor characteristics (frequency and voltage dependence), etc. The considered error sources are:

[53]See Section 4.2.9.

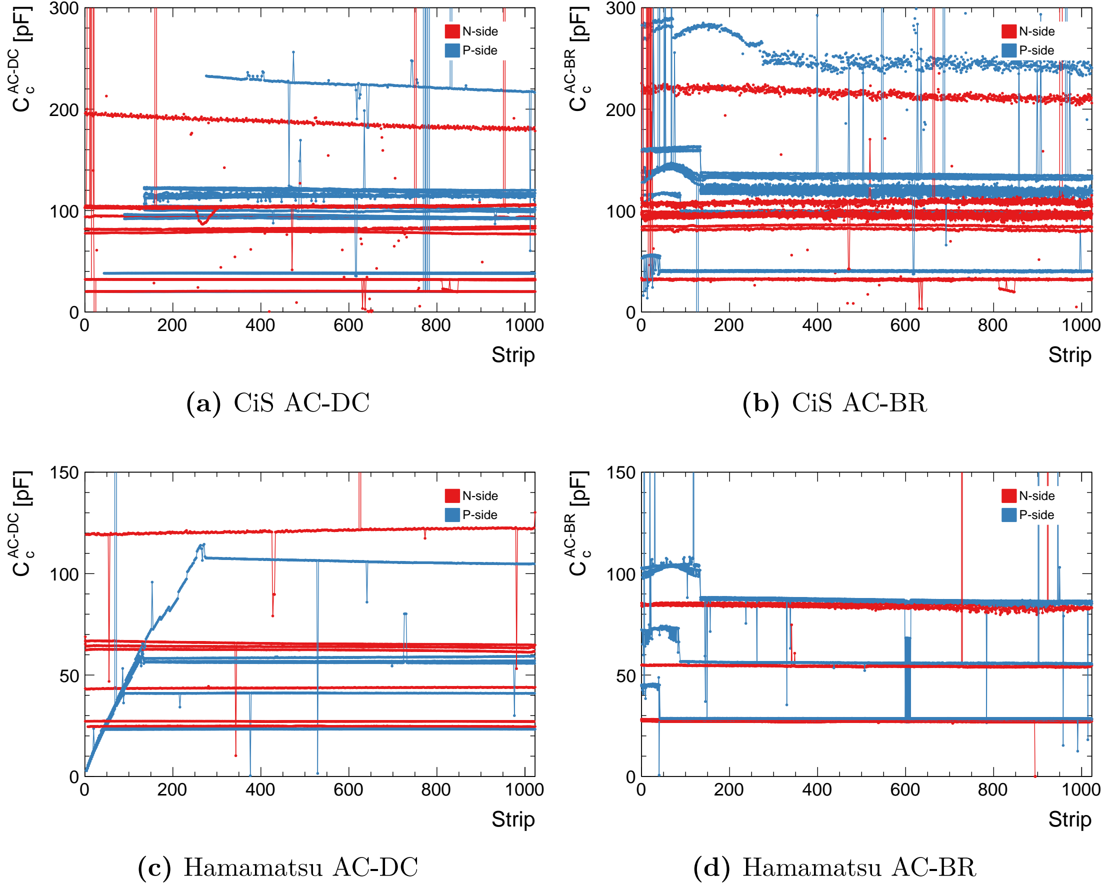

(a) CiS AC-DC

(b) CiS AC-BR

(c) Hamamatsu AC-DC

(d) Hamamatsu AC-BR

Figure 4.53.: Measured coupling capacitance C_m of the 32 investigated CBM06 prototype sensors of all sizes: both CiS and Hamamatsu are shown. Measurements were performed on both sides of the sensor. AC-DC and AC-BR indicate the measurement configuration. The data for CiS $62 \times 124\,\mathrm{mm}^2$ sensor are plotted without interconnecting lines due to the large number of defects. The short strips on the p side of the CiS sensors were not measured in the AC-DC configuration due to the special arrangement of the DC pads. The short strips on the p side in the AC-BR configuration show a higher capacitance due to the contribution of the 2$^{\mathrm{nd}}$ metal layer.

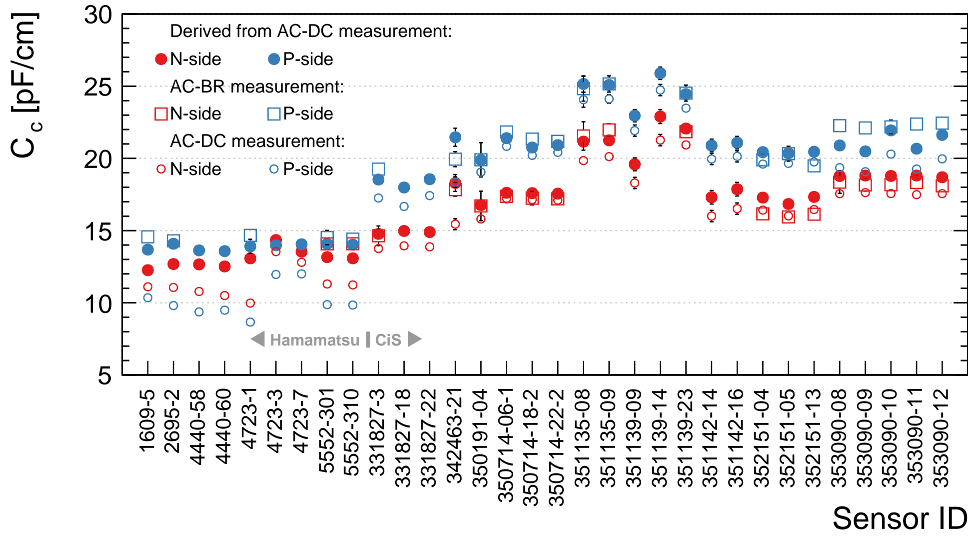

Figure 4.54.: Coupling capacitance of the investigated CBM06 prototype sensors. Each data point represents the average of 1024 strips on one side of the sensor. The error bars indicate one standard deviation. Direct measurement in the AC-BR configuration is compared to a capacitance estimated from the AC-DC measurement using Eq. 4.47. The raw AC-DC data are also shown for comparison. Values are normalized to the length of the strip.

- The random error due statistical fluctuations was estimated by repeating the measurements of the same strip several times. The measured values were always normally distributed with a standard deviation of about 10 fF, which indicates high measurement precision. A typical distribution at a frequency of 1 kHz is shown in Fig. 4.55a.

- The error due to the contact resistance can be estimated by repeating the measurement after lifting needles up and down on the contact pads. The measured capacitance was always within the quoted precision, which indicated no problems due to contact resistance.

- The accuracy of an LCR meter depends on the measured impedance and phase angle and was estimated for each measurement using the equation from the device's measurement accuracy specification [105]. The accuracy at 1 kHz was 1.5 % and 0.1 % for the lowest and highest measured C_c values of 30 pF and 280 pF, respectively. At lower frequencies, the accuracy of the LCR meter degrades dramatically.

- Cabling, needles, switching matrix introduce a huge stray impedance between the instrument's calibration plane and the microstrip sensor. To ensure the above accuracy values, "OPEN/SHORT" compensation procedures are performed. A typical open-circuit capacitance after zeroing is

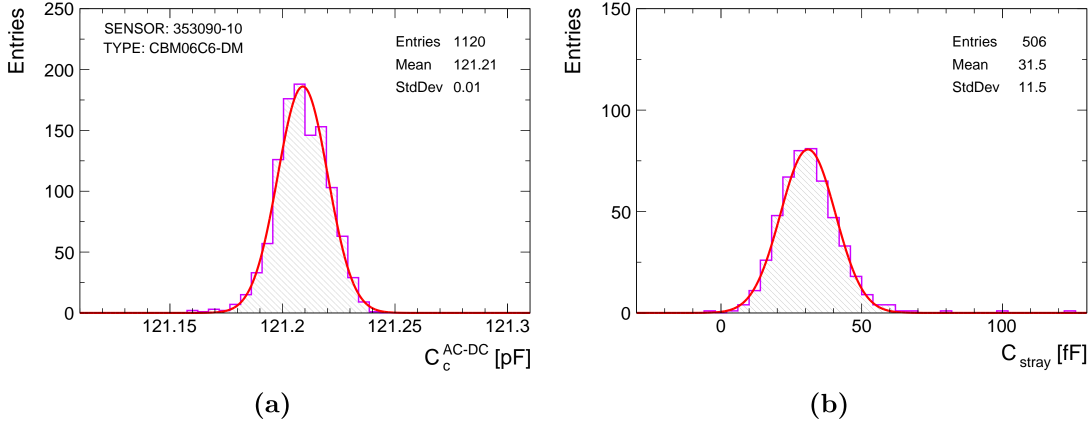

(a) **(b)**

Figure 4.55.: (a) Normal distribution of coupling capacitance of a single strip and (b) stray capacitance of an open circuit measured in AC-DC configuration. The frequency of the test signal is 1 kHz. Note the different unit prefix in each plot.

shown in Fig. 4.55b. It was always below 100 fF at 1 kHz for the specified circuit configuration.

- The accuracy of an LCR meter depends on the dissipation factor D of the capacitor. In the AC-BR configuration, the accuracy is reduced because the phase angle differs from $-90°$ and hence the dissipation factor becomes large. Accuracy has to be multiplied by $\sqrt{1 + D^2}$ if $D > 0.1$.

- The high-frequency gain error is irrelevant for the coupling capacitance. A correction procedure applied to CF curves is discussed in Section 3.3.2.

- The systematic error due to floating neighboring strips was assumed to not exceed 0.1 %. In the AC-DC configuration, their effect is removed by guarding the bias ring.

- A systematically lower capacitance is measured in the AC-DC configuration due to the discussed voltage dividing effect of R_{imp}/R_{poly}. It was studied using SPICE simulations and a correction is applied according to Eq. 4.47. The propagated uncertainty is about 2 %.

- A systematic error for Hamamatsu sensors might be caused by a biasing condition. The strip-by-strip measurements in the AC-BR configuration were performed at 100 V, which gave a 1–2 pF larger capacitance on the n side. Refer to Fig. 4.51 for detailed information on bias voltage dependence.

- A significant systematic error might arise due to sub-optimal frequency settings, especially in the AC-BR configuration. Higher frequencies are preferred because of the increased accuracy of the LCR meter. However, it should not exceed the corner frequency, which can be lower than 1 kHz for

$62 \times 124\,\text{mm}^2$ sensors. The corresponding error is undefined until the CF curve is measured.

- The presence of the 2nd metal layer on the p side gives a systematic contribution to the measured C_c. For regular long strips, it is about 1 %. Short strips show 15–30 pF higher measured capacitance compared to long strips as shown in Fig. 4.53.

In most cases, the measurement uncertainty does not exceed 1–2 % and is dominated by the accuracy of the LCR meter. The situation can become much worse if the systematic effects mentioned above are not properly taken into account. Therefore, special attention should always be paid to the electrical circuit and the measurement conditions.

4.2.6. Strip Backplane Capacitance

The strip backplane capacitance is the capacitance of one strip implant to the opposite side of the sensor. It contributes to the total strip capacitance[54], and therefore has to be accurately determined. In a typical sensor with a pitch of 50 µm and a thickness of about 300 µm, its contribution to C_{tot} is less than about 20 % [142].

The most convenient way to estimate the strip backplane capacitance is to measure global CV characteristic, where the sensor bulk capacitance is measured as a function of reverse bias voltage. Bulk capacitance is the capacitance of all strips to the backplane of the sensor. In the first-order approximation, the strip backplane capacitance C_b can be estimated as:

$$C_b = \frac{C_{bulk}}{N_{strips}} \tag{4.49}$$

where C_{bulk} is the bulk capacitance of the sensor, N_{strips} is the number of strips on the measured side. For CBM06 sensors, $N_{strips} = 1024$ on each side.

Measurement method

The measurement of the strip backplane capacitance is similar to the measurement of the bulk capacitance, described in Section 4.1.3. The connection scheme is shown in Fig. 4.56. The voltage source is connected to the bias rings of the p and n sides of the sensor. The measured side is kept at the ground potential. The impedance is measured by the LCR meter. A three-terminal connection technique is used. The *LO* terminal of the LCR meter is connected to the DC pad of the strip, and its *HI* terminal is connected to the bias ring on the backside. This configuration will be referred to as DC-BP. It is necessary to connect the guard

[54] See Section 4.2.9.

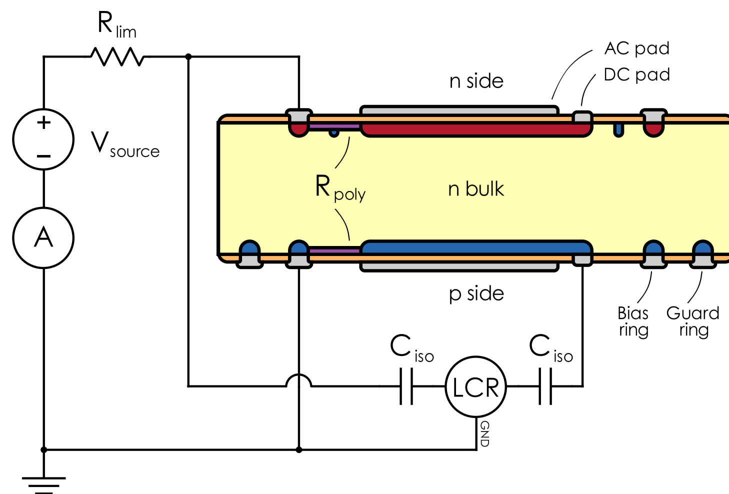

Figure 4.56.: Connection scheme for measurement of the strip backplane capacitance. The *HI* terminal of the LCR meter supplies a test signal to the bias ring on the opposite side, and its *LO* terminal is connected to the DC pad of the strip. The capacitors C_{iso} block the sensor DC current from feeding into the LCR meter.

terminal to the bias ring on the side where the strip is probed. Otherwise, the full bulk capacitance will be measured. To avoid interference between the bias voltage source and the LCR meter, decoupling capacitors C_{iso} and resistor R_{lim} are used in the circuit. The requirements and their nominal values are described in Section 4.1.3. It is important to consider the voltage drop across R_{lim} when biasing the sensor. No additional resistor is needed at the *LO* terminal of the voltage source, as this will only result in an additional voltage drop.

Two types of measurements are performed:

- Capacitance-Voltage characterization — measurement of the strip backplane capacitance as a function of bias voltage at a fixed frequency of the test signal. The bias voltage is increased up to 200 V in steps of 5 V, and the capacitance and phase angle are recorded after a delay of about 5 s.

- Capacitance-Frequency characterization — measurement of the frequency dependence of the strip backplane capacitance for a fully depleted sensor. A logarithmic frequency sweep of 44 points from 100 Hz to 2 MHz is used. Capacitance and phase angle are recorded at each step.

Capacitance model

The impedance magnitude of the surrounding components have to be taken into account to select the appropriate model for the strip backplane capacitance measurement. The sensor is assumed to be biased beyond the full depletion point, so its bulk capacitance is minimized. The expected values of C_b for CBM06 sensors

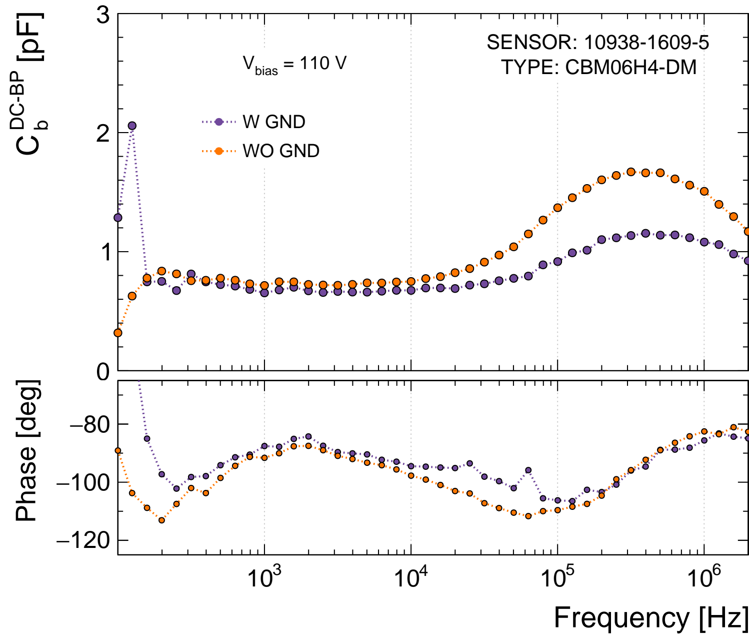

Figure 4.57.: Frequency dependence of the strip backplane capacitance measured with and without grounding of neighboring strips around the central one. At high frequencies, where the interstrip impedance drops, the AC current from neighboring strips is also measured, resulting in an increase in capacitance. Their contribution is removed by connecting their DC pads to ground. The residual contribution is due to the coupling capacitance that shunts the implant.

are about 1 pF, resulting in 159 MΩ reactance at 1 kHz signal frequency. The parallel resistance R_b should be in the GΩ range. The resistance of the strip implant is in series with C_b and can reach 1 MΩ. Both the $C_s - R_s$ and $C_p - R_p$ models should give close results over a wide frequency range as long as the dissipation factor remains low.

R_{imp} and C_b are distributed along the strip and form the RC low-pass filter network. This should lead to a frequency dependence similar to that of the coupling capacitance C_c[55]. The measured frequency dependence of C_b for the CBM06H4 sensor is shown in Fig. 4.57. To understand it, the equivalent circuit of three adjacent strips is considered in Fig. 4.58. Neighboring implants are coupled through the interstrip capacitance C_{is}. It is about 3 times larger than C_b for a typical CBM06 sensor. This means that in addition to the AC current flowing through the central implant, an additional current flows through C_b to the neighboring implants and then through C_{is} to the implant being measured. As a result, the measured capacitance is increased. To remove this extra capacitance, the bias ring is set to ground potential. The implants are connected to the bias ring via R_{poly}. The current from neighbors does not flow through C_{is} for the

[55]See Fig. 4.45 for reference.

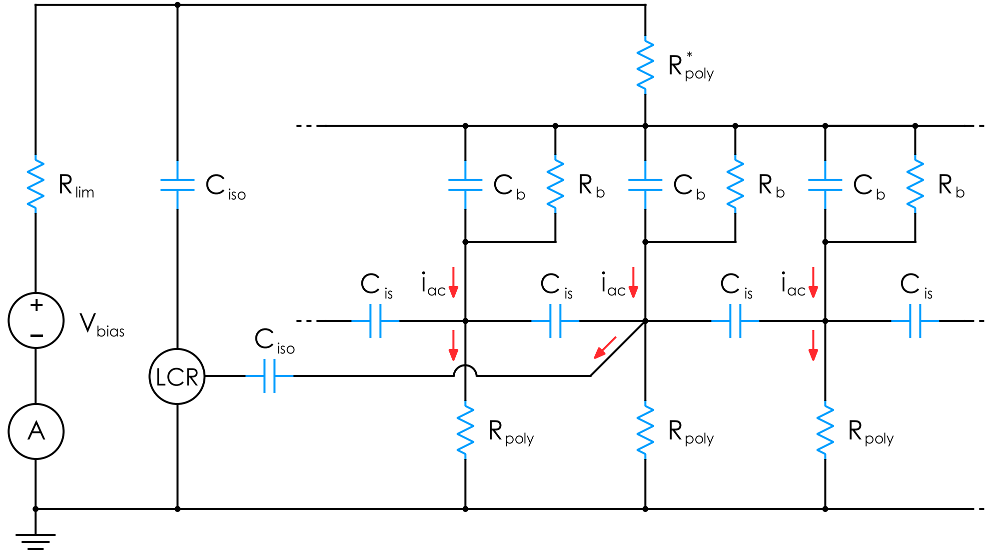

Figure 4.58.: Equivalent circuit of three strips of the CBM microstrip sensor with the LCR meter connected for the strip backplane capacitance measurement. C_b and R_b represent the backplane capacitance and the parallel resistance assigned to one strip. C_{is} is the interstrip capacitance. R^*_{poly} is the equivalent polysilicon resistor of the opposite side.

frequencies:

$$f \ll \frac{1}{2\pi R_{poly} C_{is}}. \tag{4.50}$$

Therefore, for the CBM06H4 sensor, the strip backplane capacitance can be measured below approximately 20 kHz, where a plateau is observed for the CF curve. At high frequencies, when the interstrip reactance drops below the R_{poly} value, the neighboring strips again contribute to the measured current. It can be avoided by connecting the DC pads to the guard terminal. However, a comparison of the measured capacitance in Fig. 4.57 with and without the grounding of neighboring strips indicates an additional effect at high frequencies. It turned out that the reactance of the coupling capacitance C_c drops and starts to shunt R_{imp}. Its contribution can be removed by grounding a metal strip.

The measurement circuit of the strip backplane capacitance is affected by the voltage dividing effect of R_{imp}/R_{poly} as described for the coupling capacitance in Section 4.2.5. Therefore, Equation 4.47 has to be applied to the measured values of C_b to obtain the actual capacitance between the implant and the backplane.

Experimental setup

The setup configuration for this particular type of measurement is not very different from the configuration for the global CV measurement described in Section 4.1.3. The difference is that one probe needle is required to contact the

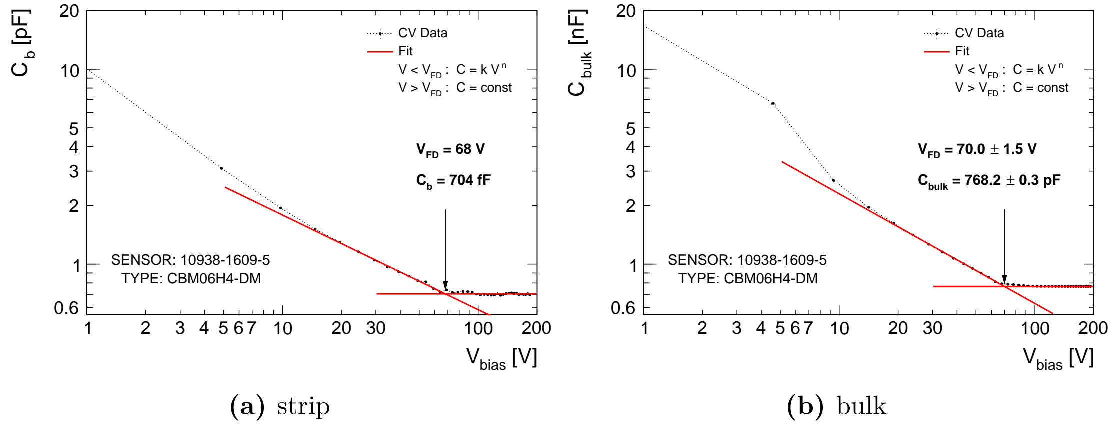

(a) strip **(b)** bulk

Figure 4.59.: Capacitance-Voltage characteristic of (a) one strip and (b) the entire bulk of the CBM06H4 sensor. The frequency of the test signal is 2 kHz. Note the difference in vertical scale units for each plot.

DC pad of the strip. Two additional probe needles are used for measurement with grounded neighboring strips. The guard terminal of the QuadTech 7600+ LCR meter is connected to the *LO* terminal of the Keithley 2410 source-measure unit and the bias ring of the sensor. The measurements are performed using a Keithley 708B [106] switching matrix. The connection of devices is described in Section 3.3.1. The matrix channel configuration is given in Appendix C.

The same compensation procedures as for the global CV measurement and for the coupling capacitance should be followed. It should be noted that the accuracy of the QuadTech 7600+ LCR meter may degrade significantly when measuring high impedance at low frequency. For the expected capacitance values of about 1 pF, the accuracy of the device at 2 kHz is about 30 %, while at 20 kHz it is already 4 %[56]. Therefore, it is recommended to use the highest possible frequency.

Results for CBM prototype sensors

To confirm that the bulk capacitance C_{bulk} is a parallel combination of individual strip capacitances, the CV characteristic of one strip is compared with that of the entire bulk for the CBM06H4 sensor in Fig. 4.59. Both capacitances reach their minimum at the same bias voltage, which corresponds to the full depletion voltage of the investigated sensor. The measured value of C_b corresponds to C_{bulk} according to Eq. 4.49 within the described systematic effects and the accuracy of the LCR meter. The measured bulk capacitance[57] was then used to estimate the strip backplane capacitance. A summary of the obtained values for 27 investigated CBM06 sensors from both vendors is shown in Fig. 4.60. The difference between

[56] The quoted accuracy values are calculated using the CBM06 sensor parameters and according to the QuadTech 7600+ LCR meter measurement accuracy specification [105].
[57] See Section 4.1.3 for details and Appendix B for summary of the bulk parameters.

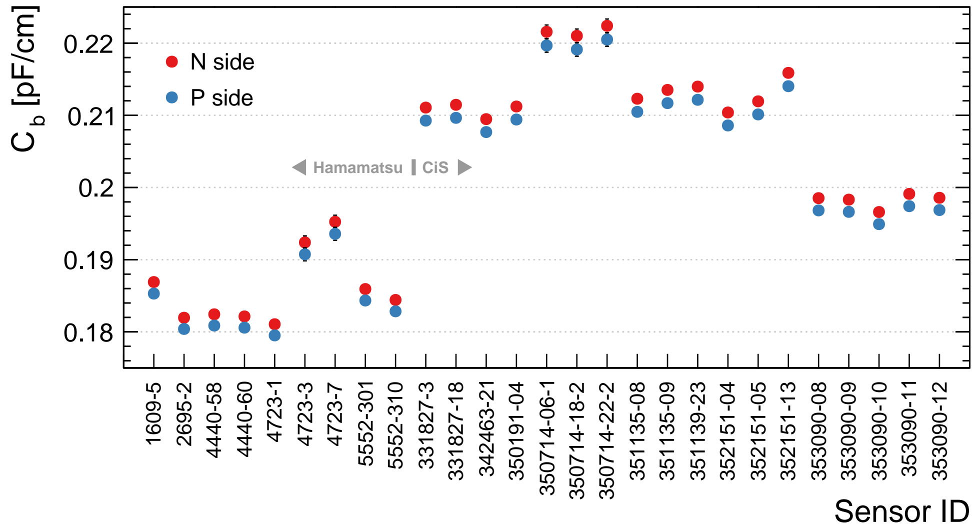

Figure 4.60.: Strip backplane capacitance of the investigated CBM06 prototype sensors. The values are derived from the bulk capacitance C_{bulk} obtained in global CV measurements. The p-side strips are slightly longer due to the stereo angle of that side. The difference in capacitance between the two vendors is due to the different wafer thickness. The error bars indicate the propagated uncertainty in C_{bulk}.

the two sides comes from the fact that the strips on the p side are longer than those on the n side due to the stereo angle:

$$l_p = \frac{l_n}{\cos 7.5°}. \tag{4.51}$$

The difference in values between the two vendors is due to different thickness of the wafers[58]. The $62 \times 22\,\mathrm{mm}^2$ sensors from both vendors show higher capacitance values, which means they are thinner. The CiS sensors belonging to batch 353090 were manufactured using thicker wafers and it is reflected in the capacitance values. Taking into account that the implants on CiS sensors are twice as wide as those on Hamamatsu sensors, it can be concluded that the strip backplane capacitance does not depend on the width of the implant. This is in agreement with Ref. [143] where it was stated that the backplane capacitance should be determined by strip pitch and wafer thickness.

4.2.7. Interstrip Capacitance

The parasitic capacitance can allow signal to leak between otherwise isolated components. In microstrip sensors, it is the interstrip capacitance — the capacitance between adjacent strips. The interstrip capacitance diverts a fraction of the charge from the metal strip. This leads to a decrease in the signal and an

[58]See Fig. 4.22 to compare the thickness of the sensors.

increase in crosstalk[59] between strips. Therefore, it is desirable to minimize its value.

The interstrip capacitance depends on the strip geometry and is usually parameterized as a function of implant width to pitch ratio w/p. It can be minimized with narrow strip implants, as reported in Ref. [142]. The strip pitch is related to the position resolution of the sensor, which is defined by the requirements of the experiment. For the CBM sensors, which are 300 µm thick and have a pitch of 58 µm, the interstrip capacitance is expected to be the dominant contribution to the total strip capacitance. Therefore, it requires an accurate determination. In addition to the geometry dependence, the interstrip capacitance on the n side of the sensor depends on the characteristics of the isolation structure. For the sensor with p-stop, it can be minimized with wider p-blocking implants [142]. The CiS sensors use moderated p-spray isolation, and the interstrip capacitance depends on its dose [72].

The CBM06 sensors manufactured by CiS and Hamamatsu differ in w/p ratio, isolation structure and are manufactured on substrates with different crystal orientation[60]. This should be reflected in the capacitance values and requires systematic measurements for all strips on both sides before final submission for production readiness. Since the interstrip capacitance is very sensitive to the surface state, it is necessary to study its evolution under irradiation. However, this is beyond the scope of this work.

In an AC-coupled sensor, the interstrip capacitance consists of the contributions to all surrounding strips. Typically, it is dominated by the implant-to-implant capacitance to first neighbors. Metal-to-metal and cross-couplings are expected to be much smaller. Only some combination of these contributions can be measured, requiring a careful design of the measurement method. This section focuses on determination of the interstrip capacitance to the first neighbor and the total interstrip capacitance[61]. The estimation of the individual contributions is performed using SPICE simulations and is discussed in Chapter 5.

Measurement method

The interstrip capacitance is measured by contacting implants or metal layers of the adjacent strips. It is possible to limit the interstrip capacitance measurement to a single interstrip gap. In this work, two measurement configurations with different number of contacted strips are used: 4-probe and 3-probe. The connection schemes are shown in Fig. 4.61. The impedance of the circuit is measured by the LCR meter. A three-terminal connection technique is used. In a 4-probe configuration, the sensing terminals of the LCR meter are connected to two neighboring strips. One strip on each side of this pair of strips is connected to the grounding

[59] Crosstalk is the redistribution of a signal between the strips due to the interstrip capacitance.
[60] Refer to Chapter 2 for an overview of the CBM sensor specifications.
[61] The capacitance of one strip to all remaining strips

probe. In a 3-probe configuration, three consecutive strips are probed: the central one is connected to the HI terminal of the LCR meter, and the outer two are connected to the LO terminal. The rest of the strips remain floating. A bias voltage source is connected to the bias ring on each side of the sensor. The measured side is kept at ground potential and connected to the guard terminal of the LCR meter. Capacitors $C_{iso} = 1\,\mu\mathrm{F}$ are used in the circuit to avoid unwanted current flowing to the LCR meter terminals when probing defective strips. They do not distort measurement of capacitance in the expected 1–10 pF range. Multi-probe measurement using DC pads is inconvenient on the CBM sensors. Therefore, AC pads are used for measurements in this work.

Three types of measurements are performed for all sensors:

- Capacitance-Voltage characterization — measurement of the bias voltage dependence of the interstrip capacitance at the test signal frequency of 1 MHz. The bias voltage is increased in steps of 5 V up to 200 V. The capacitance and phase angle are recorded after a delay of about 5 s.

- Capacitance-Frequency characterization — measurement of the frequency dependence of the interstrip capacitance at a bias voltage of ±150 V or higher. A logarithmic frequency sweep of 44 points from 100 Hz to 2 MHz is used. Capacitance and phase angle are recorded at each step.

- Strip-by-strip measurement of the interstrip capacitance at 1 MHz frequency and ±150 V bias voltage for all 1024 strips on each side of the sensor. The choice of frequency and bias condition is discussed later in the text.

There are also other methods to measure the interstrip capacitance. For example, in Ref. [142] the 5-probe method was used: the interstrip capacitance between one central strip and the four closest neighboring strips is measured. A similar approach was used in Ref. [59] for measurements of CBM02 prototype sensors. A different 5-probe method was used by the ATLAS collaboration in Refs. [114, 132], with three central probes measuring capacitance and two more probes connecting the outer strips to ground. In Ref. [144], the interstrip impedance was measured by supplying a sine wave signal to the AC and DC pads of six alternate strips. In this way, a total of ten interstrip impedances are measured in parallel. An alternative static method to measure the interstrip capacitance is described in Ref. [143]. One charge sensitive amplifier was connected to the strip and the other strip was connected to the step voltage source. Using the values of the input step voltage, the charge-amplifier feedback capacitance, and the output voltage, the capacitance between these two strips can be calculated.

Capacitance model

The interstrip impedance is the impedance directly between two strips. In a simple approximation, two isolated strips can be represented by the equivalent circuit

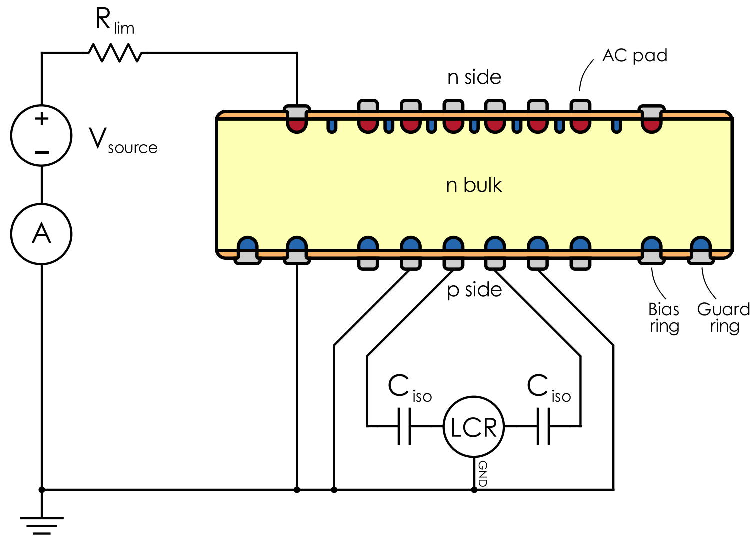

(a) 4-probe

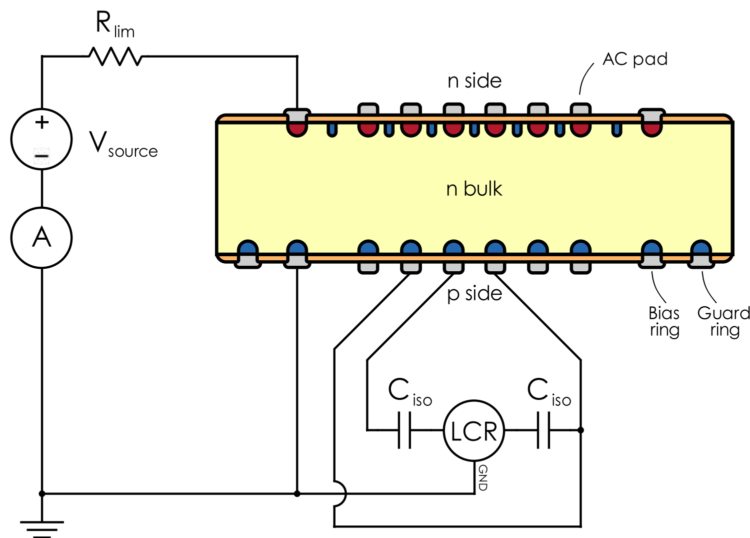

(b) 3-probe

Figure 4.61.: Connection schemes for measurement of the interstrip capacitance of a microstrip sensor. Two configurations are used in this work: with 4 and with 3 probes. In both cases, the sensing terminals of the LCR meter are connected to the AC pads of the neighboring strips. In the 4-probe configuration, the two outer strips are connected to the guard terminal of the LCR meter. In the 3-probe configuration, the strips are not guarded. The bias ring is kept at ground potential. Capacitors C_{iso} are 1 µF each.

shown in Fig. 4.62a. It includes metal-to-metal C_{is}^{AC} and implant-to-implant C_{is}^{DC} capacitance. The resistance R_p represents the parallel resistance of the surface layer between the two implants. It depends on the surface state and may vary depending on the operating conditions of the sensor. The resistance of the metal strip can be neglected. Therefore, the parallel $C_p - R_p$ model should give an appropriate description. Admittance is more convenient to calculate parameters of this circuit:

$$Y_m = \frac{1}{R_p} + \frac{1}{jX_{is}^{AC}} + \frac{1}{jX_{is}^{DC}} = \frac{1}{R_p} + jw(C_{is}^{AC} + C_{is}^{DC}) \tag{4.52}$$

where $w = 2\pi f$ is the frequency of the test signal. Then the capacitance of the two-component parallel model is:

$$C_p = C_{is}^{AC} + C_{is}^{DC}. \tag{4.53}$$

In an AC-coupled sensor, the coupling capacitance C_c between the implant and the metal is a part of the current path. The modified equivalent circuit of two isolated strips is shown in Fig. 4.62b. C_{is}^{AC} is in parallel with the series combination of C_c and C_{is}^{DC}. The admittance of this circuit when measuring between the AC pads:

$$Y_m = \frac{1}{jX_{is}^{AC}} + \frac{1}{2jX_c + \dfrac{jR_pX_{is}^{DC}}{R_p + jX_{is}^{DC}}}. \tag{4.54}$$

Then the parallel capacitance of the equivalent two-component model is the imaginary part of the admittance:

$$C_p = \frac{\operatorname{Im} Y_m}{w} = C_{is}^{AC} + \frac{{}^1\!/\!{}_2 C_c + w^2R_p^2({}^1\!/\!{}_2 C_c + C_{is}^{DC})^2 \dfrac{{}^1\!/\!{}_2 C_c C_{is}^{DC}}{{}^1\!/\!{}_2 C_c + C_{is}^{DC}}}{1 + w^2R_p^2({}^1\!/\!{}_2 C_c + C_{is}^{DC})^2}. \tag{4.55}$$

The capacitance becomes a function of frequency and parallel resistance. Typically, R_p is in the GΩ range at the operating point for a non-irradiated sensor. With increasing frequency, C_p becomes:

$$C_p = C_{is}^{AC} + \frac{{}^1\!/\!{}_2 C_c C_{is}^{DC}}{{}^1\!/\!{}_2 C_c + C_{is}^{DC}} \tag{4.56}$$

and will approach the capacitance in Eq. 4.53 for $C_c \gg C_{is}^{DC}$. When R_p becomes small or comparable to X_{is}^{DC}, C_p approaches another limit:

$$C_p = C_{is}^{AC} + \frac{C_c}{2}, \tag{4.57}$$

which is the case at lower frequencies.

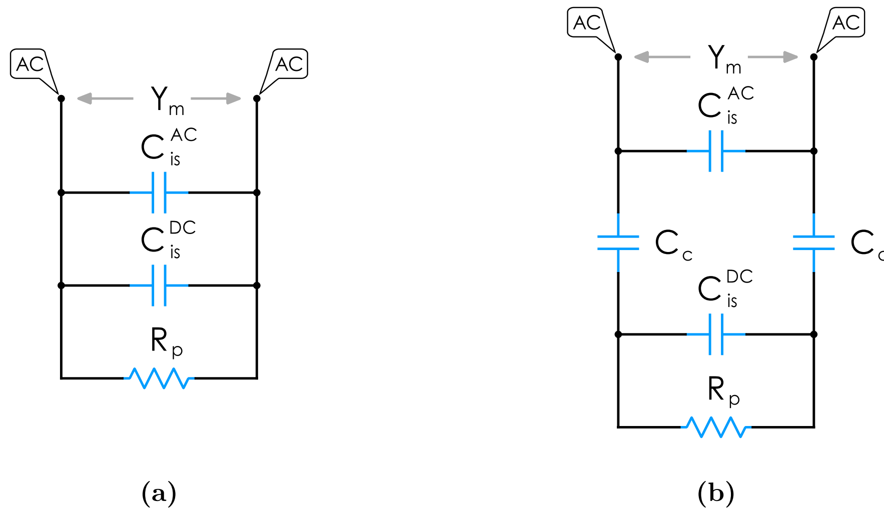

Figure 4.62.: Equivalent circuit models of the gap between two strips for the estimation of the interstrip capacitance: (a) ideal parallel model and (b) model with coupling capacitors C_c bridging implants and metals. The AC labels indicate contacts to the AC pads. C_{is}^{AC} and C_{is}^{DC} represent the metal-to-metal and implant-to-implant interstrip capacitance. Y_m denotes the measured admittance.

Now let's consider the actual sensor. The equivalent circuit model of four strips connected to the LCR meter to measure interstrip capacitance in a 4-probe configuration is shown in Fig. 4.63. The two measured strips have impedance paths to other strips as well as to the backplane. To limit the measured admittance to in-between two strips only, the two outer strips are grounded. Then the current flowing through the neighboring interstrip gaps will not affect the measurement. Each strip also has the backplane capacitance C_b, which is another parallel component in the measured admittance. The capacitance to the backplane of all other strips is represented by the bulk capacitance C_{bulk}. It provides a low impedance path to ground for the AC signal. Therefore, the backplane also does not contribute to the measured interstrip capacitance.

Each strip is connected to the bias ring through a polysilicon resistor R_{poly} that shunts the interstrip capacitance. This is equivalent to the low parallel resistance case of the simple model where $R_p = 2R_{poly}$ and will affect the measurement. Since the branch $R_{poly} - BR - R_{poly}$ is parallel to C_{is}^{DC}, the effect of this path can be removed by connecting the bias ring to the guard terminal. Then the current flowing through R_{poly} does not flow into the ammeter. However, this introduces a new problem due to the series combination of the coupling capacitance C_c and R_{poly}. On one side of the interstrip gap, the voltage between the implant and the bias ring is reduced due to the dividing effect of C_c and R_{poly}. On the other side of the gap, C_c and R_{poly} divide the current so that it does not all flow into the ammeter. In both cases, in a simple approximation, the voltage and current

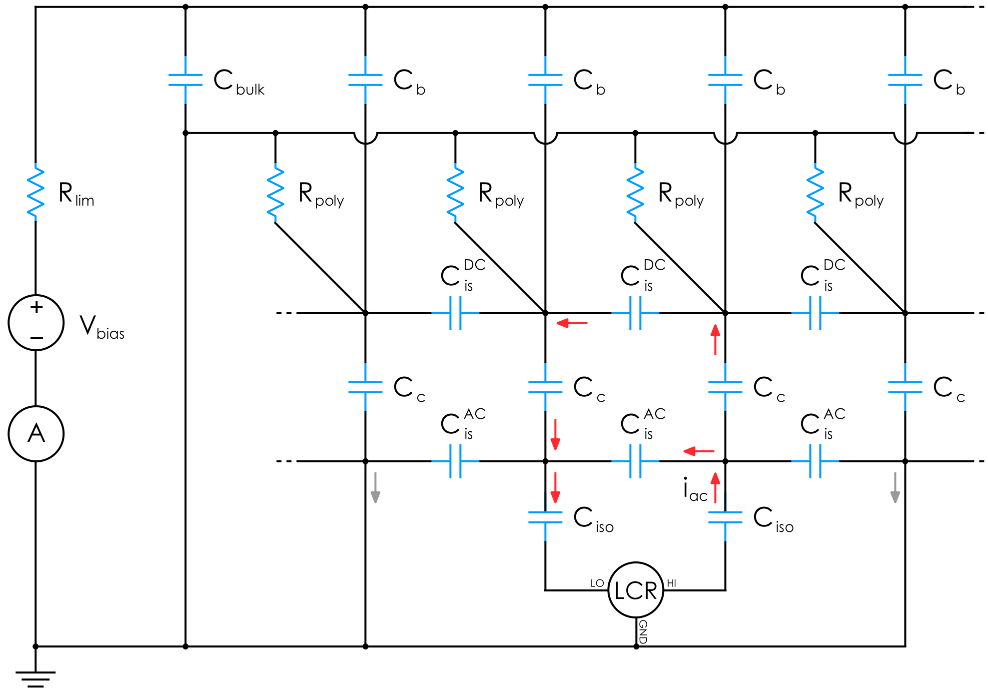

Figure 4.63.: Equivalent circuit of four strips of the CBM microstrip sensor with the LCR meter connected to measure interstrip capacitance in a 4-probe configuration. The implants are connected to the backplane via C_b and to the grounded bias ring via R_{poly}. C_{bulk} is the total bulk capacitance. The red arrows schematically show the current that flows through the interstrip capacitance components C_{is}^{AC} and C_{is}^{DC} and is picked up by the *LO* terminal of the LCR meter. The gray arrows schematically represent the current that flows into the grounded bias ring.

ratios are proportional to:

$$\frac{R_{poly}}{R_{poly} + jX_c}. \tag{4.58}$$

Since C_c is an actual circuit element, the dividing effect cannot be completely removed. It can be minimized by increasing the frequency so that the reactance of the coupling capacitance becomes negligible. This sets the lower limit of the measurement frequency:

$$f \gg \frac{1}{2\pi R_{poly} C_c}. \tag{4.59}$$

For a typical CBM06 sensor with $R_{poly} = 1\,\mathrm{M\Omega}$ and $C_c = 100\,\mathrm{pF}$ it is about 15 kHz. Below that, X_c becomes high and the error due to the voltage/current divider is large, leading to a reduced measured capacitance. It should be noted that the actual sensor has a more complex dependence due to the distributed resistance of the implant.

The obtained frequency dependencies for CBM $62 \times 62\,\mathrm{mm}^2$ sensors from CiS and Hamamatsu are shown in Fig. 4.64. As expected, the measured capacitance

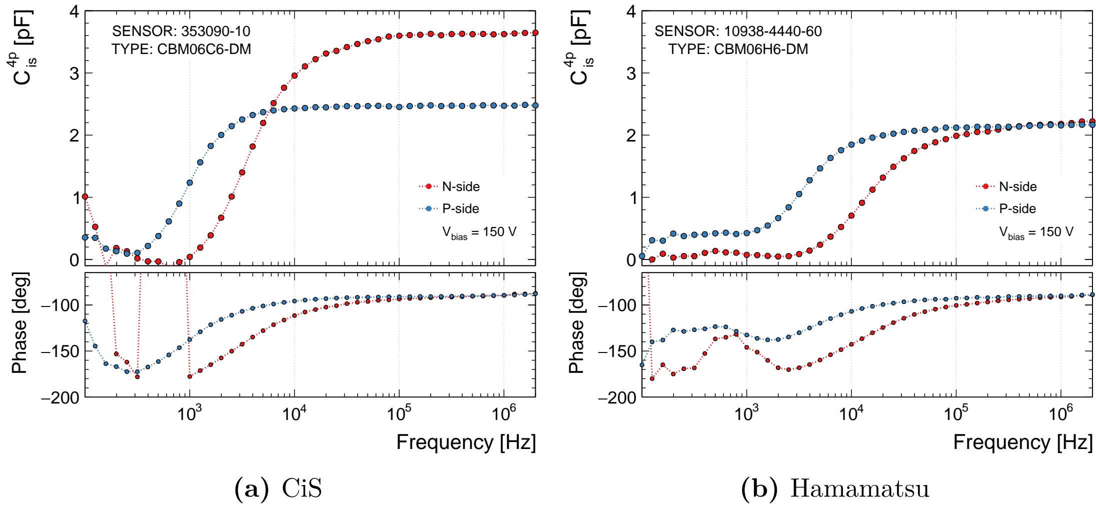

(a) CiS **(b)** Hamamatsu

Figure 4.64.: Frequency dependence of the interstrip capacitance measured on both sides of the CBM06 sensors in a 4-probe configuration: two $62 \times 62\,\mathrm{mm}^2$ sensors from CiS and Hamamatsu. At low frequencies, the reduced capacitance is measured due to the voltage/current dividing effect of C_c/R_{poly}. At high frequencies, the interstrip capacitance to one neighbor is measured.

decreases at low frequencies. At high frequencies, where the phase angle approaches $-90°$, the full interstrip capacitance is measured in accordance with the parallel model. The difference in the position of the inflection point between the two sensors is due to the different values of R_{poly} and C_c[62]. On the n side, additional effects due to the isolation structure have to be taken into account to explain the position of the inflection point of the CF curve. It was reproduced and confirmed by SPICE simulations and is discussed in Chapter 5. All strip-by-strip measurements in the 4-probe configuration were performed at 1 MHz, where the phase angle is $-90°$ and the capacitance is on the plateau for all investigated sensors.

When measurements are performed on the DC pads of the CBM sensors, the frequency dependence of the measured capacitance changes. The effect of R_{poly} and C_c is removed. Now C_c is in series with C_{is}^{AC}. The resistance of the implant forms a low-pass filter with C_{is}^{DC}, which leads to a frequency dependence similar to that of the coupling capacitance. The measurement frequencies:

$$f \ll \frac{1}{2\pi R_{imp} C_{is}^{DC}}. \tag{4.60}$$

In addition, the R_{imp}/R_{poly} voltage dividing effect becomes relevant. Because of this effects and inconvenient location of the DC pads on prototype sensors, the measurements were performed using the AC pads. The DC pads were used to test the model.

[62]See Sections 4.2.2 and 4.2.5 for the corresponding measured values.

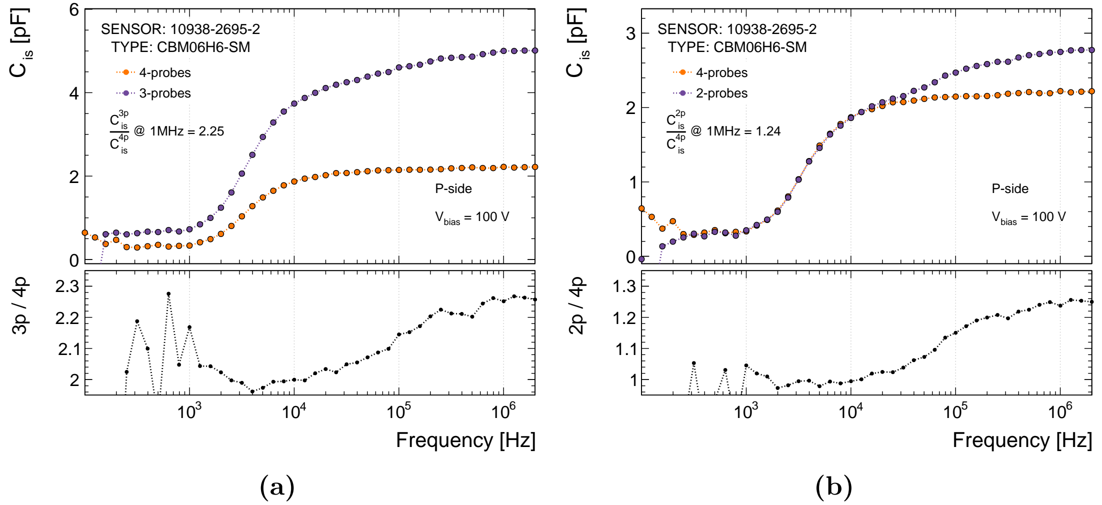

Figure 4.65.: Frequency dependence of the interstrip capacitance measured on the CBM06H6 sensor in different configurations: comparison of (a) 4-probe and 3-probe configurations, (b) 4-probe and 2-probe configurations. The capacitance measured in the 4-probe configuration is the interstrip capacitance to one neighbor, while the other configurations include contributions from the remaining strips.

Comparison of methods

The capacitance measured in the 4-probe configuration was shown to be the interstrip capacitance to one neighboring strip only. Strips exhibit coupling to the rest of the strips, not just to the first neighbor. Lifting the grounding probes and measuring in a 2-probe configuration allows this additional capacitance to be included. In a 3-probe configuration, the total interstrip capacitance is measured. Figure 4.65 shows a comparison of CF curves between different configurations. Measurement without grounding probes requires higher frequencies so that the measured capacitance becomes saturated. Therefore, the quoted capacitance ratios are given for a frequency of 1 MHz.

Average ratios at 1 MHz and for both p and n sides:

$$\begin{aligned} CiS: &\ 2.18 \pm 0.05 \\ Hamamatsu: &\ 2.24 \pm 0.03 \end{aligned}$$

where errors are one standard deviation. The ratios for Hamamatsu and CiS sensors agree within one sigma. It can be concluded that the remaining strips contribute only about 10 % to the total interstrip capacitance. This is consistent with the estimate given in Ref. [145]. In Refs. [132, 114], a comparison of the capacitance measured by the 5-probe and 3-probe methods for the ATLAS microstrip sensors gave a ratio of 2.19 at 1 MHz. This result is in good agreement with the results obtained for CBM06 sensors.

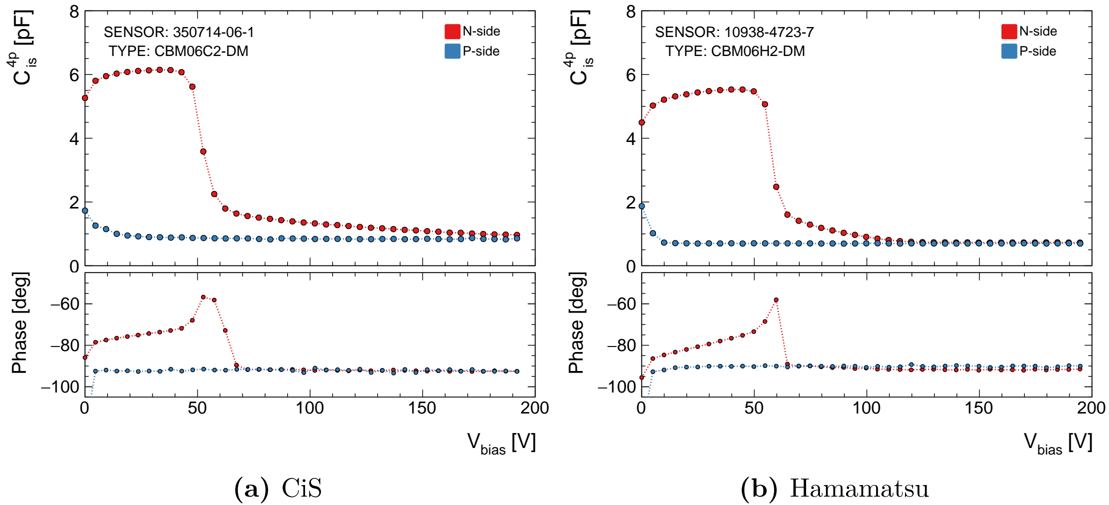

(a) CiS **(b)** Hamamatsu

Figure 4.66.: Bias voltage dependence of the interstrip capacitance measured on both sides of the CBM06 sensors in a 4-probe configuration. Results are shown for two $62 \times 22\,\mathrm{mm}^2$ sensors from both vendors. The frequency of of the test signal is 1 MHz. The full depletion voltage of both sensors is about 70 V.

Bias voltage dependence

In contrast to the strip coupling capacitance, the interstrip capacitance strongly depends on the bias condition, which affects the state of the surface layer between the strips. Figure 4.66 shows the bias voltage dependence of the interstrip capacitance for two CBM06 $62 \times 22\,\mathrm{mm}^2$ sensors from CiS and Hamamatsu. The measurements were performed in a 4-probe configuration. The capacitance on the p side shows a little dependence at low bias voltage. Once the interstrip gap is depleted, it does not change with bias voltage. The phase angle remains at $-90°$, indicating a capacitive circuit.

The n-side capacitance is affected by the absence of strip isolation before full depletion of the bulk. At low biases, the interstrip gap is equivalent to a low-impedance path between two series-connected coupling capacitors. This results in a high measured capacitance with the phase angle changing in response to depletion. When the depletion boundary approaches n implants, isolation develops, which is accompanied by a drop in the phase angle to about $-90°$. After the bulk is depleted, changes in response to bias voltage can take place only in the surface region. For the Hamamatsu sensor with p-stop isolation, the gaps between the n implant and the p stop are filled with an electron layer at V_{FD}, which increases the interstrip capacitance. It depletes with further increase in bias voltage. The interstrip capacitance decreases, reaching a plateau at around 120 V. Similar values in the range of 10–20 V were obtained for other Hamamatsu sensors, which may be due to different oxide charge content. Therefore, strip-by-strip measurements on Hamamatsu sensors were performed at 150 V to ensure the surface depletion.

In contrast, the capacitance on the n side of the CiS sensor progressively decreases with the bias voltage. This is a typical behavior of sensors employing p-spray isolation techniques. It can be understood considering the fact that in the gap between the main p-doping region and the n-implant, the p-spray dose is moderated down to about 1 % of the central region [72]. Depending on the quality of the dielectric layer, it may not be enough to compensate for the oxide charge, which leads to a build-up of the electron accumulation layer. It slowly depletes with the bias voltage and the capacitance decreases. This measured dependence is consistent with simulations for CiS sensors in Ref. [72]. Since the capacitance on the n side does not develop a plateau in the investigated voltage range, it was decided to perform strip-by-strip measurements on CiS sensors at 150 V. When comparing the results, the dependence of the interstrip capacitance on the bias voltage should be taken into account.

Experimental setup

The interstrip capacitance measurement uses the same device setup as described for the strip coupling capacitance[63]: a Keithley 2410 is used to supply the bias voltage and a QuadTech 7600+ LCR meter is used to measure the capacitance. The LCR meter has to be used in “Slow Mode”, which allows for a higher accuracy on expense of measurement time. When measuring sub-pF values on $62 \times 22\,\mathrm{mm}^2$ sensors, it is advisable to enable the “Median Mode”. The measurements are performed using a Keithley 708B [106] switching matrix. The matrix channel configuration is given in Appendix C.

The strips are contacted by tungsten needles with a tip diameter of 5 µm. Figure 4.67 shows the location of the needles on the AC pads and the corresponding arrangement of the measurement probes in a 4-probe configuration. All strip measurements are performed using a dedicated probe station. In contrast to other capacitances, the interstrip capacitance is very sensitive to the residuals that exist in the measurement setup. Therefore, it is necessary to perform all compensation procedures described in Section 3.3.2. “OPEN/SHORT” zeroing procedures of the LCR meter have to be performed in “Slow Mode”. The accuracy of the compensation is very sensitive to the geometry of the connection. Therefore, spacing between the needles should remain the same for both zeroing and actual measurement. Re-zeroing is required when switching between 4-probe and 3-probe configurations, AC or DC pads.

Since the interstrip capacitance is measured at high frequencies (> 100 kHz), the “GAIN” correction procedure becomes important. It is described in Section 3.3.2. Figure 4.68 shows an example of applying the correction for the CBM06C4 sensor. The discrepancy becomes significant above about 300 kHz. While measurement on the p side is possible at lower frequencies for most sensors, “GAIN” correction becomes important on the n side where the capacitance

[63] See Section 4.2.5 for details.

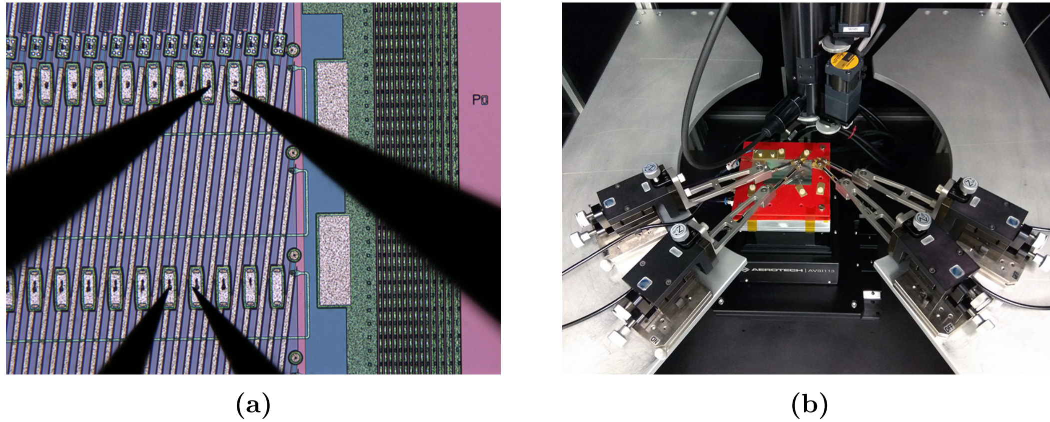

(a) **(b)**

Figure 4.67.: Location of the needles on the AC pads and arrangement of the probes inside the probe station for the interstrip capacitance measurement in the 4-probe configuration. The capacitance is measured between the two central strips and the outer two are grounded. The probes are on the steel table, which is grounded. The sensor is placed in the red test socket, which is attached to the vacuum chuck.

plateaus above 200 kHz. It should be noted that the gain error depends on the measurement setup and must be re-evaluated if any changes are made. In particular, the corrections established for the probe configuration shown in Fig. 4.67 cannot be applied to the capacitance measured in the 3-probe configuration.

Results for CBM prototype sensors

The interstrip capacitance was measured for a total of 9 Hamamatsu and 19 CiS sensors of all sizes. Figure 4.69 shows the measured capacitance of the investigated CBM06 sensors from both vendors. Due to the location of the AC pads, the measurements were performed for every second pair of strips in one pass. Overall, the capacitance profiles are very uniform for all sensors. Some CiS sensors have nonuniform strip-to-strip capacitance, and some exhibit non-linear profiles. The interstrip capacitance is very sensitive to the surface state, and observed nonuniformities may be related to the manufacturing process. The CiS $62 \times 124\,\mathrm{mm}^2$ sensor belongs to an experimental batch produced from 6 inch wafers. The conducted measurements can be useful feedback for the manufacturer. The vertical spikes in the measurement data are associated with defective strips.

The short strips on the *p* side of the double-metal sensors have higher capacitance values. Measurements of single-metal sensors show that short strips have the same capacitance per unit length as long strips. Therefore, the additional capacitance comes from the 2$^{\mathrm{nd}}$ metal lines. However, due to the 4-probe configuration, the measured capacitance of the short strips does not include the full contribution of the 2$^{\mathrm{nd}}$ metal layer[64].

[64] See Section 4.2.8 for details.

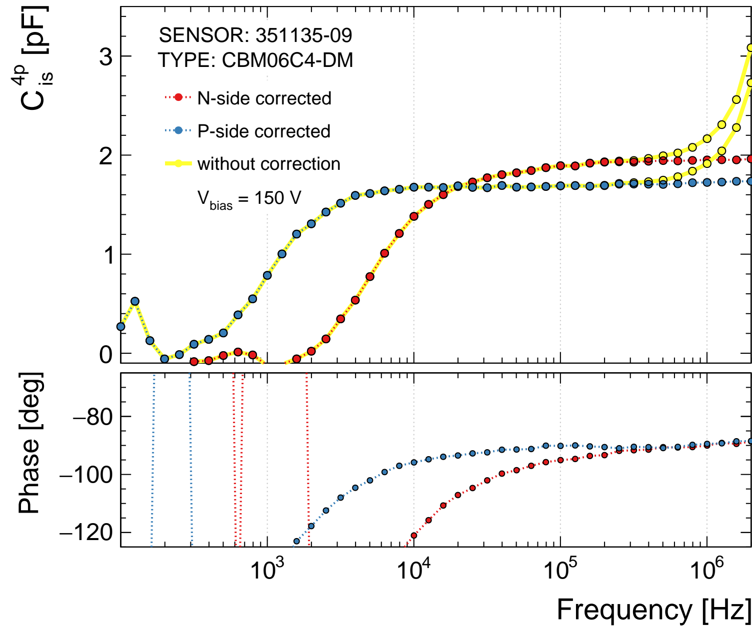

Figure 4.68.: Frequency dependence of the interstrip capacitance measured on both sides of the CBM06 sensor in a 4-probe configuration with and without correction for the gain error. On the n side the effect is more critical, while on the p side measurements can be performed at lower frequencies.

The obtained interstrip capacitance for all investigated sensors is summarized in Fig. 4.70. Each data point represents the average of 512 strips for each side of the sensor. The error bars indicate one standard deviation. These results should be considered as the capacitance to one neighbor only. Similar capacitance values were obtained for both p and n sides of the Hamamatsu sensors. This was not expected because the interstrip capacitance on the n side is usually higher. Therefore, the obtained results indicate optimal measurement conditions and high dielectric quality, which makes the measured capacitance mainly a function of the geometry. The interstrip capacitance of CiS sensors was expected to be higher due to wider strip implants. In contrast to the Hamamatsu sensors, the measured capacitance for CiS sensors has a significant spread of values. Since the sensors come from different batches, these capacitance values may indicate sensitivity to processing parameters affecting the surface layer. In particular, the dose tuning for the p-spray is the major factor on the n side.

The average interstrip capacitance values (to one neighbor) for the n and p sides of the CBM06 prototype sensors are:

$$\begin{aligned} CiS: &\ (n) 0.54 \pm 0.05\,\mathrm{pF/cm},\ (p) 0.46 \pm 0.05\,\mathrm{pF/cm} \\ Hamamatsu: &\ (n) 0.37 \pm 0.01\,\mathrm{pF/cm},\ (p) 0.36 \pm 0.01\,\mathrm{pF/cm} \end{aligned}$$

where the uncertainties represent one standard deviation. The p-side values for 353090 batch are excluded from the average estimation due to manufacturing

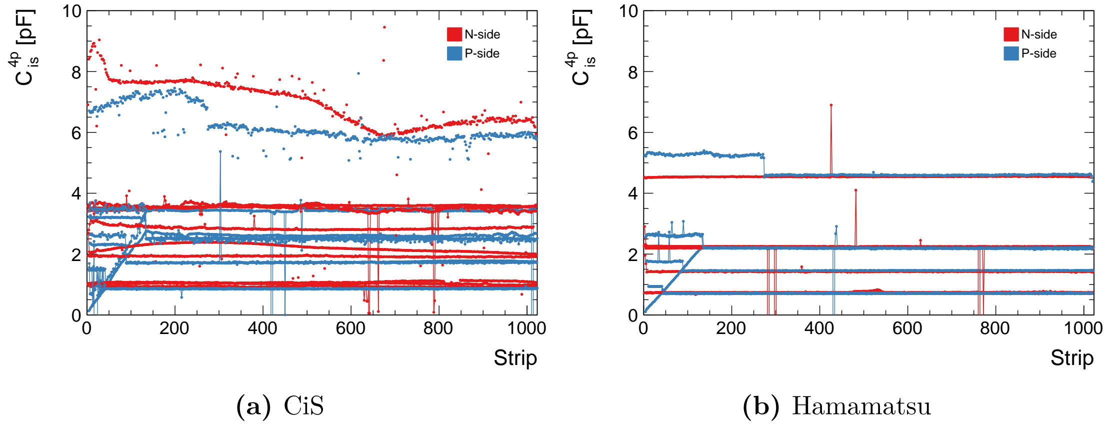

(a) CiS **(b)** Hamamatsu

Figure 4.69.: Measured interstrip capacitance C_{is} of 28 investigated CBM06 prototype sensors of all sizes: both CiS and Hamamatsu are shown. Measurements were performed on both sides of the sensor in a 4-probe configuration at a bias voltage of ±150 V and a frequency of 1 MHz. The data for CiS 62 × 124 mm^2 sensor are plotted without interconnecting lines due to the large number of defects.

issues identified for these sensors. TCAD simulations of the CiS sensors were performed in Ref. [72] and yielded values of 0.56 pF/cm and 0.37 pF/cm for the n and p sides, respectively. This is in excellent agreement with the measured values on the n side, while the measured values on the p side are slightly higher.

Reference [146] provides an experimental parameterization of the total interstrip capacitance in terms of width w and pitch p of the strips for *p-in-n* sensors:

$$C_{is} = \left(0.1 + 1.5\frac{w + 20\,\mu\text{m}}{p}\right)\ \text{pF/cm} \tag{4.61}$$

with a standard deviation around the best line fit of about 0.05 pF/cm. Applying it to the CBM06 sensors gives 0.88 pF/cm and 1.13 pF/cm for Hamamatsu and CiS sensors, respectively. This is in fair agreement with the capacitance measured in the 3-probe configuration, which is 0.82 pF/cm and 1.01 pF/cm for the Hamamatsu and CiS sensors, respectively.

Uncertainties

The random error was estimated by repeating the measurements for a pair of strips several times. The measured interstrip capacitance was always normally distributed with a standard deviation of about 5 fF, which indicates high precision and stability of the measurement. A typical distribution at a frequency of 1 MHz is shown in Fig. 4.71a.

The interstrip capacitance shares similar sources of systematic errors with the coupling capacitance. The most relevant ones are mentioned here:

- The error due to contact impedance can become significant when measuring the interstrip capacitance with $C_p - R_p$ model. It may be caused by,

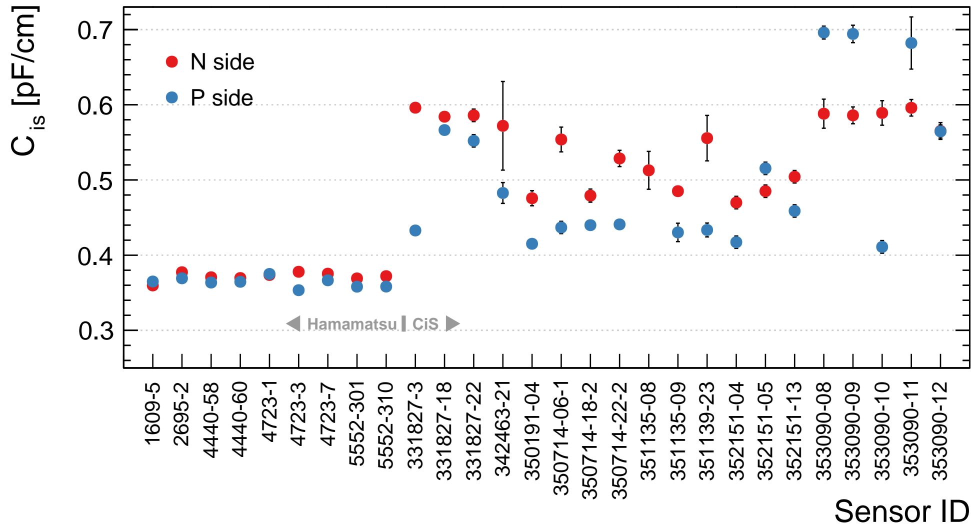

Figure 4.70.: Interstrip capacitance of the investigated CBM06 prototype sensors. Each data point represents the average of 512 strips for each side of the sensor. The error bars indicate one standard deviation. Values are normalized to the length of the strip. It should be noted that the strip implants of CiS sensors are twice as wide as those of Hamamatsu sensors. The shown capacitance corresponds to the interstrip capacitance to one neighbor only.

for example, incomplete removal of passivation at the AC pads. This was observed for the CiS $62 \times 124\,\mathrm{mm}^2$ sensor and could be a possible reason of the observed non-uniform capacitance profile.

- The accuracy of the LCR meter depends on the measured impedance and phase angle and was estimated for each measurement using the equation from the device's measurement accuracy specification [105]. "Slow speed" was used for all measurements. The accuracy at 1 MHz was 2.3 % and 0.8 % for the measured capacitances of 1 pF and 10 pF, respectively.

- To ensure the above accuracy values, "OPEN/SHORT" compensation procedures are performed. A typical open-circuit capacitance after zeroing is shown in Fig. 4.71b. It was always below 50 fF at 1 MHz in the 4-probe configuration. This can be a source significant systematic uncertainty when measuring $62 \times 22\,\mathrm{mm}^2$ sensors with a typical capacitance of about 700 fF. Attention has to be paid to relative positions of the needles. If they change between measurements, re-zeroing is required.

- The gain error has a large effect on the interstrip capacitance at high frequencies. With the present setup and measurement configuration, it results in approximately 10 % systematically higher measured capacitance at 1 MHz. Its effect is shown in Fig. 4.68. All capacitance measurements were

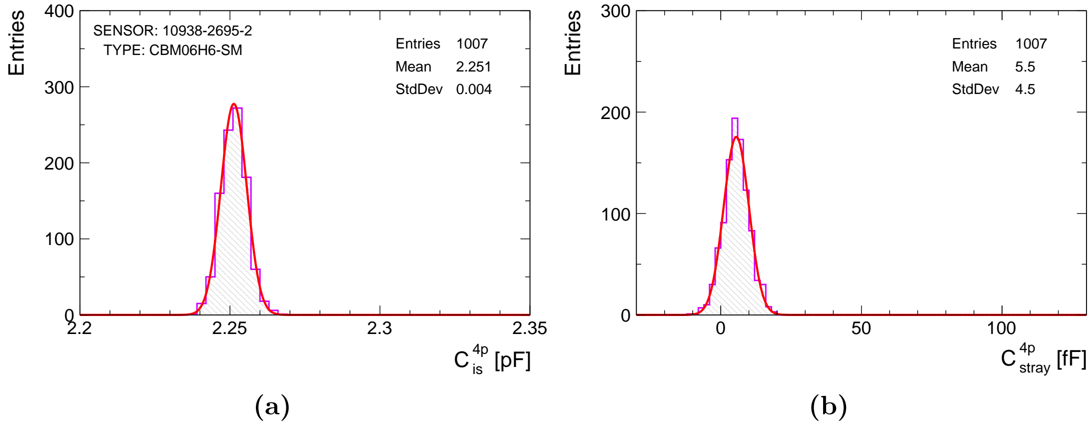

Figure 4.71.: (a) Normal distribution of interstrip capacitance to one neighbor and (b) stray capacitance of an open circuit measured in the 4-probe configuration. The frequency of the test signal is 1 MHz. Note the different unit prefix in each plot.

corrected for gain error according to the developed correction procedure[65].

- A significant systematic error might arise due to measurements at a sub-optimal frequency or bias voltage. The optimal measurement conditions were discussed for the case of the CBM microstrip sensors. To avoid errors, it is recommended to perform the CV and CF characterization before strip-by-strip scan.

- A comparison of the measured capacitance for sensors with single- and double-metal technologies shows that when measuring in a 4-probe configuration, the contribution of the 2nd metal layer is effectively removed for full-length strips on the p side. However, for short strips, it contributes up to 1 pF.

- It is important to ensure the reliability of the ground connections, otherwise it can lead to unpredictable systematic errors.

Overall, the measurement uncertainty is dominated by the accuracy of the LCR meter. Under optimal measurement conditions, after correction for gain error, it never exceeded 5 % for the case of the $62 \times 22\,\mathrm{mm}^2$ sensor.

Observed problems

The importance of the CF characterization can be demonstrated by the example of the CBM sensors of batch 353090. Figure 4.72 shows the measured frequency dependence of the interstrip capacitance on the randomly selected strips of the p

[65]See Section 3.3.2 for details.

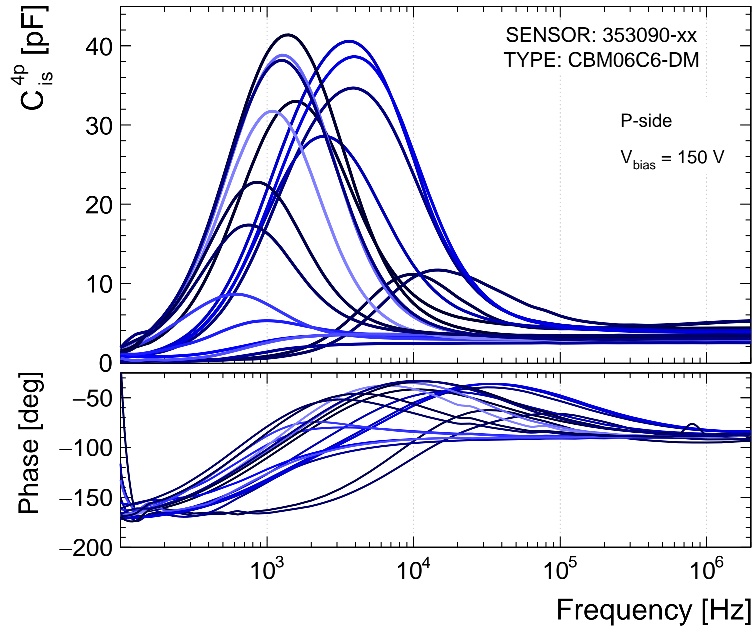

Figure 4.72.: Frequency dependence of the interstrip capacitance measured on the *p* side of the CBM06 sensors of batch 353090. Measurements were performed on randomly selected strips of five sensors in a 4-probe configuration. The observed shapes are explained by the low interstrip resistance, which shunts the interstrip capacitance at low frequencies.

side for five sensors. An unexpected peak structure was observed at low frequencies and a substantially higher capacitance at 1 MHz than for other CiS sensors. A careful investigation revealed a low interstrip resistance on the *p* side, which was attributed to a manufacturing process problem. The low resistance shunts the interstrip capacitance so that the coupling capacitance of the two strips is measured in series. At very low frequencies, the signal is shunted to ground through polysilicon resistors, so a peak structure appears instead of plateau. This was confirmed by SPICE simulations of the CiS sensors[66] and later by direct resistance measurements. A similar peak structure can be observed on the *n* side when performing measurements at bias voltage below full depletion. The same peak structure was also reported in Ref. [147] for the ATLAS *n-in-p* prototype sensors after proton irradiation to a fluence of $2 \times 10^{15}\,\mathrm{n}_{eq}/\mathrm{cm}^2$.

4.2.8. Overlap Capacitance

The CBM sensors use double-metal technology on the *p* side. Short strips in two opposite corners of the sensor appear due to the stereo angle of the *p* side. Two short strips are connected by a 2nd metal line. Therefore, both sides of the sensor

[66]See Section 5.4 for detailed information on simulation results.

can be readout from the same edge. The disadvantage of this technology is that it introduces a network of capacitances due to the overlap between 1st and 2nd metal layer strips. It contributes to the total strip capacitance and increases the noise. Therefore, it is necessary to estimate this additional contribution to C_{tot} for both short interconnected and long regular strips.

The double-metal technology has already been used in the production of the microstrip sensors for the CDF experiment at Tevatron [148, 149], CLEO II at CESR [144], H1 at HERA [150], etc. Typically, it was implemented on the n side of the sensor, where the 1st metal strips were rotated by a stereo angle of 90° relative to the p-side strips. The number of the 2nd metal lines was the same as the number of the 1st metal strips. The measurement of the overlap capacitance was implemented by breaking the 2nd metal line before the via connection and measuring the capacitance between the bias ring and the corresponding AC pad. For the CBM sensors, this will not work because the AC pads belong to the 1st metal layer strips. Therefore, the overlap capacitance is estimated based on the results of the coupling capacitance measurements.

Capacitance model

The second metal layer introduces a network of new capacitances on the p side of the CBM sensor. The two main components are the capacitance between adjacent 2nd metal lines and the capacitance due to the overlap between the 1st and 2nd metal layer strips. Due to the small stereo angle of 7.5° of the CBM sensors, the distance between the 2nd metal lines is about 440 µm. Therefore, the inter-line capacitance can be neglected and it is not considered further. The dominant contribution is expected to come from the overlap capacitance C_{ov}.

Every 2nd metal line overlaps with every 1st metal strip of the p side. The number of such overlaps is $N_{strips}-1$, where $N_{strips} = 1024$ is the number of strips of the CBM sensor. This number is constant for each 2nd metal line and the same for all sensor sizes. The equivalent circuit of the p-side strips with an additional capacitive network introduced by one 2nd metal line is shown in Fig. 4.73. The overlap capacitance is connected in series with coupling capacitance C_c of the corresponding long strip. Since $C_{ov} \ll C_c$, their series combination gives the overlap capacitance. All $N_{strips} - 1$ overlap capacitances are in parallel with the coupling capacitance $C_c = C_{cl} + C_{cr}$ of two short strips that are connected by the 2nd metal line.

Every 1st metal strip overlaps with every 2nd metal line. The number of such overlaps depends on the size of the sensor, which determines the number of short strips N_{short}. The equivalent circuit of one 1st metal strip with an additional capacitive network due to the overlaps with all 2nd metal lines is shown in Fig. 4.74. The capacitances due to these overlaps are in series with the coupling capacitance $C_c = C_{cl} + C_{cr}$ of the corresponding short interconnected strips and in parallel with the coupling capacitance C_c of the long strip.

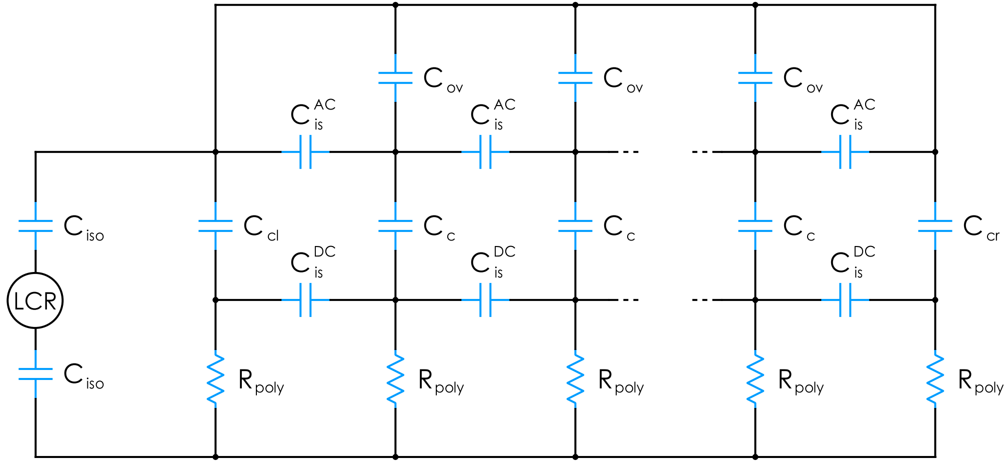

Figure 4.73.: Equivalent circuit of the p side of the CBM microstrip sensor representing the additional capacitive network due to the overlap capacitance C_{ov} introduced by one 2$^{\text{nd}}$ metal line. An LCR meter is connected in the AC-BR configuration to measure the coupling capacitance $C_c = C_{cl} + C_{cr}$ of the two short strips. In this configuration, each overlap capacitance appears in series with the corresponding coupling capacitance and is added to the measured capacitance. C_{is}^{AC} and C_{is}^{DC} are the components of the interstrip capacitance, and R_{poly} is the polysilicon resistance.

When measuring the coupling capacitance in the AC-BR configuration[67], the additional capacitance due to the 2$^{\text{nd}}$ metal layer is added to the measured one. Its contribution is different for interconnected short and regular long strips, as can be concluded from the considered equivalent circuits. The measured capacitance of the interconnected short strips is:

$$C_m = (C_{cl} + C_{cr}) + (N_{strips} - 1)C_{ov} + (N_{short} - 1)C_{ov} + 2C_{is}^{AC} \tag{4.62}$$

where C_{is}^{AC} is the metal-to-metal interstrip capacitance parallel to the first and last overlap capacitance, as can be seen from the equivalent circuit in Fig. 4.73. For long strips, only the overlaps associated with the 1$^{\text{st}}$ metal strip contribute:

$$C_m = C_c + N_{short}C_{ov} + 2C_{is}^{AC} \tag{4.63}$$

where C_{is}^{AC} contributes via the neighboring 1$^{\text{st}}$ metal strips. Subtracting Eq. 4.63 from Eq. 4.62 gives:

$$\Delta C_m = C_\Delta + (N_{strips} - 2)C_{ov} \tag{4.64}$$

where C_Δ is the capacitance due to the resulting longer length of the two interconnected strips and it is about 1.5 pF for the CBM sensors. Then, the overlap capacitance can be estimated as:

$$C_{ov} = \frac{\Delta C_m - C_\Delta}{N_{strips} - 2}. \tag{4.65}$$

[67] See Section 4.2.5 for description of the AC-BR configuration.

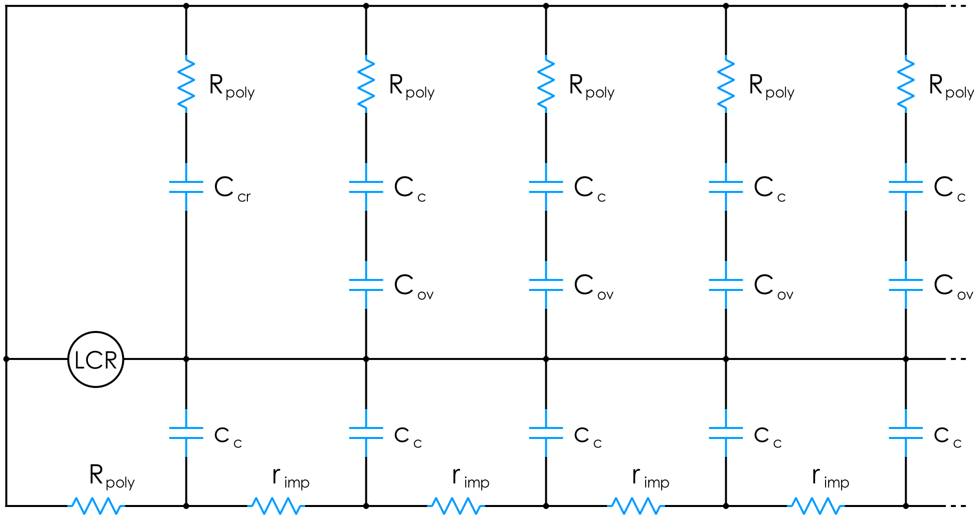

Figure 4.74.: Equivalent circuit of the p side of the CBM microstrip sensor representing one strip with the additional capacitive network due to the overlap capacitance C_{ov} with all 2nd metal lines. The strip is represented by the distributed coupling capacitance c_c and implant resistance r_{imp}. An LCR meter is connected in the AC-BR configuration to measure the coupling capacitance. Each overlap capacitance is in series with the corresponding coupling capacitance C_c and contributes to the measured capacitance. R_{poly} is the polysilicon resistance.

Results for CBM prototype sensors

Figure 4.75 shows the capacitance ΔC_m for CiS and Hamamatsu double-metal sensors of all sizes. It was obtained from the measurement results of the coupling capacitance shown in Fig. 4.53. $62 \times 124\,\text{mm}^2$ sensors are excluded from the analysis. There is a significant difference in the capacitance trend between two vendors. ΔC_m is the same for all Hamamatsu sensors, which corresponds to the described model. In contrast, it increases with the size for CiS sensors, indicating the presence of an additional capacitive contribution. It turned out that every 2nd metal line, right after and before the vias, goes over the bias ring implant[68]. This introduces an additional capacitive component due to the 2nd metal layer. In the AC-BR configuration, it is added to the measured capacitance of the short strips. On CBM sensors, an increase in size by 2 cm adds 44 additional 2nd metal lines. This explains the increase in ΔC_m by a constant value of about 5 pF with increasing sensor size.

A straight line was fitted to the data in Fig. 4.75 and the capacitance due to the overlaps was extracted from the intersection with the vertical axis. Then, the

[68]See Fig. 2.1.

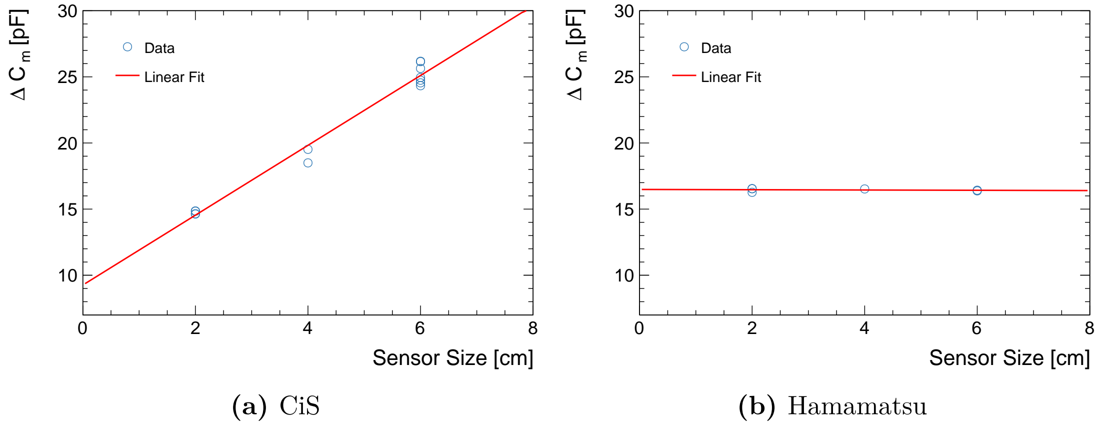

(a) CiS **(b)** Hamamatsu

Figure 4.75.: Additional capacitance of the short strips due to the overlap between the 2nd metal routing line and all strips of the 1st metal layer. Two different cases are observed: the additional capacitance is the same for all Hamamatsu sensors, while it increases with the size of the CiS sensors.

overlap capacitance C_{ov} was calculated using Eq. 4.65:

$$CiS: \ 8\,\text{fF}$$
$$Hamamatsu: \ 15\,\text{fF}$$

The 2nd metal lines are narrower on CiS sensors, resulting in a lower capacitance value. The obtained values are in good agreement with the estimate based on the simple parallel-plate capacitor model.

Such small overlap capacitance means that the coupling due to the 2nd metal layer between any two strips is negligible compared to other parasitic capacitances. This also confirms the results of crosstalk studies through the 2nd metal layer between pairs of channels of the CBM05 prototype sensors. No signs of distant channel correlation were observed in Ref. [57]. However, the cumulative effect of all overlap capacitances results in a significant contribution to the total strip capacitance. In particular, this is the case for short strips, while it is about 1 pF for long strips. Although the overlap capacitance of the CiS sensors is smaller compared to the Hamamatsu sensors, an additional significant contribution was found to come from the overlap between the 2nd metal lines and the bias ring. Therefore, such effects have to be considered at the design stage to avoid undesirable capacitive couplings.

4.2.9. Total Strip Capacitance

Each metal strip is capacitively coupled to all surrounding metal strips, implants and the backplane. One of the most important parameters of the sensor is the total capacitance of the metal strip towards all these electrodes which are kept at

a fixed potential[69]. For microstrip sensors with strip pitch smaller than the sensor thickness, the interstrip capacitance is the largest contributor to the total strip capacitance, while the strip backplane capacitance should contribute less than about 20 % [142]. The total strip capacitance constitutes the load capacitance at the input of the front-end amplifier and dominates its noise.Typically, it is parameterized as a linear function of capacitance and expressed in terms of the equivalent noise charge[70]:

$$ENC[e^-] = a \cdot C_{load} + b \tag{4.66}$$

where C_{load} is the load capacitance, a is the coefficient that relates the chip noise to the capacitance, and b defines the chip's internal noise. In the CBM detector module, the load capacitance is increased by the capacitance of the microcable that connects the microstrip sensor to the front-end chip. It is desirable to minimize the load capacitance to maximize the signal-to-noise ratio.

The STS performance depends on the system noise and is evaluated by simulations assuming a value of 1000 ENC [39]. Realistic simulations show that the track reconstruction and momentum resolution are almost unaffected as long as the noise remains below about 1500 ENC. However, it significantly degrades for higher noise levels [57, 151]. The corresponding total strip capacitance used for system simulation and optimization was assumed to be 1 pF/cm. No experimental data were available for the CBM06 prototype sensors. Therefore, it is necessary to determine the total strip capacitance to ensure that such low noise levels are achievable with the current design of the CBM sensor.

There are different ways to estimate the total strip capacitance of a microstrip sensor: direct measurement, summation of all parasitic capacitances, derivation from noise measurements in the detector module with actual electronics. This section is devoted to the evaluation of the total strip capacitance of the CBM06 prototype sensors.

Summation method

The total strip capacitance can be determined as the sum of all parasitic capacitances of one strip. Considering the sensor capacitive network described in the previous sections, it includes the interstrip capacitance and the backplane capacitance. Under operating conditions, the backplane capacitance is very small, and the interstrip capacitance becomes the most important and dominant contribution. Therefore, by carefully measuring these capacitances, the total strip capacitance can be estimated using a simple relationship:

$$C_{tot} = C_{is} + C_b \tag{4.67}$$

[69] In microstrip sensors, the metal strips are read out by the charge-sensitive amplifiers that set the virtual ground potential.

[70] Microstrip sensors measure deposited charge, so system noise is conventionally expressed as equivalent noise charge (ENC). It is equal to the sensor signal, which gives a signal-to-noise ratio of one.

where C_{is} is the total interstrip capacitance, i.e., the capacitance to the neighbors on both sides of the strip, increased by about 10 % due to the presence of all remaining strips, and C_b is the strip backplane capacitance. On the p side, an additional contribution comes from the overlap capacitance:

$$C_{tot} = C_{is} + C_b + \sum C_{ov} \tag{4.68}$$

where C_{ov} is the overlap capacitance.The measurement of each of the capacitances is described in Sections 4.2.6, 4.2.7, and 4.2.8.

Direct method

The total strip capacitance can be measured by feeding an AC voltage signal to all electrodes and measuring the induced AC current on a single metal strip. Different measurement approaches are reported in the literature. For example, in Refs. [148, 149] only one probe was used to contact the metal strip while the other strips were left floating. The induced current was picked up from the bias ring of the opposite side. In Refs. [152, 153, 154], the two closest neighboring strips were AC-coupled to the backplane during the measurements. The effect of all remaining strips was neglected. The total strip capacitance is then the sum of the body capacitance and the capacitance to the closest neighbors. An agreement within about 20 % between direct measurement and sum of the constituents was reported. Unfortunately, it turned out that a straight-forward comparison is inappropriate.

The summation method relies on the model of the sensor as a capacitive network of known constituents. A real sensor contains additional resistive elements, which results in non-trivial frequency dependencies of the measured impedance parameters. An LCR meter, such as the QuadTech 7600 used in this work, uses a simple two-component model to describe circuit impedance. Such a model fails to properly describe a complex circuit, such as for the total strip capacitance measurement. An additional problem comes from the complexity of the connections for this type of measurement and, as a result, complex residuals that are more difficult to account for with a simple “OPEN/SHORT” compensation. Sensitivity to ground reference is a subject of separate discussion.

Because of these facts, in this work the summation method was preferred over the direct measurement of the total strip capacitance. Even though, the uncertainty of such an estimate may be higher[71] than that of the direct measurement, the accuracy is expected to be higher with the summation method[72].

Results for CBM prototype sensors

Figure 4.76 summarizes the total strip capacitance for all investigated CBM06 sensors. The given values are obtained by summing up the measurement results

[71] Quadrature sum of uncertainties in all capacitances.

[72] Due to the accurate measurement of individual capacitive components.

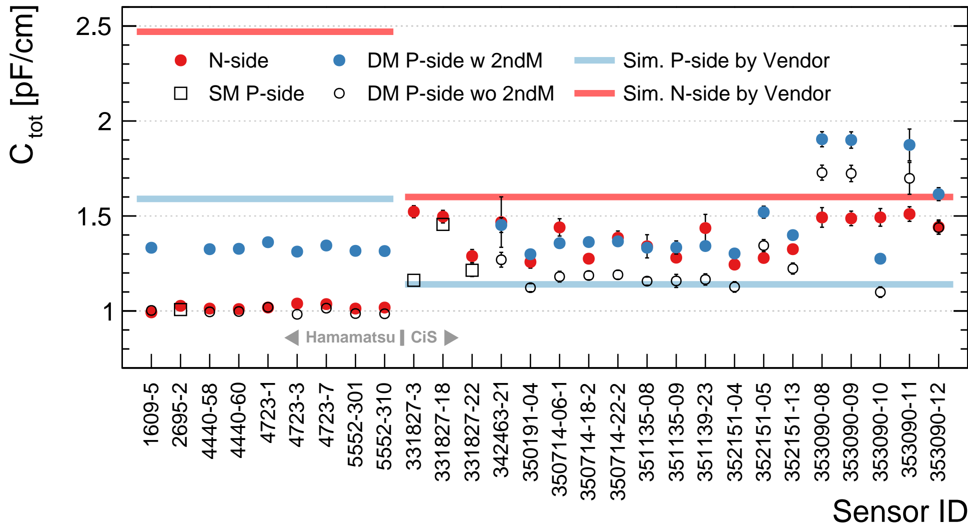

Figure 4.76.: Total strip capacitance of the investigated CBM06 prototype sensors. Each data point is the sum of the total interstrip and backplane capacitances. The p-side values for double-metal (DM) sensors are shown with and without the contribution of the 2nd metal layer. The values are normalized to the length of the strip. For comparison, the w/p ratio of 0.17 and 0.34 for the Hamamatsu and CiS sensors, respectively, should be taken into account.

described in Sections 4.2.6 and 4.2.7. For double-metal sensors, the results of Section 4.2.8 were used. Uncertainties were estimated summing up the uncertainties in the individual contributions in quadrature. The relative uncertainties for the Hamamatsu sensors are less than 1.5 %, while for the CiS sensors they are higher due to the larger spread of the interstrip capacitance values. The values for the p side of the double-metal sensors are shown with and without the contribution of the 2nd metal layer. They agree well with the total strip capacitance of the single-metal sensors. The sensors of batch 353090 exhibit high capacitance values due to the interstrip isolation problem on the p side.

The average total strip capacitance values for the n and p sides of the CBM06 prototype sensors are:

$$\begin{aligned} CiS: &\ (n)1.39 \pm 0.10\,\text{pF/cm},\ (p)1.37 \pm 0.07\,\text{pF/cm} \\ Hamamatsu: &\ (n)1.02 \pm 0.02\,\text{pF/cm},\ (p)1.33 \pm 0.02\,\text{pF/cm} \end{aligned}$$

where the values on the p side include the contribution of the 2nd metal layer. The uncertainties indicate one standard deviation.It should be noted that the total capacitance of short interconnected strips on the p side is increased by the additional contribution shown in Fig. 4.75. It is 15 pF and 13 pF[73] for Hamamatsu and CiS sensors, respectively.

[73] For $62 \times 22\,\text{mm}^2$ sensors. See Section 4.2.8 for details.

The resulting total strip capacitance is slightly larger than that used in the noise simulation for the STS. Implications for the noise performance are discussed in the next subsection. Figure 4.76 also shows values provided by vendors. Good agreement is observed for the p side of the CiS sensors, while the discrepancy on the n side is due to the difference in bias voltage. The CiS data correspond to 120 V, and 150 V is used as a reference in this work. The discrepancy for Hamamatsu sensors cannot be explained.

The total strip capacitance can be parameterized as a linear function of the width-to-pitch ratio w/p. Reference [146] provides an experimental parameterization for the p-side strips in the range $0.1 < w/p < 0.6$:

$$C_{tot} = \left(0.8 + 1.7\frac{w}{p}\right) \text{ pF/cm} \tag{4.69}$$

with a standard deviation around the best line fit of about 0.05 pF/cm. The corresponding w/p ratios for the Hamamatsu and CiS sensors are 0.17 and 0.34, respectively. The values of the capacitance according to this parameterization are slightly higher than those estimated in this work. This is also consistent with the parameterization in Ref. [74] for sensors of similar geometry. Reference [74] also provides the capacitance parameterization for the n side of sensors with p-stop implants. For geometries similar to the CBM06 sensors, it yields a value of about 2 pF/cm. However, the authors note that the capacitance values continue to decrease with bias voltage.

Implications on noise

The noise of the charge sensitive amplifier (CSA) strongly depends on the capacitive load. For the final STS detector module, it consists of the total strip capacitance C_{tot} and the microcable capacitance C_{cable}:

$$C_{load} = l_{strip}C_{tot} + l_{cable}C_{cable} \tag{4.70}$$

where l_{strip} and l_{cable} are the length of the sensor strip and the cable trace, respectively. Various combinations of sensor sizes and microcables will result in the load capacitance in the 12–40 pF range[74].

Comprehensive noise studies of the STS detector modules with the STS-XYTER readout ASIC were conducted in Ref. [151]. First, low leakage capacitors in the 1–40 pF range were used to represent the module. Then, microcables of different lengths were bonded onto the chips and the overall noise was determined. It turned out that the noise is the same for both capacitors and microcables of the same capacitance. In both cases, the fit of the experimental data resulted in

[74] In the STS detector, the modules come in various combinations of 15–47 cm long read-out microcables and sensors with 2, 4, 6 and 12 cm strip length. The capacitance of the microcable was measured in Section 3.3.3.2 and the corresponding value is 0.38 ± 0.02 pF/cm.

a linear dependence on the load capacitance for the slow channel [151]:

$$ENC[e^{-}] = 27.3e/\text{pF} \cdot C_{load} + 494e \tag{4.71}$$

where the offset term reproduces the intrinsic noise level of the bare STS-XYTER chip. A comparison to the noise levels of the assembled detector modules leads to a conclusion that the total strip capacitance C_{tot} measured in this work corresponds to the load capacitance seen by the CSA at its input.

The noise performance of the fully-assembled STS modules is reported in Refs. [155, 156]. In most cases, the observed average noise levels were below $1500e$ for both sensor sides. The noise of the detector module with the $62 \times 62\,\text{mm}^2$ sensor and 42 cm long microcable after assembly onto a ladder was found to be close to $1000e$ [157], which corresponds to the expected value of the model. This proves that the total strip capacitance of the CBM06 microstrip sensors satisfies the CBM specifications and allows the required noise levels to be achieved. It should be noted that the noise of the short strips in all modules was always higher by about $500e$ compared to the long strips. This is consistent with the estimate that takes into account the additional contribution of the overlap capacitance measured in this work.

The discussion of these parameters assumes that the sensor is biased to the operating point where it is intended to be used. Measurement of the module noise as a function of the bias voltage shows that it remains approximately constant on the p side [64, 151]. On the n side, it drops almost to a plateau after about 120 V. This is consistent with the observed bias voltage dependence of the interstrip capacitance[75] and confirmed that the proper operating voltage for the system is greater than 120 V.

It can be concluded that the total strip capacitance of about 1.3 pF/cm measured in this work represents an acceptable load for the STS-XYTER chip. Even though, the measured capacitance is slightly larger than assumed for the noise simulation, the corresponding microcable capacitances is about 20 % smaller than initially assumed [109]. Therefore, an acceptable pre-irradiation noise level can be achieved with microstrip sensors of the CBM06 type.

4.3. Strip Integrity

Integrity tests are performed to detect various defects of the electrical elements present on both sides of the silicon microstrip sensor. The most common classes of defects are discontinuities in the coupling dielectric layer, metal strips, and implants. Defects are discussed in detail in Section 6.3. The CBM specification sets a limit on the number of defective channels not to exceed 1.5 % [64]. Therefore, reliable measurement methods are necessary to detect defective strips.

[75] See Section 4.2.7.

4.3.1. Coupling Dielectric Layer

A very thin dielectric layer between the implant and the metal strip is required to achieve the coupling capacitance values of $> 10\,\mathrm{pF/cm}$. A typical thickness of a standard layer of silicon oxide SiO_2 is about 200 nm. From a manufacturing point of view, the production of such a thin layer over a large area of about $72\,\mathrm{cm}^2$ is a challenging task. Even with today's technological advances, failures occur that lead to weak spots in the dielectric layer. Typically, this is characterized by either an electrical short between the implant and the metal strip, called a "pinhole", or a low ohmic connection. Pinholes in the coupling dielectric layer compromise the AC readout and are the only defect type that is potentially dangerous for the readout ASIC. The corresponding channel loses its working point if a too large current flow or voltage transient occurs [158]. To increase reliability, a second layer of silicon nitride Si_3N_4 is usually produced. Thus, the yield of the coupling capacitors can be significantly increased. In addition, higher coupling capacitance and improved voltage tolerance can be achieved with stacked dielectrics [139].

The integrity of the coupling capacitors is of particular importance for the CBM double-sided microstrip sensors. A large number of defective channels reduces the track reconstruction efficiency and momentum resolution [64], so it should be kept low. This puts strict requirement on the yield of the coupling capacitors and requires careful and reliable tests to detect defective ones.

Measurement method

Defects in the coupling dielectric layer can be detected by two methods. The first is based on measuring the coupling capacitance in the same way as described in Section 4.2.5. However, this method is not reliable because it depends on the resistance R_{ph} of the pinhole. Its magnitude relative to capacitive reactance affects the measured capacitance. The second method is based on applying a DC voltage across the coupling capacitor and measuring the current. This method is preferred because it provides an unambiguous pinhole signal.

Similar to the measurement of the coupling capacitance, two configuration are used: AC-DC and AC-BR. The connection schemes are shown in Fig. 4.77. The voltage source V_{test} applies the test voltage across the coupling capacitor. Its HI terminal is connected to the AC pad of the strip, and its LO terminal is connected to the bias ring or the DC pad, depending on the selected configuration. The bias ring of the measured side is kept at ground potential. The resulting current is measured by the picoammeter A_2.

The advantage of the AC-BR configuration is that the measurement circuit includes a polysilicon resistor connected in series. It limits the current in case of a pinhole. In contrast, a discrete resistor $R_s = 1\,\mathrm{M\Omega}$ is used for this purpose in the AC-DC configuration. However, a disadvantage of the AC-BR configuration is that a defective polysilicon resistor can mask a defective capacitor.

A test voltage of 20 V is applied across the coupling capacitors of the CBM06

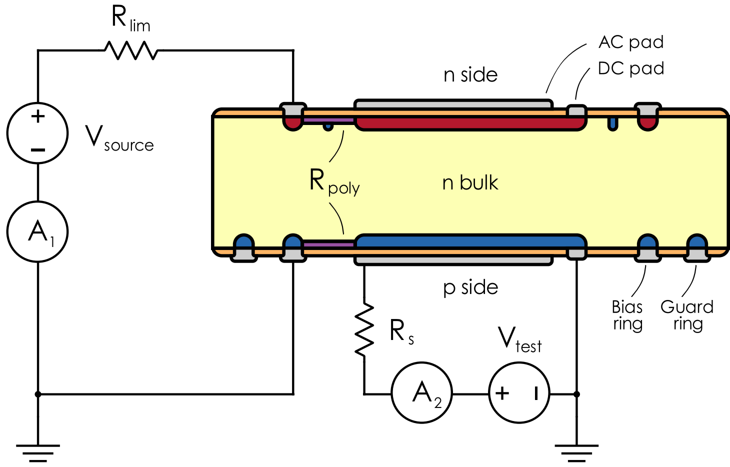

(a) AC-DC

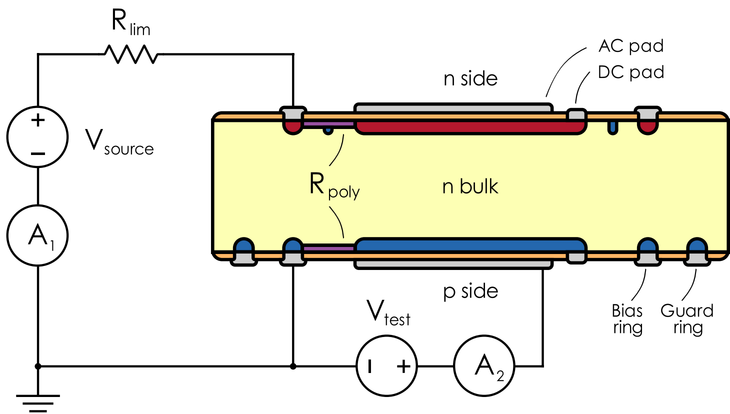

(b) AC-BR

Figure 4.77.: Connection schemes for testing of the coupling capacitors. Two configurations are used in this work: AC-DC and AC-BR. The voltage source V_{test} supplies DC voltage across the coupling capacitor, and the current is measured by the picoammeter A_2. In the AC-DC configuration, the series resistor R_s limits the current in the case of a pinhole, while in the AC-BR, the polysilicon resistor R_{poly} fulfills this role.

sensors. The voltage was chosen to ensure that all low-impedance spots are detected with sufficient current. Another requirement was that V_{test} should exceed V_{PT}, which is about 10 V for the CBM06 prototype sensors[76]. If the coupling dielectric layer is intact, the measured current corresponds to the noise level of the measurement setup. Typically, values below 100 pA are measured. The pinhole current depends on R_{ph}. The resistance of the defective capacitor with the voltage applied across it can vary in a wide range: from a relatively low resistance to an electrical short. When the test voltage is applied, the picoammeter will measure the capacitor charge current. Therefore, a delay of 1 s is introduced before the measurement. In addition, the test voltage should be applied gradually so as not to destroy the capacitor with a sudden voltage. Reference [130] reported that a voltage increase of 10 V/ms resulted in permanent damage to the coupling capacitors.

Experimental setup

The setup for testing the coupling capacitors is the same as for the other DC measurements in this work. A Keithley 6487 [104] voltage source and picoammeter are used to apply voltage across the coupling capacitor and measure the current. Compliance current limit of 2.5 mA was selected. The current measurement range was set to 200 nA with automatic up-range if a higher current is measured.

The measurements are performed using a Keithley 708B [106] switching matrix. The connection of devices is described in Section 3.3.1. The matrix channel configuration is given in Appendix C.

A dedicated probe station with high positioning accuracy is an essential tool for this type of measurement. Before probing each strip, several preparatory procedures are performed: alignment, coordinate calibration, and measurement of the height profile[77] of the contact pads. The location of the needles is similar to that described for the coupling capacitance measurement[78]. The AC-BR configuration is preferred because all 1024 strips can be measured in one pass at the same edge of the sensor.

Results for CBM prototype sensors

The coupling capacitors were tested for a total of 9 Hamamatsu and 23 CiS sensors of all sizes, resulting in about 54 000 checked strips. The quality of the coupling capacitor was characterized by the maximum dielectric current when 20 V is applied across it. “Good” capacitors usually draw current below 100 pA. An order of magnitude higher current was considered a sign of a defective dielectric layer. A current of several hundred µA or higher is a sign of actual “pinhole”. The strip data analysis was based on this simple criteria.

[76]See Section 4.2.3 about the punch-through voltage determination.
[77]See Section 3.2.8
[78]See Section 4.2.5.

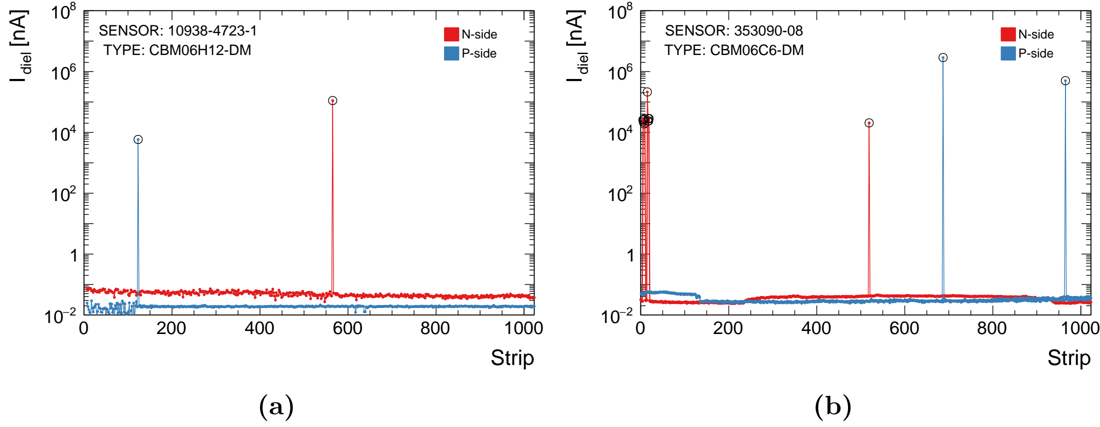

(a) **(b)**

Figure 4.78.: Examples of the pinhole test results: (a) a typical strip scan of the CBM06 prototype sensor with only a few detected pinholes; (b) the detected pinholes for the first few strips on the n side are defects caused by a deep scratch.

An example of a typical strip scan of the coupling capacitors is shown in Fig. 4.78a. Table 4.1 summarizes the amount of detected defective coupling capacitors for all investigated CBM06 sensors. The results are consistent with the data provided by the vendors for the strip numbers of the defective capacitors. Some of the sensors have significantly more defects than reported by CiS. After visual inspection, scratches were found on the surface of some sensors. A deep scratch results in a coupling short and causes a high leakage current. An example of this defect for the CBM06C6 sensor is shown in Fig. 4.78b.

The CiS $62 \times 124\,\mathrm{mm}^2$ sensor comes from the first experimental production using 6 inch wafers. Therefore, fraction of defective capacitors for this sensor is relatively high: 2 % and 5 % on p and n sides, respectively.

It was found that approximately 90 % of the defective capacitors on the p side of the Hamamatsu sensors belong to the short strips. This was not observed for single-metal sensors from Hamamatsu. No associated surface damage was detected for these strips. Therefore, it should be related to the manufacturing process.

Some CiS sensors (e.g., 351139-23) have a few more pinholes as reported by the vendor than measured in this work. This was due to the measurement method used by the vendor, resulting in pinholes being reported twice for the short strips.

The CBM specification requires that defective strips not exceed a level of 1.5 % [64]. It can be concluded that both manufacturers can produce sensors with sufficient quality of the coupling dielectric layer, and only improper handling can compromise it.

Table 4.1.: Summary of the results of testing coupling capacitors on the CBM06 prototype sensors.

Sensor ID	Size, cm	Manufacturer		Uni-Tuebingen	
		p-side	n-side	p-side	n-side
Manufactured by Hamamatsu					
10938-1609-5	4	4	0	4	0
10938-2695-2	6	0	1	0	1
10938-4440-58	6	7	0	6	0
10938-4440-60	6	4	0	4	0
10938-4723-1	12	1	1	1	1
10938-4723-3	2	–	–	0	0
10938-4723-7	2	–	–	0	0
10938-5552-301	6	2	1	2	1
10938-5552-310	6	1	0	1	0
Manufactured by CiS					
331827-3	6	0	0	0	0
331827-18	6	5	0	8	16
331827-22	6	0	0	–	–
342463-21	12	29	61	21	50
350191-04	6	2	0	18	1
350714-06-1	2	8	0	8	3
350714-18-2	2	0	0	0	0
350714-22-2	2	0	0	0	0
351135-08	4	3	0	3	0
351135-09	4	1	0	1	0
351139-09	4	0	0	1	0
351139-14	4	0	2	0	6
351139-23	4	5	0	3	0
351142-14	4	5	1	5	1
351142-16	4	1	1	1	2
352151-04	6	1	0	1	0
352151-05	6	0	0	0	0
352151-13	6	16	0	16	0
353090-08	6	2	1	2	12
353090-09	6	2	0	2	4
353090-10	6	3	3	2	3
353090-11	6	0	0	0	3
353090-12	6	0	0	2	1

5. SPICE Simulation of Microstrip Sensors

It was shown in Chapter 4 that measuring the electrical parameters of the microstrip sensor is not a simple task. Sensor elements form a complex impedance network. In addition, electrical parameters such as capacitance and resistance are spatially distributed along the strips and bulk. The two-component model can not adequately represent the actual parameters of the microstrip sensor. As a result, the measured parameters exhibit a strong frequency dependence. The analytical approach becomes too complicated. To better understand the sensor and to interpret the measurement results, SPICE[1] simulations were performed for the CBM microstrip sensors. The LTspice XVII [159] simulation software was used for this purpose.

The simulation made it possible to find out the relationship between the measured and actual parameters of the sensor. They helped to adjust the procedures for measuring individual parameters. They were useful for identifying systematic effects and developing correction procedures. The simulation results, in addition to the measurements, provided useful feedback to the manufacturer. In particular, the recognition of the interstrip resistance problem of CiS sensors is covered in the following sections.

The simulation approach is not new and has been used by many experimental groups to reproduce the frequency dependence of measured capacitances. One of the first successful attempts using SPICE is reported in Refs. [74, 145].

5.1. SPICE Model

A detailed model of the CBM microstrip sensor for the simulation was developed based on the experimental results of Chapter 4 and taking into account the experiences reported in the literature. Capacitors and resistors are used as the basic building blocks for the sensor impedance network. It is also necessary to properly represent the measuring device, grounding schemes and parasitics that affect certain measurements. It should be noted that in some cases simplified models will be used, for example, as in the case of the bulk capacitance.

[1]Simulation Program with Integrated Circuit Emphasis.

5.1.1. Microstrip Sensor

The main electrical element of the microstrip sensor is the strip. Its metal and implant electrodes are divided into segments consisting of resistors r_m and r_{imp}[2] as shown in Fig. 4.46. Capacitors c_c connect each pair of r_m and r_{imp} and represent the coupling capacitance of the strip.

The measurement of strip parameters was designed in such way that the effect of the surrounding strips was either minimized or could be estimated. Therefore, the SPICE model contains only five strips. Each strip is connected to a common bias ring via a single resistor R_{poly} at the alternating ends.

The strips in the model are interconnected by interstrip elements, which include the metal-to-metal c_{is}^{AC} and implant-to-implant c_{is}^{DC} capacitance. The resistor r_{is} in parallel to c_{is}^{DC} represents the resistance of the surface layer between the strips.

Each strip is coupled to the backplane via the bulk capacitance c_b and the resistance r_b. The backplane itself is not structured in the model. It includes only resistive elements that connect it to the bias ring.

The model is constructed of cells as shown in Fig. 5.1. One cell corresponds to a slice perpendicular to the strips. The number of cells was increased until convergence between experimental and simulated data was observed at high frequency. It was found that 15 cells/cm is sufficient for this task. A 100-cell model was used for $62 \times 124\,\mathrm{mm}^2$ sensors due to performance limitations.

The initial values for the model parameters were taken from the specification[3] and measurement results of Chapter 4.Some of the parameters could not be measured directly, but were restricted using other parameters. Elements of the model and their initial values are listed in Table 5.1. They are calculated for each sensor according to its size and the number of cells in the model.

The SPICE model does not include next-to-next interstrip couplings due to the use of grounding probes. Metal-to-implant cross couplings are expected to be of the order or less than metal-to-metal capacitance. For the sake of model simplicity, it was only included in the extended model. The second metal layer of the p side was represented by an additional capacitance to the bias ring only for specific connection schemes. To simulate the n-side strips, isolation p-stop structures were added to the SPICE model. This will be discussed in Section 5.4. The SPICE model for DC simulation was simplified and includes only the resistive network of the strip.

Additional elements had to be included to represent the bias voltage source. It is connected to the bias rings via 1 MΩ resistors. Additional capacitors have been added to account for the bulk capacitance, the cable capacitance, the capacitance to ground, etc.

[2]Here, lowercase letters are used to represent the parameters of the small segments of the sensor elements in the SPICE model.

[3]See Chapter 2.

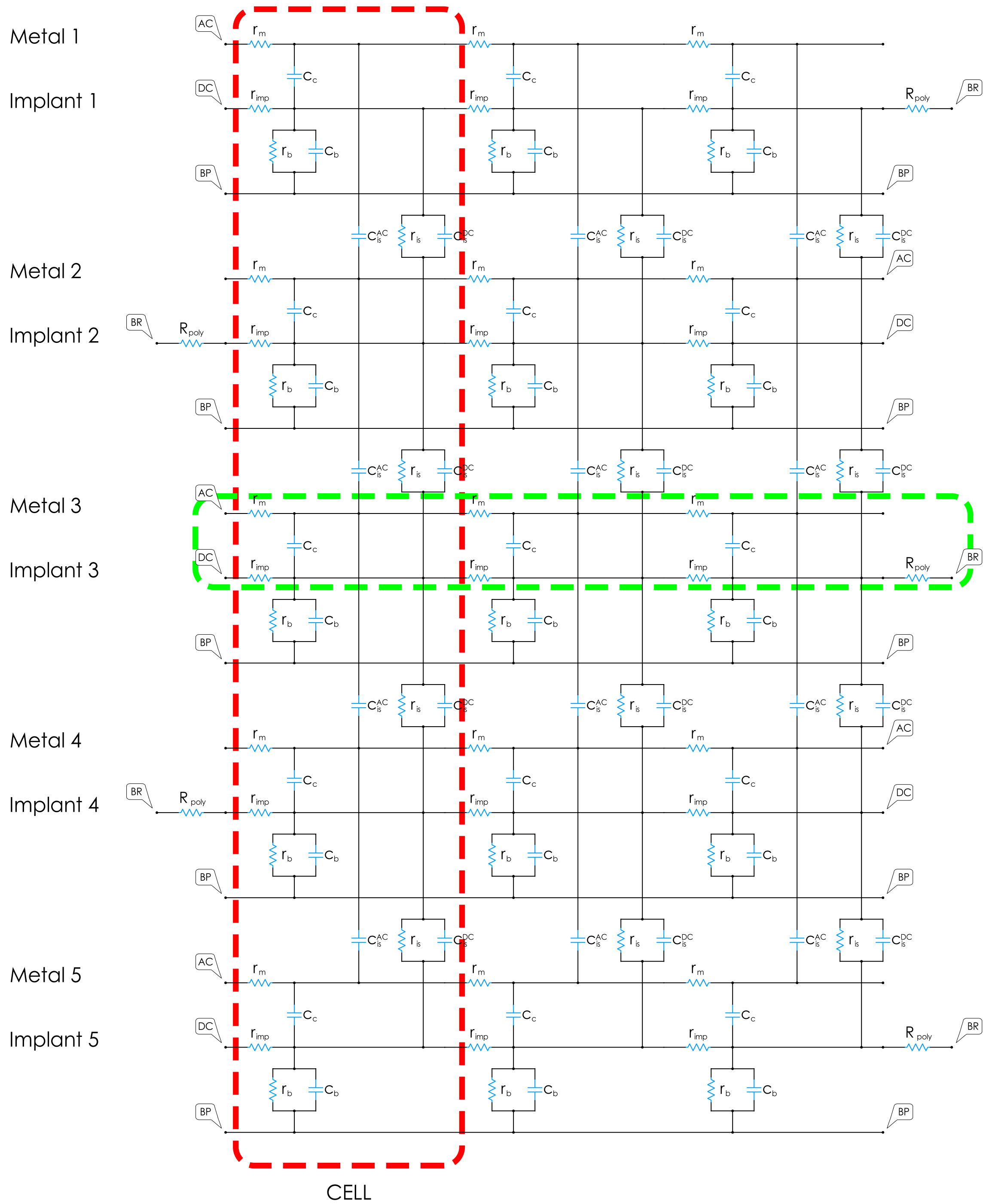

Figure 5.1.: SPICE model for simulating CBM microstrip sensors. It contains five strips, which are divided into cells. The red dashed line encircles one cell. The model shown consists of three cells, while the actual simulation used models with up to 100 cells. The green dashed line encircles the central strip, which includes the metal, implant and coupling capacitance. The model elements and their initial values are listed in Table 5.1. The labels *AC* and *DC* indicate the connection points of the AC and DC pads. The labels *BR* and *BP* denote the bias ring and the backplane.

Table 5.1.: Initial values of the electrical parameters for the SPICE model of the CBM microstrip sensor. The variables “size” and “cells” specify the size of the sensor and the number of cells in the model.

Parameter	Symbol	Value
Implant resistance	r_{imp}	$100\,\mathrm{k\Omega} \cdot$ size/cells
Coupling capacitance	c_c	$15\,\mathrm{pF/cm} \cdot$ size/cells
Metal resistance	r_m	$15\,\Omega/\mathrm{cm} \cdot$ size/cells
Polysilicon resistance	R_{poly}	$R_{DC} - r_{imp} \cdot$ cells
Interstrip resistance	r_{is}	$100\,\mathrm{M\Omega/cm} \cdot$ size $\cdot$ cells
Interstrip capacitance AC	c_{is}^{AC}	$0.05\,\mathrm{pF/cm} \cdot$ size/cells
Interstrip capacitance DC	c_{is}^{DC}	$0.4\,\mathrm{pF/cm} \cdot$ size/cells
Backplane capacitance	c_b	$0.2\,\mathrm{pF/cm} \cdot$ size/cells
Backplane resistance	r_b	$100\,\mathrm{M\Omega/cm} \cdot$ size $\cdot$ cells

5.1.2. LCR Meter

The LCR meter supplies a small AC voltage signal and measures the induced current and its phase shift. Impedance is given by:

$$Z = |Z|e^{j\theta} = \frac{|V_{meas}|}{|I_{meas}|}e^{j\theta} \tag{5.1}$$

where $|V_{meas}|$ is the voltage amplitude across the DUT[4], $|I_{meas}|$ is the current through the DUT, θ is the corresponding phase shift. One is interested in such electrical parameters as capacitance and resistance. The LCR meter evaluates these parameters from the real and imaginary parts of the impedance, assuming a series or parallel two-component equivalent circuit for the DUT:

$$C_s = -\frac{1}{\omega|Z|\sin\theta} \qquad R_s = |Z|\cos\theta \tag{5.2}$$

$$C_p = -\frac{1}{\omega|Z|}\sin\theta \qquad R_p = \frac{|Z|}{\cos\theta} \tag{5.3}$$

where ω is the angular frequency.

The SPICE model of the LCR meter is based on the same principle. It was simulated by introducing an AC voltage source at a point corresponding to the location of the *HI* probe. The current was recorded at the location of the *LO*

[4]Device under test.

probe by placing another voltage source, which is set to source 0 V. The capacitance is evaluated using the SPICE functions $Ph(x)$ and $Mag(x)$ for complex data:

$$C_s = -\frac{1}{w \cdot \frac{Mag\left(V(AC_pad_3)\right)}{Mag\left(I(Amp)\right)} \cdot \sin\left(Ph(I(Amp)) - Ph(V(AC_pad_3))\right)} \tag{5.4}$$

$$C_p = -\frac{1}{w \cdot \frac{Mag\left(V(AC_pad_3)\right)}{Mag\left(I(Amp)\right)}} \cdot \sin\left(Ph(I(Amp)) - Ph(V(AC_pad_3))\right) \tag{5.5}$$

The guard terminal was simulated by connecting the respective strips and/or bias ring to a common ground.

5.1.3. Running the Simulation

To run a simulation, it is necessary to define the type of analysis to be performed. Since the main goal is to reproduce the frequency dependence of the measured capacitance, the small signal AC analysis was performed in the frequency range from 100 Hz to 2 MHz. Ten points per decade are simulated at frequencies that correspond to experimental data. The following SPICE directive defines the type of analysis:

```
.ac dec 10 100 2Meg
```

The analysis was repeatedly performed by stepping through the model parameters that directly affect the measured electrical quantities. For example, the directive:

```
.step param Cc 1.0p 1.4p 0.01p
```

steps through the coupling capacitance c_c from 1.0 pF to 1.4 pF in steps of 0.01 pF. The remaining model parameters were subjected to uniform Monte Carlo variations with mean values as listed in Table 5.1. The simulated frequency response curves are compared to that measured with the LCR meter for every sensor. Least squares minimization was used to determine parameter values for the SPICE model which best fit the experimental data.

5.2. Strip Coupling Capacitance

First, the measured coupling capacitance was simulated. The AC-DC and AC-BR configurations[5] were implemented in the SPICE model. The corresponding

[5] A detailed description of the measurement configurations is provided in Section 4.2.5.

capacitance was calculated in the series model using Eq. 5.4. Figure 5.2 shows an example of simulation results for the CBM $62 \times 62\,\mathrm{mm}^2$ sensor manufactured by Hamamatsu. The simulated frequency response curves fit the experimental data for both sides of the sensor well. Simulation of the AC-DC and AC-BR configurations results in the same set of parameters, indicating that the constructed SPICE model provides a correct description of the CBM microstrip sensor. It describes well the drop in the measured capacitance at high frequencies and confirms the conclusions of Section 4.2.5. The simulation results indicate that the capacitance measured in the AC-BR configuration can be considered a good approximation of the actual coupling capacitance when measured at low frequency within the plateau region. The SPICE model also reproduces the effect of R_{imp}/R_{poly} divider, which results in a lower measured capacitance in the AC-DC configuration.

The design of the CBM sensors does not allow a direct measurement of the resistance parameters of the strip. Only the combined value of the implant and polysilicon resistance was measured[6] and used in the simulation to constrain the parameter space. The obtained average implant resistance values for the n and p sides of the CBM06 prototype sensors are:

$$\begin{aligned} CiS: &\ (n)46 \pm 2\,\mathrm{k\Omega/cm},\ (p)49 \pm 3\,\mathrm{k\Omega/cm} \\ Hamamatsu: &\ (n)34 \pm 1\,\mathrm{k\Omega/cm},\ (p)121 \pm 4\,\mathrm{k\Omega/cm} \end{aligned}$$

where the uncertainties indicate one standard deviation of values of the simulated sensors[7]. While the value of the implant resistance is similar on both sides of the CiS sensors, it is significantly larger on the p side of the Hamamatsu sensors. This explains why the coupling capacitance measured in the AC-DC configuration on the p side of the Hamamatsu sensors has the lowest value.

It was pointed out that the simple relationship between actual and measured coupling capacitance described by Eq. 4.43 does not take into account the spatial distribution of the strip parameters. The SPICE simulations were used to investigate the relationship between the actual capacitance and the capacitance measured in the AC-DC configuration. The simulation was performed for polysilicon resistance values in the range from $0.1\,\mathrm{M\Omega}$ to $100\,\mathrm{M\Omega}$. Large values of R_{poly} correspond to the case without a current loss to the bias ring. Implant resistance and coupling capacitance values were simulated within typical ranges for each sensor size and for the two vendors. The AC-DC capacitance values were extracted at a frequency of 1 kHz. The simulation results are shown in Fig. 5.3 as a function of the R_{imp}/R_{poly} ratio. It was found that the dependence of the measured capacitance on the R_{imp}/R_{poly} ratio can be described by a simple relationship:

$$\frac{C_c^{AC-DC}}{C_c^{actual}} = \frac{a}{1 + \dfrac{R_{imp}}{R_{poly}}} + b \tag{5.6}$$

[6] See Section 4.2.2.
[7] A total of 9 Hamamatsu and 23 CiS sensors.

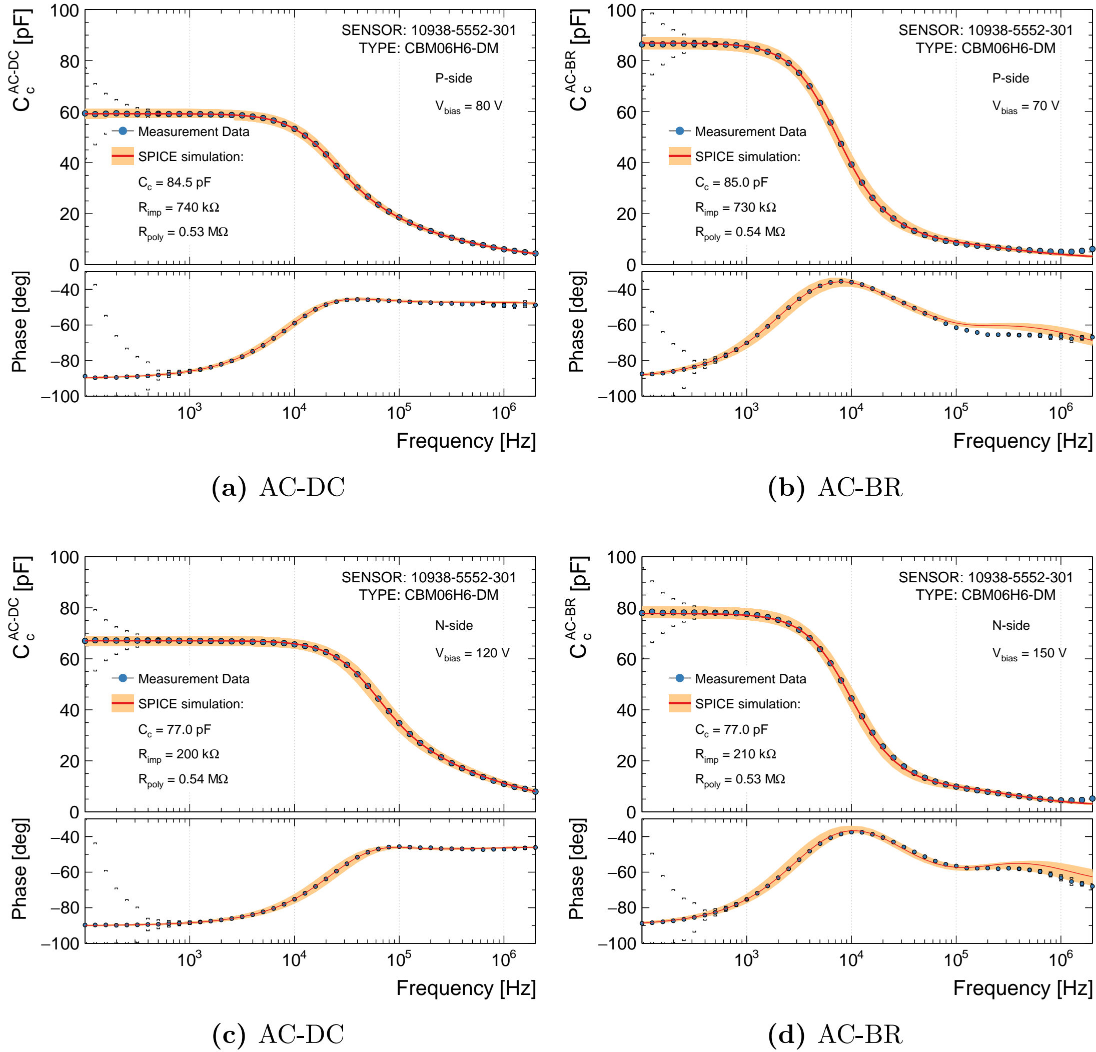

Figure 5.2.: SPICE simulation of the frequency dependence of the strip coupling capacitance measured in the AC-DC and AC-BR configurations for both sides of the CBM06 microstrip sensor. Simulation results for Hamamatsu $62 \times 62\,\mathrm{mm}^2$ sensor are shown. The orange band includes all simulated curves that fall in 3σ around the capacitance measured at low frequency. The red curve represents the best fit with the parameters that are quoted in each plot.

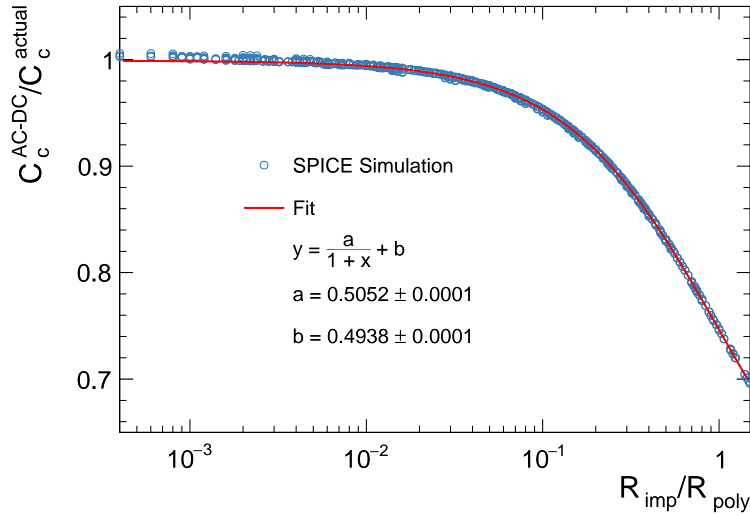

Figure 5.3.: Dependence of the capacitance simulated in the AC-DC configuration on the R_{imp}/R_{poly} ratio. The data points are the outcome of the SPICE simulation for a wide range of c_c and r_{imp} parameters. R_{poly} was simulated from relatively low values that can be seen as a short circuit to the bias ring to relatively high values that approximate an isolated strip.

where $a = 0.5052$ and $b = 0.4938$ are the fit parameters, C_c^{AC-DC} is the capacitance simulated in the AC-DC configuration, $C_c^{actual} = \sum c_c$ is the actual coupling capacitance that can be obtained using the AC-BR configuration. When R_{poly} is comparable to or lower than R_{imp}, the measured capacitance is less than the actual capacitance. If $R_{poly} \to 0$, only half of the actual capacitance is measured. When $R_{poly} \gg R_{imp}$, it approaches the actual coupling capacitance. Since the measurement in the AC-BR configuration has lower accuracy and a narrower frequency range, the AC-DC configuration is preferable. To measure the coupling capacitance independent of the R_{imp}/R_{poly} ratio, it is recommended to place DC pads near the polysilicon resistors when designing the microstrip sensor.

Since the strip is not an isolated object, the frequency dependence of the measured coupling capacitance is sensitive to other electrical parameters of the strip. The SPICE simulation allows detailed study of the related effects by stepping through each model parameter while fixing others. Figure 5.4 shows the simulated CF curves for the coupling capacitance determined in the AC-BR and AC-DC configurations[8]. The phase is plotted next to the CF curves because it reflects changes in circuit impedance. Each of the inspected parameters has a distinct effect on the frequency dependence of the measured coupling capacitance:

- In the AC-BR configuration, the capacitance C_c^{AC-BR} at low frequency corresponds to and is determined by the SPICE coupling capacitance C_c. Only

[8]Here, the AC-DC configuration only applies to designs where the DC pad and the polysilicon resistor are at opposite ends of the strip. This does not affect the AC-BR configuration.

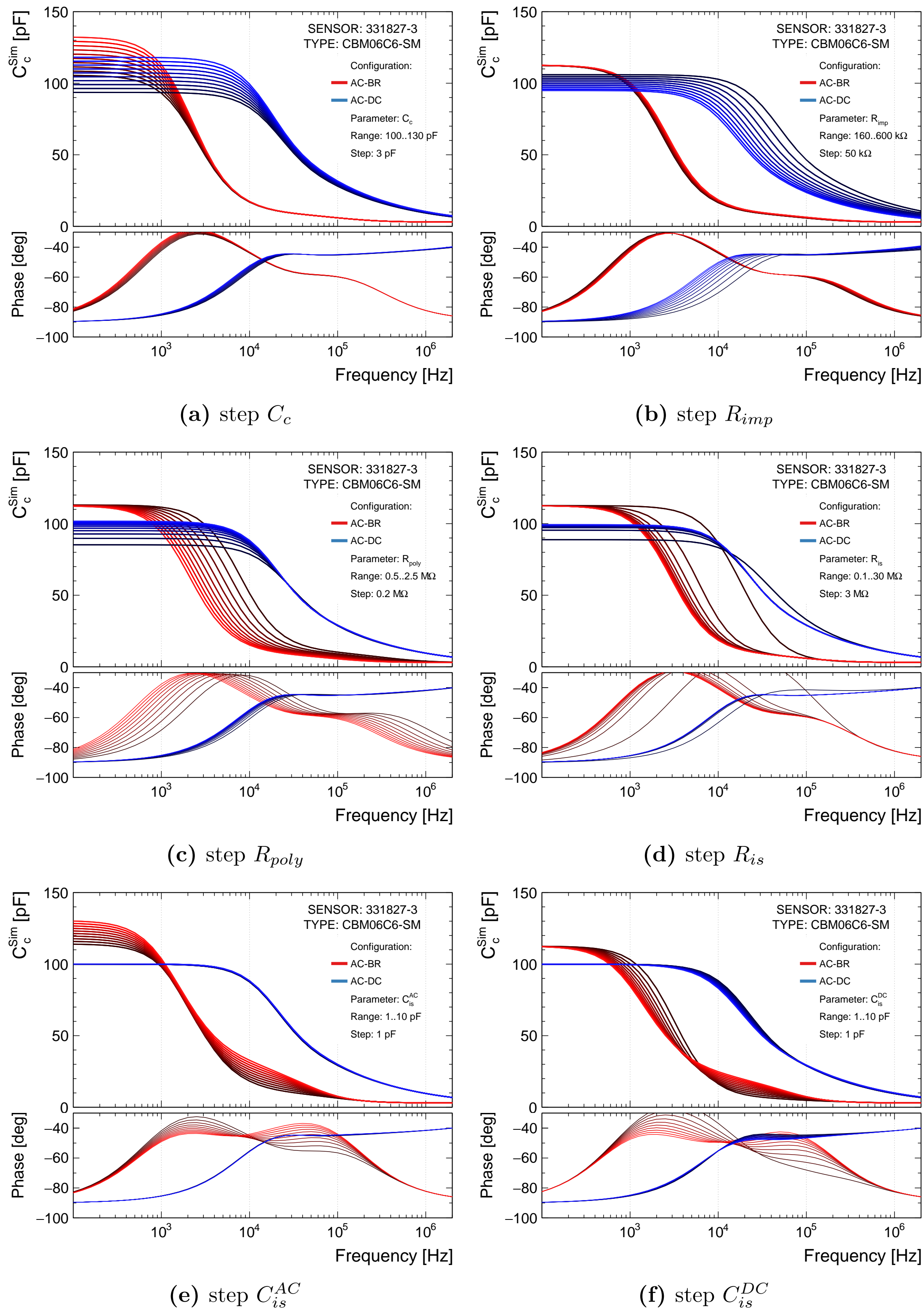

(a) step C_c **(b)** step R_{imp}

(c) step R_{poly} **(d)** step R_{is}

(e) step C_{is}^{AC} **(f)** step C_{is}^{DC}

Figure 5.4.: SPICE simulation of the influence of the electrical parameters of the strip on the coupling capacitance determined in the AC-DC and AC-BR configurations.

increasing the interstrip capacitance C_{is}^{AC} increases C_c^{AC-BR} because they are connected in parallel in the AC-BR configuration. The position of the inflection point of the CF curve is mostly determined by R_{poly}. Higher values reduce the frequency range that can be used to measure coupling capacitance. Low values of the interstrip resistance R_{is} shift the inflection point towards higher frequencies, which is equivalent to reducing the polysilicon resistance. The shift in the opposite direction occurs at high values of the interstrip capacitance C_{is}^{DC}.

- In the AC-DC configuration, the capacitance C_c^{AC-DC} at low frequency is reduced and depends on the SPICE coupling capacitance C_c, the polysilicon resistance R_{poly} and the implant resistance R_{imp} according to the relationship in Eq. 5.6. The implant resistance is the only parameter that directly affects the position of the inflection point of the CF curve in the AC-DC configuration. A low interstrip resistance R_{is} reduces the effective polysilicon resistance and, in turn, further reduces the capacitance C_c^{AC-DC}. The interstrip capacitance has no significant effect on the coupling capacitance in the AC-DC configuration.

The metal resistance R_m is much smaller than the implant resistance and does not affect the coupling capacitance in the studied frequency range.The obtained information can be useful for quality assurance of microstrip sensors in order to identify potential problems.

5.3. Bulk Capacitance

The bulk capacitance of a microstrip sensor above full depletion has a similar frequency dependence as the strip coupling capacitance. In a first-order approximation, it can be described by a model with the same equivalent circuit as shown in Fig. 4.46 for one strip. The strips on the p and n sides of the sensor are combined into one for each side. They are connected to the bias ring via a combined bias resistance $R_{poly}/1024$. The simulation model consists of 50 cells, where every cell consists of one resistor $R_{imp}^{n/p}/1024/cells$ for each side and capacitors $C_{bulk}/1024/cells$ interconnecting these resistors. Resistors $R_{bulk} \cdot cells$ were added in parallel with the bulk capacitors to simulate the bulk resistance.

Figure 5.5a shows the frequency dependence of the bulk capacitance for the Hamamatsu $62 \times 22\,\mathrm{mm}^2$ sensor. Even with such a simplified model, an agreement between simulation and measurement is achieved. The position of the inflection point of the CF curve is determined by the R_{poly} value, similar to the coupling capacitance in the AC-BR configuration. The implant resistance has little impact. It can be concluded that the capacitance measured within the plateau region in the two-component assumption is a good approximation of the actual bulk capacitance for an over-depleted sensor.

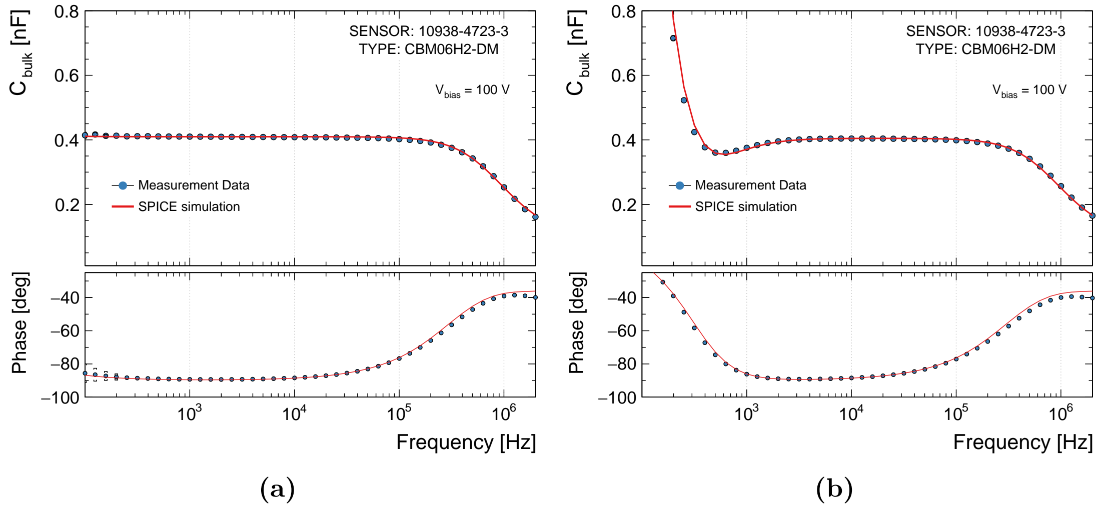

(a) **(b)**

Figure 5.5.: SPICE simulation of the bulk capacitance measured for the CBM06 microstrip sensor at a bias voltage of 100 V. Measured and simulated CF curves are shown for the Hamamatsu $62 \times 22\,\text{mm}^2$ sensor. (a) A case of a properly arranged measurement circuit. (b) There is no grounding of the bias voltage source.

It was shown in Section 4.1.3 that grounding, isolation of devices, etc. have a severe effect on measurement of the bulk capacitance. The effect was reliably reproduced in SPICE. An example of the frequency dependence of the bulk capacitance for the Hamamatsu $62 \times 22\,\text{mm}^2$ sensor is shown in Fig. 5.5b. Typically, the CV characteristic is measured at 1 kHz. If the voltage source has insufficient insulation or no grounding, the reduced capacitance is measured at 1 kHz. This shows the importance of the frequency scan to detect circuit design faults and to ensure a high quality of CV measurements.

5.4. Interstrip Capacitance

A 4-probe configuration[9] with grounded neighboring strips was implemented in the SPICE model to simulate the measured interstrip capacitance. The corresponding capacitance was calculated in the parallel model using Eq. 5.5. Figure 5.6 shows an example of simulation results for two $62 \times 62\,\text{mm}^2$ CBM06 sensors manufactured by CiS and Hamamatsu. The simulated frequency response curves fit the experimental data for both sides of the sensors well. The constructed SPICE model allows to reproduce all the features of the CF curves and confirms the model of the interstrip gap discussed in Section 4.2.7. The simulation results indicate that the capacitance measured at high frequencies (within the plateau) in the 4-probe configuration can be considered a good approximation of the capacitance to the first neighboring strip.

[9] A detailed description of the measurement configurations is provided in Section 4.2.7.

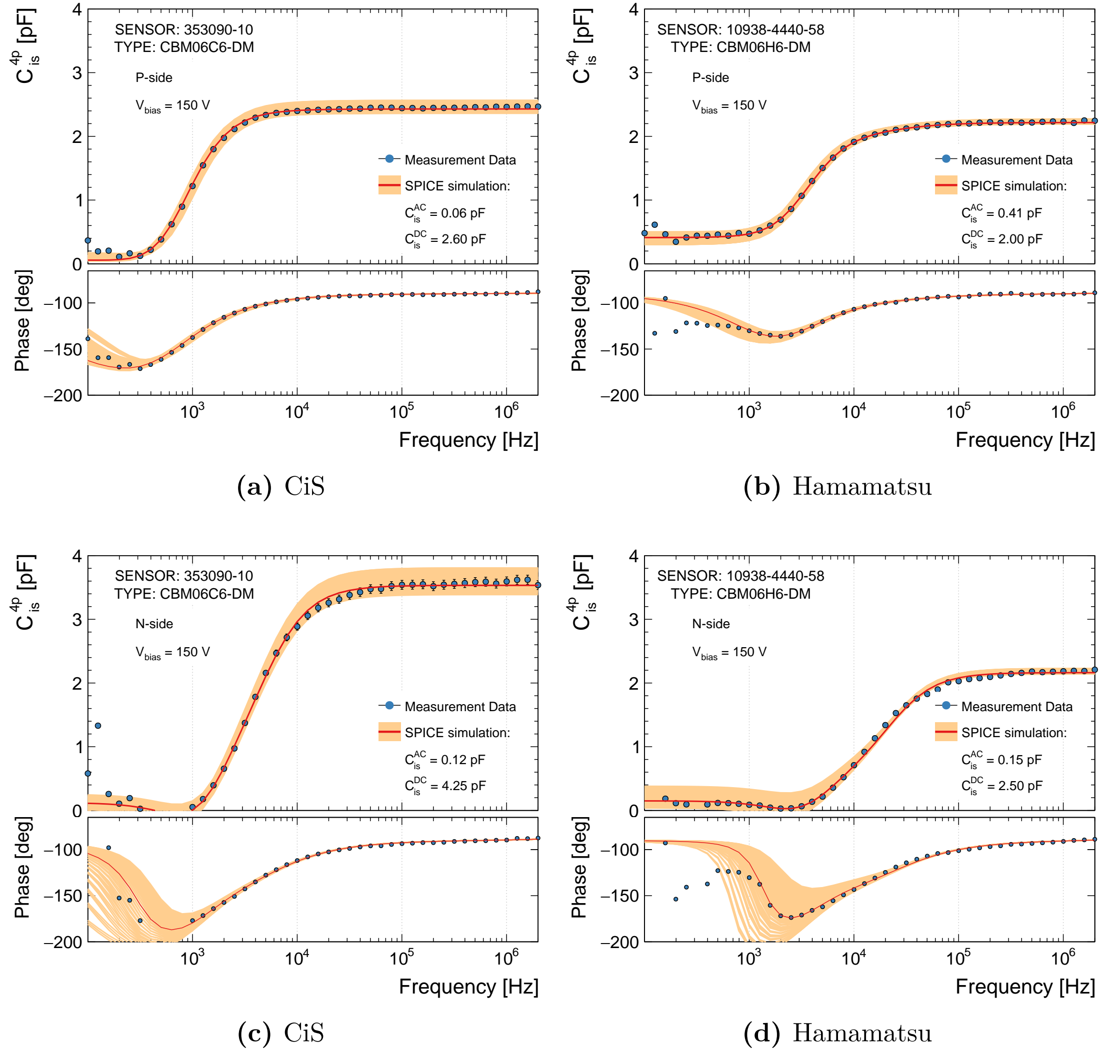

(a) CiS **(b)** Hamamatsu

(c) CiS **(d)** Hamamatsu

Figure 5.6.: SPICE simulation of the frequency dependence of the interstrip capacitance measured in the 4-probe configuration for both sides of the CBM06 microstrip sensor. Simulation results for two $62 \times 62\,\mathrm{mm}^2$ sensors from CiS and Hamamatsu are shown. The orange band includes all simulated curves that fall in 3σ around the capacitance measured at 1 MHz frequency. The red curve represents the best fit with the interstrip parameters that are quoted in each plot. The rest of the electrical parameters have the values defined in the SPICE simulation of the coupling capacitance.

The same SPICE model used to simulate the p-side interstrip capacitance could not reproduce the shape of the frequency dependence of the n-side interstrip capacitance. The model was modified by adding an additional implant strip between the two probed strips. Its purpose is to represent an isolation structure on the n side of the sensor. The isolation strip was connected to the bias ring via a series connection of a capacitor and a resistor with values adjusted for each sensor[10]. This effectively introduces another voltage divider that reduces the measured capacitance and the frequency range where it can be measured. The simulation results for the n side show that its interstrip capacitance has to be measured at frequencies above 1 MHz.

It was shown in Section 4.2.7 that the measured interstrip capacitance depends on many electrical parameters of the strip. The SPICE simulation allows detailed study of these dependencies by stepping through each model parameter while fixing others. Figure 5.7 shows the simulated CF curves for the interstrip capacitance determined in the 4-probe configuration. The phase is plotted next to the CF curves because it reflects changes in circuit impedance. The measured interstrip capacitance at high frequencies is determined only by its C_{is}^{AC} and C_{is}^{DC} components. Since C_{is}^{AC} is the capacitance directly between the metal strips, it is not affected by the parallel circuit of C_{is}^{DC}, and its contribution is present over the entire frequency range. Typically, the capacitance C_{is}^{AC} did not exceed 0.05 pF/cm for the investigated sensors, and C_{is}^{DC} was the dominant term. Low frequencies are shunted to a grounded bias ring, so the measured capacitance is reduced. The position of the inflection point of the CF curve is determined only by the R_{poly} and C_c parameters. In addition, smaller C_c values reduce the measured interstrip capacitance, in agreement with Eq. 4.56. The implant resistance R_{imp} has no significant effect on the interstrip capacitance measured at AC pads.

A specific dependence on the R_{is} parameter is observed. The interstrip resistance is in parallel with the capacitance C_{is}^{DC}. When it becomes low compared to the reactance of C_{is}^{DC}, the measured interstrip capacitance at low frequencies approaches the value of $C_c/2$ according to Eq. 4.57. However, the lowest frequencies are cut by the R_{poly} and C_c parameters. Therefore, a characteristic peak structure develops instead of a plateau. Such a peak structure was observed on the p side of the CBM06 prototype sensors from batch 353090. Figure 5.8 shows the SPICE simulation results for two sensors with the R_{is} parameter 0.35 MΩ and 3.7 MΩ. Such low interstrip resistance values degrade the strip isolation and render the microstrip sensor ineffective as a position-sensitive device.

5.5. Strip Leakage Current

It was stated in Section 4.2.1 that it is not possible to measure the full strip leakage current with the present design of the CBM sensors. The main problem

[10]Typically, the capacitance was about 10 pF, and the resistance was several MΩ.

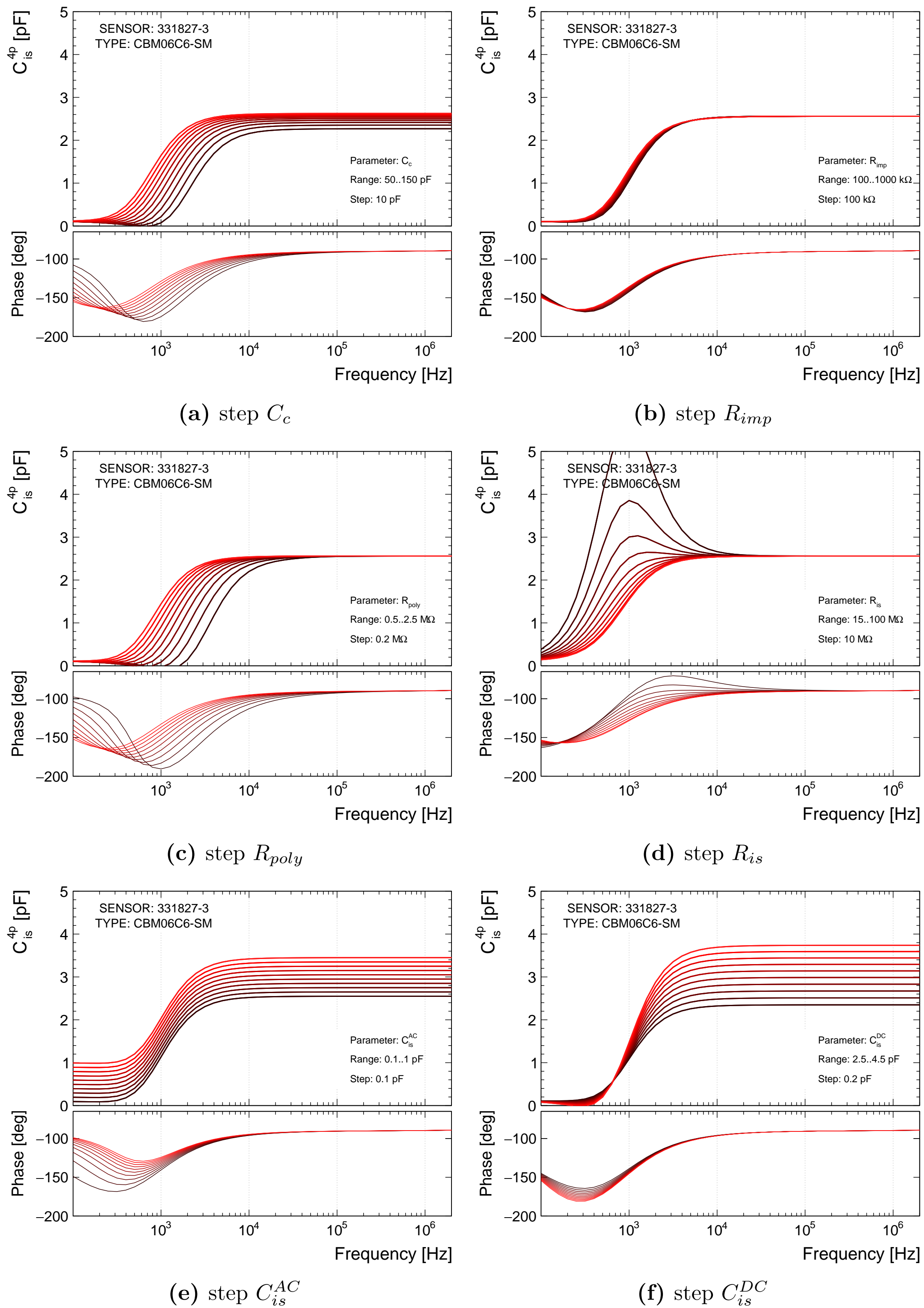

(a) step C_c

(b) step R_{imp}

(c) step R_{poly}

(d) step R_{is}

(e) step C_{is}^{AC}

(f) step C_{is}^{DC}

Figure 5.7.: SPICE simulation of the influence of the electrical parameters of the strip on the interstrip capacitance determined in the 4-probe configuration.

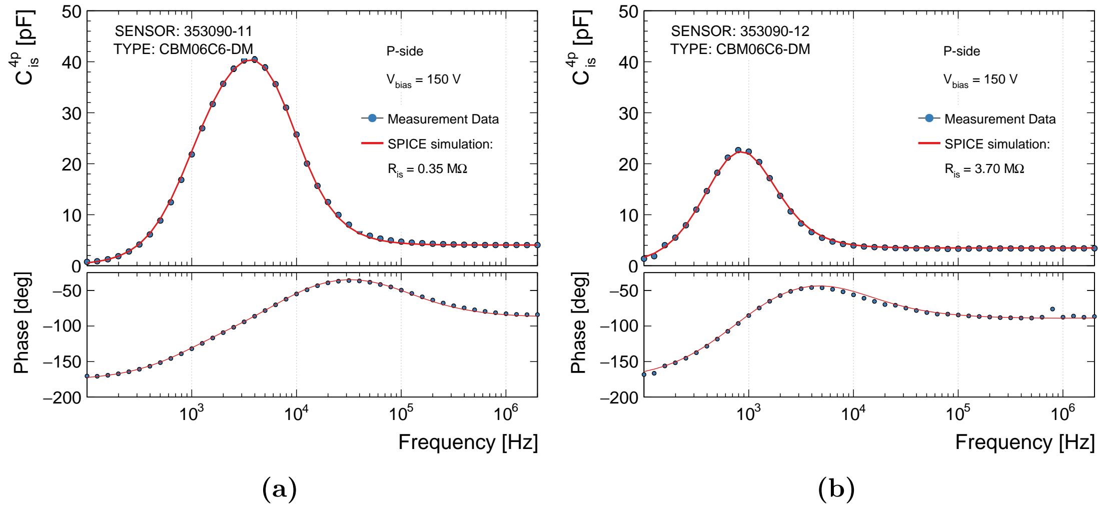

Figure 5.8.: SPICE simulation of the frequency dependence of the *p*-side interstrip capacitance measured for CBM06 microstrip sensors from batch 353090. The low interstrip resistance leads to the development of a characteristic peak structure at lower frequencies. Two examples of CiS sensors with different values of the interstrip resistance are shown.

is the finite resistance of the implant, which is comparable to the polysilicon resistance of the CBM sensors. While the measurement of the strip leakage current for sensors with the DC pad near the polysilicon resistor gives the total strip current I^{total}_{strip}, only a fraction is measured if the DC pad is at the opposite end of the strip. A simple relationship was obtained in Section 4.2.1 by analyzing the resistive network of the strip sensor. However, the strip implant cannot be represented by a single resistor, but has a distributed resistance along the entire length. The leakage current is collected by the implant along its entire length, and thus Eq. 4.16 gives only an approximate relationship between the measured and the total strip current.

The SPICE simulations were performed to investigate the relationship between measured and total strip leakage current. The sensor model is simplified and includes only one strip implant, which is connected to the bias ring via the polysilicon resistor R_{poly}. The strip implant is divided into cells, which consist of the implant resistance r_{imp} and the current source I_s, which represents a portion of the strip leakage current. A model with 100 cells was used for simulation. Figure 5.9 shows the SPICE model of one strip. The simulation was performed for polysilicon resistance values in the range from 0.1 MΩ to 100 MΩ. Implant resistance values were simulated within typical ranges for each sensor size and for two vendors. The strip current $I^{total}_{strip} = \sum I_s$ was stepped through 1 nA up to 10 nA, which corresponds to the typical range of strip current of the CBM06 sensors. The current through resistors R_{DC} and R_{poly} is recorded.

The simulation results are shown in Fig. 5.10 as a function of the R_{imp}/R_{poly}

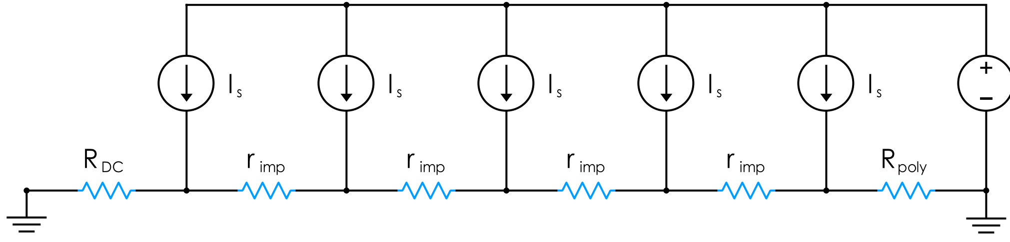

Figure 5.9.: SPICE model for simulation of the strip leakage current measurement of the CBM06 prototype sensors. It contains one strip divided into cells. Each cell consists of an implant resistance r_{imp} and a current source I_s.

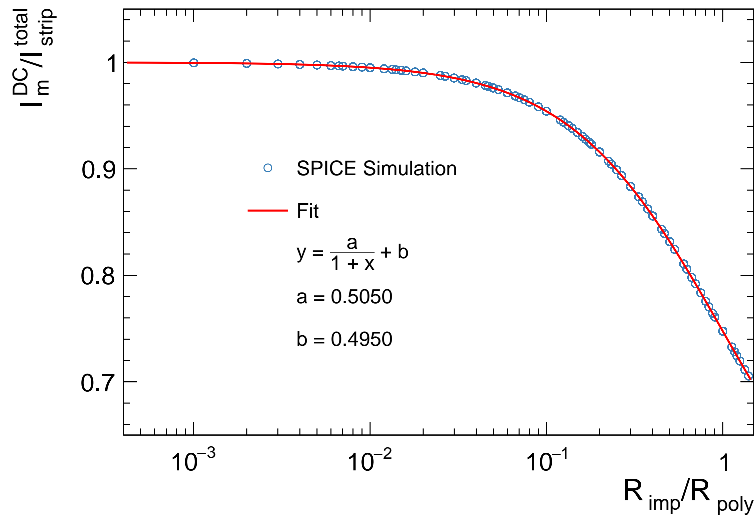

Figure 5.10.: Dependence of the strip current on the R_{imp}/R_{poly} ratio. The data points are the outcome of the SPICE simulation. I_m^{DC} is the current measured at the DC pad and I_{strip}^{total} is the total strip current.

ratio where $R_{imp} = \sum r_{imp}$. They confirm that the current measured at the DC pad is only a fraction of the total strip current and allow the actual current to be estimated knowing the appropriate resistances. The obtained dependence on the R_{imp}/R_{poly} ratio is the same as for the measured coupling capacitance C_c^{AC-DC} shown in Fig. 5.3. An obvious difference is visible for very low values of the R_{imp}/R_{poly} ratio, where the $I_m^{DC}/I_{strip}^{total}$ ratio approaches unity and C_c^{AC-DC}/C_c^{actual} goes higher. This is because one strip is simulated for the strip leakage current, while five strips are simulated for the coupling capacitance. When R_{imp}/R_{poly} becomes low, the current flowing through the neighbors flows to the measured strip, instead of the bias ring. Therefore, the measured capacitance is higher and is consistent with Eq. 4.35.

6. CBM-STS Quality Assurance Program

Stringent STS performance requirements, non-repairability of the detector modules, high cost of its components demand reliable and efficient quality assurance (QA) procedures. The STS will use 876 double-sided double-metal microstrip sensors assembled into detector modules[1]. A series of quality control tests have to be performed for each sensor before module assembly. An in-depth investigation of the final prototype sensors, labeled as CBM06, resulted in the specifications for acceptance criteria for series production. This chapter addresses aspects of the electrical qualification of the microstrip sensors as a part of the STS QA program.

6.1. Acceptance Criteria

Acceptance of each sensor is based on several criteria. Firstly, the manufactured sensors must comply with the CBM specifications for the global electrical parameters:

- Full depletion voltage in the range $40\,\mathrm{V} < V_{FD} < 150\,\mathrm{V}$;
- Breakdown voltage not lower than 200 V;
- Total leakage current below $125\,\mathrm{nA/cm^2}$ at a bias voltage of 200 V.

In addition, there are specifications for the values of the strip parameters:

- Strip coupling capacitance $C_c > 10\,\mathrm{pF/cm}$;
- Polysilicon bias resistance $R_{poly} = 1\,\mathrm{M\Omega}$. The minimum acceptable value is $0.5\,\mathrm{M\Omega}$, and the maximum is $2\,\mathrm{M\Omega}$;
- Total strip capacitance $C_{tot} < 1.5\,\mathrm{pF/cm}$;
- Strip backplane capacitance $C_b = 0.18\,\mathrm{pF/cm} \pm 15\,\%$;
- Metal strip resistance $R_m < 12\,\Omega/\mathrm{cm}$;

[1]See Section 1.4 for description of the STS detector module.

- Interstrip resistance $R_{is} > 1\,\mathrm{G\Omega}$.

The CBM sensors have 1024 strips on each side. They collect electron-hole pairs created by charged particles. Therefore, the integrity of the strips is of high importance. The acceptance criteria also require:

- The maximum number of defective strips is below 1.5 % of all strips. This corresponds to 15 strips on each side of the sensor.

- Defective strip clusters contain not more than $2 - 3$ strips to avoid “dead” bands in the detector acceptance.

The specification for the number of defective strips comes from the STS performance considerations and is explained in the following section.

6.2. Strip Defect Rate

The influence of the fraction of non-operational (“dead”) channels on the STS performance was evaluated using simulations in Ref. [160]. Figure 6.1 shows the track reconstruction efficiency and momentum resolution of the STS as a function of the fraction of dead channels in the detector modules. For the overall performance of the STS, it is necessary to keep the total number of dead channels low. Increasing their fraction from 0 % to 3 % leads to a decrease in the track reconstruction efficiency by 1 %, from 95.5 % to 94.5 %. One channel can become non-operational due to a defect in the strip, in the micro-cable, or the readout chip. A request for zero defective strips will reduce the number of accepted sensors and, as a result, increase the total cost. A large number of defective strips would put more stringent requirements on the integrity of micro-cables and readout chips.

Therefore, it was specified that CBM microstrip sensors are allowed to have up to 1.5 % defective strips. Sensors exceeding the specified acceptance limit can be kept as spares. For reliable acceptance, it is necessary to consider the types of strip defects and their impact on the entire readout channel.

6.3. Defect Classes

The most common strip defects experienced when testing microstrip sensors can be grouped into the following classes:

- Pinholes — an electrical short or low ohmic contact between the metal layer and implant of the strip. It is the only strip defect that is potentially dangerous for the readout electronics. Pinholes in the coupling capacitor lead to the current flow into or out of the charge sensitive amplifier. Its effect depends on the level of the current and can compromise the functionality

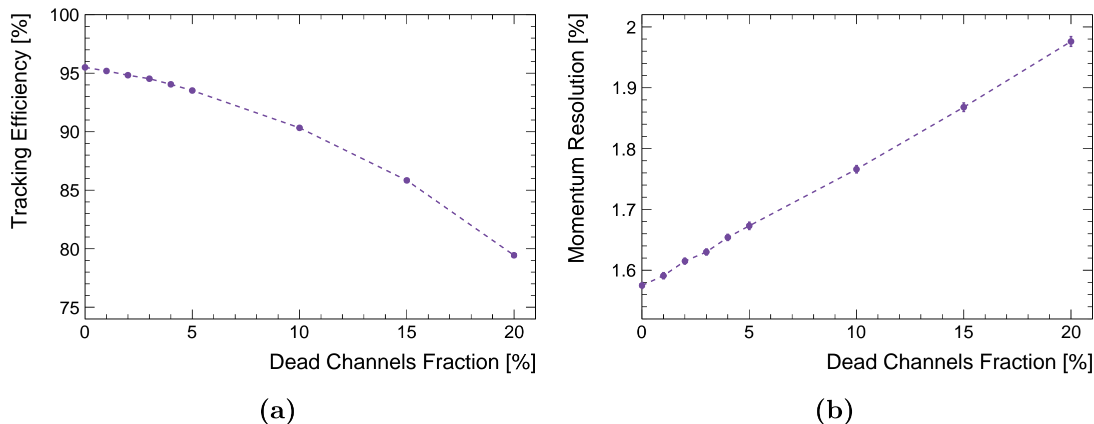

(a)

(b)

Figure 6.1.: Dependence of the track reconstruction efficiency and the momentum resolution of the Silicon Tracking System on the fraction of non-operational (dead) channels in the detector modules. The data are for fast tracks with $p > 1\,\text{GeV}/c$. The data are courtesy of Hanna Malygina [160].

of the circuit, starting from a degradation of the noise performance of the affected channel, saturation of the amplifier's output, or up to a permanent damage of the channel or even the chip [161]. Pinholes can appear during the sensor fabrication process or throughout the handling in the laboratory. Usually, the probe needles can damage the coupling capacitor, resulting in a short circuit.

- Breaks — a discontinuity in the implant or the metal of the strip. They pose no danger to the readout electronics. Breaks reduce the dimensions of the coupling capacitor and thus affect the signal amplitude. It is possible to read the signal from the polysilicon resistor to the point where the implant is broken. Whereas the sensitive area is not affected when the metal line is broken. Both cases lead to a deterioration of the signal-to-noise of the channel. In addition, the broken metal line can lead to an increase in the strip leakage current due to the disturbed electric field near the implant. Implant breaks can appear during the fabrication process, and typical examples are shown in Fig. 6.2a-6.2b. Figure 6.2c shows an example of an extremely large cluster. Another type of break is a discontinuity in the routing line in the 2nd metal layer of the CBM sensors. It completely disconnects the short strip in the opposite corner from the readout electronics. A typical example is shown in Fig. 6.2h. Figure 6.2g shows an example of a break caused by the vacuum pick-up tool.

- Shorts — an electrical connection between two or more neighboring implants or metal strips. They pose no danger to the readout electronics. Channels with shorted strips have a higher load capacitance and, as a result, noise. In addition, shorted strips share the collected charge, which leads to the

appearance of multi-strip hits and loss of position resolution. Shorts can appear during the fabrication process, and typical examples are shown in Fig. 6.2i-6.2j. Another specific type of short circuit is between the n-side implant strips due to a discontinuity in the p-stop implant. It is referred to as a p-stop break and typical examples are shown in Fig. 6.2d-6.2e. Figure 6.2f shows an example of an extremely large defect cluster.

- Polysilicon faults — implantation defects that compromise normal biasing of the strips. Low polysilicon resistance results in increased channel noise. An example of a defect due to a failure in pattern formation is shown in Fig. 6.2k. For the same reason, polysilicon residues can appear in the inter-strip area, as shown in Fig. 6.2l. It can potentially short-circuit the affected strips, depending on the fabrication technology.

- Dielectric faults — Figure 6.2m shows an example of Si_3N_4 film residues outside of the pattern. The defect is not critical, but may affect the strip leakage current.

- Passivation opens — holes in the upper passivation layer of the sensor. A typical example is shown in Fig. 6.2n. Exposed metal strips can be shorted if the passivation open is filled with a conductive material.

- Dust — tiny objects of any sort that accumulate on the surface of the sensor. Usually, it can be easily removed with a nitrogen spray gun. An example of two different objects on the surface of the sensor is shown in Fig. 6.2q and Fig. 6.2r.

- Scratches — damage to the surface layer of the sensor due to improper handling. Most scratches have a strong negative impact on the sensor performance. They can interrupt the metal strips, and damage the coupling dielectric layer and the implant strips underneath it. Typically, this results in a high leakage current, which increases the noise of the corresponding channel. A deep scratch may result in a pinhole-type defect. An example of a serious defect caused by a probe needle is shown in Fig. 6.2p. Figure 6.2o shows an example of the contact pads affected by multiple scratches. Such contact pads are not suitable for bonding.

- Leaks — strips with a leakage current higher than the typical value. Most defects can cause an increase in strip current. It may also be an indication of the inhomogeneity of the silicon wafer. It leads to an increase in the noise of the corresponding channel. In combination with a pinhole, it can saturate the amplifier's output.

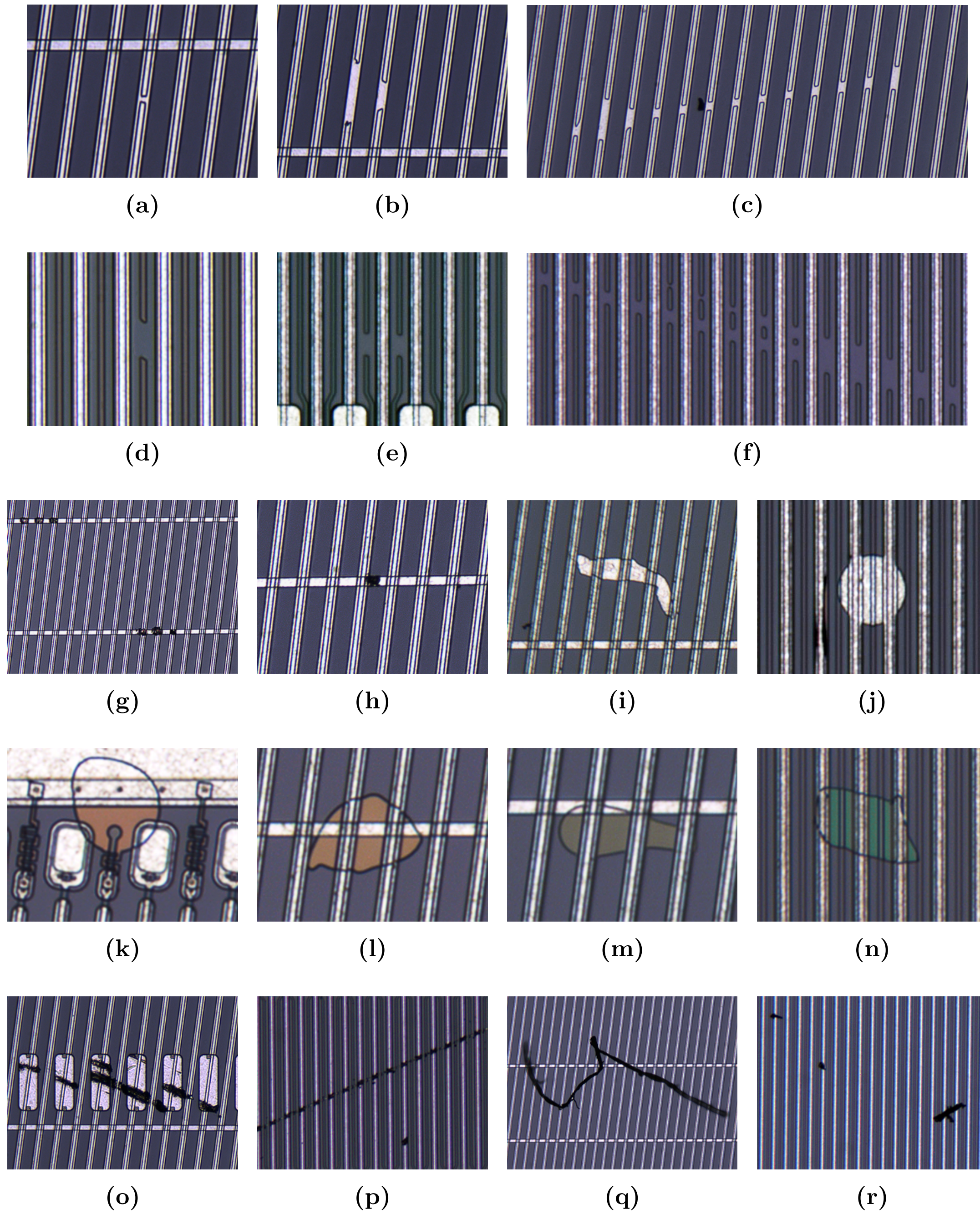

Figure 6.2.: Typical strip defects of the microstrip sensors that can be identified visually. See text for details.

6.4. Quality Control Tests

A deviation of the electrical parameters from the nominal values can indicate a defect in the sensor. Therefore, the measurement of the electrical characteristics is a good approach to quality assurance. The combination of optical and electrical inspections allows to find and identify all types of defects.

Every sensor is tested by the manufacturer before shipping to the GSI/FAIR campus. Inspection prescriptions for the manufacturer are specified in a corresponding technical note in Ref. [63]. After delivery, all sensors undergo a series of quality checks, including optical and electrical.

Optical inspection is performed for all delivered sensors. Objectives are to control the geometrical parameters of the sensors and search for macroscopic defects. This is an important test since most of the defects that affect the electrical behavior of the sensors are easily detected. Advanced methods were developed at the University of Tübingen [100].

Electrical inspection comprises two steps: basic (sensor) tests and strip tests. Basic tests consist of IV and CV characterization. The bias voltage scan is extended to 500 V, which is the maximum voltage before the breakdown to ensure high charge collection efficiency of the irradiated CBM sensors. The electrical inspection of strips focuses on two aspects: integrity and compliance of the parameters with the CBM specifications. The goal of the integrity tests is to identify defective strips. The standard set includes “pinhole” and “open/short” tests performed in the AC-BR configuration for every strip. Strip leakage current is not included in the standard set of integrity tests. It is measured only for sensors with suspicious IV characteristics. The electrical quality control tests are summarized in Table 6.1, and Chapter 4 provides a detailed description of the measurements. Basic tests are performed for every sensor, while strip tests are performed on a sample basis. Since parameter variations within batches are smaller than variations across batches, a representative percentage of the sensors will be inspected by the collaboration. It can be adjusted after qualifying the first delivery.

6.5. Infrastructure

The quality control of the delivered microstrip sensors is performed by the CBM collaboration in the GSI Detector Laboratory. The test stations are set-up in the cleanroom equipped with air filtering (class 10000). In addition, temperature and humidity are controlled[2].

For the optical inspection, a modular and highly flexible optical setup was developed at the University of Tübingen [100]. It is equipped with an XY motorized inspection table, a motorized Z stage with controllable zoom and focus stages. The setup performs the quality control of the surface and geometrical

[2]Temperature: $22 \pm 1\,^{\circ}$C. Relative humidity: $21 \pm 2\,\%$.

Table 6.1.: Description of the electrical quality control tests.

Tests	Volume	Parameter	Conditions
Sensor level			
IV	100 %	I_{150}, V_{BD}	bias up to 500 V, in 5 V steps
CV	100 %	V_{FD}, C_{bulk}	bias up to 200 V, in 2 V steps, frequency $f_{test} = 2\,\mathrm{kHz}$
Strip level			
Pinhole	10 %	I_{diel}	$V_{test} = 20\,\mathrm{V}$
Open/Short	10 %	C_c^{AC-BR}, ESR^{AC-BR}	$C_s - R_s$ mode, $f_{test} = 300\,\mathrm{Hz}$, bias $V_{bias} = \pm 100\,\mathrm{V}$
AC scan	1 %	$C_c(f, V)$, $C_{is}(f, V)$, C_{tot}	frequency $f_{test} = 100\,\mathrm{Hz} - 2\,\mathrm{MHz}$, bias up to 200 V
DC scan	1 %	$R_{DC}(V)$, $R_{is}(V)$, I_{strip}	bias up to 200 V, in 5 V steps, $V_{test} = 0 - 1\,\mathrm{V}$, in 0.2 V steps

parameters of the CBM microstrip sensors.

Basic electrical tests require a relatively simple setup with a properly configured and calibrated LCR meter. In contrast, strip integrity tests require a dedicated probe station with switching circuitry. A highly specialized and automated setup for the electrical characterization of the sensors was developed at the University of Tübingen[3].

To avoid transportation of the sensors between distributing and testing sites, the optical and electrical Tübingen setups were transferred to GSI in fall 2019 [162]. Figure 6.3 shows a general view of the setups installed in the cleanroom of the GSI Detector Laboratory.

6.6. Test Sockets for Sensors

Microstrip sensors require biasing for electrical inspection. A dedicated socket based on miniature spring-loaded pins[4] has been developed and produced in the industry [163, 164]. It allows two-sided contacting for bias application without

[3]See Chapter 3 for a complete description of the setup.

[4]Pogo pins.

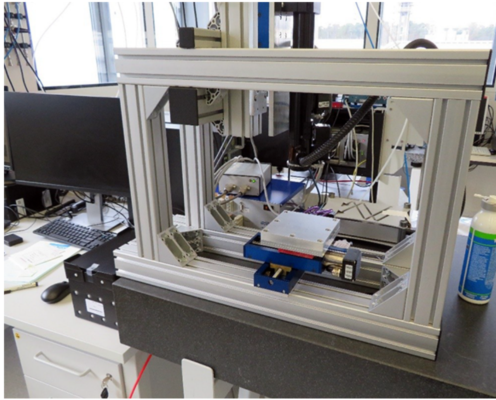

(a)

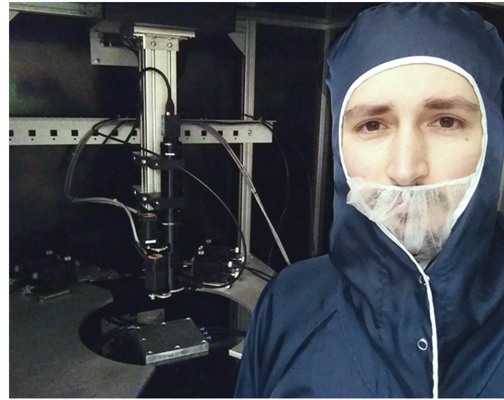

(b)

(c)

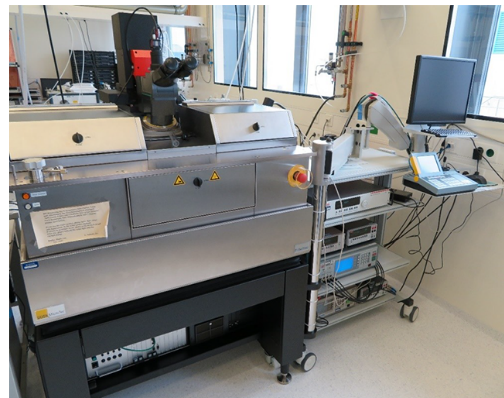

(d)

Figure 6.3.: CBM Quality Test Center at the GSI Detector Laboratory, Darmstadt: (a) custom-built automated setup for optical inspection of sensors, (b) interior of the custom-built automated setup for electrical inspection of strips, (c) setup for basic electrical characterization of sensors, (d) commercial wafer prober Suss PA300PS used during prototyping stage and for testing the irradiated CBM sensors.

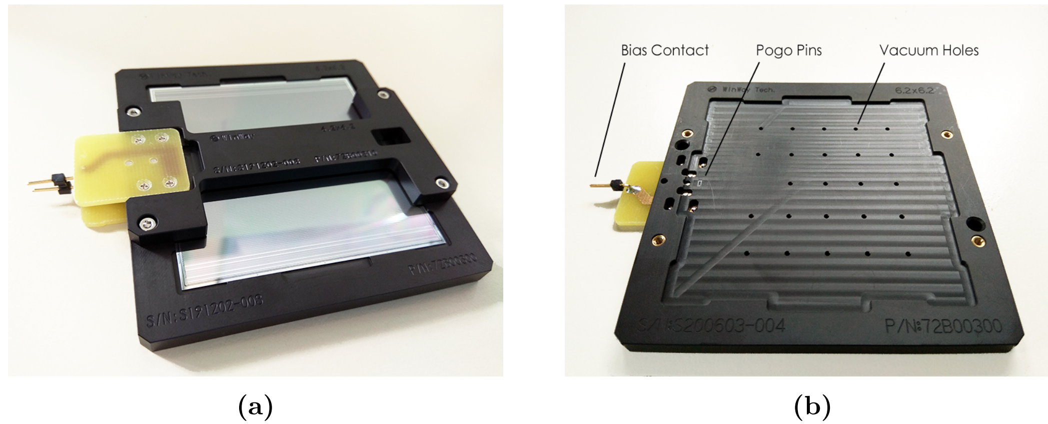

(a) (b)

Figure 6.4.: Test socket with pogo pins for CBM microstrip sensors: (a) general view with the assembled $62 \times 62\,\mathrm{mm}^2$ sensor; (b) the bottom part of the socket.

the necessity of wire bonding. Figure 6.4a shows a general view of the socket with the assembled $62 \times 62\,\mathrm{mm}^2$ sensor. Individual variants were produced for each sensor size.

During strip-by-strip measurements, the sensor is fixed by vacuum suction to the metal chuck through the holes in the bottom plate of the socket. This ensures that the height profile of the sensor does not change under the pressure of a contacting needle. Figure 6.4b shows the bottom plate of the socket where the vacuum holes and pin positions are visible. To ensure that the application of vacuum does not cause substantial mechanical stress on the sensor, the leakage current is continuously monitored during all strip tests.

The produced test sockets simplify handling and reduce the time required to prepare the microstrip sensor for the electrical inspection.

6.7. Needles and Contact Pads

The AC contact pads are used for the electrical inspection of the sensors both at the manufacturing facilities and at the CBM quality test center. The probe needles are placed on the contact pads, which are not used for bonding during the assembly process[5]. Good contact quality is essential for the repeatability and accuracy of the measurements. Tungsten needles with a 5 µm tip diameter are used. They are mounted on the probe arm at about 30° allowing for safe contact with the AC pad. A height profile is recorded before placing the needles to ensure reliable contact for all 1024 strips[6]. Once the needles are positioned, the automated strip testing procedure can be launched. The Z coordinate of the sensor is automatically adjusted for every strip. Figure 6.5 shows the CBM

[5] 1st row of the AC pads on the p side and 2nd row on the n side are reserved for bonding.
[6] See Section 3.2.8 for a description of the procedure.

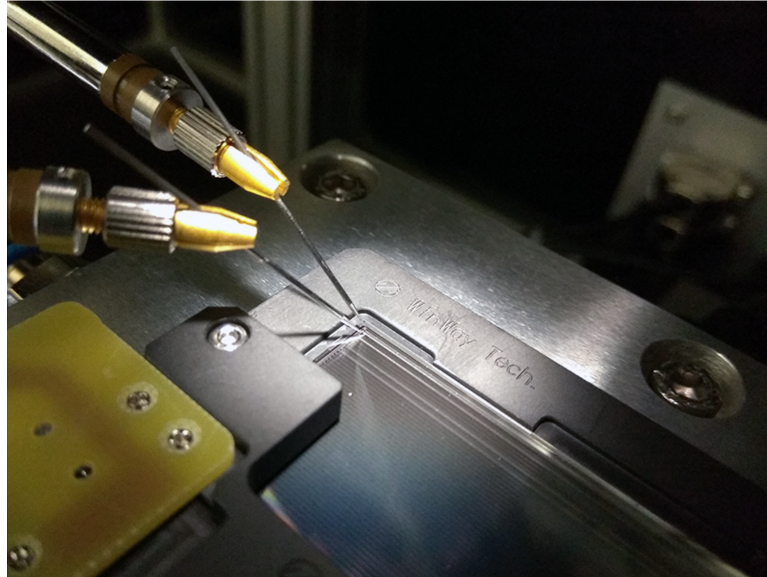

Figure 6.5.: CBM microstrip sensor under the probe needles that are positioned to contact the AC pads of the first two strips. The sensor is assembled in the test socket and placed on the vacuum chuck. It is ready for the strip integrity tests.

microstrip sensor and the probe needles positioned for the strip integrity tests.

Aluminum debris accumulates on the needles during the probe process. This affects the contact resistance. After measuring each side of the sensor, the needles should be cleaned with a soft brush. The needles also tend to bend as the number of contacts made increases. Therefore, they are replaced with a new set after testing five double-sided sensors.

6.8. Strip Data Analysis

It is important to keep the total number of defective strips within the specified limits to ensure a proper STS performance. The strip integrity tests were designed for the CBM microstrip sensors to detect all defects that could lead to a non-operational or faulty readout channel. A dedicated set includes "pinhole" and "open/short" tests[7]. Three quantities are measured in the AC-BR configuration for every strip: dielectric current I_{diel}, series capacitance C_c^{AC-BR}, equivalent series resistance ESR^{AC-BR}. The measured parameters deviate from the typical values in the presence of a defect. The task is to find such deviations and recognize the corresponding types of defects.

[7] See Table 6.1 for details.

6.8.1. Signatures of Defects

Various defects can be recognized by their signatures in the strip data. Specifics of the sensor design and measurement procedure have to be taken into account. In particular, the measured capacitance and resistance parameters will differ for even and odd strips of the CBM sensor that are affected by the same defect.

- Pinholes are characterized by the dielectric current I_{diel}. Its value depends on the resistance of the pinhole R_{ph}. Typically, it is below 100 pA if the coupling capacitor is intact. An order of magnitude higher current indicates a defect in the dielectric layer. In the AC-BR measurement configuration, the current of several µA is the signature of the actual pinhole for the CBM sensors. The capacitance and resistance parameters will deviate from typical values if R_{ph} becomes too low or comparable to the reactance of the coupling capacitor.

- Metal breaks reduce the area of the coupling capacitors, so the measured series capacitance is always lower than the typical value. Figure 6.6a shows a schematic representation of two neighboring strips affected by a metal break. Since all strips are contacted from the same edge, the measured equivalent series resistance shows different behavior for even and odd strips. It is lower than the typical value for strip i:

$$ESR^{AC-BR} = R_{poly} + x \cdot R_{imp}/3 \tag{6.1}$$

  and larger than the typical value for strip i+1:

$$ESR^{AC-BR} = R_{poly} + x \cdot R_{imp}/3 + (1-x)R_{imp} \tag{6.2}$$

  where x is the fraction of the strip with the measured capacitance.

- Implant breaks, similar to metal ones, reduce the area of the coupling capacitors. Figure 6.6b shows that both even and odd strips have C_c^{AC-BR} and ESR^{AC-BR} parameters reduced in proportion to the measured fraction of the strip. It should be noted that the implant and metal breaks for strip i share similar signatures.

- Metal shorts are characterized by the measured capacitance increased in proportion to the number of shorted metal strips:

$$C_c^{AC-BR} = N \cdot C_{typical}. \tag{6.3}$$

  The ESR^{AC-BR} parameter is, in turn, reduced due to the parallel connection of polysilicon resistors. Figure 6.6c shows a schematic representation of a metal short between two strips. The signature is the same for even and odd strips and should not depend on the position of the short.

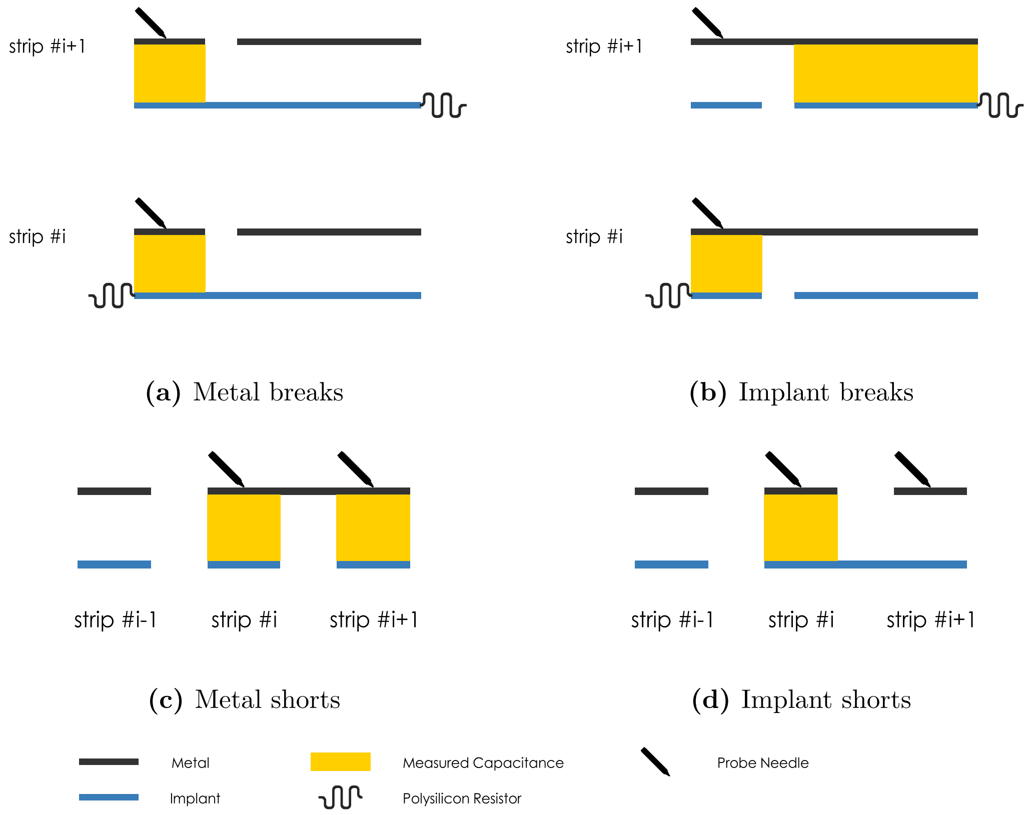

Figure 6.6.: Schematic representation of broken and shorted strips of the microstrip sensor. The measured capacitance and resistance parameters are different for even and odd stripes affected by the same defect.

- Implant shorts do not affect the measured series capacitance, whereas the ESR^{AC-BR} parameter is always reduced compared to the typical value. Figure 6.6d shows a schematic representation of an implant short between two strips. Obviously, ESR^{AC-BR} differs for even and odd strips when measuring from the same edge, but always remains in the range:

$$ESR_{typical}/2 < ESR^{AC-BR} < ESR_{typical}. \tag{6.4}$$

SPICE simulations were performed for the CBM sensors to better understand and confirm the signatures of the corresponding defect types. Figure 6.7 shows the simulated C_c^{AC-BR} and ESR^{AC-BR} parameters for two neighboring strips and three defect types: metal break, implant break, and implant short. The signatures of the metal breaks follow the predicted behavior for both even and odd strips. It was necessary to introduce the parameters R_b and R_s, which represent the resistance of the implant "break" and "short", respectively. The resistance signature of the implant short satisfies the condition 6.4, and higher values of R_s

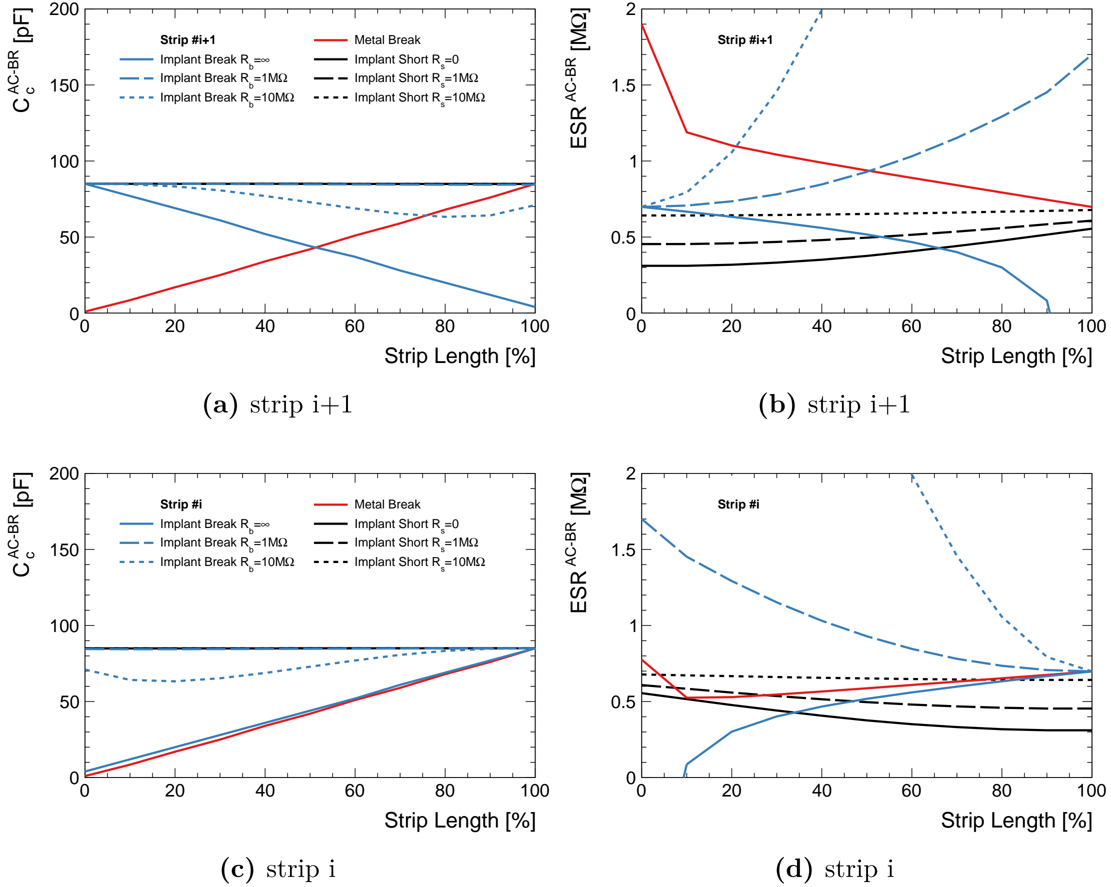

(a) strip i+1 (b) strip i+1

(c) strip i (d) strip i

Figure 6.7.: SPICE simulation of the capacitance and resistance parameters for the AC-BR configuration and for various defect types. Simulations were performed as described in Chapter 5 for the CBM sensor with the following parameters: C_c = 85 pF, R_{imp} = 700 kΩ, R_{poly} = 0.5 MΩ. The parameters R_b and R_s represent the resistance of the implant "break" and "short", respectively. The fraction of the strip involved in the measurement, that is, the position of the defect along the strip, is plotted on the horizontal axis.

make the defect less noticeable due to increased isolation between the implants. The finite resistance R_b dramatically changes the behavior of the implant break signatures. Its C_c^{AC-BR} parameter does not decrease proportionally to the fraction of the measured capacitance, and a larger capacitance is always observed. Whereas, its ESR^{AC-BR} parameter shows higher than typical values. For low values of R_b, the capacitance signature of implant breaks disappears completely. This is, for example, the case of the n-side implants, where the presence of the electron accumulation layer leads to low resistances. Therefore, an increase in ESR^{AC-BR} becomes a reliable signature of the implant break. On the other hand, very high values of the ESR^{AC-BR} parameter may indicate insufficient inter-strip isolation.

6.8.2. Detection of Defective Strips

The detection of defective strips is based on the application of thresholds to the measured parameters. Pinholes can be detected by applying a global threshold to I_{diel}. The same approach does not work well for the C_c^{AC-BR} and ESR^{AC-BR} parameters. Thresholds have to be applied locally for each strip. This requires knowledge of strip parameter values in the absence of a defect. The median filtering technique was used to determine the typical parameter values. It is widely used in digital signal and image processing because it preserves edges while effectively removing noise. A 1D standard median filter was implemented in this work. Its performance depends on the window size. Since defects often appear in clusters, the median filter must recognize and filter them instead of considering such strips as a structure in the measurement data. The results of the optical inspection of the CBM sensors [165] indicate that clusters of more than five defective strips are not likely to be present, while clusters of up to 18 strips were observed. A window size of 15 was used for most of the tested sensors.

After filtering, it is necessary to determine the threshold values for deciding when the strip can be declared as defective. Local thresholds were calculated for each sensor and side, based on the standard deviation of the measurement data. A strip was marked as defective if one of its parameters deviated from the filtered values by 5σ. Such a threshold proved to be sufficient to detect all defective strips on sensors of different sizes and avoid false detection. Ultimate sensitivity depends on the quality of measurement data. Figure 6.8 shows an example of the application of this method to the CBM sensor to detect defective strips.

6.8.3. Recognition of Strip Defects

Strips marked as defective after filtering are subject to defect analysis. The efficient recognition of defects requires careful consideration of their signatures. Figure 6.7 shows that in some cases the defects may share some of the signatures. Therefore, the decision-making sequence is organized in a way to provide

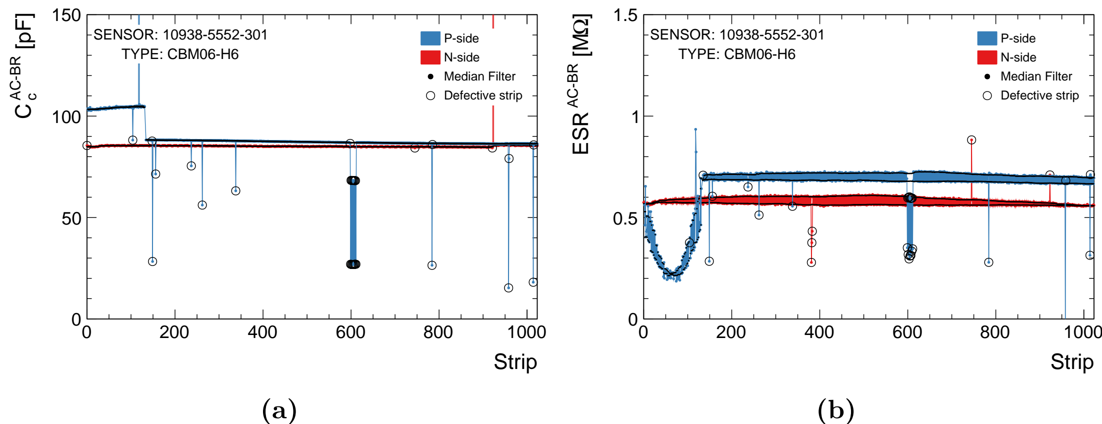

Figure 6.8.: Application of the median filter and local thresholds to strip data for detection of defective strips. All outliers are reliably detected and ultimate sensitivity depends on the quality of measurement data.

unambiguous recognition of defects. Figure 6.9 shows a simplified flowchart diagram of the developed defect-recognition algorithm. Before starting, a contact loss check is performed over the entire data set using mean squared error. Pinholes are checked first because they also affect the capacitance and resistance parameters of the strip and can lead to the wrong assignment of the defect class. Further recognition steps are based only on the capacitance C_c^{AC-BR} and resistance ESR^{AC-BR} parameters of the strip. In rare cases, defects are not recognized. Typically, this is due to a bad contact between the needle and the AC pad. It is a good practice to check the corresponding strip under a microscope.

The defect detection and recognition algorithm was tested for the CBM microstrip sensors of all sizes. As an example, Table 6.2 summarizes the detected and recognized defects for the prototype sensor 10938-5552-301. The p side of this sensor suffers from a large number of broken implants. In particular, a cluster of 14 consecutive breaks[8] accounts for almost half of all defects. All identified defects were confirmed optically, which confirms the reliability and effectiveness of the method.

6.9. Quality of the CBM sensors

6.9.1. Prototype Testing Results

32 prototype sensors for the CBM experiment were fully characterized at the University of Tübingen. The strip parameters were intensively studied using a dedicated custom-built probe station. Chapter 4 gives a detailed overview of the conducted tests and their results. In particular, Table 4.1 shows the results of

[8] See Fig. 6.2c.

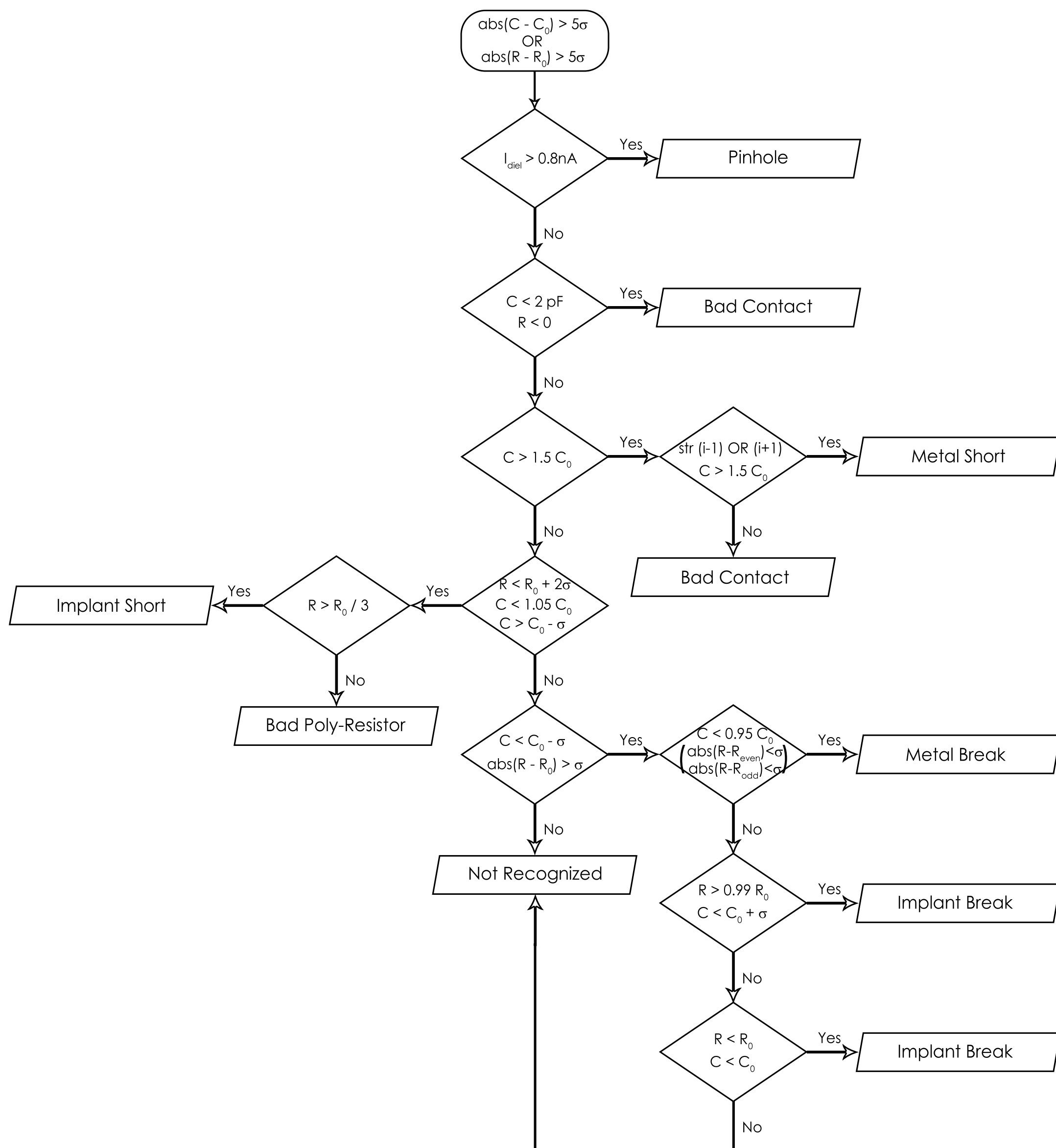

Figure 6.9.: A flowchart diagram representing the process of defect recognition. It provides unambiguous recognition of all strip defects that affect its integrity. C and R denote the measured values, while C_0 and R_0 are the outcome of the median filter. σ denotes the standard deviation of the corresponding parameter. It should be noted that the strips with the 2nd metal lines include additional nodes to recognize defects of the 2nd metal layer. It is omitted here for simplicity.

Table 6.2.: Results of the defect recognition for the prototype sensor 10938-5552-301.

Defect type	p side	n side
Pinholes	118, 119	923
Metal breaks	104	–
Implant breaks	135, 148, 149, 156, 237, 262, 338, 598 – 611, 784, 785, 958, 959, 1014, 1015	745, 921
Metal shorts	–	–
Implant shorts	–	381, 382, 383
Total	30(2.93 %)	6(0.59 %)

the "pinhole" test for the investigated sensors. The fraction of defective coupling capacitors was found to be less than 0.5 % and consistent with the vendor's data. Strip capacitance, strip resistivity, and polysilicon bias resistors meet the required specifications or can be upgraded to them. Both CiS and Hamamatsu have demonstrated that CBM06 sensors can be produced with high quality.

6.9.2. Production Testing Results

At the time of writing this dissertation, Hamamatsu Photonics has manufactured 1202 microstrip sensors for the CBM experiment. Hamamatsu carried out the detection of pinholes and defects of the metal layer. All delivered sensors comply with the requirement of less than 1.5 % defective strips. Other types of defects were not detected by the manufacturer. Therefore, the CBM collaboration performs optical and electrical inspections. Most of the tested sensors meet the CBM specifications of non-irradiated sensors for leakage current and full depletion voltage [113], as well as for the number of defective strips [165].

The electrical inspection of strips was performed for 80 sensors. It included: one complete batch of $62 \times 22\,\mathrm{mm}^2$ sensors, one sensor from each delivered batch, and additional sensors with a large number of defects. While the results confirm the optical inspection results for implant breaks, implant shorts, metal breaks, and metal shorts, the electrical inspection also identifies pinholes. Figure 6.10 shows the combined map of defective strips for n and p sides of all inspected sensors. On the n side, it was found that most of the identified pinholes are located in two regions: around strip numbers 350 and 700. On the p side, an increased number of defects is observed for groups of strips that are connected via the 2$^{\mathrm{nd}}$ metal layer. The optical inspection revealed a circular pattern for the defects on both sides of the sensors. Identified regions in Fig. 6.10 with an increased number of defects

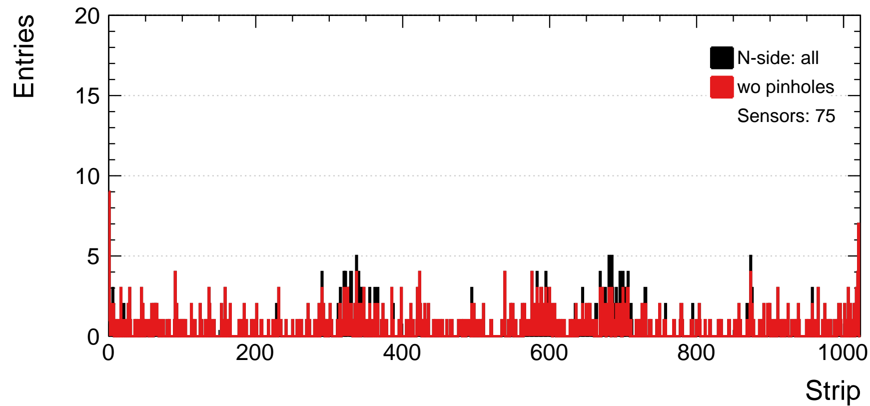

(a) n side

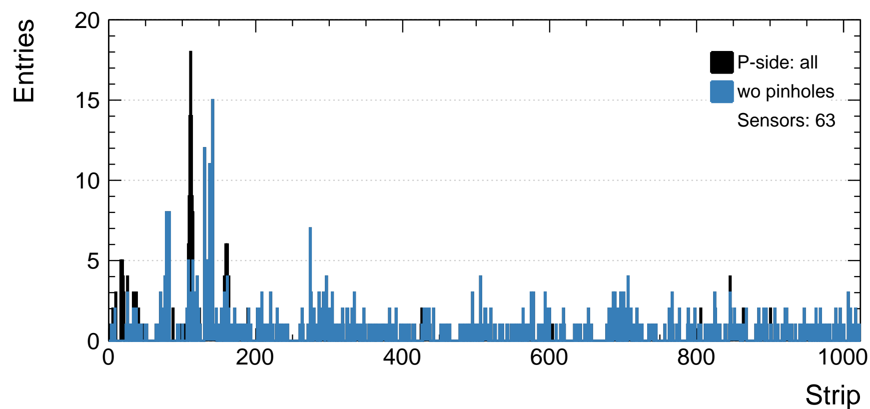

(b) p side

Figure 6.10.: Map of accumulated defective strips for n and p sides of the CBM sensors. The data for all sensor variants is combined. The different number of sensors for n and p sides is due to the identified contact loss for some sensors.

correlate with this pattern. It was attributed to the usage of a vacuum tool to handle the sensor during production at the manufacturing site. The distribution of defects in other regions is quite uniform, without any tendencies.

Further analysis, including grading of the sensors, is ongoing. The overall quality grade will be finally calculated based on the information available from all inspections. The sensor characteristics and inspection results are stored in a dedicated component database. The information will be relevant later as an input for selecting the appropriate sensor during the module and ladder assembly.

7. Summary

The Silicon Tracking System of the CBM experiment imposes strict requirements on the component quality of the detector module, which consists of a microstrip sensor, a signal-transmission micro-cable, and a readout ASIC. One of the main objectives of this thesis was the development of quality assurance and control procedures for the CBM microstrip sensors. The path was completed from the development and construction of the custom test station, characterization and simulation of prototypes, to the final qualification of series production of the sensors.

As part of this thesis, a custom probe station was designed and built at the University of Tübingen. Dedicated calibration procedures were developed for the mechanical and optical systems of the probe station. Alignment, coordinate calibration, and height adjustment procedures were implemented for the microstrip sensors. This ensures accurate positioning of the microstrip sensor under the probe needles during strip-by-strip measurements. The probe station was equipped with a switching matrix and precise measuring devices. This allowed to automate the measurement routines, reduce the inspection time, and eliminate possible testing errors. LabVIEW-based software was developed to automate all calibration procedures and provide flexibility in operating the probe station.

In this work, considerable experimental effort was devoted to the accurate measurement of capacitance. Although offset correction procedures are relatively standard, the additional high-frequency error due to complex residuals is not eliminated by standard procedures. This results in an increase in measured capacitance of up to 57 % at the frequency at which strip capacitance is normally measured. Therefore, a special correction procedure was developed for automatic correction of the measured capacitance.

32 prototype sensors for the CBM experiment were thoroughly investigated at the University of Tübingen using the custom-built probe station. The prototype sensors of 4 different sizes were manufactured by CiS and Hamamatsu. The electrical parameters measured for the microstrip sensors are the leakage current, the full depletion voltage, various strip capacitances and strip resistances. The measurement methods and recommendations for characterization are provided. Detailed capacitance models were developed for the strip coupling, interstrip, backplane, and overlap capacitances. For the first time, systematic measurements of the electrical parameters for all 1024 strips of the CBM sensors were performed. This led to an accurate determination of the total strip capacitance, which is an important parameter that determines the detector noise and thus influences

the design of the readout electronics. Experimental efforts were accompanied by SPICE simulations of prototype sensors. It proved useful in understanding the electrical circuitry of the sensor and establishing the relationship between measured and actual strip parameters. As a result of the investigations, a detailed description of the prototype sensors was provided to the STS working group. This made it possible to define the specifications for series production of the microstrip sensors.

As a result of the conducted studies, quality control tests and acceptance criteria for CBM microstrip sensors were defined. Series production took place in 2020 and about 1200 microstrip sensors were manufactured by Hamamatsu Photonics for the STS. To avoid transportation of the sensors between distributing and testing sites, it was decided in the STS project to transfer the Tübingen probe station to the GSI Detector Laboratory. The electrical inspection of the strips was performed for about 7 % of all sensors. Within this thesis, a dedicated algorithm was developed to detect and recognize defective strips. The fraction of defective strips was found to be within specifications. However, it should be noted that a significant number of implant breaks were detected for some of the inspected sensors. Most strip defects can be identified visually and a correlation with the optical inspection has been established. Quality control of the sensors after delivery to GSI allows for the rejection of defective sensors, as well as providing input data for the module assembly stage.

In summary, this thesis covers a variety of topics related to the microstrip sensors and their electrical characteristics. Future detector systems will require new advanced sensor technologies with high spatial resolution, radiation hardness, and timing precision at the same time. But the principle remains the same: an understanding of the performance of the sensor can be obtained from a detailed electrical characterization. Therefore, elaborate quality assurance of the sensors is a prerequisite for a successful experiment.

Appendix A.

List of the Investigated CBM Microstrip Sensors

Table A.1.: List of the investigated CBM microstrip sensors.

Sensor ID	Processing	Size, mm^2	CBM name
	Manufactured by Hamamatsu		
10938-1609-5	DSDM	62×42	CBM06H4
10938-2695-2	DSSM	62×62	CBM06H6
10938-4440-58	DSDM	62×62	CBM06H6
10938-4440-60	DSDM	62×62	CBM06H6
10938-4723-1	DSDM	62×124	CBM06H12
10938-4723-3	DSDM	62×22	CBM06H2
10938-4723-7	DSDM	62×22	CBM06H2
10938-5552-301	DSDM	62×62	CBM06H6
10938-5552-310	DSDM	62×62	CBM06H6
13847-0123-3	DSDM	62×62	CBM06H6
13847-0341-3	DSDM	62×62	CBM06H6
13847-0417-1	DSDM	62×22	CBM06H2
13847-0433-4	DSDM	62×124	CBM06H12
13847-0534-3	DSDM	62×62	CBM06H6
13847-0608-4	DSDM	62×124	CBM06H12
	Manufactured by CiS		
331827-3	DSSM	62×62	CBM06C6
331827-18	DSSM	62×62	CBM06C6

Continuation of Table A.1

Sensor ID	Processing	Size, mm^2	CBM name
331827-22	DSSM	62×62	CBM06C6
342463-21	DSDM	62×124	CBM06C12
350191-04	DSDM	62×62	CBM06C6
350714-06-1	DSDM	62×22	CBM06C2
350714-18-2	DSDM	62×22	CBM06C2
350714-22-2	DSDM	62×22	CBM06C2
351135-08	DSDM	62×42	CBM06C4
351135-09	DSDM	62×42	CBM06C4
351139-09	DSDM	62×42	CBM06C4
351139-14	DSDM	62×42	CBM06C4
351139-23	DSDM	62×42	CBM06C4
351142-14	DSDM	62×42	CBM06C4
351142-16	DSDM	62×42	CBM06C4
352151-04	DSDM	62×62	CBM06C6
352151-05	DSDM	62×62	CBM06C6
352151-13	DSDM	62×62	CBM06C6
353090-08	DSDM	62×62	CBM06C6
353090-09	DSDM	62×62	CBM06C6
353090-10	DSDM	62×62	CBM06C6
353090-11	DSDM	62×62	CBM06C6
353090-12	DSDM	62×62	CBM06C6

DSSM – double-sided, single-metal
DSDM – double-sided, double-metal

Appendix B.

Measured Bulk Parameters of the CBM Prototype Sensors

Table B.1.: Bulk parameters of the CBM prototype sensors extracted in the IV-CV measurements.

Sensor ID	V_{FD} [V]	$V_{BD}{}^{*}$ [V]	I_{150V} [nA/cm^2]	C_{bulk} [pF]	ρ_{bulk} [kΩ cm]	N_{eff} 10^{11} [cm^{-3}]	d_{sensor} [µm]
			Manufactured by Hamamatsu				
10938-1609-5	70	365	37.1	768	5.4	8.5	311
10938-2695-2	69	370	27.4	1123	5.8	8.0	319
10938-4440-58	74	305	20.9	1126	5.3	8.7	318
10938-4440-60	62	325	13.5	1124	6.4	7.2	319
10938-4723-1	47	245	8.7	2273	8.6	5.4	320
10938-4723-3	69	610	9.5	395	5.2	8.9	304
10938-4723-7	70	840	11.9	400	5.0	9.2	300
10938-5552-301	53	545	6.2	1147	7.2	6.4	312
10938-5552-310	52	530	6.0	1138	7.5	6.2	315
13847-0123-3	64	–	39.4	1113	6.4	7.2	322
13847-0341-3	63	–	18.7	1117	6.4	7.3	321
13847-0433-4	77	400	36.4	2237	5.3	8.6	325
13847-0534-3	72	405	35.1	1102	5.6	8.2	322
13847-0608-4	77	400	22.7	2254	5.3	8.7	323
			Manufactured by CiS				
331827-3	79	208	379.6	1308	3.8	12.1	289
331827-18	76	280	106.7	1311	3.9	11.7	288

Continuation of Table B.1

Sensor ID	V_{FD} [V]	$V_{BD}{}^*$ [V]	I_{150V} [nA/cm^2]	C_{bulk} [pF]	ρ_{bulk} [kΩ cm]	N_{eff} 10^{11} [cm^{-3}]	d_{sensor} [µm]
331827-22	–	250	86.3	–	–	–	–
342463-21	57	30	994.2	2624	5.3	8.7	290
350191-04	69	500	364.5	1309	4.4	10.6	288
350714-06-1	69	735	102.2	449	4.1	11.4	278
350714-18-2	72	325	92.5	448	3.9	11.9	279
350714-22-2	73	330	83.7	451	3.8	12.4	277
351135-08	74	310	128.0	871	4.0	11.5	288
351135-09	66	335	135.8	876	4.5	11.4	286
351139-09	–	470	132.5	–	–	–	–
351139-14	–	480	66.2	–	–	–	–
351139-23	81	260	89.3	880	3.6	12.8	285
351142-14	–	440	193.6	–	–	–	–
351142-16	–	380	47.6	–	–	–	–
352151-04	90	535	183.1	1304	3.3	13.8	289
352151-05	70	237	159.6	1314	4.2	11.0	287
352151-13	74	144	253.8	1338	3.9	11.9	282
353090-08	89	250	131.7	1231	3.8	12.1	307
353090-09	84	245	129.0	1230	4.0	11.4	307
353090-10	96	380	146.7	1220	3.6	12.8	310
353090-11	87	205	141.8	1235	3.9	11.9	306
353090-12	85	250	449.7	1232	4.0	11.6	307

* Breakdown voltage as observed in the total leakage current measurement. In the case of a “soft” breakdown, this value does not represent actual breakdown voltage and is only for orientation.
See Sections 4.1.1 4.1.2 4.1.3 for more details.

Appendix C.

Switching Matrix Channel Configuration

Table C.1.: The configuration of the switching matrix channels for electrical measurements performed in this work.

Measurement Type	Channel List
Global CV characteristic	1C07,1G01,1H02,1H08
Global CV characteristic with grounded GR	1C03,1C07,1G01,1H02,1H08
Strip leakage current	1C02,1D03,1E02
Polysilicon bias resistance	1C02,1D03,1E09,1F09
Metal strip resistance	1C03,1D04,1E09,1F09
Strip coupling capacitance (AC-DC)	1C02,1G04,1H03
Strip coupling capacitance (AC-BR)	1C07,1G02,1G08,1H03(1H04)
Strip backplane capacitance	1C02,1G01,1H03
Interstrip capacitance (4-probe)	1C02,1C04,1C06,1G03,1H05
Interstrip capacitance (3-probe)	1C02,1G03,1H04,1H05
Pinhole test (AC-DC)	1C02,1C03,1D04,1E07,1F08
Pinhole test (AC-BR)	1C02,1D03,1E09,1F09

Cold switching is used, which means that all channels have to be closed before a signal is applied and can be reopened when no signal is present.

Bibliography

[1] F. Hartmann. Silicon tracking detectors in high-energy physics. *Nucl. Instrum. Meth. A*, 666:25–46, 2012. http://dx.doi.org/10.1016/j.nima.2011.11.005.

[2] S. Seidel. Silicon strip and pixel detectors for particle physics experiments. *Phys. Rept.*, 828:1–34, 2019. http://dx.doi.org/10.1016/j.physrep.2019.09.003.

[3] J. Kemmer. Fabrication of low noise silicon radiation detectors by the planar process. *Nucl. Instrum. Meth.*, 169:499–502, 1980. http://dx.doi.org/10.1016/0029-554X(80)90948-9.

[4] B. Hyams, U. Kotz, E. Belau, et al. A Silicon Counter Telescope to Study Short-lived Particles in High-energy Hadronic Interactions. *Nucl. Instrum. Meth.*, 205:99–105, 1983. http://dx.doi.org/10.1016/0167-5087(83)90177-1.

[5] E. Belau, J. Kemmer, R. Klanner, et al. Silicon detectors with 5 um spatial resolution for high energy particles. *Nuclear Instruments and Methods in Physics Research*, 217(1):224–228, 1983. http://dx.doi.org/https://doi.org/10.1016/0167-5087(83)90138-2.

[6] G. Batignani et al. The Aleph silicon vertex detector. *Nucl. Phys. B Proc. Suppl.*, 23:291–296, 1991. http://dx.doi.org/10.1016/0920-5632(91)90060-R.

[7] N. Bingefors et al. The DELPHI microvertex detector. *Nucl. Instrum. Meth. A*, 328:447–471, 1993. http://dx.doi.org/10.1016/0168-9002(93)90663-3.

[8] V. Chabaud et al. (DELPHI). The DELPHI silicon strip microvertex detector with double sided readout. *Nucl. Instrum. Meth. A*, 368:314–332, 1996. http://dx.doi.org/10.1016/0168-9002(95)00699-0.

[9] D. Amidei et al. (CDF). The Silicon Vertex Detector of the Collider Detector at Fermilab. *Nucl. Instrum. Meth. A*, 350:73–130, 1994. http://dx.doi.org/10.1016/0168-9002(94)91156-8.

[10] P. T. Lukens (CDF). The CDF IIb Detector Technical Design Report. 2003.

[11] V. M. Abazov et al. (D0). The Upgraded D0 detector. *Nucl. Instrum. Meth. A*, 565:463–537, 2006. arXiv:physics/0507191, http://dx.doi.org/10.1016/j.nima.2006.05.248.

[12] P. Chochula et al. (DELPHI Silicon Tracker Group). The DELPHI Silicon Tracker at LEP-2. *Nucl. Instrum. Meth. A*, 412:304–328, 1998. http://dx.doi.org/10.1016/S0168-9002(98)00344-1.

[13] M. Moll. *Radiation damage in silicon particle detectors: Microscopic defects and macroscopic properties*. Dissertation, Hamburg U., 1999.

[14] G. Aad et al. (ATLAS). The ATLAS Experiment at the CERN Large Hadron Collider. *JINST*, 3:S08003, 2008. http://dx.doi.org/10.1088/1748-0221/3/08/S08003.

[15] S. Chatrchyan et al. (CMS). The CMS Experiment at the CERN LHC. *JINST*, 3:S08004, 2008. http://dx.doi.org/10.1088/1748-0221/3/08/S08004.

[16] K. Aamodt et al. (ALICE). The ALICE experiment at the CERN LHC. *JINST*, 3:S08002, 2008. http://dx.doi.org/10.1088/1748-0221/3/08/S08002.

[17] Technical Design Report for the ATLAS Inner Tracker Strip Detector. Technical report, CERN, Geneva, 2017. https://cds.cern.ch/record/2257755.

[18] A. Tumasyan et al. (CMS Collaboration). The Phase-2 Upgrade of the CMS Tracker. Technical report, CERN, Geneva, 2017. http://dx.doi.org/10.17181/CERN.QZ28.FLHW.

[19] G. Contin et al. The STAR Heavy Flavor Tracker (HFT): focus on the MAPS based PXL detector. *Nucl. Part. Phys. Proc.*, 273-275:1155–1159, 2016. http://dx.doi.org/10.1016/j.nuclphysbps.2015.09.181.

[20] B. Abelev et al. (ALICE). Technical Design Report for the Upgrade of the ALICE Inner Tracking System. *J. Phys. G*, 41:087002, 2014. http://dx.doi.org/10.1088/0954-3899/41/8/087002.

[21] E. D. R. R. P. Group. The 2021 ECFA detector research and development roadmap. Technical report, Geneva, 2020. http://dx.doi.org/10.17181/CERN.XDPL.W2EX.

[22] G.-F. Dalla Betta and M. Povoli. Progress in 3D Silicon Radiation Detectors. *Front. in Phys.*, 10:927690, 2022. http://dx.doi.org/10.3389/fphy.2022.927690.

[23] Technical Design Report for the ATLAS Inner Tracker Pixel Detector. 2017. http://dx.doi.org/10.17181/CERN.FOZZ.ZP3Q.

[24] N. Herrmann (CBM). Status and Perspectives of the CBM experiment at FAIR. *EPJ Web Conf.*, 259:09001, 2022. http://dx.doi.org/10.1051/epjconf/202225909001.

[25] A. D. Falco (NA60+). The Physics program of the NA60+ experiment at the CERN SPS. *CPOD2021*. https://indico.cern.ch/event/985460/contributions/4264615/attachments/2211234/3742919/adf_cpod.pdf.

[26] P. Steinbrecher (HotQCD). The QCD crossover at zero and non-zero baryon densities from Lattice QCD. *Nucl. Phys. A*, 982:847–850, 2019. arXiv:1807.05607, http://dx.doi.org/10.1016/j.nuclphysa.2018.08.025.

[27] A. Andronic, P. Braun-Munzinger, K. Redlich, et al. Decoding the phase structure of QCD via particle production at high energy. *Nature*, 561(7723):321–330, 2018. arXiv:1710.09425, http://dx.doi.org/10.1038/s41586-018-0491-6.

[28] W.-j. Fu, X. Luo, J. M. Pawlowski, et al. Hyper-order baryon number fluctuations at finite temperature and density. *Phys. Rev. D*, 104(9):094047, 2021. arXiv:2101.06035, http://dx.doi.org/10.1103/PhysRevD.104.094047.

[29] F. Gao and J. M. Pawlowski. QCD phase structure from functional methods. *Phys. Rev. D*, 102(3):034027, 2020. arXiv:2002.07500, http://dx.doi.org/10.1103/PhysRevD.102.034027.

[30] P. Senger. Probing Compressed Baryonic Matter. *Universe*, 8(2):61, 2022. http://dx.doi.org/10.3390/universe8020061.

[31] I. C. Arsene, L. V. Bravina, W. Cassing, et al. Dynamical phase trajectories for relativistic nuclear collisions. *Phys. Rev. C*, 75:034902, 2007. arXiv:nucl-th/0609042, http://dx.doi.org/10.1103/PhysRevC.75.034902.

[32] M. Hanauske, J. Steinheimer, L. Bovard, et al. Concluding Remarks: Connecting Relativistic Heavy Ion Collisions and Neutron Star Mergers by the Equation of State of Dense Hadron- and Quark Matter as signalled by Gravitational Waves. *J. Phys. Conf. Ser.*, 878(1):012031, 2017. http://dx.doi.org/10.1088/1742-6596/878/1/012031.

[33] B. P. Abbott et al. (LIGO Scientific, Virgo). GW170817: Observation of Gravitational Waves from a Binary Neutron Star Inspiral. *Phys. Rev. Lett.*, 119(16):161101, 2017. arXiv:1710.05832, http://dx.doi.org/10.1103/PhysRevLett.119.161101.

[34] M. C. Miller et al. PSR J0030+0451 Mass and Radius from *NICER* Data and Implications for the Properties of Neutron Star Matter. *Astrophys. J.*

Lett., 887(1):L24, 2019. arXiv:1912.05705, http://dx.doi.org/10.3847/2041-8213/ab50c5.

[35] S. Huth et al. Constraining Neutron-Star Matter with Microscopic and Macroscopic Collisions. *Nature*, 606:276–280, 2022. arXiv:2107.06229, http://dx.doi.org/10.1038/s41586-022-04750-w.

[36] B. Friman, C. Hohne, J. Knoll, et al., editors. *The CBM physics book: Compressed baryonic matter in laboratory experiments*, volume 814. 2011. http://dx.doi.org/10.1007/978-3-642-13293-3.

[37] T. Galatyuk. Future facilities for high μ_B physics. *Nucl. Phys. A*, 982:163–169, 2019. http://dx.doi.org/10.1016/j.nuclphysa.2018.11.025.

[38] T. Ablyazimov, A. Abuhoza, R. P. Adak, et al. Challenges in QCD matter physics – The scientific programme of the Compressed Baryonic Matter experiment at FAIR. *The European Physical Journal A*, 53(3), 2017. http://dx.doi.org/10.1140/epja/i2017-12248-y.

[39] J. Heuser, W. Müller, V. Pugatch, et al. (CBM). *[GSI Report 2013-4] Technical Design Report for the CBM Silicon Tracking System (STS)*. GSI, Darmstadt, 2013. http://repository.gsi.de/record/54798.

[40] A. Malakhov and A. Shabunov, editors. *Technical Design Report for the CBM Superconducting Dipole Magnet*. GSI, Darmstadt, 2013. https://repository.gsi.de/record/109025.

[41] N. Herrmann, editor. *Technical Design Report for the CBM Time-of-Flight System (TOF)*. GSI, Darmstadt, 2014. https://repository.gsi.de/record/109024.

[42] S. Chattopadhyay, Y. P. Viyogi, P. Senger, et al., editors. *Technical Design Report for the CBM : Muon Chambers (MuCh)*. GSI, Darmstadt, 2015. https://repository.gsi.de/record/161297.

[43] C. Höhne, editor. *Technical Design Report for the CBM Ring Imaging Cherenkov Detector*. CBM Technical Design Reports. 2013. https://repository.gsi.de/record/65526.

[44] C. Blume, C. Bergmann, and D. Emschermann, editors. *The Transition Radiation Detector of the CBM Experiment at FAIR : Technical Design Report for the CBM Transition Radiation Detector (TRD)*. FAIR, Darmstadt, 2018. http://dx.doi.org/10.15120/GSI-2018-01091.

[45] F. Guber and I. Selyuzhenkov, editors. *Technical Design Report for the CBM Projectile Spectator Detector (PSD)*. GSI, Darmstadt, 2015. https://repository.gsi.de/record/109059.

[46] P. Senger and V. Friese (CBM Collaboration). CBM Progress Report 2021. Technical Report 2022, 2022. http://dx.doi.org/10.15120/GSI-2022-00599.

[47] *mCBM@SIS18*. CBM. CBM Collaboration, GSI, Darmstadt, 2017. http://dx.doi.org/10.15120/GSI-2019-00977.

[48] J. M. Heuser, V. Pugatch, H. Schmidt, et al. Description of the STS microstrip sensors for series production. CBM-STS Note CBM-TN-19005, GSI, 2019.

[49] J. M. Heuser and U. Frankenfeld (The STS Workgroup). Production Readiness Review for the STS Carbon Fiber Ladders. STS Module and Ladder Assembly CBM-TN-19006, GSI, 2019.

[50] V. Borshchov et al. Micro-Cables for the CBM-STS Detector Modules. CBM Technical Note CBM-TN-20003, 2021.

[51] M. Shiroya, D. Emschermann, E. Clerkin, et al. (CBM). Update on the simulation geometry for the Silicon Tracking System. *CBM Progress Report 2021*, (CBM-PR-2021):38, 2022.

[52] I. Tymchuk, V. Borshchov, M. Protsenko, et al. (CBM). Status report on micro-cable production for the Silicon Tracking System. *CBM Progress Report 2021*, (CBM-PR-2021):24, 2022.

[53] K. Kasinski, R. Szczygiel, P. Otfinowski, et al. (CBM). Testing and diagnostic features of the STS/MUCH-XYTER2 ASIC. *CBM Progress Report 2016*, pages 36–37, 2017. http://repository.gsi.de/record/201318.

[54] K. Kasinski, R. Kleczek, and R. Szczygiel. Front-end readout electronics considerations for Silicon Tracking System and Muon Chamber. *JINST*, 11(02):C02024, 2016. http://dx.doi.org/10.1088/1748-0221/11/02/C02024.

[55] K. Agarwal, A. Dominguez-Salguero, I. Elizarov, et al. (CBM). Mechanics of STS cooling and progress on the STS thermal demonstrator. *CBM Progress Report 2021*, (CBM-PR-2021):29, 2022.

[56] K. Agarwal, U. Frankenfeld, and H. R. Schmidt (CBM). STS sensor cooling: concept, calculations and CFD simulations. *CBM Progress Report 2020*, (2021-00421):30–31, 2021. http://dx.doi.org/10.15120/GSI-2021-00421.

[57] H. Malygina. *Hit reconstruction for the Silicon Tracking System of the CBM experiment*. Dissertation, Johann Wolfgang Goethe-Universität, 2018. http://publikationen.ub.uni-frankfurt.de/opus4/frontdoor/index/index/year/2018/docId/46401.

[58] A. Lymanets. *Development of prototype components for the Silicon Tracking System of the CBM Experiment at FAIR*. Dissertation, Johann Wolfgang Goethe-Universität Frankfurt, 2013. https://repository.gsi.de/record/53954.

[59] I. Sorokin. *Characterization of silicon microstrip sensors, front-end electronics, and prototype tracking detectors for the CBM experiment at FAIR*. Dissertation, Johann Wolfgang Goethe-Universität Frankfurt, 2014. https://repository.gsi.de/record/97618.

[60] M. Singla. *The Silicon Tracking System of the CBM experiment at FAIR : development of microstrip sensors and signal transmission lines for a low-mass, low-noise system*. Dissertation, Johann Wolfgang Goethe-Universität Frankfurt, Frankfurt am Main, 2014. https://repository.gsi.de/record/97533.

[61] P. Larionov. *Systematic irradiation studies and Quality Assurance of silicon strip sensors for the CBM Silicon Tracking System*. Dissertation, Johann Wolfgang Goethe-Universität Frankfurt, 2016.

[62] J. M. Heuser and H. R. Schmidt (CBM). Silicon Tracking System – Summary. *CBM Progress Report 2019*, pages 14–15, 2020. http://dx.doi.org/10.15120/GSI-2020-00904.

[63] J. M. Heuser, O. Bertini, J. Eschke, et al. (CBM). Start of STS microstrip sensor series production and testing. *CBM Progress Report 2019*, pages 16–19, 2020. http://dx.doi.org/10.15120/GSI-2020-00904.

[64] J. M. Heuser, V. Pugatch, H. R. Schmidt, et al. Production Readiness Review for the Silicon Sensors of the CBM Silicon Tracking System. CBM-STS Note CBM-TN-18010, GSI, 2019.

[65] CiS Research Institute of Microsensors GmbH. [Online; accessed 16-August-2020], https://www.cismst.org.

[66] Hamamatsu Photonics K.K. [Online; accessed 16-August-2020], http:/www.hamamatsu.com.

[67] V. Radicci et al. A comparison on radiation tolerance of <100> and <111> silicon substrates of microstrip detectors. *Nucl. Instrum. Meth.*, A476:744–750, 2002. http://dx.doi.org/10.1016/S0168-9002(01)01667-9.

[68] N. Demaria et al. New results on silicon microstrip detectors of CMS tracker. *Nucl. Instrum. Meth. A*, 447:142–150, 2000. http://dx.doi.org/10.1016/S0168-9002(00)00182-0.

[69] G. Lutz. *Semiconductor Radiation Detectors*. Springer, 2001. http://dx.doi.org/10.1007/978-3-540-71679-2.

[70] C. J. Schmidt. Determination of the optimum sensor thickness. CBM-STS Note, GSI, 2017.

[71] H. Malygina. Private communication, 2017.

[72] L. Long, C. J. Schmidt, and J. M. Heuser. Fine-tuning of p-spray parameters for double-sided silicon strip sensors. CBM-STS Note 2017-1, GSI, 2017.

[73] T. Wittig. Private communication, 2018.

[74] E. Barberis et al. Capacitances in silicon microstrip detectors. *Nucl. Instrum. Meth.*, A342:90–95, 1994. http://dx.doi.org/10.1016/0168-9002(94)91414-1.

[75] S. Braibant et al. (CMS). Investigation of design parameters and choice of substrate resistivity and crystal orientation for the CMS silicon microstrip detector. CMS-NOTE 2000-011, 2000.

[76] L. Borrello, A. Messineo, E. Focardi, et al. (CMS). Sensor Design for the CMS Silicon Strip Tracker. CMS-NOTE 2003-020, 2003.

[77] I. Momot, M. Teklishyn, C. Simons, et al. (CBM). Charge collection studies of silicon microstrip sensors with different read-out bonding configurations using perpendicular β-particles. *CBM Progress Report 2016*, page 28, 2017. http://repository.gsi.de/record/201318.

[78] A. Affolder et al. Radiation damage in the LHCb Vertex Locator. *JINST*, 8:P08002, 2013. arXiv:1302.5259, http://dx.doi.org/10.1088/1748-0221/8/08/P08002.

[79] I. Momot, J. M. Heuser, H. Malygina, et al. (CBM). Charge collection of n-irradiated prototype CBM-STS microstrip sensors. *CBM Progress Report 2015*, page 26, 2016. http://repository.gsi.de/record/186952.

[80] V. Dobishuk, J. M. Heuser, V. Pugatch, et al. (CBM). Characterization of the CBM06H6 double-metal silicon sensor readout via 20 cm long microcables. *CBM Progress Report 2017*, page 27, 2018.

[81] W. Zubrzycka and K. Kasinski (CBM). Noise considerations for the STS/MUCH readout ASIC. *CBM Progress Report 2017*, page 32, 2018. http://dx.doi.org/10.15120/GSI-2018-00485.

[82] L. Rossi, P. Fisher, T. Rohe, et al. *Pixel Detectors: From Fundamentals to Applications*. Springer, 2006. http://dx.doi.org/10.1007/3-540-28333-1.

[83] Hamamatsu Photonics K.K. Stealth Dicing Technology and Applications. Technical Information TLAS9004E, 2005. https://www.hamamatsu.com/resources/pdf/etd/SD_tech_TLAS9004E.pdf.

[84] J. M. Heuser. Private communication, 2017.

[85] I. Momot, J. M. Heuser, M. Teklishyn, et al. (CBM). Charge collection efficiency of irradiated STS silicon micro-strip sensors. *CBM Progress Report 2017*, page 23, 2018. http://dx.doi.org/10.15120/GSI-2018-00485.

[86] I. Momot, J. M. Heuser, M. Teklishyn, et al. Evaluation of the STS sensor prototypes irradiated with 23 MeV proton beam using relativistic beta-electrons. CBM-STS Note 2018-1, GSI, 2018.

[87] item Industrietechnik GmbH. [Online; accessed 22-August-2016], https://www.item24.de/en/productworld/building-kit-system/item-profiles/.

[88] THOME Präzision GmbH. [Online; accessed 11-January-2022], https://www.thome-precision.com/.

[89] National Instruments LabVIEW. [Online; accessed 30-September-2020], https://www.ni.com.

[90] Aerotech GmbH. [Online; accessed 12-January-2022], https://www.aerotech.com/motion-and-positioning/.

[91] Gebr. Becker GmbH. [Online; accessed 21-January-2022], https://www.becker-international.com/de/en/.

[92] Norgren GmbH. [Online; accessed 21-January-2022], https://www.norgren.com/de/en/list/directional-control-valves.

[93] Cascade Microtech, Inc (FormFactor, Inc.). [Online; accessed 21-January-2022], https://www.formfactor.com/products/probes/.

[94] Signatone Corporation. [Online; accessed 21-January-2022], https://www.signatone.com/products/tips_holders/.

[95] Navitar. [Online; accessed 23-January-2022], https://navitar.com/products/imaging-optics/high-magnification-imaging/12x-zoom-motorized/.

[96] StarLight Opto-Electronics GmbH. [Online; accessed 23-January-2022], https://shop.starlight-oe.com/en/microscopy/fiber-optic/cold-light-sources-48/.

[97] The Imaging Source Europe GmbH. [Online; accessed 23-January-2022], https://www.theimagingsource.com/products/industrial-cameras/usb-3.0-color/dfk23u274/.

[98] F. James and M. Roos. Minuit - a system for function minimization and analysis of the parameter errors and correlations. *Computer Physics Communications*, 10(6):343–367, 1975. `http://dx.doi.org/https://doi.org/10.1016/0010-4655(75)90039-9`.

[99] National Instruments. *NI Vision Concepts Manual*. National Instruments Corporation, 2005. 372916E-01, `https:/ni.com/info`.

[100] E. Lavrik. *Development of quality assurance procedures and methods for the CBM Silicon Tracking System*. Dissertation, Eberhard Karls Universität Tübingen, 2017. `https://cbm-wiki.gsi.de/cgi-bin/view/Public/Thesis2017`.

[101] E. Lavrik, U. Frankenfeld, S. Mehta, et al. High-precision contactless optical 3D-metrology of silicon sensors. *Nucl. Instrum. Meth. A*, 935:167–172, 2019. arXiv:1812.00917, `http://dx.doi.org/10.1016/j.nima.2019.04.039`.

[102] E. Lavrik, M. Shiroya, H. R. Schmidt, et al. Optical inspection of the silicon micro-strip sensors for the CBM experiment employing artificial intelligence. *Nucl. Instrum. Meth. A*, 1021:165932, 2022. arXiv:2107.07714, `http://dx.doi.org/10.1016/j.nima.2021.165932`.

[103] Keithley Instruments. *Model 2400 Series SourceMeter User's Manual*. Keithley Instruments, Inc., 28775 Aurora Road, Cleveland, Ohio 44139, 7 edition, 2002. 2400S-900-01 Rev. G.

[104] Keithley Instruments. *Model 6487 Picoammeter/Voltage Source Reference Manual*. Keithley Instruments, Inc., 28775 Aurora Road, Cleveland, Ohio 44139, 1 edition, 2002. 6487-901-01 Rev. A.

[105] IET Labs. *7600+ Precision LCR Meter User and Service Manual*. IET Labs, Inc., 1 Expy Plaza, Roslyn Heights, NY 11577, 2014. 7600+ im, `https://www.ietlabs.com`.

[106] Keithley Instruments. *Models 707B and 708B Switching Matrix User's Manual*. Keithley Instruments, Inc., 28775 Aurora Road, Cleveland, Ohio 44139, 2013. 707B-900-01 Rev. B.

[107] Keithley Instruments. *Model 7072-HV High Voltage Semiconductor Matrix Card Instruction Manual*. Keithley Instruments, Inc., 28775 Aurora Road, Cleveland, Ohio 44139, 2002. 7072-HV-901-01 Rev. B.

[108] J. L. Agram et al. The silicon sensors for the Compact Muon Solenoid tracker: Design and qualification procedure. *Nucl. Instrum. Meth.*, A517:77–93, 2004. `http://dx.doi.org/10.1016/j.nima.2003.08.175`.

[109] D. Soyk, H. Faber, and C. J. Schmidt (CBM). Capacitance studies of the CBM STS microcable stack-up. *CBM Progress Report 2016*, pages 44–45, 2017. `http://repository.gsi.de/record/201318`.

[110] ROOT Data Analysis Framework. [Online; accessed 30-September-2020], https://root.cern.

[111] A. Chilingarov. Temperature dependence of the current generated in Si bulk. *JINST*, 8(10):P10003, 2013. http://dx.doi.org/10.1088/1748-0221/8/10/P10003.

[112] F. Hartmann. Evolution of Silicon Sensor Technology in Particle Physics. *Springer Tracts Mod. Phys.*, 231:204, 2009.

[113] O. Bertini, K. Schuenemann, M. Shiroya, et al. (CBM). Basic electrical inspection of silicon microstrip sensors for the STS. *CBM Progress Report 2020*, (2021-00421):16–19, 2021. http://dx.doi.org/10.15120/GSI-2021-00421.

[114] J. Bohm et al. Evaluation of the bulk and strip characteristics of large area n-in-p silicon sensors intended for a very high radiation environment. *Nucl. Instrum. Meth.*, A636:S104–S110, 2011. http://dx.doi.org/10.1016/j.nima.2010.04.093.

[115] P. R. Turner (LHCb Liverpool VELO Group). VELO module production: Sensor testing. LHCb-NOTE 2007-072, 2007.

[116] A. Bischoff, N. Findeis, D. Hauff, et al. Breakdown protection and long term stabilization for Si detectors. *Nucl. Instrum. Meth.*, A326:27–37, 1993. http://dx.doi.org/10.1016/0168-9002(93)90329-G.

[117] L. Evensen, A. Hanneborg, B. S. Avset, et al. Guard ring design for high voltage operation of silicon detectors. *Nucl. Instrum. Meth.*, A337:44–52, 1993. http://dx.doi.org/10.1016/0168-9002(93)91136-B.

[118] D. Bisello, M. Da Rold, L. Franzin, et al. Radiation effects on breakdown in silicon multiguarded diodes. *Nuovo Cim.*, A109:1343–1350, 1996. http://dx.doi.org/10.1007/BF02773520.

[119] G. A. Beck, A. A. Carter, T. W. Pritchard, et al. Radiation-tolerant breakdown protection of silicon detectors using multiple floating guard rings. *Nucl. Instrum. Meth.*, A396:214–227, 1997. http://dx.doi.org/10.1016/S0168-9002(97)00749-3.

[120] L. Andricek et al. Design and test of radiation hard p+ n silicon strip detectors for the ATLAS SCT. *Nucl. Instrum. Meth.*, A439:427–441, 2000. http://dx.doi.org/10.1016/S0168-9002(99)00901-8.

[121] O. Koybasi, G. Bolla, and D. Bortoletto. Guard Ring Simulations for n-on-p Silicon Particle Detectors. *IEEE Transactions on Nuclear Science*, 57(5):2978–2986, 2010. http://dx.doi.org/10.1109/TNS.2010.2063439.

[122] J. Schwandt. *Design of a Radiation Hard Silicon Pixel Sensor for X-ray Science*. Dissertation, Universität Hamburg, 2014.

[123] J. Rahn. Depletion characteristics of silicon microstrip detectors. (SCIPP-93-12), 1993.

[124] G. Auzinger. *Silicon Sensor Development for the CMS Tracker Upgrade*. Ph.D. thesis, CERN, 2013-10-22.

[125] RF Cafe. Coaxial Cable Specifications. [Online; accessed 10-January-2019], `http:/www.rfcafe.com/references/electrical/coax-chart.htm`.

[126] G. Giacomini. *Noise characterization of silicon strip detectors - comparison of sensors with and without integrated JFET source-follower.*. Ph.D. thesis, Trieste U., 2007.

[127] L. Bardelli, G. Poggi, G. Pasquali, et al. A method for non-destructive resistivity mapping in silicon detectors. *Nucl. Instrum. Meth.*, A602:501–505, 2009. `http://dx.doi.org/10.1016/j.nima.2009.01.033`.

[128] M. Hufschmidt, E. Fretwurst, E. Garutti, et al. The influence of edge effects on the determination of the doping profile of silicon pad diodes. *Nucl. Instrum. Meth.*, A867:231–236, 2017. arXiv:1605.00778, `http://dx.doi.org/10.1016/j.nima.2017.04.020`.

[129] J. M. Heuser, L. Long, and S. Chatterji. Prototype microstrip sensor CBM05: Description of wafer properties, layout, dimensions and cross section. CBM-STS Note 2013-02, GSI, 2013.

[130] D. Dannheim. *The Silicon Strip Detectors of the ZEUS Microvertex Detector*. Ph.D. thesis, Hamburg U., 1999. `http://www-library.desy.de/cgi-bin/showprep.pl?desy-thesis99-027`.

[131] G. Dellacasa et al. (ALICE). ALICE technical design report of the inner tracking system (ITS). 1999.

[132] S. Lindgren et al. Testing of surface properties pre-rad and post-rad of n-in-p silicon sensors for very high radiation environment. *Nucl. Instrum. Meth.*, A636:S111–S117, 2011. `http://dx.doi.org/10.1016/j.nima.2010.04.094`.

[133] H. F. W. Sadrozinski et al. Punch-through protection of SSDs in beam accidents. *Nucl. Instrum. Meth.*, A658(1):46–50, 2011. `http://dx.doi.org/10.1016/j.nima.2011.06.085`.

[134] K. Hara, N. Hamasaki, Y. Takahashi, et al. Design of Punch-Through Protection of Silicon Microstrip Detector against Accelerator Beam Splash. *Phys. Procedia*, 37:838–843, 2012. `http://dx.doi.org/10.1016/j.phpro.2012.02.427`.

[135] M. Mikestikova et al. Study of surface properties of ATLAS12 strip sensors and their radiation resistance. *Nucl. Instrum. Meth.*, A831:197–206, 2016. http://dx.doi.org/10.1016/j.nima.2016.03.056.

[136] J. Fernández Tejero. *Design and Optimization of Advanced Silicon Strip Detectors for High Energy Physics Experiments.* Dissertation, Barcelona, Autonoma U., 2020. https://inspirehep.net/literature/1844635.

[137] K. Kasinski, W. Zubrzycka, and R. Szczygiel (CBM). Towards STS-XYTERv2.1, a new STS/MUCH prototype readout chip. *CBM Progress Report 2017*, page 30, 2018. http://dx.doi.org/10.15120/GSI-2018-00485.

[138] Keithley Instruments. *Low Level Measurements Handbook: Precision DC Current, Voltage, and Resistance Measurements.* 28775 Aurora Road, Cleveland, Ohio 44139, 7 edition, 2014. https://download.tek.com/document/LowLevelHandbook_7Ed.pdf.

[139] G.-F. Dalla Betta, M. Boscardin, and L. Bosisio. A comparative evaluation of integrated capacitors for AC-coupled microstrip detectors. *Nucl. Instrum. Meth.*, A411(2):369–375, 1998. http://dx.doi.org/10.1016/S0168-9002(98)00332-5.

[140] V. Kulibaba, N. Maslov, S. Potin, et al. Interstrip Resistance of a Semiconductor Microstrip Detector. *Problems of Atomic Science and Technology*, 5:180–182, 2001.

[141] IET Labs. *LCR Measurement Primer, 1st Edition.* IET Labs, Inc., 2018. 030122, https://www.ietlabs.com.

[142] E. Barberis et al. Measurement of interstrip and coupling capacitances of silicon microstrip detectors. In *IEEE 1992 Nuclear Science Symposium and Medical Imaging Conference (NSS/MIC 1992) Orlando, Florida, October 26-31, 1992*, pages 198–200. 1992. http://lss.fnal.gov/archive/other/scipp-92-14.pdf.

[143] K. Yamamoto, K. Yamamura, et al. A study on the interstrip capacitance of double-sided silicon strip detectors. *Nucl. Instrum. Meth. A*, 326(1):222–227, 1993. http://dx.doi.org/10.1016/0168-9002(94)91440-0.

[144] J. P. Alexander et al. Studies of double sided, double metal silicon strip detectors. *Nucl. Instrum. Meth. A*, 342:282–286, 1994. http://dx.doi.org/10.1016/0168-9002(94)91440-0.

[145] E. Barberis et al. Analysis of capacitance measurements on silicon microstrip detectors. *IEEE Trans. Nucl. Sci.*, 41:785–790, 1994. http://dx.doi.org/10.1109/23.322807.

[146] S. Braibant et al. Investigation of design parameters for radiation hard silicon microstrip detectors. *Nucl. Instrum. Meth. A*, 485:343–361, 2002. http://dx.doi.org/10.1016/S0168-9002(01)02120-9.

[147] M. Mikestikova, Z. Kodek, and J. Stastny (ATLAS Upgrade Strip Sensor). Evaluation of Bulk and Surface Radiation Damage of Silicon Sensors for the ATLAS Upgrade. *PoS*, Vertex2014:050, 2015. http://dx.doi.org/10.22323/1.227.0050.

[148] M. Frautschi, M. Hoeferkamp, and S. Seidel. Capacitance measurements of double-sided silicon microstrip detectors. *Nuclear Instruments and Methods in Physics Research Section A: Accelerators, Spectrometers, Detectors and Associated Equipment*, 378(1):284–296, 1996. http://dx.doi.org/https://doi.org/10.1016/0168-9002(96)00467-6.

[149] D. Bortoletto, A. F. Garfinkel, A. D. Hardman, et al. Capacitance measurements of double-metal double-sided silicon microstrip detectors. *Nucl. Instrum. Meth.*, A383:104–109, 1996. http://dx.doi.org/10.1016/S0168-9002(96)00663-8.

[150] D. Pitzl, R. Eichler, W. Erdmann, et al. Evaluation of double sided, AC coupled, double metal silicon strip detectors for H1 at HERA. *Nucl. Instrum. Meth. A*, 348:454–460, 1994. http://dx.doi.org/10.1016/0168-9002(94)90779-X.

[151] A. Rodriguez Rodriguez. *The CBM Silicon Tracking System front-end electronics : from bare ASIC to detector characterization, commissioning and performance*. Dissertation, Goethe University Frankfurt, 2019. Dissertation, Goethe University Frankfurt, 2020, https://repository.gsi.de/record/234795.

[152] F. Lehner, P. Sievers, O. Steikamp, et al. Description and evaluation of multi-geometry silicon prototype sensors for the LHCb Inner Tracker. 2002.

[153] G. Baumann et al. (LHCb). Pre-series sensor qualification for the Inner Tracker of LHCb. LHCb-NOTE 2005-037, 2005.

[154] J. Gassner, S. Heule, F. Lehner, et al. Capacitance measurements on silicon micro-strip detectors for the TT station of the LHCb experiment. 2003.

[155] A. Rodriguez Rodriguez, J. Lehnert, A. Lymanets, et al. (CBM). Verification of the STS-XYTERv2.1 energy calibration using a 241-Am source. *CBM Progress Report 2020*, (2021-00421):26–27, 2021. http://dx.doi.org/10.15120/GSI-2021-00421.

[156] O. Maragoto Rodriguez, J. Lehnert, A. Lymanets, et al. (CBM). Test and characterization of fully assembled STS modules. *CBM Progress*

Report 2020, (2021-00421):36–37, 2021. http://dx.doi.org/10.15120/GSI-2021-00421.

[157] U. Frankenfeld, J. Lehnert, A. Lymanets, et al. (CBM). Integration of mSTS Unit 3 and evaluation of ladder operation performance. *CBM Progress Report 2020*, (2021-00421):42, 2021. http://dx.doi.org/10.15120/GSI-2021-00421.

[158] M. Pöttgens. *Development and Evaluation of Test Stations for the Quality Assurance of the Silicon Micro-Strip Detector Modules for the CMS Experiment*. Ph.D. thesis, Aachen, Tech. Hochsch., 2007. http://cds.cern.ch/record/1292761.

[159] LTspice XVII (x64). [Online; accessed 4-September-2021], https://www.analog.com/en/design-center/design-tools-and-calculators/ltspice-simulator.html.

[160] H. Malygina. Detector inefficiency study. CBM-STS Workgroup Meeting / Private communication, 2016. https://indico.gsi.de/event/3886/.

[161] K. Kasinski and W. Zubrzycka (The STS Workgroup). Consequences of Pinholes in STSXyter Operation. STS Module and Ladder Assembly CBM-TN-20004, GSI, 2020.

[162] I. Panasenko, H. R. Schmidt, E. Lavrik, et al. (CBM). A Custom Probe Station for Testing of CBM Silicon Strip Detectors. *CBM Progress Report 2019*, (CBM-PR-2019):20, 2020. http://dx.doi.org/10.15120/GSI-2020-00904.

[163] Win Way Technology Co., Ltd. [Online; accessed 16-November-2021], https://www.winwayglobal.com/.

[164] O. Bertini. Private communication, 2020. Dedicated test sockets for the CBM microstrip sensors.

[165] E. Lavrik, M. Shiroya, O. Bertini, et al. (CBM). Results of the series optical inspection of STS silicon micro-strips sensors. *CBM Progress Report 2020*, (2021-00421):22–24, 2021. http://dx.doi.org/10.15120/GSI-2021-00421.

List of Figures

1.1. The number of readout channels versus the silicon area for the strip detectors of the particle physics experiments 3
1.2. Sketch of the phase diagram of strongly-interacting matter represented in the plane of temperature and baryochemical potential . . . 5
1.3. Interaction rates achieved by existing and planned heavy ion experiments as a function of center-of-mass energy 7
1.4. The CBM experimental setup 8
1.5. The Silicon Tracking System of the CBM experiment 9
1.6. STS detector component prototypes 10
1.7. Dependence of the track reconstruction efficiency and momentum resolution of the Silicon Tracking System on the overall system noise . 12

2.1. Layouts of the CBM silicon microstrip sensors manufactured by Hamamatsu and CiS 13
2.2. Schematic view of the n side of the CBM microstrip sensor manufactured by CiS 16
2.3. Strip grid of the CBM microstrip sensor 17
2.4. A photo of the CBM microstrip sensors of 4 different sizes 19
2.5. Interconnecting technologies for short strips of the CBM prototype sensors 20
2.6. A close-up view of the polysilicon resistors of the CiS and Hamamatsu sensors 21
2.7. Schematic drawing of the guard ring structure of the CBM sensor manufactured by CiS 22
2.8. Alignment marks in the corners of the CiS and Hamamatsu sensors . 23
2.9. Strip numbering scheme for CBM06 prototype sensors 24

3.1. View of the custom-built probe station which is installed in a cleanroom at the University of Tübingen 30
3.2. Custom-made multi-zone vacuum chuck for the CBM microstrip sensors 32
3.3. Schematic representation of three coordinates frames of the probe station: motors, camera, microstrip sensor 34
3.4. Characterization of the optical system of the probe station 35
3.5. Calibration grid for the optical system of the probe station 36
3.6. Principles of sensor alignment and coordinate calibration 38
3.7. Example of the acquired focus curve with a fitted Lorentzian function 39
3.8. Measurement of the object height by auto-focusing method 40

3.9. Height map of the p side of the CBM prototype sensor obtained with auto-focusing method 41
3.10. Z profile of the AC pad row and the corresponding positioning profile used for height adjustment during the electrical inspection of strips . 42
3.11. Performance estimation of the probe station in terms of accuracy and repeatability of the positioning of the sensor under the probe needle 43
3.12. The scheme of connection of devices to the switching matrix of the probe station 45
3.13. Capacitance measurement with the probe station 46
3.14. Gain error compensation method that is implemented in the probe station 47
3.15. Results of the electrical performance cross-check using CMS test-structures 48
3.16. Results of the capacitance measurements of the STS micro-cables . . 49
3.17. The graphical user interface of the probe station control program . . 50
3.18. Camera, sensor, and system tabs of the probe station control program 51
3.19. The graphical user interface of the electrical inspection program . . . 53
3.20. Summary window of the strip electrical inspection 54

4.1. Connection scheme for the total leakage current measurement of the microstrip sensor 57
4.2. Current-voltage characteristic of the microstrip sensor manufactured by CiS and determination of its breakdown voltage 58
4.3. Current-voltage characteristics of the investigated CBM06 prototype sensors 59
4.4. The slope of the IV curves of the investigated sensors. 60
4.5. Guard ring structure of the CBM06 sensor manufactured by CiS . . 61
4.6. Connection scheme for simultaneous measurement of bias and guard ring currents of the microstrip sensor 62
4.7. Bias and guard ring currents of the CBM06H12 sensor as a function of the bias voltage 63
4.8. Potentials of *p*- and *n*-side guard rings as a function of the bias voltage of the CBM06H12 sensor 64
4.9. Typical bias and guard ring currents as a function of the bias voltage of CBM06 prototype sensors manufactured by CiS 65
4.10. Potentials of the 14 floating guard rings of the CiS sensor as a function of the bias voltage and as a function of the GR position relative to the bias ring at V_{bias} = 100, 200, 300 and 400 V 66
4.11. Leakage current and guard ring potentials as a function of the bias voltage of the CBM06C12 prototype sensor 67
4.12. Edge region of the CBM06C12 sensor 342463-21 with deep large-scale chips 68
4.13. Potentials of the 14 floating guard rings of the CBM06C6 sensor with short circuit between the four innermost rings 69
4.14. Manufacturing and handling defects of the guard ring structure detected on the CBM06C6 sensor 353090-11 69

4.15. IV characteristics of the CBM06C2 sensor with different numbers of active guard rings on the p side 70
4.16. Connection scheme for measurement of the CV characteristic of the microstrip sensor 73
4.17. Bulk capacitance and phase angle as a function of bias voltage measured at different frequencies of the test signal 74
4.18. Bulk capacitance as a function of test frequency at different bias voltages and for sensors of different sizes 75
4.19. CV characteristic and its properties 77
4.20. Frequency dependence of the bulk capacitance for the case with a floating and grounded voltage source 79
4.21. Comparison of the full depletion voltages and bulk resistivity that were determined in this work with the data provided by the vendors for the investigated CBM06 sensors 81
4.22. Comparison of the total sensor thickness determined by electrical and optical methods 82
4.23. Connection scheme for measurement of the leakage current of an individual strip 84
4.24. Equivalent circuit of the p side of the CBM microstrip sensor with a picoammeter connected between the DC pad and the bias ring to measure the strip leakage current 85
4.25. Measured leakage current of each strip of the 17 investigated CBM06 sensors 86
4.26. Comparison between the measured strip current on the p and n sides and the total leakage current 87
4.27. Correlation between irregular strip leakage current and visually identified defects 88
4.28. Connection scheme for the DC resistance measurement of one strip on the CBM06 sensor 90
4.29. Equivalent circuit of the p side of the CBM microstrip sensor with a picoammeter and a voltage source connected between the DC pad and the bias ring to measure the DC resistance 91
4.30. DC resistance measurement: IV curve for one strip of the p side of the CBM06H2 sensor 92
4.31. Measured DC strip resistance of 23 CBM06 prototype sensors under investigation 94
4.32. Dependence of the measured DC resistance on the physical length of the strip for the investigated sensors 95
4.33. Polysilicon bias resistance of the investigated CBM06 prototype sensors determined in the DC resistance measurements 96
4.34. Dependence of the DC resistance of the strip on the bias voltage for the CBM06H12 sensor 97
4.35. The observed non-uniformity of the measured DC resistance of the short strips on the p side of the Hamamatsu sensors 98

4.36. Drawings of the punch-through structures of the CBM06 microstrip sensor manufactured by CiS . . . 99
4.37. Equivalent circuit of one strip with its PTP structures on the *p* side of the CBM prototype sensor . . . 100
4.38. IV characteristic and effective resistance of one strip on the *p* side of the CBM06C6 sensor . . . 102
4.39. Effective resistance R_{eff} as a function of the test voltage for all investigated CBM06 sensors . . . 103
4.40. Connection schemes for the metal strip resistance measurement on the CBM microstrip sensors . . . 104
4.41. Strip metal resistance measurement: IV curve for one strip of the CBM06H4 sensor . . . 105
4.42. Equivalent circuit for the metal strip resistance measurement . . . 106
4.43. Metal strip resistance of the investigated CBM06 prototype sensors . 108
4.44. Connection schemes for measurement of the coupling capacitance of one strip . . . 110
4.45. Frequency dependence of the coupling capacitance measured in the AC-BR configuration on the CBM06C6 sensor . . . 112
4.46. Equivalent circuit of one strip, where physically distributed capacitance and resistance are represented as a series combination of *RC* stages . . . 113
4.47. Frequency dependence of the coupling capacitance measured on the *p* side of CBM06 sensors of different sizes using the $C_s - R_s$ model . 114
4.48. Equivalent circuit models of a strip for estimation of the measured coupling capacitance . . . 116
4.49. Frequency dependence of the coupling capacitance and the effect of grounding on its measurement . . . 118
4.50. Frequency dependence of the coupling capacitance measured in the AC-DC configuration on the CMS baby-sensor from the “standard half-moon” structure . . . 120
4.51. Bias voltage dependence of the coupling capacitance measured in the AC-DC configuration on both sides of the CBM06 sensors . . . 121
4.52. Needles placement for the coupling capacitance measurement in AC-DC and AC-BR configurations . . . 122
4.53. Measured coupling capacitance C_m of the 32 investigated CBM06 prototype sensors of all sizes . . . 124
4.54. Coupling capacitance of the investigated CBM06 prototype sensors . 125
4.55. Normal distribution of coupling capacitance of a single strip and stray capacitance of an open circuit measured in AC-DC configuration . . 126
4.56. Connection scheme for measurement of the strip backplane capacitance 128
4.57. Frequency dependence of the strip backplane capacitance measured with and without grounding of neighboring strips around the central one . . . 129

4.58. Equivalent circuit of three strips of the CBM microstrip sensor with the LCR meter connected for the strip backplane capacitance measurement . . . 130
4.59. Capacitance-Voltage characteristic of one strip and the entire bulk of the CBM06H4 sensor . . . 131
4.60. Strip backplane capacitance of the investigated CBM06 prototype sensors . . . 132
4.61. Connection schemes for measurement of the interstrip capacitance of a microstrip sensor . . . 135
4.62. Equivalent circuit models of the gap between two strips for the estimation of the interstrip capacitance . . . 137
4.63. Equivalent circuit of four strips of the CBM microstrip sensor with the LCR meter connected to measure interstrip capacitance in a 4-probe configuration . . . 138
4.64. Frequency dependence of the interstrip capacitance measured on both sides of the CBM06 sensors in a 4-probe configuration . . . 139
4.65. Frequency dependence of the interstrip capacitance measured on the CBM06H6 sensor in different configurations . . . 140
4.66. Bias voltage dependence of the interstrip capacitance measured on both sides of the CBM06 sensors in a 4-probe configuration . . . 141
4.67. Location of the needles on the AC pads and arrangement of the probes inside the probe station for the interstrip capacitance measurement in the 4-probe configuration . . . 143
4.68. Frequency dependence of the interstrip capacitance measured on both sides of the CBM06 sensor in a 4-probe configuration with and without correction for the gain error . . . 144
4.69. Measured interstrip capacitance C_{is} of 28 investigated CBM06 prototype sensors of all sizes . . . 145
4.70. Interstrip capacitance of the investigated CBM06 prototype sensors . 146
4.71. Normal distribution of interstrip capacitance to one neighbor and stray capacitance of an open circuit measured in the 4-probe configuration . . . 147
4.72. Frequency dependence of the interstrip capacitance measured on the p side of the CBM06 sensors of batch 353090 . . . 148
4.73. Equivalent circuit of the p side of the CBM microstrip sensor representing the additional capacitive network due to the overlap capacitance C_{ov} introduced by one 2nd metal line . . . 150
4.74. Equivalent circuit of the p side of the CBM microstrip sensor representing one strip with the additional capacitive network due to the overlap capacitance C_{ov} with all 2nd metal lines . . . 151
4.75. Additional capacitance of the short strips due to the overlap between the 2nd metal routing line and all strips of the 1st metal layer . . . 152
4.76. Total strip capacitance of the investigated CBM06 prototype sensors 155
4.77. Connection schemes for testing of the coupling capacitors . . . 159
4.78. Examples of the pinhole test results . . . 161

5.1. SPICE model for simulating CBM microstrip sensors 165
5.2. SPICE simulation of the frequency dependence of the strip coupling capacitance measured in the AC-DC and AC-BR configurations for both sides of the CBM06 microstrip sensor 169
5.3. Dependence of the capacitance simulated in the AC-DC configuration on the R_{imp}/R_{poly} ratio 170
5.4. SPICE simulation of the influence of the electrical parameters of the strip on the coupling capacitance determined in the AC-DC and AC-BR configurations 171
5.5. SPICE simulation of the bulk capacitance measured for the CBM06 microstrip sensor at a bias voltage of 100 V 173
5.6. SPICE simulation of the frequency dependence of the interstrip capacitance measured in the 4-probe configuration for both sides of the CBM06 microstrip sensor 174
5.7. SPICE simulation of the influence of the electrical parameters of the strip on the interstrip capacitance determined in the 4-probe configuration 176
5.8. SPICE simulation of the frequency dependence of the p-side interstrip capacitance measured for CBM06 microstrip sensors from batch 353090 177
5.9. SPICE model for simulation of the strip leakage current measurement of the CBM06 prototype sensors 178
5.10. Dependence of the strip current on the R_{imp}/R_{poly} ratio 178

6.1. Dependence of the track reconstruction efficiency and the momentum resolution of the Silicon Tracking System on the fraction of non-operational (dead) channels in the detector modules 181
6.2. Typical strip defects of the microstrip sensors that can be identified visually 183
6.3. CBM Quality Test Center at the GSI Detector Laboratory 186
6.4. Test socket with pogo pins for CBM microstrip sensors 187
6.5. CBM microstrip sensor under the probe needles that are positioned to contact the AC pads of the first two strips 188
6.6. Schematic representation of broken and shorted strips of the microstrip sensor 190
6.7. SPICE simulation of the capacitance and resistance parameters for the AC-BR configuration and for various defect types 191
6.8. Application of the median filter and local thresholds to strip data for detection of defective strips 193
6.9. A flowchart diagram representing the process of defect recognition . 194
6.10. Map of accumulated defective strips for n and p sides of the CBM sensors 196

List of Tables

2.1. Properties of the silicon wafers for the CBM microstrip sensors . . . 25
2.2. Geometrical properties of the CBM microstrip sensors 26
2.3. Electrical properties of the CBM microstrip sensors 27
2.4. The number of sensors required for the construction of the STS . . . 28

3.1. Aerotech motor axes specifications 31

4.1. Summary of the results of testing coupling capacitors on the CBM06 prototype sensors 162

5.1. Initial values of the electrical parameters for the SPICE model of the CBM microstrip sensor 166

6.1. Description of the electrical quality control tests 185
6.2. Results of the defect recognition for the prototype sensor 10938-5552-301 195

A.1. List of the investigated CBM microstrip sensors 199

B.1. Bulk parameters of the CBM prototype sensors extracted in the IV-CV measurements 201

C.1. The configuration of the switching matrix channels for electrical measurements performed in this work 203

Acknowledgments

First of all, I would like to thank my supervisor, Prof. Dr. Hans Rudolf Schmidt, for the incredible opportunity to work in detector research. Under his guidance, I was able to complete the path from the development and construction of the custom test station, characterization and simulation of prototypes, to the final qualification of series production of the CBM sensors. The success of my work was largely dependent on his detailed feedback on sensor testing, ideas and advice. I am especially grateful to him for carefully proofreading the dissertation, for many useful comments and remarks, and for his patience. Working in his group gave me a better understanding of the high-energy physics and detector fields.

Furthermore, I am sincerely grateful to Prof. Dr. Valerii Pugach for introducing me to the CBM experiment and developing my interest in silicon detectors.

I would like to express my deep gratitude to Dr. Anton Lymanets, who guided me at the beginning of my work, helped me enter the field of microstrip sensor quality assurance, supported me and provided useful advice and discussions.

I would like to express my special thanks to Dr. Evgenii Lavrik for our cooperation on quality assurance tasks, for discussing the results of microstrip sensor testing, for sharing his experience with NI LabVIEW, and for his support.

I would like to thank Dr. Christian J. Schmidt, who provided critical feedback on my first measurements, which initiated a detailed study of the sensor capacitances. Special thanks to Dr. Johann M. Heuser and Dr. Ulrich Frankenfeld for helpful feedback on microstrip sensor testing, which led to an efficient quality control process.

Special thanks to Kshitij Agarwal for many productive discussions on our projects, helpful feedback and support, and of course football news. I would also like to thank Dr. Hanna Malygina for our productive discussions on microstrip sensors, for sharing the results of her work and for her support. I thank my colleagues Olga Bertini, Evgenia Momot, Shaifali Mehta, Eduard Friske, Elena Volkova, Shahid Khan, Das Susovan, Martin Völkl. It was really a pleasure to work with all of them. I am also thankful to the CBM-STS group for the friendly atmosphere.

For proof-reading of my thesis and many helpful comments, I am indebted to Prof. Dr. Hans Rudolf Schmidt, Dr. Anton Lymanets, Kshitij Agarwal, Dr. Olga Bertini.

Finally, I would like to express my sincere gratitude to my school physics teacher Yuriy Buryak, who opened the world of physics to me.